

Extracellular Vesicles and the Glioblastoma Microenvironment

Sybren Lein Nikola Maas

**Extracellular Vesicles and
the Glioblastoma Microenvironment**

**Extracellulaire membraanblaasjes en
de directe omgeving van glioblastomen**
(met een samenvatting in het Nederlands)

Proefschrift

ter verkrijging van de graad van doctor aan de Universiteit Utrecht op gezag van
de rector magnificus, prof. dr. H.R.B.M. Kummeling, ingevolge het besluit van het
college voor promoties in het openbaar te verdedigen op
donderdag 4 april 2019 des middags te 12.45 uur

door

Sybren Lein Nikola Maas

geboren op 10 september 1985
te Utrecht

Extracellular Vesicles and the Glioblastoma Microenvironment

© Sybren Lein Nikola Maas 2019

ISBN: 978-90-393-7104-6

Cover design: Elisa Calamita, persoonlijkproefschrift.nl

Layout and design: Elisa Calamita, persoonlijkproefschrift.nl

Printing: Ridderprint BV | www.ridderprint.nl

The printing of this thesis was financially supported by BCRM, Chipsoft and Distrilab BV.

Promotor: Prof. dr. P.A.J.T. Robe

Copromotor: Mr. dr. M.L.D. Broekman

Table of Contents

Chapter 1	General Introduction	7
Chapter 2	Quantification of nanosized extracellular membrane vesicles with scanning ion occlusion sensing	33
Chapter 3	Possibilities and limitations of current technologies for quantification of biological extracellular vesicles and synthetic mimics	65
Chapter 4	Glioblastoma-derived extracellular vesicles modify the phenotype of monocytic cells	97
Chapter 5	Glioblastoma Hijacks Microglial Transcriptional Networks independently of TREM2	135
Chapter 6	Summary and Discussion	189
Addenda	Nederlandse Samenvatting	208
	List of publications	216
	Curriculum vitae	218
	Dankwoord	220

Dit proefschrift werd (mede) mogelijk gemaakt met financiële steun van Stichting Chanrone, De Hersenstichting, Rene Vogels Stichting, Schumacher Kramer Foundation, Vrienden van het UMCU, KWF en het Nijbakker-Morra Stipendium

1

General Introduction

Adapted from:

Extracellular Vesicles: Unique Intercellular Delivery Vehicles

Sybren L.N. Maas^{1,2}, Xandra O. Breakefield¹ and Alissa M. Weaver³

¹Department of Neurology and Center for Molecular Imaging Research, Department of Radiology, Massachusetts General Hospital and Program in Neuroscience, Harvard Medical School, Boston, MA 02114, USA. ²Department of Neurosurgery, Brain Center Rudolf Magnus, Institute of Neurosciences, University Medical Center, Heidelberglaan 100, 3584 CX Utrecht, The Netherlands ³Departments of Cancer Biology and Cell and Developmental Biology, Vanderbilt University School of Medicine and Department of Pathology, Microbiology, and Immunology, Vanderbilt University Medical Center, Nashville, TN 37232, USA

Trends in Cell Biology 27 (3), 172-188 (2017)

And:

Multidimensional communication in the microenvirons of glioblastoma

Marieke L. Broekman^{1,2}, Sybren L.N. Maas^{1,2}, Erik R. Abels¹, Thorsten R. Mempel^{3,4}, Anna M. Krichevsky⁵, Xandra O. Breakefield¹

¹Department of Neurology and Center for Molecular Imaging Research, Department of Radiology, Massachusetts General Hospital and Program in Neuroscience, Harvard Medical School, Boston, MA, USA. ²Department of Neurosurgery, Brain Center Rudolf Magnus, Institute of Neurosciences, University Medical Center, Heidelberglaan, Utrecht, Netherlands. ³The Center for Immunology and Inflammatory Diseases and Department of Medicine, Massachusetts General Hospital, Charlestown, MA, USA. ⁴Program in Immunology, Harvard Medical School, Boston, MA, USA. ⁵Department of Neurology, Ann Romney Center for Neurologic Diseases, Initiative for RNA Medicine, Brigham and Women's Hospital and Harvard Medical School, Boston, MA, USA.

Nature Reviews Neurology 14, 482-495 (2018)

Glioblastomas are the most common primary brain tumors in adult patients¹. Because of their diffuse invasive nature, total surgical resection of glioblastoma is not possible, resulting in recurrence even after adjunctive chemo- and radiotherapy¹. With no significant changes to the standard of care in the past 20 years, median lifespan from time of diagnosis to death remains about 15 months for patients undergoing surgery and adjuvant chemo- and radiotherapy^{1,2}. This bleak outcome has stimulated ongoing efforts to reveal new insights into tumor components and surrounding cells in order to develop new strategies for keeping this tumor at bay.

Recent studies and new technologies have provided a deeper layer of understanding of what makes these tumors so formidable, but have also demonstrated the complexity of glioblastoma tumors. Deep sequencing of the genome and transcriptome together with study of the epigenome of glioblastoma cells has revealed both genetic and epigenetic differences among tumor cells within the same glioblastoma, with basically many of the genetic drivers being represented in almost every glioblastoma^{3,4}.

The 2016 WHO classification system for diffuse glioma now defines subtypes of intrinsic brain tumors that predict their prognosis, importantly mutations in IDH1/2 and chromosome 1p/1q co-deletions confer a better outcome⁵. Experimental transcriptome classification has defined three molecular subtypes in glioblastoma wild-type IDH tumors: proneural, classical, and mesenchymal⁴. Bulk analysis of a glioblastoma tumor will render a dominant molecular subclass, but work on the single cell level has revealed that glioblastoma tumors harbor individual cells from all three subclasses^{3,4}. Additionally, 45 driver genes have been found in glioblastoma⁶, with common driver mutations including TP53, ATRX, TERT, NF1, PTEN and EGFR⁵. All together, this illustrates that glioblastoma is heterogeneous and thus most likely will require combinatorial approaches for different subtypes of tumor cells even within a single glioblastoma tumor.

Along with a deeper understanding of the genetic and phenotypic variability within glioblastoma, the field has also gained increasing awareness of the ability of these tumors to manipulate normal cells in the brain to subservise the tumor⁷. Almost all cell types in the tumor environs are affected. This includes stimulation of angiogenesis and co-option of existing vasculature⁸, suppression of immune cell functions⁹, disarming of microglia and macrophages that are supposed to recognize and fight off foreign elements in the brain^{10,11}, seduction of astrocytes to join in tumor-support¹², and even

changes in the extracellular matrix (ECM) to facilitate invasion¹³. On the flip side, new insights into the presence of adaptive immune cells in the brain and the presence of a central nervous system (CNS) lymphatic system^{14,15} might give rise to therapeutics opportunities through manipulation of this system to recognize tumor neo-antigens¹⁶, as currently clinically applied for some melanoma and lung cancer patients. Overall, glioblastoma recruits normal cells in its environs to promote growth, sustenance and encroachment of the tumor into the brain (**Figure 1**).

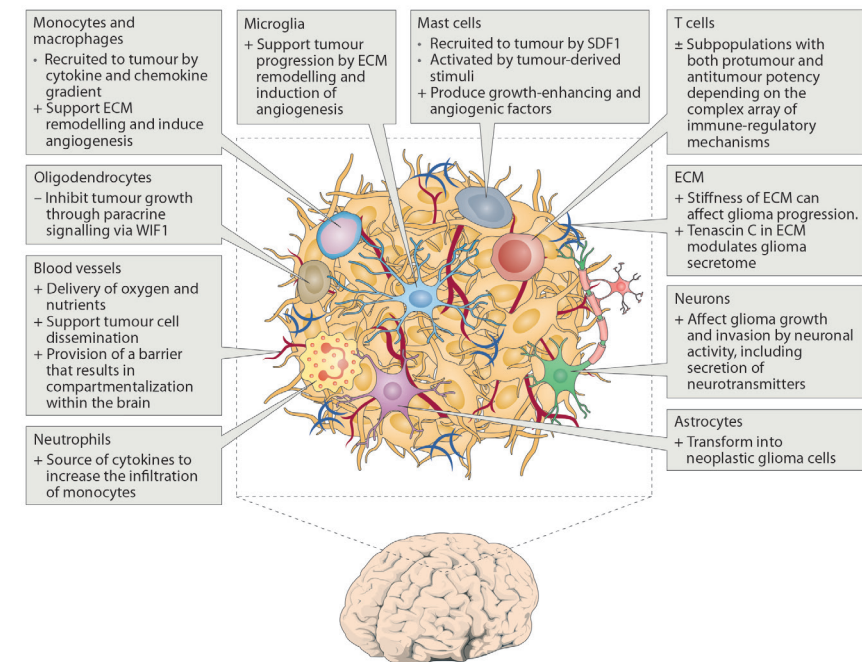


Figure 1: Glioblastoma microenvironment. The glioblastoma environ consists of tumour cells, extracellular matrix (ECM), blood vessels, innate immune cells (monocytes, macrophages, mast cells, microglia and neutrophils), T cells and non- tumorous neurons, astrocytes and oligodendrocytes. +, protumour function; -, antitumour function; ±, mixed protumour and antitumour functions; SDF1, stromal cell-derived factor 1; WIF1, WNT inhibitory factor 1.

Interaction between glioblastoma and microglia, monocytes or macrophages.

The glioblastoma micro- environment contains brain-resident microglia and infiltrating monocytes. Once monocytes have infiltrated the tumor, they can differentiate into macrophages^{26,27}^{17,18}. Although often grouped together under the term tumor-

associated macrophages or myeloid cells (TAMs), these cells represent distinctly different populations¹⁷. Microglia are derived from immature yolk sac progenitors during early embryonic development and maintain themselves in the brain through self-renewal^{19,20}. In non-pathological settings, microglia are the main innate immune cells in the brain and are important in the defense against pathogens and noxious stimuli²¹. Glioblastoma leads to some disruption of the blood–brain barrier (BBB), which enables bone marrow haematopoietic stem cell-derived monocytes and macrophages to infiltrate the tumor^{17,18,22}. Studies have shown that in specific cases up to 50% of the glioblastoma mass can consist of TAMs¹¹. Chimeric and cell lineage models have shown that the exact composition of TAMs changes over time^{17,22}. One study examined the infiltration of peripheral immune cells in a chimeric GL261 mouse glioma model that received head-protected irradiation, in which BBB disruption due to irradiation is avoided. Fluorescently tagged myeloid-derived monocytes and macrophages transplanted into these mice constituted up to 25% of TAMs in the glioblastoma tumor after 21 days, with lower percentages of myeloid-derived TAMs observed at earlier time points²². The influx of myeloid-derived monocytes in mouse glioblastoma tumors was confirmed in a haematopoietic stem cell lineage tracing model, in which >35% of TAMs were myeloid-derived¹⁷. As such, the population of glioblastoma TAMs can progress from strictly microglial in early phases to a mixture of microglia and infiltrating monocytes and macrophages in late phases of tumor progression. In mice, accurate separation of microglia and macrophages can be obtained by fluorescence-activated cell sorting using α M integrin (also known as CD11b) and receptor-type tyrosine-protein phosphatase C (also known as CD45) markers¹⁷. In humans, α 4 integrin (also known as CD49D) can accurately separate these two cell types in tumors¹⁷. In this chapter, when studies used these specific markers for separation of microglia and myeloid-derived cells we refer to the cellular subpopulation studied, otherwise the generic term ‘TAMs’ is used.

TAM recruitment.

The recruitment of TAMs to glioma is mostly mediated by cytokine and chemokine gradients released by glioblastoma cells (**Figure 2**). These factors have been extensively reviewed elsewhere and include CC-chemokine ligand 2 (CCL2; also known as MCP1) and CCL7 (also known as MCP3), glial cell line-derived neurotrophic factor (GDNF), hepatocyte growth factor (HGF), SDF1, tumor necrosis factor (TNF), VEGF, ATP, macrophage colony-stimulating factor 1 (CSF1) and granulocyte–macrophage colony-stimulating factor (GM–CSF)^{11,23}. TAMs can also be recruited to a specific subset of

glioblastoma cells, such as oligodendrocyte transcription factor 2 (OLIG2)-expressing and transcription factor SOX2-expressing tumor-initiating cells, which secrete periostin to recruit TAMs^{34,24}. Medical interventions can also stimulate TAM recruitment; for example, intracranial biopsies can increase infiltration of circulating monocytes into the tumor in a CCL2-dependent manner²⁵. Microglia and macrophages themselves also secrete CCL2 to increase infiltration of CCR2+Ly6C+ monocytes, thus creating a positive feedback loop for the continued infiltration of myeloid cells²⁶.

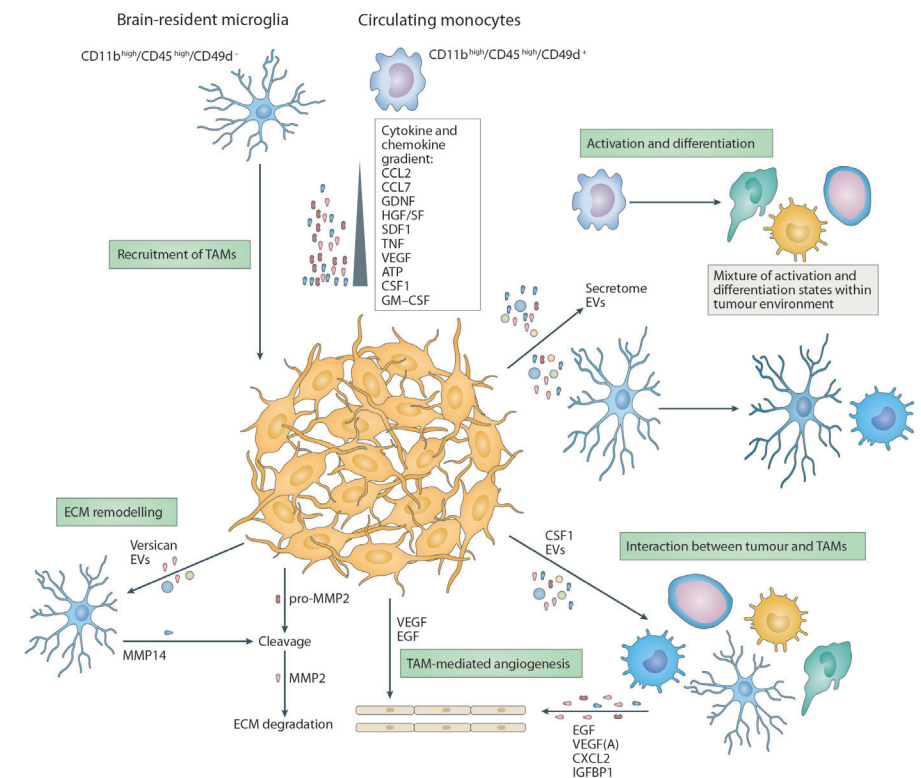


Figure 2: Interactions between glioma and TAMs. Recruitment of tumour-associated macrophages or myeloid cells (TAMs), including blood monocytes and brain-resident microglia, is based on the gradient of chemokines and cytokines released by the glioblastoma cells. Once recruited, TAMs can be activated and differentiated under the influence of the secretome and extracellular vesicles (EVs) released by the tumour. The various recruited and activated TAMs can affect tumour growth by promoting angiogenesis through secretion of epidermal growth factor (EGF), vascular endothelial growth factor (VEGF), CX-chemokine ligand 2 (CXCL2) and insulin-like growth factor-binding protein 1 (IGFBP1). This process is further promoted by the release of tumour-derived VEGF and EGF. Invasion and growth of the tumour are accomplished by remodelling the extracellular matrix (ECM) surrounding the tumour. For example, versican and EVs from the tumour induce the release of matrix metalloproteinase 14 (MMP14) by microglia. The release will facilitate the cleavage of tumour-derived pro-MMP2 following extracellular degradation by the active enzyme MMP2. CCL2, CC-chemokine ligand 2 (also known as MCP1); CSF1, macrophage colony-stimulating factor 1; GDNF, glial cell line-derived neurotrophic factor; HGF, hepatocyte growth factor; SDF1, stromal cell-derived factor 1; TNF, tumour necrosis factor.

TAM activation state.

Interaction between glioblastoma cells and TAMs is multifactorial and occurs both in close proximity by direct cell–cell contact and distantly by the release of soluble and membrane-encased factors. This secretome consists of a multitude of molecules, including soluble lipids, cytokines and chemokines^{23,27}. Glioblastomas also release extracellular vesicles (EVs) that contain a cargo of many types of molecules that have been shown to influence TAM status in a combinatorial way in culture and *in vivo*^{28,29}. Ultimately, the combination and timing of all glioblastoma-released factors determine the activation state and function of TAMs.

The traditional model of the activation states of TAMs describes a binary system of either tumor-suppressive (M1) or tumor-supportive (M2) macrophages³⁰. This model was based on stimulation of cells in culture by IFN γ , lipopolysaccharide (LPS) or IL-4 and was later extended to include M2 subtypes activated by other types of stimulation, comprising M2a (IL-4 and IL-13), M2b (immune complexes, Toll-like receptor (TLR) or IL-1R) and M2c (IL-10)³¹. However, RNA sequencing extended the number of stimuli to a combination of 28 known factors and revealed that a wide spectrum of activation states could be induced. The findings demonstrated that macrophage differentiation is much more complex than the binary M1–M2 model³², even when stimulated in culture. This complexity became more apparent when microglia, monocytes and macrophages were isolated from glioblastoma *in vivo* and analysed by RNA sequencing. The most upregulated genes were found to be shared between traditional M1, M2a, M2b and M2c transcriptomes, suggesting that the activation state *in vivo* is very different from that in culture^{17,33–35}. Single-cell sequencing confirmed that activation of both M1 and M2 signatures can be observed even in individual cells in an *in vivo* brain trauma model³⁶. Consequently, the M1 and M2 designations are being replaced by more precise situation-specific models³⁰. Altogether, these findings suggest that TAMs express gene sets *in vivo* that are associated with stimulation by different factors, highlighting the variety of information transfer in the tumor microenvironment.

TAMs contribute to tumor proliferation.

The role of secreted molecules on TAM function and, subsequently, on tumor growth has been studied extensively¹¹. This interplay between glioblastoma cells and TAMs is especially apparent in tissue remodeling and is necessary for glioblastoma cells to infiltrate the brain. One group of proteins that is crucial in tissue remodelling is matrix metalloproteinases (MMPs)³⁷. In glioblastoma, MMP2 has an important role in

ECM degradation, which facilitates glioblastoma cell migration and invasion³⁸. MMP2 is released in a precursor form (pro-MMP2) that is cleaved by MMP14 to an active state¹¹. However, glioblastoma cells secrete pro-MMP2, but not MMP14. Conversely, microglia in the tumor microenvironment are a major source of MMP14. Two different glioblastoma-derived factors act to increase microglial MMP14 release^{29,39}. First, the ECM protein versican is released from glioma and induces MMP14 release by TAMs through its upstream receptor TLR2³⁹. Second, studies of cell-culture models have shown that glioblastoma-derived EVs can also induce microglial expression of MMP14 RNA, although the mechanism and *in vivo* relevance remain to be elucidated²⁹.

Owing to their rapid growth, glioblastomas are in constant need of neovascularization and release angiogenic factors, such as EGF and VEGF²³. Additionally, in glioblastoma, microglia and macrophages accumulate around blood vessels and also produce the pro-angiogenic chemokines VEGF and CXC-chemokine ligand 2 (CXCL2)⁴⁰. Furthermore, glioblastoma cells might promote angiogenesis indirectly through microglial cells, as CSF1 secreted by glioblastoma cells *in vitro* induces microglia cells to release insulin-like growth factor-binding protein 1 (IGFBP1), which can induce angiogenesis⁴¹. RAGE (receptor for advanced glycation end products; also known as AGER) is thought to play a part in a number of diseases, including tumors. In tumor-bearing mice, RAGE ablation increases survival by reducing the levels of VEGFA secreted by infiltrating TAMs, which results in leaky (rather than fully developed) vasculature and disturbed tumor perfusion⁴². Thus, TAMs have a crucial role in tumor angiogenesis through multiple signaling mechanisms.

Overall, the interaction between glioblastoma and TAMs is bidirectional and multifactorial. This plethora of paracrine loops can determine the ultimate effects of TAMs on tumor growth and can differ depending on local variables such as hypoxia, the extent of necrosis, TAM infiltration density and/or TAM activation state.

Novel modes of intercellular communication in the glioblastoma micro-environment

This glioblastoma “take over” of the brain involves multiple types of communications and directives exchanged among tumor cells and surrounding cells. Soluble factors secreted by cells that serve as signaling molecules by binding to receptors on target cells, including TGF- β , IL6, Notch, PDGF, EGF, VEGF, SDF-1 have been discussed above. The importance of other routes of communication are now actively investigated (**Figure**

3). These newly recognized transit routes can transmit “non-secretable” molecules, including transcription factors, directive RNAs and DNA, and even mitochondria and nuclei. One mode of communication is transfer of molecules between adjacent cells through gap junctions. Gap junctions allow for the transfer of Ca^{2+} , ATP, metabolites and microRNAs (miRNAs) between adjacent cells^{43,44}. Connexins, which form a structural component of these junctions, are associated with increased invasiveness of gliomas⁴⁵. Tumor cells can also be linked up by “tunneling” nanotubes and microtubes which form gap junctions or a cytoplasmic continuum between cells to allow transport of both molecules and organelles⁴⁶⁻⁴⁸. Microtubes are implicated in regrowth of tumors after surgery and conferring resistance to chemotherapy⁴⁹, although they are not apparent in some glioma models²⁸. Transfer of non-secretable proteins and nucleic acids through EVs, briefly discussed before, is another mode of intercellular communication that is actively studied. This thesis focuses (in part) on the interaction of glioblastoma tumor cells and cells of the innate immune system through EVs.

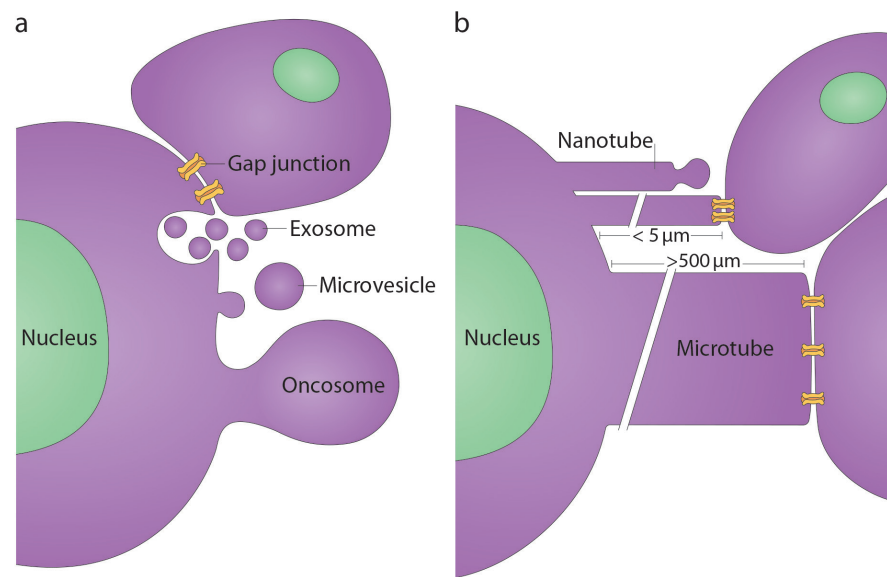


Figure 3: routes of communication between tumour cells and cells in their environs. (A) Gap junctions (24 nm in diameter) form across the adjacent membranes of cells that are in physical contact, enabling the passage of small molecules. Cells also release exosomes (50–100 nm) from multivesicular bodies that fuse with the plasma membrane. In addition, microvesicles (100–200 nm) and even large oncosomes (1–10 μm) bud off from the plasma membrane and can interact with and be taken up by other cells. **(B)** Tunnelling nanotubes (50–200 nm in width and up to 5 μm in length) extend out from cells and can either bud off vesicles at their tips or form gap junctions with other cells. Microtubes extend out from tumour cells (1–2 μm in width and >500 μm in length) and can form gap junctions with other cells.

Extracellular vesicles

It has become increasingly clear that cells release vesicles of varying sizes through both the endosomal pathway and by budding from the plasma membrane. These vesicles are referred to by a variety of names, including exosomes, microvesicles (ectosomes), microparticles and oncosomes, collectively termed EVs. Interest in EVs was stoked by the finding that they contain RNA^{50,51}, with the implication that their protein and RNA content might be transferred between cells as a previously unrecognized form of intercellular communication. Indeed, the structure of EVs allows for protected and directed transfer of informative molecules between cells. Initial studies found both mRNAs and non-coding RNAs (ncRNAs), such as miRNAs, stably contained within EVs and showed that these molecules together with other EV cargo could be transferred to recipient cells in culture with functional consequences.

Different cell types are continuously exchanging EVs over short and long distances in vivo. In addition to their functions in communication, these vesicles also serve to eliminate molecules from cells, such as modified RNA⁵² and amyloid proteins⁵³. These “discarded cargoes”, however, can have consequences to neighboring cells, such as spreading of neuropathological diseases through the brain through toxic amyloids⁵³.

A number of EV subtypes have been characterized. Traditionally, exosomes are small EVs (sEVs; < 150 nm) released through multivesicular bodies (MVBs) in the endosomal pathway. Vesicles can also bud off the plasma membrane, apparently in a manner similar to that of retroviruses⁵⁴, forming EVs in the 200–500 nm range. These shed vesicles are called microvesicles or ectosomes. However, smaller vesicles (~100 nm) have also been described to bud from the plasma membrane and may be isolated together with exosomes⁵⁵. Other modes of release include formation of EVs at the ends of microvillar-like protrusions, which can be accentuated by increased cellular content of hyaluronan⁵⁶. In cancer cells, even larger EVs (1–10 μm in diameter), termed large oncosomes, can bleb off the cell membrane^{57,58}. In addition, when cells undergo apoptosis they dissociate into membrane bound apoptotic bodies of different sizes, which are hard to distinguish from other types of EVs, but may contain relatively more genomic DNA. A major challenge for the future and a current focus of the field is to both define and isolate distinct subpopulations, either according to their biogenesis mechanism or their molecular content.

EVs are unique in that they can be viewed as cell “biopsies” that are released as free, relatively stable entities that can distribute over short and long distances within the extracellular spaces and biofluids of organisms. Their stability is attributed in part to the lipid content of their membranes, which are enriched in cholesterol, sphingomyelin, annexin, phosphatidylserine and glycosphingolipids, as compared to the cellular plasma membrane⁵⁹. EVs have the ability to protect internal cargo and the potential to deliver it to specific cell types through ligand-receptor interactions. One intriguing parameter is their potential to cross tissue barriers. Several studies even support their ability to cross the blood-brain barrier (e.g. ⁶⁰). Although the mechanism is not known, one possibility is that EVs transcytose through endothelial cells, entering a cell through the endocytic system and exiting through MVBs. Their potential for addressability and barrier penetration makes them promising therapeutic delivery vehicles⁶¹. Their universal presence in all biofluids, release from all different cell types in the body, changes in molecular content based on cell of origin and pathophysiological state of cells makes them remarkable biomarkers⁶².

EVs are thought to be formed by multiple mechanisms. In all cases, lipid curvature must be induced to form either an inward-budding vesicle within the endocytic system (exosomes) or an outward budding vesicle at the plasma membrane (microvesicles). For exosomes, several mechanisms have been described. The best-characterized mechanism involves recruitment of the endosomal sorting complex required for transport (ESCRT) machinery to ubiquitinated proteins in the early endosome. The ESCRT machinery consists of four protein complexes (ESCRT-0, -I, -II, and -III) along with accessory proteins (Alix, VPS4, VTA-1) that sequentially act to bind future exosome cargoes and form intraluminal vesicles (ILVs) incorporating those cargoes⁶³. Notably, the ESCRT-III complex forms spirals that induce the inward budding and fission of vesicles in order to form MVBs⁶⁴⁻⁶⁶. An alternate pathway of exosome formation, more recently described, involves synthesis of ceramide as a mechanism to induce vesicle curvature and budding⁶⁷. Certain cargoes have been shown to preferentially depend on ceramide synthesis^{67,68} for their presence in ILVs of MVB. A third mechanism that has been proposed for exosome biogenesis is tetraspanin-mediated organization of specific proteins, such as the amyloidogenic protein, premelanosome protein (PMEL)⁶⁹.

For EVs that are formed by direct budding from the plasma membrane, e.g. microvesicles, the molecular mechanisms of biogenesis are even less well characterized. One mechanism involves recruitment of the same ESCRT machinery that promotes formation

of ILVs in MVB and viral budding. Thus, both exosomes and microvesicles can be formed and pinched off through recruitment of the negative curvature-promoting ESCRT III proteins⁶³⁻⁶⁶. In one case, the adaptor protein, arrestin domain containing protein 1 (ARRDC1) was shown to recruit ESCRT proteins TSG101 (ESCRT-I) and VPS4 (accessory protein) to the plasma membrane⁵⁵. Vesicle budding can occur in response to plasma membrane wounding, as a mechanism to repair damaged membrane^{70,71}. Similar to exosome biogenesis, mechanisms that generate or alter asymmetry of the plasma membrane with respect to lipids also appear to be important⁷². These mechanisms include alterations in activity of enzymes that transfer lipids from one leaflet of the plasma membrane, such as flippases, floppases, and scramblases⁷³. Shedding of vesicles has been shown to occur from multiple aspects of the plasma membrane, including at microvillar protrusions of intestinal epithelial cells⁷⁴ and from cells engineered to overexpress hyaluronan synthase⁷⁵, as well as from cilia⁷⁶.

EV release.

Extracellular vesicles (EVs) are released from cells by a variety of mechanisms, depending on their mode of biogenesis⁷⁷ (**Figure 4**). Microvesicles are released quite simply when they pinch off from the cell surface. Exosomes, which derive from the endocytic system, are released when MVBs fuse with the plasma membrane. An alternate fate for MVBs is fusion with lysosomes, which leads to degradation and recycling of their protein, nucleotide and lipid contents. As exosomes carry growth factors and other signaling molecules, fusion of MVB with lysosomes should turn off autocrine signaling. By contrast, fusion with the plasma membrane to release exosomes directly into the cytoplasm could both promote autocrine and paracrine signaling. A number of steps could affect the intracellular decision to degrade or release exosomes, including intracellular transport of MVB along microtubules to the plasma membrane, creation of docking sites at the plasma membrane, or recruitment of Soluble NSF Attachment Protein Receptor (SNARE) proteins that mediate fusion with either lysosomes or the plasma membrane. In addition, autophagosomes have been shown to fuse with MVBs and target them to lysosomes. Molecular regulators implicated in exosome release include multiple molecules implicated in MVB docking including the GTPases Rab27a, Rab27b, Rab35, and Ra1A⁷⁸⁻⁸⁰, and the cortical actin regulator, cortactin⁸¹, as well as the fusion regulator synaptotagmin-7⁸².

The topology of EVs is similar to cells, with extracellular receptors and ligands positioned on the outside, and cytoplasmic proteins and RNAs on the inside. Thus, in order

for EVs to functionally communicate with cells, different types of interactions may be involved. This could include release of EV contents in the extracellular space, EV binding to the cell surface, EV-plasma membrane fusion, and uptake by endocytosis (**Figure 4**). For stimulation of cell signaling by EV-associated extracellular ligands, EVs may directly interact with cognate receptors located on the plasma membrane of cells (or vice versa). This recognition may also serve as a means of “addressing” EVs to certain cell types^{83,84}. Such ligand-receptor interactions likely accounts for many targeted biological effects of EVs, including those caused by EV-carried growth factors, angiogenic factors and extracellular matrix (ECM) proteins. For delivery of RNAs or cytoplasmic proteins, EVs must not only bind to, but also release their contents into recipient cells, either by direct fusion with the plasma membrane or with the endosomal membrane after endocytosis.

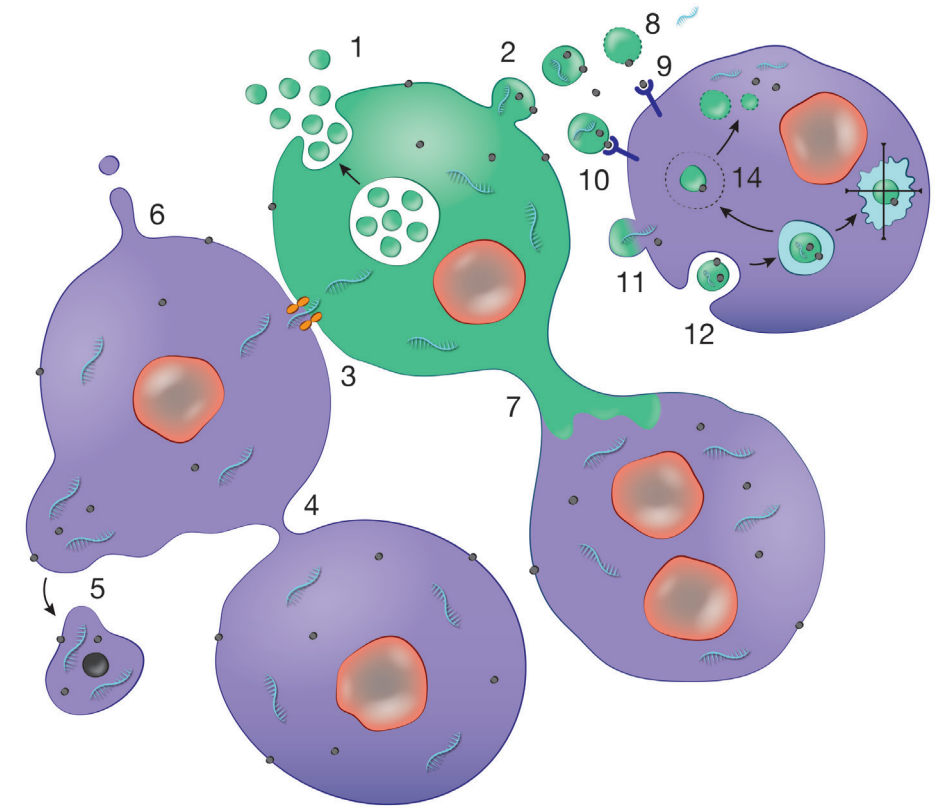


Figure 4. Cellular Sharing of Macromolecular Information. Cells have numerous ways of exchanging molecules that are facilitated by being maintained within a membrane boundary. These include deployment of extracellular vesicles (EVs) by: (1) release of exosomes through fusion of multivesicular bodies (MVBs) with the plasma membrane; and (2) budding of microvesicles off the plasma membrane. (3) In addition, cells in physical contact can form gap junctions allowing exchange of small molecules, including miRNAs. Other modes include: (4) connection of cells through nanotubes; (5) blebbing off of larger vesicles, especially from cancer cells (e.g. large oncosomes); (6) formation of membrane protrusions that release vesicles from their tips; and (7) larger-diameter microtubules connecting cells. In the case of EVs, there are numerous ways for information transfer: (8) lysis of vesicles in the extracellular space releasing their contents, including (9) free ligands and (10) ligands on the surface of vesicles, which stimulate receptors on the cell surface. Uptake of EV cargo can occur through: (11) fusion of the vesicle with the plasma membrane; or (12) uptake by different types of endocytosis. In the latter case, the fate of the vesicle and its contents can be: (13) progression through the degradative pathway to lysosomes; and/or (14) escape from the endosome compartment to release its contents into the cell cytoplasm, where they may be functional.

EVs in malignancies

As discussed before, the tumor microenvironment includes different normal cell types that function as an ecosystem to support tumor growth, invasion, and metastasis. These

tumor-associated cells include endothelial cells, fibroblasts, pericytes, histiocytes and infiltrating immune cells, as well as astrocytes, microglia and infiltrating macrophages in the brain⁸⁵. While cell-to-cell communication is often attributed solely to soluble chemokines, cytokines, small molecules and growth factors⁸⁵, in recent years a multitude of studies have implicated EVs as having a significant impact in the tumor microenvironment (**Figure 5**)⁸⁶.

As tumors progress, they outgrow the in situ vascular network, thereby generating hypoxic regions. Hypoxia induces the release of neo-vascularization-stimulating factors. In culture, after uptake of glioblastoma-derived EVs, levels of vascular endothelial growth factor (VEGF) increase in endothelial cells and activate the VEGF-receptor 2 in an autocrine manner⁸⁷. Under hypoxic conditions, glioblastoma-derived EVs are also enriched for hypoxia-regulated mRNAs and proteins. Compared to EVs produced under normoxic conditions, the EVs released from hypoxic tumors act to increase the activation of the ERK1/2 MAPK, PI3K/AKT, and FAK pathways in recipient endothelial cells, resulting in more endothelial cell sprouting - an early step in neo-vascularization⁸⁸.

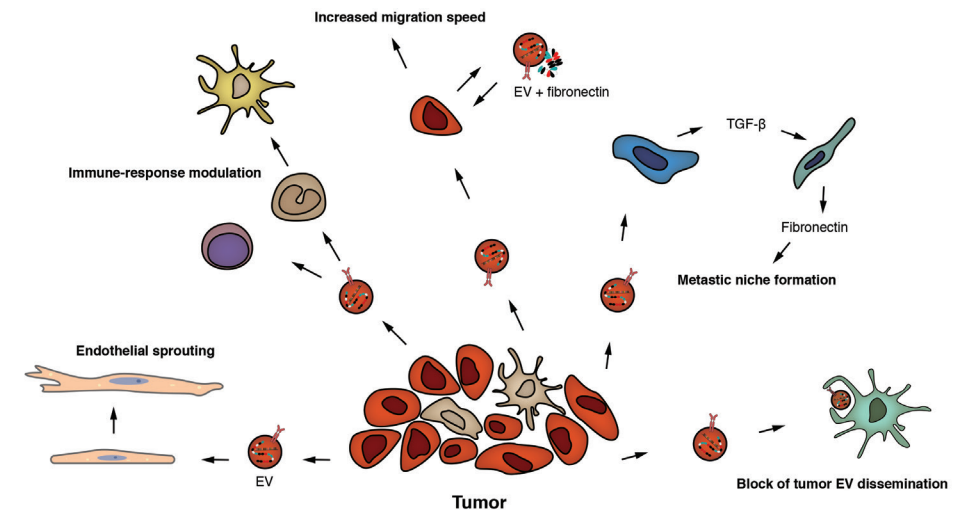


Figure 5. Role of Extracellular Vesicles (EVs) in Malignancies. Cancer-derived EVs influence both stromal and tumor cells. These EVs can induce endothelial sprouting and neovascularization. Incubation of cancer EVs with T cells leads to both apoptosis in CD8+ T cells and the expansion of CD4+ cells toward T regulatory cells. Monocytes differentiate toward a more tumor-supportive phenotype after incubation with cancer EVs. As cancer cells migrate, EVs from tumor cells can accelerate this process. EVs from malignant cancer cells induce less-malignant cells to migrate faster; however, the mechanism for this is unknown. Tumor cells load fibronectin onto EVs in an autocrine manner facilitating adhesion formation and rapid migration. Tumor-derived EVs can also establish metastatic niches at various locations. In the liver, cancer EVs induce transforming growth factor beta (TGF- β) production by Kupffer cells, which promotes fibronectin production by hepatic stellate cells. This fibrotic environment enhances retention of neutrophils and macrophages in the liver creating a favorable metastatic niche. In some cases, however, local cells may counter the effect of cancer EVs, such as subcapsular macrophages that limit dissemination of cancer EVs from lymph nodes.

Myofibroblasts are fibroblasts that are activated to express α -smooth muscle actin (α -SMA). Myofibroblasts are relatively absent in normal tissue, but highly present in the tumor microenvironment. Similar to their function in non-cancer fibrotic diseases, their pro-tumor function is probably in large part due to their secretion of different ECM components⁸⁵. In prostate cancer, cultured fibroblasts can be differentiated into myofibroblasts by uptake of prostate cancer EVs containing transforming growth factor (TGF)- β 1⁸⁹. In vivo, the synergy between fibroblasts and tumor cells in promoting tumor growth is reduced by knock-down of Rab27a in prostate cancer cells, a potential regulator of exosome release. However, it cannot be ruled out that the observed effects may be due to the effects of Rab27a knockdown on additional cellular processes or secretion modes.

The tumor microenvironment contains many immune cells, which are often inhibited in their ability to kill tumor cells. Recently, immune checkpoint therapy which targets inhibitory PD-1 and CTLA-4 signaling has been successful in treating subsets of patients with multiple tumor types by reactivating suppressed T and NK cells⁹⁰. TAMs are often implicated in this suppression and can also induce apoptosis in T cells through the expression of TRAIL and Fas ligand (FasL)⁹¹. Tumor-derived EVs are likely to influence this behavior by promoting an immunosuppressive macrophage phenotype. Thus, EVs from primary glioblastoma cells were shown to skew monocyte-to-macrophage differentiation towards a tumor supportive phenotype in culture²⁹. The presence of tumor cells also increased levels of miR-21 in microglia and macrophages in culture and *in vivo*, in association with changes in their phenotype²⁸. In an *in vivo* melanoma model, macrophages more distant from the tumor have also been found to interact with tumor-derived EVs in association with suppression of tumor growth. For example, subcapsular macrophages in lymph nodes can limit tumor growth by absorbing tumor-derived EVs and preventing them from interacting with pro-tumor B cells⁹².

Like TAMs, tumor cell-derived EVs can also directly induce apoptosis in activated T-cells. For example, co-incubation of head and neck squamous cell carcinoma or melanoma cell line-derived EVs, but not normal DC-derived EVs, induced apoptosis in CD8+ T-cells⁹³. The tumor-derived EVs were variably loaded with FasL, suggesting EV-FasL induced apoptosis is part of this cell death mechanism⁹³. Another mechanism by which EVs can suppress anti-tumor immunity is by altering the differentiation of CD4+ T helper cells. Thus, co-incubation of CD4+ T-cells with tumor EVs was shown to induce their differentiation towards CD4+CD25+FOXP3+ Treg cells that can suppress the cytotoxic T-cell response⁹³. Besides ligand-receptor interactions, the lipid composition of the EV-bilayer may also determine the effect of EVs on T-cells, as in ovarian cancer cell-derived EVs, phosphatidylserine linked to the outer leaflet of the EV bilayer is responsible for arresting the T-cell signaling cascade⁹⁴.

Tumor cell migration and invasion can be enhanced by EVs and likely facilitate local and distant spread of tumor cells. Some organ sites appear to be more hospitable to the metastatic seeding of particular tumor cells, termed "metastatic organotropism". Prior to formation of metastatic tumors by actual metastatic cells, these tissue sites may be primed by factors released from the primary tumors and are referred to as "pre-metastatic niches"⁹⁵. Recent studies suggest that tumor-derived EVs may be important priming factors that help set up metastatic niches, typically by interacting

with normal host cells at the metastatic site. For example, EVs from pancreatic ductal adenocarcinoma cells can initiate liver pre-metastatic niche formation by transferring migration inhibitory factor (MIF) to Kupffer cells in the liver⁸⁴. These Kupffer cells then secrete TGF- β that subsequently stimulates hepatic stellate cells to produce fibronectin. Fibronectin supports retention of macrophages and neutrophils in the liver, setting up an environment favorable for metastasis. In a syngeneic mouse model of melanoma, melanoma-derived exosomes induced lung vascular leakiness and recruited bone marrow-derived macrophages to metastatic sites⁹⁶. In addition to the role of tumor derived EVs implicated in tumor growth and progression EVs derived from normal cells can support tumor growth. For example, in metastases to the brain, EVs from astrocytes appear to have an important role in supporting local tumor growth⁹⁷. Astrocyte EV-mediated transfer of miR-19a to metastatic breast cancer cells reduced the levels of one of its target mRNAs encoding the tumor suppressor PTEN. In addition, uptake of astrocyte EVs by the metastatic cells induced chemokine CCL2 secretion promoting influx of microglial and myeloid-derived cells into the tumor microenvironment *in vivo*. Consistent with the tumor supportive role of these infiltrating cells, co-cultures of metastatic breast cancer cells and a microglial cell-line enhanced proliferation and inhibited apoptosis of the tumor cells⁹⁷.

The possible mechanisms through which certain EVs home to specific target organs and induce site-specific metastasis remains a major question. Recently, quantitative mass-spectrometry of EVs of breast or pancreatic cancer cell-lines that primarily metastasize to the lung, liver or both identified EV-integrin patterns associated with organotropic metastatic potential⁸³. EVs expressing $\alpha 6\beta 4$ and $\alpha 6\beta 1$ integrins were associated with lung metastasis, whereas those with $\alpha v\beta 5$ integrins were linked to liver metastatic potential. Conceptually, the idea that adhesion proteins can mediate metastasis to diverse sites has a certain appeal, as integrin-ECM or integrin-cell (e.g. Kupffer cells in the liver) interactions could target EVs to specific tissues or cell-types within tissues. However, it is difficult to accurately track the distribution of tumor-derived EVs in the body, and it seems likely that additional factors, such as selective vascular leakiness and the ECM of specific organs are critical in organotropism of metastasis⁹⁶. Together though, these studies suggest a role for tumor derived EVs in promoting both primary tumor growth and metastatic spread.

Aims and outline of this thesis

This thesis focuses on EVs in the glioblastoma microenvironment and specifically the interaction between glioblastoma cells and the innate immune system (i.e. microglia, monocytes and macrophages). Although research into the role of EVs in different aspects of biology is an active field of research, there are also fundamental challenges faced when working with EVs *in vitro* and *in vivo*. EVs have a diameter ranging from approximately 50 to 10,000 nm and thus the majority of EVs cannot be detected and characterized using techniques such as light microscopy or conventional flowcytometry. Therefore accurate and reproducible *in vitro* experiments are difficult to perform since simple standardizing the amount of EVs added to an experimental condition is a challenging task. This establishes the first aim of this thesis:

Aim 1: The development and evaluation of novel techniques to characterize EVs

As discussed in this chapter, research into the interaction between malignant cells and cells of the tumor micro-environment has lead to interesting observations that in general describe tumor supportive function of cells in the micro-environment after the uptake of malignant EVs. Some of this research was undertaken in glioblastoma models, however the extent of this interaction remains largely unknown. This establishes the second aim of this thesis:

Aim 2: The evaluation of the interaction between glioblastoma cells and microglia, monocytes and macrophages through EVs *in vitro* and *in vivo*

The research performed to reach these scientific aims are summarized and discussed in this thesis. In **chapter 2** tunable resistive pulse sensing (tRPS), also known as scanning ion occlusion sensing, is applied to different types of EVs and biological fluids to evaluate its capacity to characterize EVs. A novel method to apply tRPS is presenting using spiked-in control beads rather than using an external control run to characterize EVs. In **chapter 3**, three methods for the characterization of EVs are extensively tested and compared. Besides tRPS, modified methods for flow-cytometry (high-resolution flow cytometry) and nanoparticle tracking analysis are evaluated and compared. **Chapter 4** describes the results from experiments where EVs from glioblastoma cell-lines and primary cultures are added to peripheral blood mononuclear cells (PBMCs), isolated blood monocytes or microglia. The expression of cell surface proteins, cytokine expression and phagocytic capacity are discussed.

In **chapter 5** an *in vivo* model is discussed in which murine glioma derived EVs are fluorescently labeled and microglia and infiltrating monocytes and macrophages are separated and isolated using fluorescence-activated cell sorter (FACS). After sorting, RNA was isolated and extensive analysis of the RNA expression is discussed with a specific focus on the RNA expression of microglial cells that took up EVs. Finally, in **chapter 6**, the results presented in this thesis are discussed and future directions are presented.

References

1. Effects of radiotherapy with concomitant and adjuvant temozolomide versus radiotherapy alone on survival in glioblastoma in a randomised phase III study: 5-year analysis of the EORTC-NCIC trial. *10*, 459–466 (2009).
2. Brennan, C. W. *et al.* The somatic genomic landscape of glioblastoma. *Cell* **155**, 462–477 (2013).
3. Patel, A. P. *et al.* Single-cell RNA-seq highlights intratumoral heterogeneity in primary glioblastoma. *Science* **344**, 1396–1401 (2014).
4. Wang, Q. *et al.* Tumor Evolution of Glioma-Intrinsic Gene Expression Subtypes Associates with Immunological Changes in the Microenvironment. *Cancer Cell* **32**, 42–56.e6 (2017).
5. Louis, D. N. *et al.* The 2016 World Health Organization Classification of Tumors of the Central Nervous System: a summary. *Acta Neuropathologica* **131**, 803–820 (2016).
6. Parsons, D. W. *et al.* An integrated genomic analysis of human glioblastoma multiforme. *Science* **321**, 1807–1812 (2008).
7. Broekman, M. L. *et al.* Multidimensional communication in the microenvirons of glioblastoma. *Nature Reviews Neurology* **14**, 482–495 (2018).
8. Jhaveri, N., Chen, T. C. & Hofman, F. M. Tumor vasculature and glioma stem cells: Contributions to glioma progression. *Cancer Lett.* **380**, 545–551 (2016).
9. See, A. P., Parker, J. J. & Waziri, A. The role of regulatory T cells and microglia in glioblastoma-associated immunosuppression. *J Neurooncol* 1–8 (2015). doi:10.1007/s11060-015-1849-3
10. Roesch, S., Rapp, C., Dettling, S. & Herold-Mende, C. When Immune Cells Turn Bad—Tumor-Associated Microglia/Macrophages in Glioma. *Int J Mol Sci* **19**, 436–20 (2018).
11. Hambardzumyan, D., Gutmann, D. H. & Kettenmann, H. The role of microglia and macrophages in glioma maintenance and progression. *Nat. Neurosci.* **19**, 20–27 (2015).
12. Okolie, O. *et al.* Reactive astrocytes potentiate tumor aggressiveness in a murine glioma resection and recurrence model. *Neuro-Oncology* **18**, 1622–1633 (2016).
13. Pencheva, N. *et al.* Identification of a Druggable Pathway Controlling Glioblastoma Invasiveness. *Cell Rep* **20**, 48–60 (2017).
14. Aspelund, A. *et al.* A dural lymphatic vascular system that drains brain interstitial fluid and macromolecules. *J. Exp. Med.* **212**, 991–999 (2015).
15. Louveau, A. *et al.* Structural and functional features of central nervous system lymphatic vessels. *Nature* **523**, 337–341 (2015).
16. Boussiotis, V. A. & Charest, A. Immunotherapies for malignant glioma. *Oncogene* 1–21 (2018). doi:10.1038/s41388-017-0024-z
17. Bowman, R. L. *et al.* Macrophage Ontogeny Underlies Differences in Tumor-Specific Education in Brain Malignancies. *Cell Rep* **17**, 2445–2459 (2016).
18. Chen, Z. *et al.* Cellular and Molecular Identity of Tumor-Associated Macrophages in Glioblastoma. *Cancer Research* **77**, 2266–2278 (2017).
19. Ajami, B., Bennett, J. L., Krieger, C., Tetzlaff, W. & Rossi, F. M. V. Local self-renewal can sustain CNS microglia maintenance and function throughout adult life. *Nat. Neurosci.* **10**, 1538–1543 (2007).
20. Ginhoux, F. *et al.* Fate mapping analysis reveals that adult microglia derive from primitive macrophages. *Science* **330**, 841–845 (2010).
21. Hickman, S. E. *et al.* The microglial sensome revealed by direct RNA sequencing. *Nat. Neurosci.* **16**, 1896–1905 (2013).
22. Müller, A., Brandenburg, S., Turkowski, K., Müller, S. & Vajkoczy, P. Resident microglia, and not peripheral macrophages, are the main source of brain tumor mononuclear cells. *Int. J. Cancer* **137**, 278–288 (2014).
23. Li, W. & Graeber, M. B. The molecular profile of microglia under the influence of glioma. *Neuro-Oncology* **14**, 958–978 (2012).
24. Zhou, W. *et al.* Periostin secreted by glioblastoma stem cells recruits M2 tumour-associated macrophages and promotes malignant growth. *Nat Cell Biol* **17**, 170–182 (2015).
25. Alieva, M. *et al.* Preventing inflammation inhibits biopsy-mediated changes in tumor cell behavior. *Sci Rep* 1–14 (2017). doi:10.1038/s41598-017-07660-4
26. Chang, A. L. *et al.* CCL2 Produced by the Glioma Microenvironment Is Essential for the Recruitment of Regulatory T Cells and Myeloid-Derived Suppressor Cells. *Cancer Research* **76**, 5671–5682 (2016).
27. Wurdinger, T., Deumelandt, K., van der Vliet, H. J., Wesseling, P. & de Gruijl, T. D. Mechanisms of intimate and long-distance cross-talk between glioma and myeloid cells: how to break a vicious cycle. *Biochim. Biophys. Acta* **1846**, 560–575 (2014).
28. van der Vos, K. E. *et al.* Directly visualized glioblastoma-derived extracellular vesicles transfer RNA to microglia/macrophages in the brain. *Neuro-Oncology* nov244 (2015). doi:10.1093/neuonc/nov244
29. de Vrij, J. *et al.* Glioblastoma-derived extracellular vesicles modify the phenotype of monocytic cells. *Int. J. Cancer* **137**, 1630–1642 (2015).
30. Ransohoff, R. M. A polarizing question: do M1 and M2 microglia exist? *Nat. Neurosci.* **19**, 987–991 (2016).
31. Mantovani, A., Sozzani, S., Locati, M., Allavena, P. & Sica, A. Macrophage polarization: tumor-associated macrophages as a paradigm for polarized M2 mononuclear phagocytes. *Trends Immunol.* **23**, 549–555 (2002).
32. Xue, J. *et al.* Transcriptome-based network analysis reveals a spectrum model of human macrophage activation. *Immunity* **40**, 274–288 (2014).
33. Gabrusiewicz, K. *et al.* Characteristics of the Alternative Phenotype of Microglia/Macrophages and its Modulation in Experimental Gliomas. *PLoS ONE* **6**, e23902 (2011).
34. Szulzewsky, F. *et al.* Glioma-associated microglia/macrophages display an expression profile different from M1 and M2 polarization and highly express Gpnb and Spp1. *PLoS ONE* **10**, e0116644 (2015).
35. Szulzewsky, F. *et al.* Human glioblastoma-associated microglia/monocytes express a distinct RNA profile compared to human control and murine samples. *Glia* **64**, 1416–1436 (2016).
36. Kim, C. C., Nakamura, M. C. & Hsieh, C. L. Brain trauma elicits non-canonical macrophage activation states. *J Neuroinflammation* **13**, 1–12 (2016).
37. Kessenbrock, K., Plaks, V. & Werb, Z. Matrix metalloproteinases: regulators of the tumor microenvironment. *Cell* **141**, 52–67 (2010).
38. Du, R. *et al.* Matrix metalloproteinase-2 regulates vascular patterning and growth affecting tumor cell survival and invasion in GBM. *Neuro-Oncology* **10**, 254–264 (2008).
39. Hu, F. *et al.* Glioma-derived versican promotes tumor expansion via glioma-associated microglial/macrophages Toll-like receptor 2 signaling. *Neuro-Oncology* **17**, 200–210 (2014).
40. Brandenburg, S. *et al.* Resident microglia rather than peripheral macrophages promote vascularization in brain tumors and are source of alternative pro-angiogenic factors. *Acta Neuropathologica* **131**, 365–378 (2015).

41. Nijaguna, M. B. *et al.* Glioblastoma-derived Macrophage Colony-stimulating Factor (MCSF) Induces Microglial Release of Insulin-like Growth Factor-binding Protein 1 (IGFBP1) to Promote Angiogenesis. *J. Biol. Chem.* **290**, 23401–23415 (2015).
42. Chen, X. *et al.* RAGE Expression in Tumor-Associated Macrophages Promotes Angiogenesis in Glioma. *Cancer Research* **74**, 7285–7297 (2014).
43. Thuringer, D. *et al.* Transfer of functional microRNAs between glioblastoma and microvascular endothelial cells through gap junctions. *Oncotarget* **7**, 73925–73934 (2016).
44. Hong, X., Sin, W. C., Harris, A. L. & Naus, C. C. Gap junctions modulate glioma invasion by direct transfer of microRNA. *Oncotarget* **6**, 15566–15577 (2015).
45. Balça-Silva, J. *et al.* The Expression of Connexins and SOX2 Reflects the Plasticity of Glioma Stem-Like Cells. *Translational Oncology* **10**, 555–569 (2017).
46. Wang, X., Veruki, M. L., Bukoreshtliev, N. V., Hartveit, E. & Gerdes, H.-H. Animal cells connected by nanotubes can be electrically coupled through interposed gap-junction channels. *Proc. Natl. Acad. Sci. U.S.A.* **107**, 17194–17199 (2010).
47. Vignais, M.-L., Caicedo, A. X. S., Brondello, J.-M. & Jorgensen, C. Cell Connections by Tunneling Nanotubes: Effects of Mitochondrial Trafficking on Target Cell Metabolism, Homeostasis, and Response to Therapy. *Stem Cells International* 1–14 (2017). doi:10.1155/2017/6917941
48. Osswald, M. *et al.* Brain tumour cells interconnect to a functional and resistant network. *Nature* 1–19 (2015). doi:10.1038/nature16071
49. Weil, S. *et al.* Tumor microtubules convey resistance to surgical lesions and chemotherapy in gliomas. *Neuro-Oncology* **19**, 1316–1326 (2017).
50. Valadi, H. *et al.* Exosome-mediated transfer of mRNAs and microRNAs is a novel mechanism of genetic exchange between cells. *Nat Cell Biol* **9**, 654–659 (2007).
51. Skog, J. *et al.* Glioblastoma microvesicles transport RNA and proteins that promote tumour growth and provide diagnostic biomarkers. *Nat Cell Biol* **10**, 1470–1476 (2008).
52. Koppers-Lalic, D. *et al.* Nontemplated Nucleotide Additions Distinguish the Small RNA Composition in Cells from Exosomes. *Cell Rep* **8**, 1649–1658 (2014).
53. Coleman, B. M. & Hill, A. F. Extracellular vesicles – Their role in the packaging and spread of misfolded proteins associated with neurodegenerative diseases. *Semin. Cell Dev. Biol.* **40**, 89–96 (2015).
54. Gan, X. & Gould, S. J. Identification of an inhibitory budding signal that blocks the release of HIV particles and exosome/microvesicle proteins. *Molecular biology of the cell* **22**, 817–830 (2011).
55. Nabhan, J. F., Hu, R., Oh, R. S., Cohen, S. N. & Lu, Q. Formation and release of arrestin domain-containing protein 1-mediated microvesicles (ARMMs) at plasma membrane by recruitment of TSG101 protein. *Proc. Natl. Acad. Sci. U.S.A.* **109**, 4146–4151 (2012).
56. Rilla, K., Siiskonen, H., Tammi, M. & Tammi, R. Hyaluronan-coated extracellular vesicles--a novel link between hyaluronan and cancer. *Adv. Cancer Res.* **123**, 121–148 (2014).
57. Minciacchi, V. R., Freeman, M. R. & Di Vizio, D. Extracellular vesicles in cancer: exosomes, microvesicles and the emerging role of large oncosomes. *Semin. Cell Dev. Biol.* **40**, 41–51 (2015).
58. Di Vizio, D. *et al.* Large Oncosomes in Human Prostate Cancer Tissues and in the Circulation of Mice with Metastatic Disease. *AJPA* **181**, 1573–1584 (2012).
59. Record, M., Carayon, K., Poirot, M. & Silvente-Poirot, S. Exosomes as new vesicular lipid transporters involved in cell-cell communication and various pathophysiologicals. *Biochim. Biophys. Acta* **1841**, 108–120 (2014).
60. Jarmalavičiūtė, A. & Pivoriūnas, A. Exosomes as a potential novel therapeutic tools against neurodegenerative diseases. *Pharmacological Research* **113**, 816–822 (2016).
61. Lener, T. *et al.* Applying extracellular vesicles based therapeutics in clinical trials – an ISEV position paper. *Journal of Extracellular Vesicles* **4**, 30087–33 (2015).
62. Jia, S. *et al.* Emerging technologies in extracellular vesicle-based molecular diagnostics. *Expert Rev. Mol. Diagn.* **14**, 307–321 (2014).
63. Christ, L., Raiborg, C., Wenzel, E. M., Campsteijn, C. & Stenmark, H. Cellular Functions and Molecular Mechanisms of the ESCRT Membrane-Scission Machinery. *Trends Biochem. Sci.* **42**, 42–56 (2017).
64. Chiaruttini, N. *et al.* Relaxation of Loaded ESCRT-III Spiral Springs Drives Membrane Deformation. *Cell* **163**, 866–879 (2015).
65. McCullough, J. *et al.* Structure and membrane remodeling activity of ESCRT-III helical polymers. *Science* **350**, 1548–1551 (2015).
66. Lee, I.-H., Kai, H., Carlson, L.-A., Groves, J. T. & Hurley, J. H. Negative membrane curvature catalyzes nucleation of endosomal sorting complex required for transport (ESCRT)-III assembly. *Proc. Natl. Acad. Sci. U.S.A.* **112**, 15892–15897 (2015).
67. Trajkovic, K. *et al.* Ceramide triggers budding of exosome vesicles into multivesicular endosomes. *Science* **319**, 1244–1247 (2008).
68. Kajimoto, T., Okada, T., Miya, S., Zhang, L. & Nakamura, S.-I. Ongoing activation of sphingosine 1-phosphate receptors mediates maturation of exosomal multivesicular endosomes. *Nat Commun* **4**, 1–13 (2013).
69. Theos, A. C. *et al.* A Lumenal Domain-Dependent Pathway for Sorting to Intraluminal Vesicles of Multivesicular Endosomes Involved in Organelle Morphogenesis. *Developmental Cell* **10**, 343–354 (2006).
70. Jimenez, A. J. *et al.* ESCRT Machinery Is Required for Plasma Membrane Repair. *Science* **343**, 1247136–1247136 (2014).
71. Andrews, N. W., Almeida, P. E. & Corrotte, M. Damage control: cellular mechanisms of plasma membrane repair. *Trends in Cell Biology* **24**, 734–742 (2014).
72. Clark, M. R. Flippin' lipids. *Nature Publishing Group* **12**, 373–375 (2011).
73. Hugel, B., Martinez, M. C., Kunzelmann, C. & Freyssinet, J.-M. Membrane microparticles: two sides of the coin. *Physiology (Bethesda)* **20**, 22–27 (2005).
74. McConnell, R. E. *et al.* The enterocyte microvillus is a vesicle-generating organelle. *The Journal of Cell Biology* **185**, 1285–1298 (2009).
75. Rilla, K. *et al.* Hyaluronan production enhances shedding of plasma membrane-derived microvesicles. *Exp. Cell Res.* **319**, 2006–2018 (2013).
76. Wood, C. R., Huang, K., Diener, D. R. & Rosenbaum, J. L. The cilium secretes bioactive ectosomes. *Curr. Biol.* **23**, 906–911 (2013).
77. Colombo, M., Raposo, G. & Théry, C. Biogenesis, secretion, and intercellular interactions of exosomes and other extracellular vesicles. *Annu. Rev. Cell Dev. Biol.* **30**, 255–289 (2014).
78. Rab27a and Rab27b control different steps of the exosome secretion pathway. **12**, 19–30 (2009).
79. Hsu, C. *et al.* Regulation of exosome secretion by Rab35 and its GTPase-activating proteins TBC1D10A-C. *The Journal of Cell Biology* **189**, 223–232 (2010).
80. Hyenne, V. *et al.* RAL-1 controls multivesicular body biogenesis and exosome secretion. *The Journal of Cell Biology* **211**, 27–37 (2015).
81. Sinha, S. *et al.* Cortactin promotes exosome secretion by controlling branched actin dynamics. *The Journal of Cell Biology* **214**, 197–213 (2016).
82. Hoshino, D. *et al.* Exosome secretion is enhanced by invadopodia and drives invasive behavior. *Cell Rep* **5**, 1159–1168 (2013).

83. Hoshino, A. *et al.* Tumour exosome integrins determine organotropic metastasis. *Nature* **527**, 329–335 (2015).
84. Costa-Silva, B. *et al.* Pancreatic cancer exosomes initiate pre-metastatic niche formation in the liver. *Nat Cell Biol* **17**, 816–826 (2015).
85. Hanahan, D. & Weinberg, R. A. Hallmarks of cancer: the next generation. *Cell* **144**, 646–674 (2011).
86. Zomer, A. & van Rheenen, J. Implications of Extracellular Vesicle Transfer on Cellular Heterogeneity in Cancer: What Are the Potential Clinical Ramifications? *Cancer Research* **76**, 2071–2075 (2016).
87. Al-Nedawi, K., Meehan, B., Kerbel, R. S., Allison, A. C. & Rak, J. Endothelial expression of autocrine VEGF upon the uptake of tumor-derived microvesicles containing oncogenic EGFR. *Proc. Natl. Acad. Sci. U.S.A.* **106**, 3794–3799 (2009).
88. Kucharczyk, P. *et al.* Exosomes reflect the hypoxic status of glioma cells and mediate hypoxia-dependent activation of vascular cells during tumor development. *Proc. Natl. Acad. Sci. U.S.A.* **110**, 7312–7317 (2013).
89. Webber, J. P. *et al.* Differentiation of tumour-promoting stromal myofibroblasts by cancer exosomes. *Oncogene* **34**, 290–302 (2015).
90. Zou, W., Wolchok, J. D. & Chen, L. PD-L1 (B7-H1) and PD-1 pathway blockade for cancer therapy: Mechanisms, response biomarkers, and combinations. *Sci Transl Med* **8**, 328rv4–15 (2016).
91. Noy, R. & Pollard, J. W. Tumor-Associated Macrophages: From Mechanisms to Therapy. *Immunity* **41**, 49–61 (2014).
92. Pucci, F. *et al.* SCS macrophages suppress melanoma by restricting tumor-derived vesicle-B cell interactions. *Science* **352**, 242–246 (2016).
93. Wieckowski, E. U. *et al.* Tumor-derived microvesicles promote regulatory T cell expansion and induce apoptosis in tumor-reactive activated CD8+ T lymphocytes. *J. Immunol.* **183**, 3720–3730 (2009).
94. Kelleher, R. J. *et al.* Extracellular Vesicles Present in Human Ovarian Tumor Microenvironments Induce a Phosphatidylserine-Dependent Arrest in the T-cell Signaling Cascade. *Cancer Immunol Res* **3**, 1269–1278 (2015).
95. Kaplan, R. N. *et al.* VEGFR1-positive haematopoietic bone marrow progenitors initiate the pre-metastatic niche. *Nature* **438**, 820–827 (2005).
96. Peinado, H. *et al.* Melanoma exosomes educate bone marrow progenitor cells toward a pro-metastatic phenotype through MET. *Nat Med* **18**, 883–891 (2012).
97. Zhang, L. *et al.* Microenvironment-induced PTEN loss by exosomal microRNA primes brain metastasis outgrowth. *Nature* **527**, 100–104 (2015).

2

Based on:

Quantification of nanosized extracellular membrane vesicles with scanning ion occlusion sensing

Jeroen de Vrij^{1,2,3,*}, Sybren LN Maas^{2,3,*}, Malisa van Nispen¹, Miguel Sena-Esteves⁴, Ronald WA Limpens⁵, Abraham J Koster⁵, Sieger Leenstra¹, Martine L Lamfers¹ & Marike LD Broekman^{2,3}

¹Department of Neurosurgery, Erasmus Medical Center, Rotterdam, The Netherlands. ²Department of Neurosurgery, University Medical Center Utrecht, Utrecht, The Netherlands. ³Rudolf Magnus Institute of Neuroscience, University Medical Center Utrecht, Utrecht, The Netherlands. ⁴Department of Neurology & Gene Therapy Center, University of Massachusetts Medical School, MA, USA. ⁵Department of Molecular Cell Biology, Section Electron Microscopy, Leiden University Medical Center, Leiden, The Netherlands

* These authors contributed equally

Nanomedicine (Lond) 8, 1443–1458 (2013)

Abstract

Background: Cells secrete different types of membrane vesicles (MVs), which may act as important entities in normal human physiology and in various pathological processes. The established methods for quantification of MVs require purification or preanalytical handling of samples with labeling moieties. **Aim:** Our aim was to develop a method for high-throughput, labeling-free quantification of nonpurified MVs. **Materials & methods:** Scanning ion occlusion sensing technology (also known as tunable restive pulse sensing), which relies on the detection of particles upon their movement through a nanopore, was investigated for the ability to quantify nanosized MVs (<400 nm) in bodily fluids and cell culture supernatants. **Results:** Scanning ion occlusion sensing allowed for rapid and easy measurement of the concentration of MVs in all biological fluids tested. **Conclusion:** Scanning ion occlusion sensing technology enables the quantification of MVs in biological samples without the requirement of MV isolation and/or labeling. This offers a highly valuable addition to the currently used repertoire of MV quantification methods.

Introduction

Cells secrete different types of membrane vesicles (MVs). These include exosomes (~30–150 nm in size), which are formed through exocytosis of intracellularly formed multivesicular bodies, and ‘shedding particles’ (~100–1000 nm in size). Examples of the latter type of vesicles are apoptotic and necrotic vesicles, which are formed by outward budding of the cell membrane. The biological functions of MVs remain enigmatic. They have been implicated in normal mechanisms such as immune regulation, blood coagulation and signal transduction, but also in several pathological processes, including autoimmune diseases and cancer [1–6]. Tumor-derived exosomes were shown to contain proteins and (mi)RNAs that can be functionally transferred to recipient cells, leading to tumor cell proliferation, angiogenesis and modulation of immune cells [7–11]. As MVs are found in all bodily fluids, their use as diagnostic or prognostic tools is the subject of intense investigation [12–15]. MVs derived from dendritic cells have shown potential as tumor vaccines in preclinical and early-phase clinical studies [16,17]. MVs may also serve as delivery vehicles for therapeutic agents to circumvent immunogenicity problems associated with other types of drug carriers, such as liposomes or viral vectors [18,19].

Quantification of MVs in biological samples is a critical parameter in most studies in this area of research. In general, the concentration of MVs is determined through methods that require the purification of MVs and/or incubation with MV-specific labeling moieties [20,21]. We present a novel, rapid method for the quantification of extracellular MVs, based on scanning ion occlusion sensing (SIOS), also known as tunable restive pulse sensing (tRPS). The mechanism of action of SIOS is based on the passage of nanosized particles through a tunable pore, with each passage causing a drop in ionic current [22]. Using this technology, we were able to determine, in a relatively rapid and easy fashion, the concentration of MVs in a variety of biological fluids, without the requirement of MV isolation and preanalytical sample handling.

Materials & methods

Tumor cell cultures

The human glioma cell lines SNB-19 and U87-EGFRVIII [23] were cultured in DMEM (Invitrogen, CA, USA) supplemented with 10% MV-depleted fetal bovine serum

(Invitrogen). MV-depleted fetal bovine serum was prepared through ultracentrifugation at $100,000 \times g$ for 16 h followed by harvesting of the supernatant. Primary brain tumor cultures (GS245 and GS249) were derived by mechanical dissociation from fresh tumor material collected during brain tumor surgery at the Department of Neurosurgery of the Erasmus Medical Center, (Rotterdam, The Netherlands) according to a previously described protocol [24]. Tumors were classified as glioblastoma by histological diagnosis. Cells were cultured in serum-free medium (DMEM supplemented with 2% B27 medium supplement, 20 ng ml^{-1} bFGF, 20 ng ml^{-1} EGF and $5 \mu\text{g ml}^{-1}$ heparin) [25]. All cell cultures were maintained at 37°C in a humidified atmosphere of 5% CO_2 . Cell growth media were supplemented with a mixture of penicillin ($100 \text{ units ml}^{-1}$) and streptomycin ($100 \mu\text{g ml}^{-1}$; Invitrogen).

Expression of short-hairpin RNA to downregulate MV production

To reduce the number of MVs secreted by SNB-19 cells, short-hairpin RNA (shRNA) was introduced, targeted against the Rab-27b protein. The shRNA was stably introduced in the cells by using a recombinant lentivirus (LV) delivery system (GIPZ system; Open Biosystems- Thermo Scientific, FL, USA). To control for off-target shRNA effects, a nonsilencing control shRNA was included in parallel. The pGIPZ LV vector plasmids used were v2lhs173293 (miRNA targeted against Rab-27b [mature sense sequence CTCTGATGGTCAAAGTTCT]), and pGIPZ/nonsilencing-control (scrambled miRNA sequence [mature antisense sequence ATCTCGCTTGGGCGAGAGTAAG]). The pGIPZ plasmids carry a TurboGFPTM (Evrogen, Moscow, Russia)-internal ribosome entry site-puromycin cassette, which enabled the growth of LV-transduced cells under puromycin selection pressure (to select for transduced cells) and microscopic assessment of transduction efficiency through TurboGFP visualization. Production of the LVs was performed according to a previously described protocol [26]. TurboGFP visualization was used to determine the LV titer (transducing units [tu] ml^{-1}). SNB-19 cells were transduced with the LVs at a multiplicity of infection of 1 tu per cell. After culturing the cells for 2 weeks under puromycin selection pressure, downregulation of the Rab-27b mRNA in the SNB-19/shRab-27b cell line was confirmed by a standard reverse transcriptase quantitative PCR protocol. The Rab27-b mRNA expression level (normalized to the glyceraldehyde-3-phosphate dehydrogenase mRNA expression level) was $>80\%$ reduced in SNB-19/shRab-27b cells compared with the expression level in nontransduced cells or cells transduced with the nonsilencing control shRNA. The IncuCyte™ Live-Cell Imaging System (Essen BioScience, Hertfordshire, UK) was used to compare cell growth kinetics of the cell lines SNB-19/shRab-27b, and SNB-19/

shControl. Cells were plated in wells of a 24-well plate at equal densities (5000 cells per well) in $500 \mu\text{l}$ growth medium. After a 24-h incubation period (to attach the cells to the plate), the plate was positioned in the IncuCyte system. Each well was automatically photographed (using settings for phase-contrast as well as fluorescence) at four locations every 2 h for a total of 5 days, and the cell confluencies were determined by the IncuCyte software. Cell culture supernatants were harvested for MV analyses.

Preparation of samples for MV analyses

Blood and urine were obtained from healthy donors. Pleural fluid was obtained from a mesothelioma patient (kindly provided by Hegmans J, Erasmus Medical Center, Rotterdam, The Netherlands). Blood plasma was prepared by centrifugation of fresh blood (6 ml per donor) in a BD Vacutainer® (17 IU ml^{-1} lithium heparin; BD, NJ, USA). The plasma was diluted 1:1 in phosphate-buffered saline (PBS). Plasma, pleural fluid and urine samples were centrifuged at low speed to remove cells and cellular debris. MV-depleted control samples were prepared through filtering the fluids on a 100-kDa centrifugal filter unit (Millipore, MA, USA), followed by harvesting of the filtrate.

SNB-19/shControl and SNB-19/shRab-27b cells were plated in wells of a 24-well plate at equal densities (5000 cells per well) in $500 \mu\text{l}$ growth medium. After 6 days, the cell culture supernatants were harvested for MV analyses. GS245 and GS249 tumor cultures underwent equal passaging conditions after collection of the tumor material from the patients. The GS245 and GS249 cells (at passage 4) were plated at equal densities, and cell culture supernatants were harvested after 3 days. All supernatants were centrifuged at low speed to remove cells and cellular debris, before their storage at -80°C for MV analyses.

Plasma, pleural fluid and urine samples ($180 \mu\text{l}$) were loaded on separate iodixanol gradients to analyze for the presence of different types of MVs (discontinuous gradients consisting of 11 fractions, ranging from 6 to 18% iodixanol [Sigma-Aldrich, Zwijndrecht, The Netherlands] in PBS). The gradient was centrifuged at $217,000 \times g$ for 80 min, using a 41Ti Swing-Out Rotor (Beckman Coulter, CA, USA). Fractions ($11 \times 1 \text{ ml}$) were harvested from the top and stored at -80°C .

SNB-19/shControl and SNB-19/shRab-27b MVs were isolated through differential ultracentrifugation [20]. Briefly, cell culture supernatant was harvested from four 15-cm dishes after 3 days of culturing, followed by centrifugation at $300 \times g$ for 10 min and

4000 × g for 1 h to remove cell debris. MVs were concentrated by ultracentrifugation at 100,000 × g for 70 min, using a SW32 Ti Swing-Out Rotor (Beckman Coulter), requiring the use of multiple tubes per MV preparation. As an additional wash step, the MVs were resuspended in PBS, pooled for each MV preparation and again subjected to ultracentrifugation at 100,000 × g for 70 min, using a SW41 Ti Swing-Out Rotor (Beckman Coulter). The MVs were dissolved in 200 µl PBS, aliquoted and stored at -80°C. Upon the MV isolation, the cells were also harvested (by scraping cells with a spatula), followed by lyses for 30 min at 4°C in 1% Triton™ X-100 (Dow Chemical Company, MI, USA; 1 ml per dish) and centrifugation for 10 min at 13,000 × g to clarify the protein extracts.

U87-EGFRvIII exosomes were isolated through an iodixanol density gradient centrifugation protocol. After 4 days of culturing, cell culture supernatant was harvested from ten 15-cm dishes (cell confluency 80%) and centrifuged at 300 × g for 10 min to remove cell contamination. The supernatants were then centrifuged for 1 h at 4000 × g and the supernatant was filtered through a 0.22-µm filter (Corning, NY, USA) to eliminate membranous debris and MVs larger than 220 nm. To concentrate MVs, the filter eluate was applied on a 100-kDa centrifugal filter unit (Millipore), followed by a single wash step with PBS. The concentrates (in 500 µl PBS) were layered on top of a discontinuous iodixanol gradient (layered from bottom to top: 40% [1 ml], 25% [2.7 ml] and 5% [1 ml] iodixanol in PBS) and ultracentrifugation was performed for 4 h at 192,000 × g, using a SW50.1 Swing-Out Rotor (Beckman Coulter). The exosome-containing top fraction (2.5 ml) was collected and loaded on a 100-kD filter column. After centrifugation, the exosome pellet was dissolved in 3 ml PBS and again centrifuged in a 100-kD filter column to perform a single wash step. The exosome sample was loaded on top of a 30% sucrose cushion to further remove contaminating proteins and nonexosomal MVs with other densities. After centrifugation for 40 min at 100,000 × g, the 30% sucrose cushion was harvested and the sucrose was replaced with PBS (loading on a 100-kD filter column, one wash step included). The exosome preparation (500 µl in total) was aliquoted and stored at -80°C.

Quantification of MVs with SIOS technology

The qNano platform (Izon Science, Christchurch, New Zealand) was used to investigate SIOS technology for measurement of MVs in biological fluids. For the detection of MVs in the nonpurified biological fluids, the qNano was equipped with a membrane ('cruciform') of the NP200A type (Izon Science), which contains a tunable nanopore

optimized for the detection of particles with a size between 100 and 400 nm. The MV-containing samples were thawed and 70 µl per sample was added to 10 µl of an 8× diluted internal reference bead control (carboxylated polystyrene beads; 400 nm, stock concentration 7×10^9 beads ml⁻¹). For the quantification of MVs in the 6–18% iodixanol gradient, which resulted in relatively low levels of MVs, a higher dilution of beads was used: 50 µl per sample (1:1 diluted in PBS) was added to 10 µl of a 20× diluted beads stock. Spiking the samples with polystyrene beads allowed for the quantification of MVs with an 'internal control methodology'.

After placing the cruciform on the qNano, the tunable pore was manually opened by stretching the cruciform to 47 mm. The lower fluid cell was filled with PBS. A positive voltage was applied and samples were loaded in the upper fluid cell once the current was stabilized. To increase the flow rate of particles, the variable pressure module was used to apply a pressure of 0.8 kPa. Measurement time exceeded at least 100 s or 500 particle counts. Information on the concentration and size of particles was provided through measurement of the particle flow rate and the particle-specific blockage magnitude, respectively. Size-distribution plots were created (Izon Control Suite software, version 2.1) and gates were set for the population of internal control beads and the smaller-sized population of MVs. The background-to-noise signal in the bead-only sample was subtracted from the sample measurements. After determining the number of MVs in relation to the number of beads, which were present at a known concentration, the concentration of MVs could be calculated.

SIOS analyses on purified exosomes from the U87-EGFRvIII cells was performed similarly, with the exception that the qNano was equipped with an NP100A cruciform (optimized for the detection of particles with a size of 70–200 nm), and that 220-nm-sized beads (carboxylated polystyrene, stock concentration: 4.2×10^{10} beads ml⁻¹) were used as an internal standard. The exosomes were diluted ten times in PBS before analysis.

Western analysis & total-protein measurement

Fractions from the 6–18% iodixanol gradients were prepared for western analysis by boiling 20 µl per fraction in nonreducing sample buffer (62.5 mM Tris-Cl, pH 6.8; 25% glycerol; 2% sodium dodecyl sulfate (SDS); 0.01% bromophenol blue [Bio-Rad Laboratories, Venendaal, The Netherlands]) for 5 min at 95°C. All samples were subjected to standard SDS-PAGE (10% polyacrylamide running gels), and subsequent

protein transfer to polyvinylidene difluoride membranes (Immobilon™-P transfer membrane; Millipore) by electroblotting. After immunological probing of the blots with mouse anti-CD63 antibody (1:500; BD) and horseradish peroxidase-conjugated rabbit-anti-mouse secondary antibody (1:1000; Dako, Enschede, The Netherlands), horseradish peroxidase was detected by enhanced chemiluminescence.

Total protein measurements were performed to quantify MVs or exosomes. To this end, the samples were subjected to SDS-PAGE (10% running gel, protocol as described above), followed by Coomassie staining (Fermentas Page Blue; Thermo Scientific, St Leon Rot, Germany). Total protein measurement in cell lysates was performed similarly. ImageJ software (NIH, MD, USA) was used to compare the levels of Coomassie-stained proteins. For this, Coomassie-stained bands were represented as pseudo chromatograms, and values for the area under the curves were used for calculation of the relative protein amounts. In addition, a total-protein measurement was carried out with the Pierce® BCA Protein Assay Reagent Kit (Thermo Scientific), according to the manufacturer's instructions.

Quantification of MVs with immunoaffinity capturing

MVs were quantified by immunoaffinity capturing, through binding of MVs to antibody-coated latex beads followed by flow cytometric detection [27]. After two wash steps with PBS, the latex beads (aldehyde/sulfate, 4% w/v, 4 µm [Invitrogen]) were resuspended in 200 µl 2-N-morpholino ethanesulfonic acid buffer (0.025 M, pH 6). Mouse anti-human CD63 antibodies or mouse IgG1-k isotype control antibodies (3.5 µg per antibody; BD) were incubated overnight with 107 beads with horizontal shaking at 300 rpm at room temperature. The beads were washed twice with PBS and were dissolved in 1 ml glycine (100 mM, pH 7.2).

Freshly thawed MV samples (100 µl) were incubated with 5 µl antibody-coupled beads (50,000 beads) overnight at room temperature with horizontal shaking at 300 rpm. The beads were washed twice in PBS, 4% bovine serum albumin and incubated with a 1:100 dilution (in 2% bovine serum albumin) of phycoerythrin-conjugated mouse anti-human CD81 IgG1 antibody (BD) for 30 min on a horizontal shaker at 300 rpm. Beads were washed once in PBS and resuspended in 200 µl PBS. The beads were loaded on a FACS-Calibur™ flow cytometer (BD) and data were analyzed with FlowJo™ software (Tree Star, OR, USA). The mean phycoerythrin fluorescence for each sample

was normalized to the mean phycoerythrin fluorescence measured for the control incubations (beads incubated with MV-depleted urine, pleural fluid or plasma).

Electron microscopy

Exosomes were absorbed for 10 min to freshly glow-discharged, carbon-coated pioloform grids. After blotting, the samples were negatively stained with a 3% uranyl acetate solution for 1 min. The samples were examined with a Tecnai™ 12 Biotwin microscope (FEI Company, Eindhoven, The Netherlands) at 120 kV, equipped with a 4 × 4 k charged-coupled device camera (FEI Company).

Results

Setting up an 'internal control methodology' to facilitate SIOS-based quantification of MVs in biological fluids

We performed various analyses on the qNano SIOS platform to investigate its usefulness for the concentration measurement of MVs in biological samples, including blood plasma, urine, pleural fluid and cell culture supernatant. Using standard settings for the quantification of microparticles [28,29] and a type of cruciform (NP200A) optimized for the detection of MVs with a size of 100–400 nm, MVs could be detected in all samples. The size-distribution profiles were similar, with the majority of MVs (>95%) being larger than 150 nm and smaller than 400 nm (mean size of ~200 nm). Although encouraging, we were unable to obtain reliable quantification data as a result of large variations in particle count rates. For this reason, an internal control methodology was set up, in which polystyrene beads of known concentration and size were added to the samples. Proof of principle was tested by adding the internal control beads (400-nm-sized) to 220-nm-sized beads, followed by five independent measurements of the same sample (**Figure 1**). Again, large variations in particle count rates were observed, thwarting direct conversion to particle concentration values (**Figure 1A**). However, reliable quantification was feasible when calculating the ratio of 220- to 400-nm-sized beads. These ratios could easily be determined, since both types of beads showed a clearly distinguishable current blockade height and current blockade duration (parameters depending on the particle size and particle size/charge, respectively) (**Figure 1B**). The blockade height histograms were used to determine the cut-off between the two populations (**Figure 1C**). We performed this strategy with samples containing different amounts of 220-nm-sized beads (dilutions of 1:1024, 1:256,

1:64 and 1:16), and calculated for each sample (from five independent measurements) the initial concentration of 220-nm-sized beads (i.e., before dilution) (**Table 1**). This revealed low variation in the calculated concentrations, ranging from 2.8 to 2.3×10^{10} particles per ml. Of importance, similar results (i.e., the calculated concentration and the variability between measurements) were obtained after dissolving the beads in MV-depleted plasma, urine, pleural fluid and cell culture supernatant (data not shown). Although more experiments are required to fully delineate the quantitative accuracy of our calculated concentrations (stock concentration 220-nm-sized beads = 4.2×10^{10} particles per ml [dry weight measurement protocol], according to the manufacturer), the results demonstrate the usability of our approach for reproducible SIOS-based quantification of nanosized particles in different fluids.

Table 1. Overview of the ratios of 220-nm to 400-nm-sized beads in samples containing different dilutions of the 220-nm-sized beads.

220-nm-sized particles	Average ratio (\pm SD)	Particles measured (10^7 ml^{-1})	Stock approximation (10^{10} ml^{-1})
1:1024	0.27 (\pm 0.09)	2.70	2.76
1:256	0.98 (\pm 0.20)	10.46	2.68
1:64	3.26 (\pm 0.58)	35.45	2.27
1:16	12.93 (\pm 2.42)	141.17	2.26

Each sample was measured five times. From the measured ratios and the known concentration of 400-nm-sized beads, the concentration of 220-nm-sized beads (in the sample as well as in the original stock before dilution) was calculated. SD: Standard deviation.

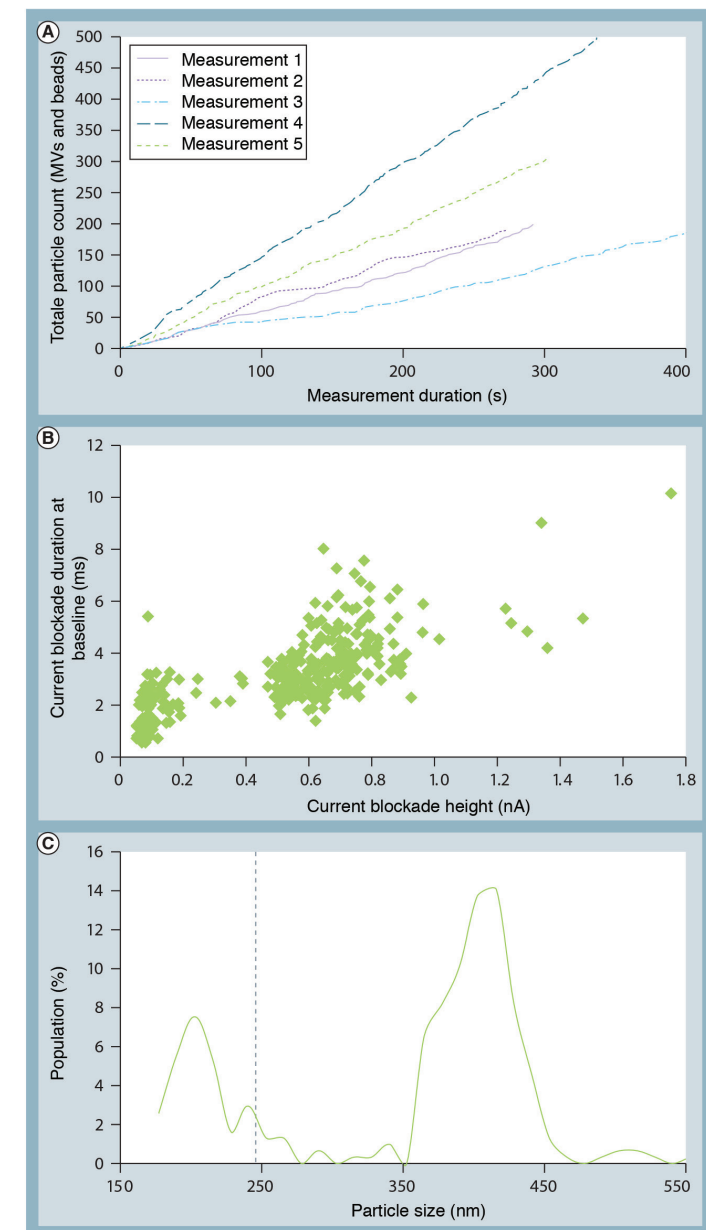


Figure 1: Scanning ion occlusion sensing analysis of samples containing 220- and 400-nm-sized polystyrene beads. (A) Particle count rates of five independent measurements on one sample (1:1024 dilution of the small beads; 1:64 dilution of the large beads). (B) The current blockade height and current blockade duration for all particles detected in one measurement. The different types of polystyrene beads show clearly distinguishable populations. (C) The current blockade height (particle size) histogram of one measurement. A cut-off particle size (indicated by the dotted line) was chosen to determine the count ratio for the two types of beads. MV: Membrane vesicle.

Quantification of MVs in bodily fluids

Implementing the method described above, we quantified the concentration of MVs in plasma, pleural fluid and urine. The size-distribution graphs showed two major populations of particles, with sizes of approximately 400 and 200 nm. A representative measurement of the plasma sample is shown in **Figure 2A**. The 400-nm population can be attributed entirely to the control beads, as this population was absent in samples without the internal control. The 200-nm population presumably represents MVs. The total particle count rate, which includes counting of the polystyrene beads as well as MVs, varied considerably between measurements of the same sample, as exemplified for the plasma sample in **Figure 2B**. Our internal control methodology, however, enabled SIOS-based quantification of MVs with good precision, as demonstrated in **Figure 2C**. In all biological samples, MVs were detected with a size of approximately 200 nm, with a concentration of approximately 10^8 MVs per ml. More MVs were detected in the plasma and pleural fluid sample compared with the urine sample.

To gain insight into the type of MV detected upon our SIOS analysis, we loaded equal amounts of the bodily fluids on an iodixanol density gradient, which has previously been shown to allow for the specific isolation of exosomes and their separation from other, nonexosomal MVs, which have slightly higher densities [30,31]. Fractions of the iodixanol gradients were harvested and western blotting after SDS-PAGE was performed to analyze for the presence of the protein CD63 (**Figure 2D**). CD63 is highly enriched in exosomes and is not, or at very low levels, present in other types of extracellular vesicles [32]. For the plasma- and pleural fluid- containing gradients, CD63 was detected (with similar intensities) in the top fractions, which are the fractions with the lowest concentrations of iodixanol. CD63 was not detected in fractions from the urine-containing gradient. Of interest, a faint band was detected in the lowest fraction of the pleural fluid-containing gradient. While keeping in mind that quantitative analysis of exosomes via western blotting can be suboptimal (e.g., expression of exosome-specific proteins may vary between exosomes from different origins [33]), our western blots suggested that the plasma and pleural fluid samples contained similar amounts of exosomes, while the level of exosomes in urine is much lower.

Next, SIOS was performed to analyze for the presence of nanosized particles in all iodixanol fractions (**Figure 2E**). In line with the western blot, particles were detected in the top fractions of the plasma- and pleural fluid-containing gradients, probably representing exosomes. No particles could be detected in the urine-containing

gradient. The concentration of particles in the iodixanol fractions was much lower compared with the concentration of particles in the original sample, which was loaded on the gradient. This was as expected, taking into account the increased volume of the iodixanol fractions compared with the loaded volume. Remarkably, particles were also detected in the fractions with the highest concentration of iodixanol. The identity of these particles, which had a similar size compared with the particles from the top fractions, remains to be determined.

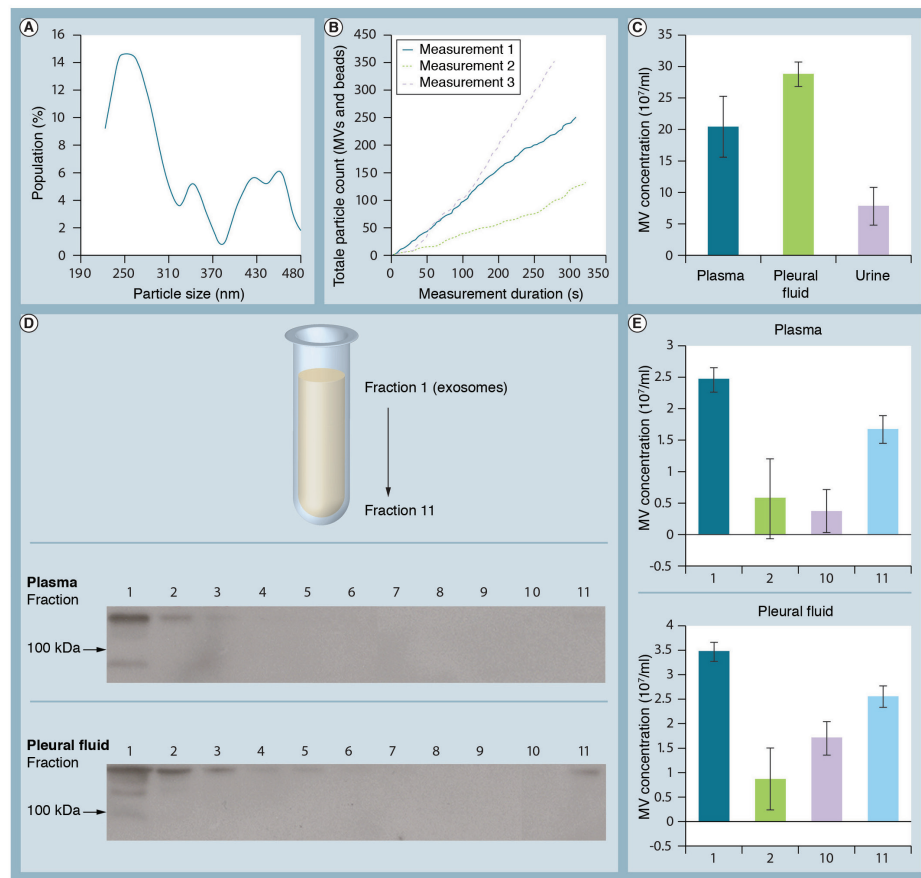


Figure 2. Scanning ion occlusion sensing analysis of membrane vesicles in bodily fluids. (A) Size-distribution histogram for one (of three) scanning ion occlusion sensing (SIOS) measurements of the plasma sample. The sample was spiked with 400-nm-sized beads as an internal control reference. Two major particle populations can be observed. (B) Particle count rates of three independent SIOS measurements of the plasma sample (spiked with 400-nm-sized beads), indicating the large variations in count rate between analyses on the same sample. (C) SIOS-based quantification of MVs in plasma, pleural fluid and urine. Error bars indicate standard deviation ($n = 3$). (D) Bodily fluids were loaded on iodixanol density gradients to allow for the separation of MV subtypes. After centrifugation, fractions were harvested from the top and subjected to western blotting (anti-CD63 antibody) to analyze for the presence of exosomes. (E) SIOS-based quantification of MVs in the iodixanol fractions. Error bars indicate standard deviation ($n = 3$). MV: Membrane vesicle.

Quantification of MVs in tumor cell cultures

Tumor cell-derived MVs may support tumor progression, for example through the induction of blood vessel formation or the suppression of non-tumor immune responses [4,7]. Furthermore, tumor-derived MVs may serve as biomarkers, as they

contain tumor-specific contents and are present in bodily fluids such as the blood [12–15]. We set out to perform various proof-of-principle analyses and to test SIOS technology for the quantification of tumor cell-derived MVs, in small volumes of cell culture supernatants.

Primary tumor cells were derived from the brain tumors of two patients and grown as cultures GS245 and GS249 in specialized (serum-free) medium. These growth conditions allow for the propagation of a tumor stem cell population, with prolonged maintenance of the cellular phenotype compared with conventional cell culture conditions [34]. Of interest, microscopic analysis showed a completely different phenotype of the cultures (**Figure 3A**). GS245 appeared to grow primarily as an adherent monolayer culture, while GS249 grew in suspension with the formation of multicellular spheres. Phenotypic differences between glioblastoma multiforme-derived primary cell cultures are not unprecedented and may reflect the existence of different glioblastoma multiforme subclasses [25,35,36]. From both cultures, cell culture supernatants were harvested and MVs were quantified by SIOS, using the internal control method (**Figure 3B, Supplementary table 1 & Supplementary Figure 1**). MVs were detected in the supernatant of both cultures, with more MVs in the supernatant from GS245. The MV size distribution had a similar profile as the profiles observed after measurement of the bodily fluids (data not shown). Next, we determined the concentration of MVs in the GS245 and GS249 supernatants with an alternative method, based on immunocapturing of MVs on latex beads (Figure 3C) [27]. Similar to the SIOS-based assay, this assay allows for the quantification of MVs in small volumes of nonpurified samples. In contrast to SIOS, however, this assay exclusively allows for the detection of exosomes, as it relies on the usage of exosome-specific antibodies directed against tetraspanin molecules. The capturing assay (using antibodies directed against the proteins CD63 and CD81) revealed a higher level of exosomes in the GS249 supernatant. Remarkably, this is in contrast to the SIOS-based analysis, which showed a relatively low level of MVs in this supernatant. These results suggest a substantial difference in the MV secretion profile between the tumor supernatants, such as a different MV-to-exosome ratio or different expression levels of the tetraspanins CD63 and CD81 on the exosomes. Further experiments using additional techniques may provide more insight.

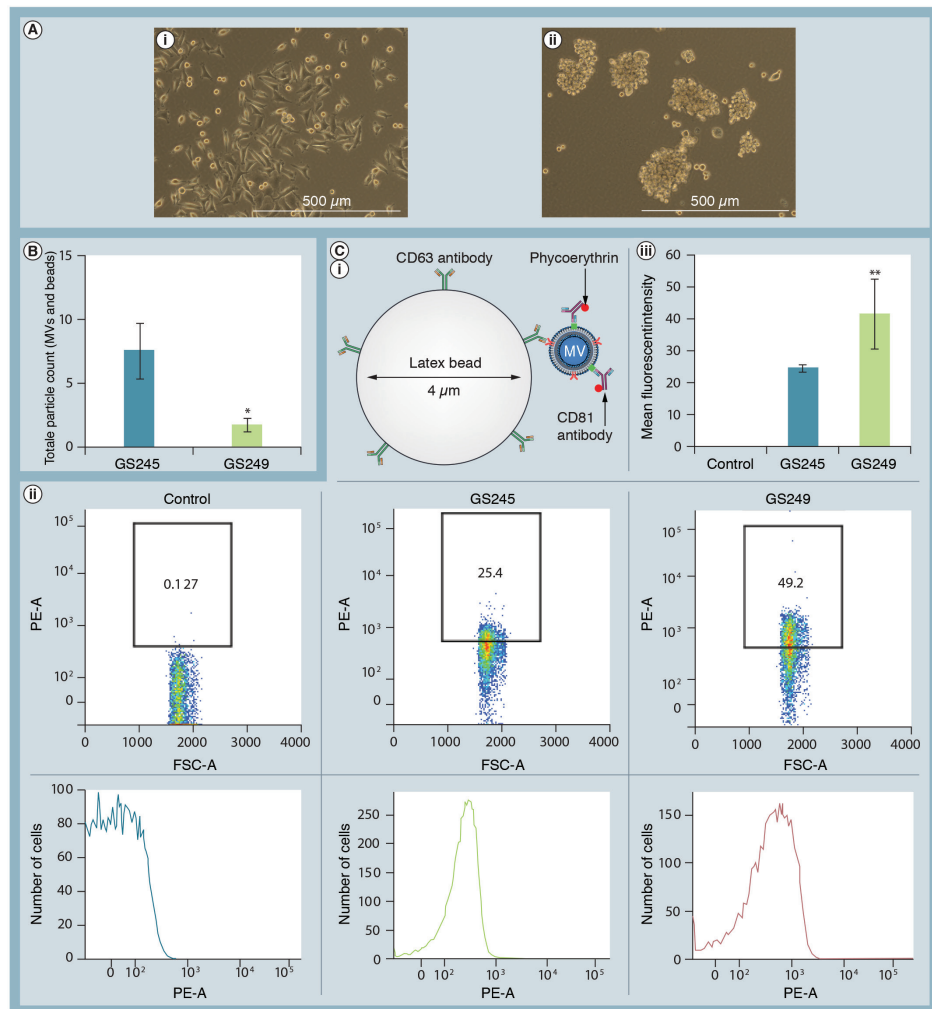


Figure 3. Quantification of membrane vesicles in the supernatant of primary brain tumor cell cultures GS245 and GS249. (A) Microscopic images of (A, i) GS245 and (A, ii) GS249 cells in culture, indicating different growth patterns. (B) Scanning ion occlusion sensing-based quantification of MVs. Error bars indicate standard deviation ($n = 4$); * $p = 0.06$. (C) Immunoaffinity capturing of MVs. (C, i) The principle of the assay is shown schematically. The MVs are bound to 4- μm -sized beads to overcome the limitation of conventional flow cytometry, which does not allow for the detection of MVs smaller than approximately 400 nm. MVs are captured on latex beads through binding anti-CD63 antibodies, followed by detection with phycoerythrin-conjugated anti-CD81 antibodies. (C, ii) The flow cytometry dot plots and histograms reveal an increase in the mean phycoerythrin fluorescence intensity of the latex beads after incubation with the GS245 and GS249 supernatants, compared with the control incubation with MV-depleted medium. The percentage of beads with high fluorescence levels also increases, as indicated by the values in the gates. (C, iii) The graph shows the MV levels expressed as mean fluorescence intensity in the supernatants and in the MV-depleted control. Error bars indicate standard deviation ($n = 2$); ** $p = 0.07$. FSC-A: Forward scatter; MV: Membrane vesicle; PE-A: Phycoerythrin.

To further demonstrate the usefulness of SIOS technology for quantification of tumor cell-derived MVs, we quantified the level of MVs in the cell culture supernatant of SNB-19 glioma cells that had been modified to express a reduced level of the Rab-27b protein. Previous work has shown that knockdown of Rab-27b interferes with the biogenesis pathway of exosomal vesicles, which may result in a reduced secretion of exosomes [27]. Of relevance to our analyses, silencing of Rab27b was reported not to modify the exosomal size, morphology and protein composition [27]. We used recombinant LVs (as schematically shown in **Figure 4A**) to express a Rab-27b-specific shRNA as well as a control shRNA in SNB-19 cells, resulting in the cell lines SNB-19/shRab-27b and SNB-19/shControl. These LVs carried a TurboGFP-internal ribosome entry site-puromycin expression cassette, which enabled the establishment of cell lines that were 100% positive for green fluorescent protein expression and, presumably, shRNA expression (**Figure 4B**). Both cell lines showed similar cell growth kinetics (**Figure 4B**), as well as cell morphology and migration kinetics. Next, the concentration of MVs was determined, using our SIOS-based method (**Figure 4C, Supplementary Table 1 & Supplementary Figure 1**). As anticipated, the SNB-19/shRab-27b cells displayed a reduction in the MV concentration. Since the downmodulation was only marginal, we performed additional analyses on MV preparations after their isolation by ultracentrifugation (**Figure 4D, Supplementary table 1 & Supplementary Figure 1**). This again demonstrated a minor decrease in MV concentration for the SNB-19/shRab-27b sample, as measured by SIOS. Furthermore, staining of proteins after SDS-PAGE, which is a more conventional type of quantification, showed a lower concentration of MVs for the SNB-19/shRab-27b sample, being approximately 80% of the concentration for the SNB-19/shControl sample, as determined by ImageJ analysis.

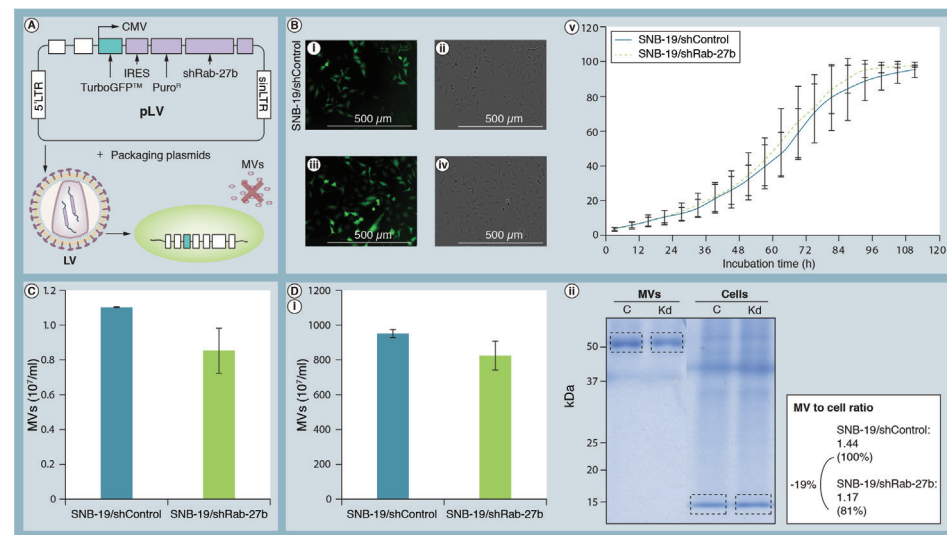


Figure 4. Scanning ion occlusion sensing-based quantification of membrane vesicles in the supernatant of the glioma cell lines SNB-19/shRab-27b and SNB-19/shControl. (A) Schematic representation of the system used to downregulate the expression of the Rab-27b protein. Recombinant LVs were used to introduce shRNA sequences in the cells. The LVs also contained sequences encoding for a puromycin resistance protein and TurboGFPTM (Evrogen, Moscow, Russia). (B, i–iv) Microscopic analysis demonstrated the establishment of cell lines that were 100% positive for incorporation of the transgenes, as shown by the expression of TurboGFP. Images (B, i & iii) have been made with UV light microscopy (to detect TurboGFP); images (B, ii & iv) result from standard light microscopy. (B, v) The IncuCyteTM Live-Cell Imaging System (Essen BioScience, Hertfordshire, UK) was used to perform cell confluency measurements on both cell lines. Error bars indicate standard deviation ($n = 4$). (C) Scanning ion occlusion sensing-based quantification of MVs in the cell culture supernatants. Error bars indicate standard definition ($n = 2$). (D, i) MVs from SNB-19/shControl and SNB-19/shRab-27b supernatants were isolated by sequential ultracentrifugation and subsequently quantified by scanning ion occlusion sensing analysis, demonstrating a minor decrease in MV concentration. Error bars indicate standard deviation ($n = 3$). (D, ii) Coomassie staining after separation of MV and cellular proteins by SDS-PAGE showed a similar reduction in MV concentration for the SNB-19/shRab-27b sample. ImageJ analysis was carried out (on the indicated fragments) to determine the MV to cell ratios, followed by calculation of the percentage decrease in MV secretion for the SNB-19/shRab-27b cells. C: shControl; CMV: Cytomegalovirus promoter; IRES: Internal ribosome entry site; Kd: shRab-27b knockdown; LTR: Long terminal repeat; LV: Lentivirus; MV: Membrane vesicle; pLV: Lentiviral expression plasmid; PuroR: Puromycin resistance.

Next, we assessed the usability of SIOS technology for quantification and size measurement of tumor cell-derived exosomes. Thereto, the protocol underwent two major modifications: usage of an NP100A cruciform (optimized for the detection of particles with a size of 70–200 nm) instead of the NP200A cruciform, and spiking of the sample with internal control beads of 220 nm instead of 400 nm upon the quantification

analyses. With this set-up, SIOS analysis was performed on purified exosomes, which had been isolated according to a standard exosome isolation protocol (Figure 5A). Exosomes were isolated from the supernatant of U87-EGFRvIII glioma cells, which produce strongly enhanced levels of exosomes (data not shown). The size-distribution profile showed the presence of exosomes within the range of 100–200 nm, with the optimum of the profile at approximately 100 nm (Figure 5B). This appeared to be in line with electron microscopic analysis, which, however, also showed the presence of (minor amounts of) exosomes smaller than 100 nm. Exosomes were then quantified with the internal control method. SIOS allowed for the separate detection of the 220-nm-sized beads and the exosomes, as displayed by two particle populations with clearly distinguishable particle size distributions (Figure 5C). Reliable quantification was achieved up to a sample dilution factor of 100 (Figure 5D, Supplementary table 1 & Supplementary Figure 1). This sensitivity was similar to the sensitivity observed after performing a total-protein staining protocol (Coomassie after SDS-PAGE) (Figure 5D), but substantially higher compared with a total-protein measurement with a BCA kit (reliable quantification up to a dilution factor of 10, revealing 0.5 mg ml^{-1} protein in the exosome preparation). Similar to the quantification of MVs described above, SIOS technology enabled the quantification of exosomes in a relatively rapid and easy fashion. As an additional proof of principle, we were able to rapidly assess the effect of multiple rounds of freeze–thawing on exosome integrity, showing no effects on exosome concentration (Figure 5E) and exosome size.

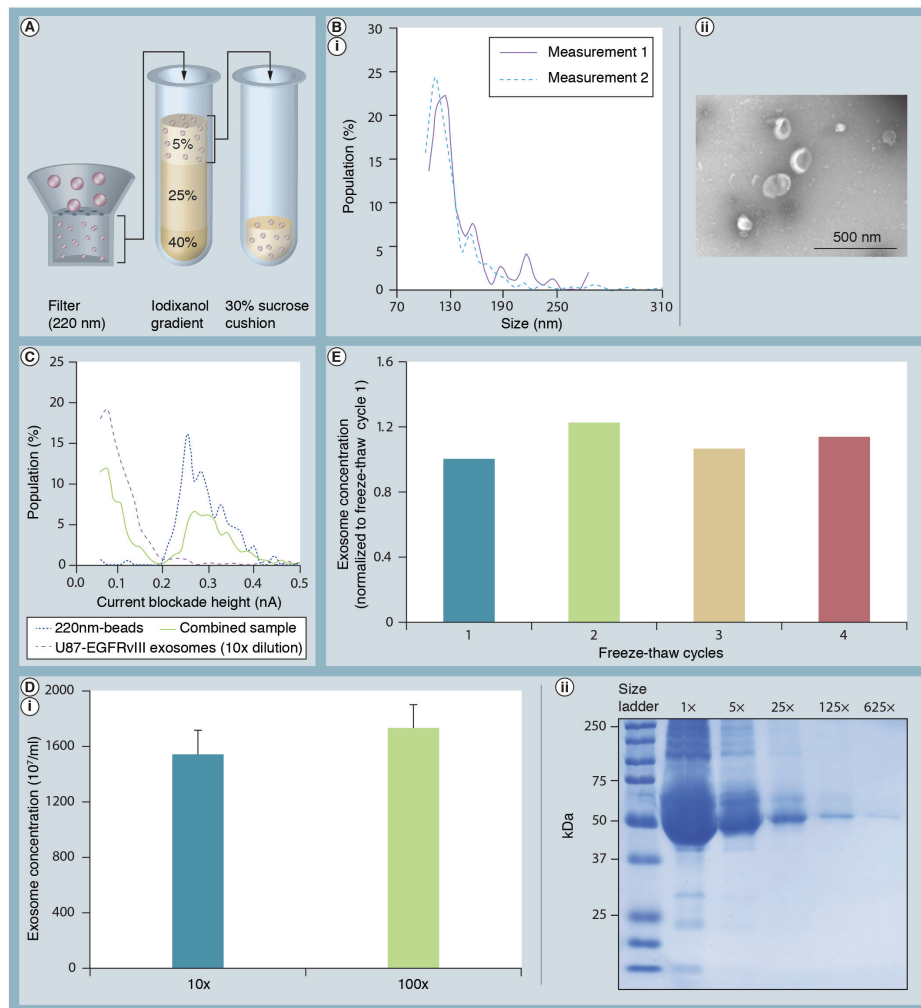


Figure 5. Scanning ion occlusion sensing-based analyses on purified exosomes from U87-EGFRvIII glioma cells. (A) Schematic representation of the protocol used to isolate exosomes. (B, i) Size-distribution diagram of the isolated exosomes, as determined by scanning ion occlusion sensing. The exosome sample and the calibration sample were measured separately to allow for the use of optimized settings for size analysis. (B, ii) Electron microscopy shows the presence of exosomes with sizes varying from approximately 70 to 180 nm. (C) Size-distribution profiles to demonstrate the separate detection of exosomes and 220-nm-sized beads upon quantification. The profiles represent samples containing exosomes only, beads only, or a mixed population of exosomes and beads. The exosome preparation was diluted ten times before analysis. (D, i) Scanning ion occlusion sensing-based quantification of purified exosomes. Dilutions of 10 \times and 100 \times were analyzed. Error bars indicate standard deviation ($n = 4$). (D, ii) Coomassie staining of exosomal proteins after their separation by SDS-PAGE. Different dilutions of the exosome preparation were loaded on to the gel. The sizes of the protein marker fragments are indicated. (E) Scanning ion occlusion sensing-based quantification of exosomes after four rounds of freeze-thawing.

Discussion

MVs have been shown to contribute to various biological processes and numerous studies are being performed to investigate their diagnostic or even therapeutic potential. For these types of studies, accurate quantification of MVs is imperative. We describe a simple and reliable method for the detection and quantification of MVs in biological fluids, including blood plasma, pleural fluid, urine and tumor cell culture supernatant, using SIOS technology.

Currently, several methods are used to assess the presence and concentration of MVs [20,21]. Most often, MVs are isolated from large volumes of fluid by ultracentrifugation sedimentation and/or density gradient flotation, followed by total-protein measurement or quantitative western analysis on MV-specific proteins. Compared with the SIOS-based method, these types of quantification have various limitations, including the requirement of large volumes of starting material and the lack of information on the size of the isolated MVs. They are also relatively time consuming, thereby hampering high-throughput screening of samples. In addition, the level and type of proteins packaged in/on MVs is not uniform. As such, protein expression may vary between exosomes derived from different cell types [33] and between subtypes of exosomes originating from one cell type [37]. In screening types of analysis, for example when comparing the effects of different therapeutics on the level of MV secretion, it may be unsuitable to use antibody-based quantification, as different conditions may differently affect the protein content of secreted MVs.

Our results demonstrate the usefulness of SIOS technology to determine the concentration of nanosized MVs in nonpurified biological samples. The method required the addition of internal control beads to the samples to correct for variations in the MV count rate. It is unknown which mechanism causes these variations. Measurement of small-sized MVs may be highly sensitive to subtle changes to the system, such as the applied pressure and temperature of the sample or cruciform. Using the internal control beads, we were able to perform highly reproducible measurements of the MV concentration on all biological fluids tested. The usefulness of the technology for comparative analysis of MV concentrations was shown through a variety of assays in different fluids, including bodily fluids and tumor cell culture supernatant. Further analysis is required to determine the accuracy of the SIOS-based measurement of MV concentration. Despite the lack of a 'gold standard', useful information may

be obtained through the use of various alternative methods, such as nanoparticle tracking analysis [38] and quantitative electron microscopy. However, these methods have not been fully optimized for analyses on MVs and it will be rather difficult to determine the accuracy of each method. In addition, it may be useful to test other types of internal control beads as a reference. The extrapolation of particle count rates to concentrations may improve when using internal control beads that resemble (subtypes of) MVs in terms of shape and/or charge. However, it is anticipated that the polystyrene beads served their purpose as calibration beads for quantification of MVs, as their usability as calibration beads for quantification was recently shown for other types of nanoparticles as well, including Baculovirus occlusion bodies, Prochlorococcus cyanobacteria and synthetic liposomes [39,40]. Liposomes are considered to resemble MVs, as they have a similar form (rounded) and surface structure (negatively charged lipid layer). These studies showed that, as expected from theoretical models [28], the particle count rate appears to be independent of the particle size or surface charge, under the condition that pressure is applied.

Our internal control method was also useful for the quantification of exosomes that were isolated from the supernatant of glioma cells. To optimize detection of the exosomes, which are generally approximately 100 nm in size, we used a smaller pore size (NP100A cruciform) and smaller beads as internal control (220-nm-sized). Using the NP200A cruciform and 400-nm-sized beads, exosomes could be quantified as well, albeit with a lower concentration (~75% lower) and a higher mean size (~200 nm). It was shown that SIOS analysis on two different dilutions of the exosomes (10 and 100×) enabled the calculation of a stock concentration (i.e., the concentration of the undiluted exosomes) without a significant difference. This demonstrates the feasibility of using polystyrene beads as internal standard to appropriately determine the concentration of MVs within a broad concentration range, even though MVs and polystyrene beads have different characteristics. Since the SIOS measurements of the exosome size were constant (in contrast to the large variations in count rate), size measurements could be carried out with separate measurements of the MV sample and the calibration sample. This allowed the use of smaller calibration beads (118 nm) and a reduced pore size (by means of manually relaxing the NP100A cruciform), compared with the concentration measurements.

Using SIOS technology, we were able to quantify MVs in blood plasma, pleural fluid and urine. To analyze for the presence of different MV types, the samples were subjected

to iodixanol density gradient centrifugation. SIOS revealed the presence of plasma and pleural fluid MVs in the top as well as in the bottom fraction of the gradient. The top (low-density) fraction was found to contain exosomes, as indicated by western analysis with CD63 staining. The identity of the MVs in the bottom (high-density) fractions remains unknown. For the pleural fluid, these high-density MVs contain minor amounts of the CD63 protein, as indicated by the appearance of a faint band on the western blot, suggesting exosomal origin. Alternatively, these MVs represent chylomicrons or other types of low-density lipoprotein particles, which can be highly abundant in bodily fluids and may have sizes that fall within the detection range of our SIOS measurement [38].

Different assays demonstrated the usability of SIOS technology for quantification of tumor cell-derived MVs. MVs were quantified in the supernatants of two primary brain tumor cell cultures, showing a significant difference between both supernatants. On the contrary, the culture supernatants displayed an opposite difference in the concentration of exosomes, as shown by an immunoaffinity capturing assay. This suggests a substantial difference in the MV secretion profile between the tumor supernatants. Possibly, the expression level of CD63 and/or CD81 tetraspanin proteins varies between MVs from different cultures, thereby affecting the quantification via immunoaffinity capturing. More in-depth studies would be highly interesting, taking into account the presumed role of tetraspanins in docking of tumor-derived exosomes to recipient cells [41]. As a second proof of principle of quantifying tumor cell-derived MVs, SIOS was used to assess the effect of downregulating Rab-27b expression on the secretion of MVs by glioma cells. Rab-27b has been described to play a role in the biogenesis of exosomes in HeLa cervical cancer cells [27]. Our SIOS-based analysis showed a marginal reduction in the secretion of MVs by SNB-19 glioma cells. This reduction was less dramatic compared with the reduction described for HeLa cells, which may be explained by the use of different quantification methodologies (SIOS for SNB-19 vs immunoaffinity capturing for HeLa) or essential differences in the biology between SNB-19 and HeLa cells. Unfortunately, our attempt to perform an immunoaffinity capturing assay on the SNB-19 supernatants was unsuccessful. No fluorescence signal was detected, presumably caused by a low concentration of exosomes or low expression of CD63 and/or CD81 proteins. As a third proof of principle of using SIOS for quantitative analyses on tumor cell-derived MVs, we were successful in measuring the concentration and size of glioma-derived exosomes. To demonstrate the potential value of the technology, measurements were carried out to

provide some more insight on the integrity of exosomes upon their storage. Currently, exosomes are stored in different buffers and at different temperatures, and it is not unlikely that these conditions have varying impact on the exosome characteristics. Our SIOS analysis showed that the concentration and size of exosomes derived from U87-EGFRVIII glioma cells are unaffected after multiple rounds of freeze–thawing.

Compared with the traditional method for MV quantification, in which protein measurement is performed on purified MV preparations, our SIOS-based methodology has several advantages. These include the use of small sample volumes (~30 μ l), the simplicity and completion of measurements in a short amount of time, the applicability to nonpurified samples, and the ability to generate information on the MV size distribution. Other technologies for MV quantification are also being explored, and it remains to be investigated how the different technologies compare with each other [42]. One technology with great potential is nanoparticle tracking analysis, which visualizes particles by relating Brownian motion to particle size [38]. This has shown to be a powerful method for size analysis, but quantitative measurements may be less precise in samples containing differently sized vesicles [43]. Alternatively, flow cytometric quantification of nanosized MVs has recently been reported [44]. For this, a conventional flow cytometry platform (with a particle size detection limit of ~400 nm [45]) was adjusted to enable the detection of particles smaller than 100 nm. However, this technology probably requires the use of a more complex measurement platform and may consume more time and effort compared with SIOS (e.g., to remove nonbound fluorescent dye from the samples). Of interest, SIOS, as well as flow cytometry, has the potential to allow for phenotypic analysis, using MV-specific molecules, such as antibodies. Recently, proof of principle was shown for the ability to use SIOS for the specific detection of a biological analyte (PDGF), using capturing beads that were coated with analyte-targeting molecules (DNA aptamers) [46]. SIOS detection of bead–PDGF aggregates enabled measurement of PDGF concentration. It will be highly interesting to investigate whether a similar strategy is applicable for the detection of subtypes of MVs. Side-by-side comparison with alternative methods, such as flow cytometry, will be imperative.

Conclusion

We have shown that SIOS technology, which relies on the detection of particles upon their passage through a tunable nanopore, is suitable for quantification of extracellular MVs. SIOS-based quantification of MVs does not require the use of antibodies or other indirect detection methods, and can be carried out on nonpurified biological fluids, including blood and cell culture supernatant. The technology may be of great use for MV-related research in general, and may lead to novel ways for diagnostic analyses on patient-derived samples.

Future perspective

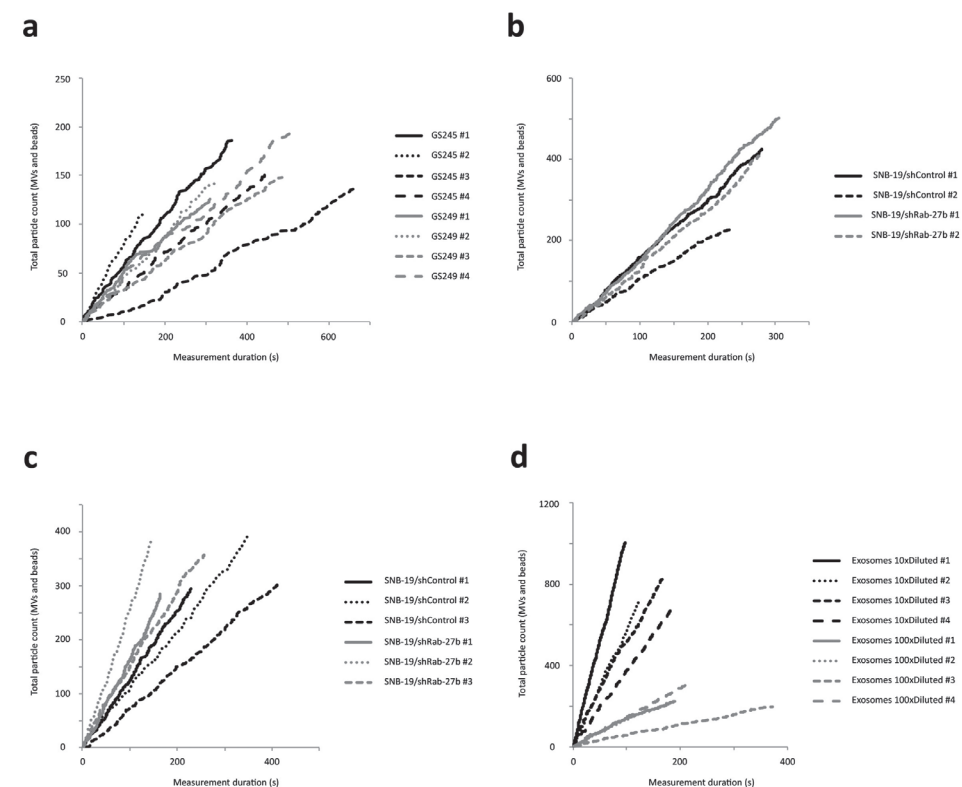
SIOS-based analysis of MVs may find various applications. As an example, the technology may allow the screening of extracellular factors (such as cytokines, pathogens, oxygen level and pH) for their ability to stimulate or repress MV secretion. Furthermore, quantification of MVs may be of value from a diagnostic or even prognostic point of view, for instance to quantify MVs in bodily fluids of cancer patients. Tumor cells have been shown to shed higher levels of MVs compared with normal fibroblasts [47], and tumor-derived MV concentrations in the blood may increase as a function of increased malignancy [48]. In addition, it may be possible to combine SIOS technology with antibodies specific for different MV surface markers. Binding of antibodies (or other molecules) to the surface of MVs may cause SIOS-detectable changes in the size and/or charge of the MVs. This would allow, for instance, the discrimination between tumor-derived MVs and nontumor-derived MVs, by means of detecting tumor-specific molecules on the MV surface.

Supplementary Data

Supplementary Table 1. Overview of SIOS quantification measurements as displayed in figures 3b, 4c, 4d and 5d.

Figure	Sample	Cruciform	Particle count	Measurement duration (s)
3b	GS245 #1	NP200A	186	367
3b	GS245 #2	NP200A	112	160
3b	GS245 #3	NP200A	138	673
3b	GS245 #4	NP200A	150	444
3b	GS249 #1	NP200A	126	312
3b	GS249 #2	NP200A	143	326
3b	GS249 #3	NP200A	148	504
3b	GS249 #4	NP200A	199	514
4c	SNB-19/shControl #1	NP200A	425	280
4c	SNB-19/shControl #2	NP200A	228	235
4c	SNB-19/shRab-27b #1	NP200A	501	307
4c	SNB-19/shRab-27b #2	NP200A	409	277
4d	SNB-19/shControl #1	NP100A	295	229
4d	SNB-19/shControl #2	NP100A	395	350
4d	SNB-19/shControl #3	NP100A	303	416
4d	SNB-19/shRab-27b #1	NP100A	285	164
4d	SNB-19/shRab-27b #2	NP100A	387	147
4d	SNB-19/shRab-27b #3	NP100A	358	257
5d	10xDiluted #1	NP100A	1005	97
5d	10xDiluted #2	NP100A	711	122
5d	10xDiluted #3	NP100A	842	171
5d	10xDiluted #4	NP100A	674	182
5d	100xDiluted #1	NP100A	226	190
5d	100xDiluted #2	NP100A	221	184
5d	100xDiluted #3	NP100A	197	374
5d	100xDiluted #4	NP100A	312	218

Measurements were performed using a NP100A cruciform (optimal size range 70 to 200 nm) or a NP200A cruciform (optimal size range 100 to 400 nm). Each measurement was performed for 100 seconds or until at least 500 particles were counted.



Supplementary Figure 1. SIOS count rate figures (measurement duration versus total particle count) indicating inter-measurement variability. (A) Supplementary to Fig. 3b, displaying count rates for four independent measurements of GS245 and GS249 cell supernatants spiked with beads. (B) Supplementary to Fig. 4c, displaying count rates for two independent measurements of SNB-19/shControl and SNB-19/shRab-27b cell supernatants spiked with beads. (C) Supplementary to Fig. 4d, displaying count rates for three independent measurements of isolated MVs from SNB-19/shControl and SNB-19/shRab-27b cells spiked with beads. (D) Supplementary to Fig. 5d, displaying count rates for four independent measurements of isolated U87/EGFRvIII exosomes (diluted 10 or 100 times) spiked with 400 nm-sized beads.

References

- 1 Jy W, Horstman LL, Ahn YS. Microparticle size and its relation to composition, functional activity, and clinical significance. *Semin. Thromb. Hemost.* 36(8), 876-880 (2010).
- 2 Mittelbrunn M, Gutiérrez-Vázquez C, Villarroya-Beltri C et al. Unidirectional transfer of microRNA-loaded exosomes from T cells to antigen-presenting cells. *Nat. Commun.* 2, 282 (2011).
- 3 Schorey JS, Bhatnagar S. Exosome function: from tumor immunology to pathogen biology. *Traffic* 9, 871-881 (2008).
- 4 Al-Nedawi K, Meehan B, Rak J. Microvesicles: messengers and mediators of tumor progression. *Cell Cycle* 8, 2014-2018 (2009).
- 5 Pegtel DM, Cosmopoulos K, Thorley-Lawson DA et al. Functional delivery of viral miRNAs via exosomes. *Proc. Natl Acad. Sci. USA* 107(14), 6328-6333 (2010).
- 6 Gyorgy B, Szabo TG, Pasztoi M et al. Membrane vesicles, current state-of-the-art: emerging role of extracellular vesicles. *Cell Mol. Life Sci.* 68, 2667-2688 (2011).
- 7 Valadi H, Ekstrom K, Bossios A, Sjostrand M, Lee JJ, Lotvall JO. Exosome-mediated transfer of mRNAs and microRNAs is a novel mechanism of genetic exchange between cells. *Nat. Cell Biol.* 9, 654-659 (2007).
- 8 Skog J, Wurdinger T, van Rijn S et al. Glioblastoma microvesicles transport RNA and proteins that promote tumor growth and provide diagnostic biomarkers. *Nat. Cell Biol.* 10, 1470-1476 (2008).
- 9 Al-Nedawi K, Meehan B, Micallef J et al. Intercellular transfer of the oncogenic receptor EGFRvIII by microvesicles derived from tumor cells. *Nat. Cell Biol.* 10, 619-624 (2008).
- 10 Al-Nedawi K, Meehan B, Kerbel RS, Allison AC, Rak J. Endothelial expression of autocrine VEGF upon the uptake of tumor-derived microvesicles containing oncogenic EGFR. *Proc. Natl Acad. Sci. USA* 106, 3794-3799 (2009).
- 11 Zhang HG, Grizzle WE. Exosomes and cancer: a newly described pathway of immune suppression. *Clin. Cancer Res.* 17, 959-964 (2011).
- 12 Rabinowits G, Gercel-Taylor C, Day JM, Taylor DD, Kloecker GH. Exosomal microRNA: a diagnostic marker for lung cancer. *Clin. Lung Cancer* 10, 42-46 (2009).
- 13 Taylor DD, Gercel-Taylor C. MicroRNA signatures of tumor-derived exosomes as diagnostic biomarkers of ovarian cancer. *Gynecol. Oncol.* 110, 13-21 (2008).
- 14 Nilsson J, Skog J, Nordstrand A et al. Prostate cancer-derived urine exosomes: a novel approach to biomarkers for prostate cancer. *Br. J. Cancer* 100, 1603-1607 (2009).
- 15 Lässer C. Exosomal RNA as biomarkers and the therapeutic potential of exosome vectors. *Expert Opin. Biol. Ther.* 12(Suppl. 1), S189-S197 (2012).
- 16 Tan A, De La Pena H, Seifalian AM. The application of exosomes as a nanoscale cancer vaccine. *Int. J. Nanomedicine* 5, 889-900 (2010).
- 17 Chaput N, Théry C. Exosomes: immune properties and potential clinical implementations. *Semin. Immunopathol.* 33, 419-440 (2010).
- 18 Zhuang X, Xiang X, Grizzle W et al. Treatment of brain inflammatory diseases by delivering exosome encapsulated anti-inflammatory drugs from the nasal region to the brain. *Mol. Ther.* 19, 1769-1779 (2011).
- 19 Alvarez-Erviti L, Seow Y, Yin H, Betts C, Lakhai S, Wood MJ. Delivery of siRNA to the mouse brain by systemic injection of targeted exosomes. *Nat. Biotechnol.* 29, 341-345 (2011).
- 20 Théry C, Amigorena S, Raposo G, Clayton A. Isolation and characterization of exosomes from cell culture supernatants and biological fluids. In: *Current Protocols in Cell Biology*. John Wiley, NY, USA, Chapter 3, Unit 3.22 (2006).
- 21 Yuana Y, Bertina RM, Osanto S. Preanalytical and analytical issues in the analysis of blood microparticles. *Thromb. Haemost.* 105, 396-408 (2010).
- 22 Sowerby SJ, Broom MF, Petersen GB. Dynamically resizable nanometre-scale apertures for molecular sensing. *Sensors Actuators B* 123, 325-330 (2007).
- 23 Nilsson RJ, Balaj L, Hulleman E et al. Blood platelets contain tumor-derived RNA biomarkers. *Blood* 118(13), 3680-3683 (2011).
- 24 Fael Al-Mayhani TM, Ball SL, Zhao JW et al. An efficient method for derivation and propagation of glioblastoma cell lines that conserves the molecular profile of their original tumors. *J. Neurosci. Methods* 176(2), 192-199 (2009).
- 25 Balvers RK, Kloezeman JK, Kleijn A et al. DNA and RNA expression profiling of serum-free primary malignant glioma cultures reveals selection for EGFR/PTEN aberrations but coverage of all (TCGA defined) gene expression signatures. Presented at: the 10th Congress of European Association Of NeuroOncology. Marseille, France, 6-9 September 2012.
- 26 Sena-Esteves M, Tebbets JC, Steffens S, Crombleholme T, Flake AW. Optimized large-scale production of high titer lentivirus vector pseudotypes. *J. Virol. Methods* 122, 131-139 (2004).
- 27 Ostrowski M, Carmo NB, Krumeich S et al. Rab27a and Rab27b control different steps of the exosome secretion pathway. *Nat. Cell Biol.* 12, 19-30 (2010).
- 28 Willmott GR, Vogel R, Yu SS et al. Use of tunable nanopore blockade rates to investigate colloidal dispersions. *J. Phys. Condens. Matter* 22, 454116 (2010).
- 29 Roberts GS, Kozak D, Anderson W, Broom MF, Vogel R, Trau M. Tunable nano/micropores for particle detection and discrimination: scanning ion occlusion spectroscopy. *Small* 6, 2653-2658 (2010).
- 30 Cantin R, Diou J, Bélanger D, Tremblay AM, Gilbert C. Discrimination between exosomes and HIV-1: purification of both vesicles from cell-free supernatants. *J. Immunol. Methods* 338(1-2), 21-30 (2008).
- 31 Tauro BJ, Greening DW, Mathias RA et al. Comparison of ultracentrifugation, density gradient separation, and immunoaffinity capture methods for isolating human colon cancer cell line LIM1863-derived exosomes. *Methods* 56(2), 293-304 (2012).
- 32 Escola JM, Kleijmeer MJ, Stoorvogel W, Griffith JM, Yoshie O, Geuze HJ. Selective enrichment of tetraspan proteins on the internal vesicles of multivesicular endosomes and on exosomes secreted by human B-lymphocytes. *J. Biol. Chem.* 273(32), 20121-20127 (1998).
- 33 Simpson RJ, Kalra H, Mathivanan S. ExoCarta as a resource for exosomal research. *J. Extracell. Vesicles* 1, 18374 (2012).
- 34 Lee J, Kotliarova S, Kotliarov Y et al. Tumor stem cells derived from glioblastomas cultured in bFGF and EGF more closely mirror the phenotype and genotype of primary tumors than do serum-cultured cell lines. *Cancer Cell* 9(5), 391-403 (2006).
- 35 Gravendeel LA, Kouwenhoven MC, Gevaert O et al. Intrinsic gene expression profiles of gliomas are a better predictor of survival than histology. *Cancer Res.* 69, 9065-9072 (2009).
- 36 Verhaak RG, Hoadley KA, Purdom E et al. Integrated genomic analysis identifies clinically relevant subtypes of glioblastoma characterized by abnormalities in PDGFRA, IDH1, EGFR, and NF1. *Cancer Cell* 17, 98-110 (2010).

- 37 Bobrie A, Colombo M, Krumeich S, Raposo G, Théry C. Diverse subpopulations of vesicles secreted by different intracellular mechanisms are present in exosome preparations obtained by differential ultracentrifugation. *J. Extracell. Vesicles* 1, 18397 (2012).
- 38 Dragovic RA, Gardiner C, Brooks AS et al. Sizing and phenotyping of cellular vesicles using nanoparticle tracking analysis. *Nanomedicine* 7, 780-788 (2011).
- 39 Yang L, Broom MF, Tucker IG. Characterization of a nanoparticulate drug delivery system using scanning ion occlusion sensing. *Pharm. Res.* 29(9), 2578-2586 (2012).
- 40 Roberts GS, Yu S, Zeng Q et al. Tunable pores for measuring concentrations of synthetic and biological nanoparticle dispersions. *Biosens. Bioelectron.* 31(1), 17-25 (2012).
- 41 Nazarenko I, Rana S, Baumann A et al. Cell surface tetraspanin Tspan8 contributes to molecular pathways of exosome-induced endothelial cell activation. *Cancer Res.* 70(4), 1668-1678 (2010).
- 42 Van der Pol E, Hoekstra AG, Sturk A, Otto C, van Leeuwen TG, Nieuwland R. Optical and nonoptical methods for detection and characterization of microparticles and exosomes. *J. Thromb. Haemost.* 8(12), 2596-2607 (2010).
- 43 Filipe V, Hawe A, Jiskoot W. Critical evaluation of nanoparticle tracking analysis by NanoSight for the measurement of nanoparticles and protein aggregates. *Pharm. Res.* 27, 796-810 (2010).
- 44 Hoen EN, van der Vlist EJ, Aalberts M et al. Quantitative and qualitative flow cytometric analysis of nanosized cell-derived membrane vesicles. *Nanomedicine* 8(5), 712-720 (2011).
- 45 Shapiro HM. *Practical Flow Cytometry* (4th Edition) . Wiley-Blackwell, NY, USA (2003).
- 46 Platt M, Willmott GR, Lee GU. Resistive pulse sensing of analyte-induced multicomponent rod aggregation using tunable pores. *Small* 8(15), 2436-2444 (2012).
- 47 Balaj L, Lessard R, Dai L et al. Tumor microvesicles contain retrotransposon elements and amplified oncogene sequences. *Nat. Commun.* 2, 180 (2011).
- 48 Logozzi M, De Milito A, Lugini L et al. High levels of exosomes expressing CD63 and caveolin-1 in plasma of melanoma patients. *PLoS ONE* 4, e5219 (2009).

3

Based on:

Possibilities and limitations of current technologies for quantification of biological extracellular vesicles and synthetic mimics

Sybrein L.N. Maas^{a,b}, Jeroen de Vrij^{a,b}, Els J. van der Vlist^c, Biaina Geragousian^{a,b}, Louis van Bloois^d, Enrico Mastrobattista^d, Raymond M. Schiffelers^e, Marca H.M. Wauben^c, Marika L.D. Broekman^{a,b}, Esther N.M. Nolte-'t Hoen^c

^a Department of Neurosurgery, University Medical Center Utrecht, The Netherlands. ^b Brain Center Rudolf Magnus, University Medical Center Utrecht, The Netherlands. ^c Department of Biochemistry & Cell Biology, Faculty of Veterinary Medicine, Utrecht University, The Netherlands ^d Department of Pharmaceutics, Utrecht Institute for Pharmaceutical Sciences, Utrecht University, Utrecht, The Netherlands.. ^e Department of Clinical Chemistry and Hematology, University Medical Center Utrecht, The Netherlands

J. Control Release 200, 87–96 (2014)

Abstract

Nano-sized extracellular vesicles (EVs) released by various cell types play important roles in a plethora of (patho)physiological processes and are increasingly recognized as biomarkers for disease. In addition, engineered EV and EV-inspired liposomes hold great potential as drug delivery systems. Major technologies developed for high-throughput analysis of individual EV include nanoparticle tracking analysis (NTA), tunable resistive pulse sensing (tRPS) and high-resolution flow cytometry (hFC). Currently, there is a need for comparative studies on the available technologies to improve standardization of vesicle analysis in diagnostic or therapeutic settings.

We investigated the possibilities, limitations and comparability of NTA, tRPS and hFC for analysis of tumor cell-derived EVs and synthetic mimics (i.e. differently sized liposomes). NTA and tRPS instrument settings were identified that significantly affected the quantification of these particles. Furthermore, we detailed the differences in absolute quantification of EVs and liposomes using the three technologies. This study increases our understanding of possibilities and pitfalls of NTA, tRPS and hFC, which will benefit standardized and large-scale clinical application of (engineered) EVs and EV-mimics in the future.

Introduction

Extracellular vesicles (EVs) are lipid membrane-enclosed vesicles released by cells and present in bodily fluids. EVs are heterogeneous in composition and size, ranging from approximately 50 to 1000 nm, with the vast majority ≤ 200 nm in size [1,2]. EVs originate from their donor cell as a result of outward budding of the plasma membrane. Alternatively, EVs form as a result of intracellular budding within late endosomes, from which vesicles are released upon fusion of these multivesicular bodies with the plasma membrane [3]. Regardless of their size and origin, 'EVs' is the collective term adopted to designate any type of cell-derived vesicle in the extracellular space. In recent years, multiple reports have demonstrated EVs to play an important role in (patho)physiological processes, such as immune responses [4], blood coagulation [5], tissue repair [6] and tumor growth [7,8].

Current research focuses on obtaining improved insight into the formation and function of EVs and on studying the potential of EVs for medical applications. One of these applications is to use EVs present in body fluids as biomarkers for diagnosis and monitoring of diseases [9,10]. In cancer, tumor-derived EVs can serve as biomarkers since they contain proteins and RNAs from their malignant donor cells [7,8]. Since tumor-derived EVs are released in easily accessible bodily fluids, such as blood or urine [7,11], analysis of these EVs for disease monitoring may circumvent biopsies [11], thereby reducing biopsy related morbidity and mortality. A second important application of EV in the medical field is their use as drug delivery systems. Although liposomes, which share the bilayered membrane structure with EVs, have been employed as drug delivery systems for many years, cross-pollination of knowledge in the liposome and EV research fields now holds high promise for improvement of current delivery systems. Various studies have indicated that EVs can be exploited as carriers for delivery of exogenous therapeutic cargoes, e.g. siRNAs, in vivo [12]. EV characteristics that facilitate efficient delivery of biological drugs include their capacity to traverse intact biological barriers (e.g. blood-brain barrier) and to deliver functional RNA into cells, as well as their stability in blood (reviewed in [13]). Current research focuses on exploiting these features to either engineer natural EV for drug delivery to specific tissues, or to design EV mimics formulated as liposomes containing relevant EV components [14].

Even though EVs are increasingly recognized as important biological and therapeutical entities, standardized methods for their analysis are still lacking [15]. Establishment of such methods is crucial for safe application of (engineered) EV in clinical practice, but EV quantification has proven technically difficult due to the small size of EVs and their heterogeneity in size and composition.

In recent years, several instruments have become available that allow detection and characterization of individual EVs. These techniques include nanoparticle tracking analysis (NTA) [16,17], tunable resistive pulse sensing (tRPS) (also known as scanning ion occlusion sensing (SIOS)) [18] and high-resolution flow cytometry (hFC) [19]. EV detection and quantification with these single-particle analysis techniques rely on distinct principles. NTA is based on the illumination of particles in suspension with a laser beam, followed by the recording of the scattered light by a light-microscope. The Brownian motion of each particle is individually tracked to determine the mean square displacement of the individual particle. Since temperature and viscosity of the suspension are known and controlled, the Stokes–Einstein equation can be used to determine the hydrodynamic diameter of each individual particle. The total number of particles is used for particle concentration estimation [16,20]. In tRPS, a non-conductive polyurethane membrane, punctured to contain a single opening, separates two fluid cells [21]. By applying a voltage across the membrane a flow of ions is induced. Once a particle moves through the nanopore, the flow of ions is altered resulting in a brief “resistive pulse” which is recorded by the instrument [22]. The size-distribution [23] and concentration [24,25] of particles can be calculated by referring the observed pulse height and rate to pulses induced by reference particles of known volume and concentration. Flow cytometric analysis of particles involves the sequential excitation of individual, fluorescently labeled particles in a liquid stream and detection of emitted light by diodes or photomultipliers [26]. In hFC, a high-end flow cytometer is optimized for the analysis of nano-particles. This optimization consists of light scattering detection at customized angles, the usage of high power lasers and high-performance photomultiplier tubes for more sensitive light detection, and application of fluorescence-based thresholding to distinguish particles of interest from noise signals [19]. In-depth description of the technical backgrounds of the techniques is beyond the scope of this manuscript and described elsewhere for NTA [16,20,27,28], tRPS [22–24] and hFC [19,29].

For accurate EV quantification and characterization, it is important to know to what extent instrument-specific variables influence particle characterization. For NTA, studies on how instrument settings affect the analysis of heterogeneous EV populations are limited [20,28,17], and the effects of specific variables on EV quantification and size-profiling by tRPS are largely unknown. For hFC, detailed reports on optimizing the instrument configuration and settings for accurate analysis of EVs and other nano-sized particles have recently been published [19,29]. In a few studies, two or three of the above described techniques have been compared. However, these studies either focused on size-profiling of synthetic beads [30,31], or did not address effects of instrument settings on EV characterization and quantification [32,33].

Here, we report a comprehensive comparative study on NTA, tRPS and hFC for analysis of populations of heterogeneous nano-sized EVs and synthetic mimics (i.e. polystyrene beads and calcein-loaded liposomes). We identified different NTA- and tRPS-variables that significantly influenced the quantification of these particles. Furthermore, we assessed the comparability of NTA, tRPS and hFC in absolute quantification of liposomes and EVs. Based on these data, we stress the importance of technical knowledge of the instruments, awareness of analytical variables, and recognition of how instrument settings affect measurements when analyzing EV populations with unknown concentration and size heterogeneity.

Materials and Methods

Polystyrene beads

115 and 203 nm polystyrene beads (Izon Science, Christchurch, New Zealand) were analyzed using tRPS and NTA. For hFC, fluorescent 100 and 200 nm polystyrene beads (yellow–green-fluorescent FluoSpheres, Invitrogen) were used.

Liposome preparation and characterization

Egg phosphatidylcholine (EPC), egg phosphatidylglycerol (EPG) (Lipoid GmbH, Ludwigshafen, Germany) and cholesterol (Sigma-Aldrich Chemie B.V., Zwijndrecht, The Netherlands) were dissolved in chloroform/methanol (1:1, v/v) in a round-bottom flask in a molar ratio of 2:0.06:1, respectively. A lipid film was prepared by rotary evaporation (Rotavapor R3, Büchi Labortechnik AG, Flawil, Switzerland), followed by drying under a stream of nitrogen. The lipid film was hydrated with 10 mM calcein

for 105 nm liposomes or 250 μ M calcein for “L146” and “L212” liposomes in HEPES buffered saline (HBS, 10 mM HEPES, 137 mM NaCl, pH 7.4). Liposomes were sized by multiple extrusion under nitrogen pressure using polycarbonate membranes (Nuclepore, Pleasanton, CA, USA) with pore sizes of 200 nm and 100 nm in a Lipex high pressure extruder (Lipex, Northern Lipids, Vancouver, Canada) or a Liposofast Extruder (Avestin, Inc, Ottawa, Canada). Non-entrapped calcein was removed with dialysis against HBS for at least 3 days using Slide-A-Lyzer dialysis cassettes with a cut off of 10 kD (Thermo Scientific, Bremen, Germany). The mean particle size of the liposomes and the polydispersity index (PDI) was determined by means of dynamic light scattering (DLS) using a Malvern ALV CGS-3 with a He-Ne laser source (Malvern Instruments, Malvern, UK). Liposome sizes (L146 and L212) were 146 nm with a PDI of 0.03 and 212 nm with a PDI of 0.07. The zeta-potential of the liposomes (ζ potential) was determined using a Malvern Zetasizer Nano-Z (Malvern Instruments, Malvern, UK). The phosphate concentrations of the liposomes were determined with a phosphate assay described by Rouser et al. [34]. For final use, L146 and L212 liposomes were diluted with HBS till a final total lipid (including cholesterol) concentration of 65 mM.

Cell culture and EV isolation

The human glioblastoma cell line U87-MG and the lymphoblastoma cell line RN were cultured in medium containing FCS depleted from bovine EVs as described previously [18,19]. After 24 h of incubation the supernatant was isolated and centrifuged at 200 \times g for 10 min, two times at 500 \times g for 10 min, followed by 10,000 \times g for 30 min. 100,000 \times g pelleted EVs were resuspended in phosphate buffered saline (PBS) containing 0.2% BSA from an ultracentrifuged stock solution [29]. EVs were fluorescently labeled with 7.5 μ M PKH67 (Sigma-Aldrich), mixed with 2.5 M sucrose, overlaid with a linear sucrose gradient (2.0–0.4 M sucrose in PBS) in an SW60 tube (Beckman) and floated into the gradient by centrifugation for 16 h at 192,000 \times g [29]. Gradient fractions were collected, diluted in PBS and analyzed. Fraction densities were determined by refractometry.

NTA

An LM14 Nanosight instrument (Nanosight Ltd, Salisbury, UK) equipped with a CMOS camera (Hamamatsu Photonics, Hamamatsu, Japan) and a 488 nm laser was used. Data acquisition and processing were performed using NTA software 2.3 build 0025. Background extraction was applied, and automatic settings were applied for the minimum expected particle size, minimum track length and blur settings. Since samples

were diluted at least 20 times in PBS, viscosity settings for water were applied and automatically corrected for the temperature used. Detection threshold and camera level settings varied as described in the Results section. Five movies of 60 s at 25 frames per second were recorded and designated as a single measurement. Only measurements with at least 1000 completed tracks were further analyzed [17]. For polystyrene bead dilutions, single measurements were performed for each dilution, whereas triplicates were recorded for liposome and EV samples.

We excluded data obtained at camera-level 15 (shutter: 1200, gain: 500) as this camera-level resulted in the detection of substantial amounts of background detection, obscuring accurate data interpretation.

tRPS

For tRPS, the qNano instrument (Izon Science Ltd, Christchurch, New Zealand) was used as described [35]. Data was recorded and analyzed using the Izon Control Suite Software version 2.2.2.111. The default minimum blockade height (0.05 nA) for particle detection was used. For sample calibration and serial dilution experiments, polystyrene beads supplied by the qNano manufacturer were used. Both 115 and 203 nm polystyrene bead dilutions were recorded using NP100 nanopores. Liposome dilutions were recorded using two different NP100 nanopores at 0.8 kPa and 1.2 kPa pressure settings. EV samples were analyzed using both an NP200 (1.2 kPa pressure) and NP150 nanopore (1.4 kPa). The buffers of EVs and calibration beads were kept identical by diluting the calibration beads in the appropriate fraction of a (mock-loaded) sucrose-based density gradient.

hFC

High-resolution flow cytometric analysis of individual EVs was performed using the BD Influx flow cytometer (Becton Dickinson, San Jose, CA, USA) with an optimized configuration, as described in detail before [29]. Light scattering was measured with a collection angle of 15–25° (reduced wide-angle FSC) and detection was performed in log mode. Samples were run at low pressure (5 PSI on the sheath fluid and 4.2 PSI on the sample) using a 140 μ m nozzle. The calculated flow rate at these settings was 52.2 μ l per minute, as determined by weighing the volume aspirated during 30 min. Fluorescent 100 nm and 200 nm polystyrene beads (yellow-green-fluorescent FluoSpheres, Invitrogen) were used for calibration of the fluorescence, reduced wide-angle FSC, and SSC settings. EVs in sucrose fractions were diluted in PBS at least 20

times and time-based quantitative measurements were performed as described before [29]. Data was acquired using Spigot software version 6.1 (Becton Dickinson). Data was further analyzed using FCS Express software (De Novo Software, Los Angeles, USA).

Statistical analysis

Data analysis was performed using Prism version 5.0 (GraphPad Software, La Jolla, CA, USA) or Microsoft Excel 2010 (Microsoft, Seattle, WA, USA). Two-tailed independent t-tests were used to test for significant differences in means. One-way ANOVA followed by Tukey's post-test was performed to test differences between multiple groups. Pearson's correlation coefficient was used to determine the correlation between dilution and the measured concentration. Significance was determined and indicated as (*) p-value ≤ 0.05 , (**) p-value ≤ 0.01 and (***) p-value ≤ 0.001 . Error bars represent the standard deviation (s.d.) unless stated otherwise.

Results

NTA-based particle quantification

Detection of nano-sized particles with NTA is influenced by two parameters: the camera-level (shutter speed and camera gain), which is set prior to data acquisition, and the detection threshold, i.e. the scattering intensity threshold above which particles are traced (set at data processing). Here, we tested how these parameters affected the quantification of nano-sized particles that differ in refractive index, size, and heterogeneity.

First, we determined the accuracy for quantification of homogeneous populations of 115 or 203 nm sized polystyrene beads, which have a high refractive index (r.i.) and consequently cause extensive light scattering. Within a 32-fold dilution range (0.9–29.0 $\times 10^8$ /ml) the measured concentrations approximated the expected concentrations for 115 and 203 nm beads (**Fig. 1A**) (R^2 : 0.969 and 0.998 respectively).

For the 115 nm beads we were also able to obtain valid measurements (N1000 completed tracks) outside this range. However, the resulting s-shaped curve (**Fig. 1A**) indicates an overestimation of particles below 0.9 $\times 10^8$ /ml and an underestimation above 29.0 $\times 10^8$ /ml, resulting in decreased correlation accuracy (R^2 : 0.859 for all measurements). Although the range of refractive indices that EVs can exhibit is largely

unknown, polystyrene beads most likely have an r.i. that is substantially higher than the r.i. of the majority of EVs [17]. Next, we tested how camera level and detection threshold settings affect the quantification of calcein-labeled liposomes, which, similar to EVs, are enclosed by a lipid bilayer. Movies were recorded, at camera level 6 (shutter: 150, gain: 250), camera level 9 (shutter: 450, gain: 250), and camera level 12 (shutter: 600, gain: 350), which represent preprogrammed NTA settings. After data acquisition each movie was processed at detection threshold 4, 6, 8 and 10 (standard software setting).

As expected, at increased camera levels the particles appeared brighter and increased detection was observed of weak-scattering particles (**Fig. 1B, top-panel**). The number of detectable particles was also increased by reducing the detection threshold (**Fig. 1B, bottom-panel**) (A complete overview of screenshots at different camera levels and detection thresholds is provided in **Suppl. Fig. S1A**). Numerical analysis of these data revealed that the quantification of liposomes is significantly influenced by the NTA settings, with measurement of higher concentrations after increasing the camera level or decreasing the detection threshold (**Fig. 1C** and **Suppl. Fig. S1B**). At both camera levels 9 and 12, accurate linearity in measured concentration was observed for multiple dilutions of liposomes (applying camera level 6 resulted in an inadequate number of completed tracks) (**Fig. 1D**). Thus, relative comparison of liposome concentrations is feasible with different NTA settings, but measurement of the exact concentration strongly depends on the camera-level and detection threshold settings. Of interest, the increased number of liposome detection after increasing the camera level is not accompanied by increased detection of smaller sized liposomes (**Suppl. Fig. S1C**). It has previously been suggested that smaller particles may be over-scattered by larger particles, which would especially occur after concentrating samples [17,36]. However, this appears not to occur for liposomes (**Suppl. Fig. S1D**).

Next, we tested to what extent the camera-level and detection threshold influence the quantification of EVs, which are more variable in size and r.i. than liposomes. For these experiments, we used EVs derived from the RN lymphoblastoma and U87-MG glioblastoma cell lines that were purified from contaminating protein aggregates by sucrose density gradient ultracentrifugation. As expected, increasing the camera level resulted in an increased brightness of detected particles (**Suppl. Fig. S2A**). Similar to the liposome analysis, different EV quantification data were obtained at different camera level settings (**Fig. 1E**). A maximum fold change of 3 was observed (camera-

level 6 versus 12 at detection threshold 10). The influence of detection threshold on particle quantification was less prominent for EVs compared to liposomes (**Fig. 1E** and **Suppl. Fig. S2B**). Similar data were obtained for the U87-MG derived EVs (data not shown). Sample dilution did not significantly influence measurement of the raw EV concentration (i.e. the measured sample concentration multiplied by the dilution factor) (**Fig. 1F**). This was corroborated by the observation that the size-distributions and mode sizes were similar at the different dilutions (**Suppl. Fig. S2C** and **S2D**). Thus, although EVs are more heterogeneous in size than liposomes, the presence of infrequent EV that displayed a higher level of scattering did not substantially affect detection of neighboring EVs.

In conclusion, camera-level and detection threshold variables were found to affect the NTA-based quantification of liposomes and EVs. The influences were more profound for the relatively homogeneous liposomes than for the heterogeneous EVs.

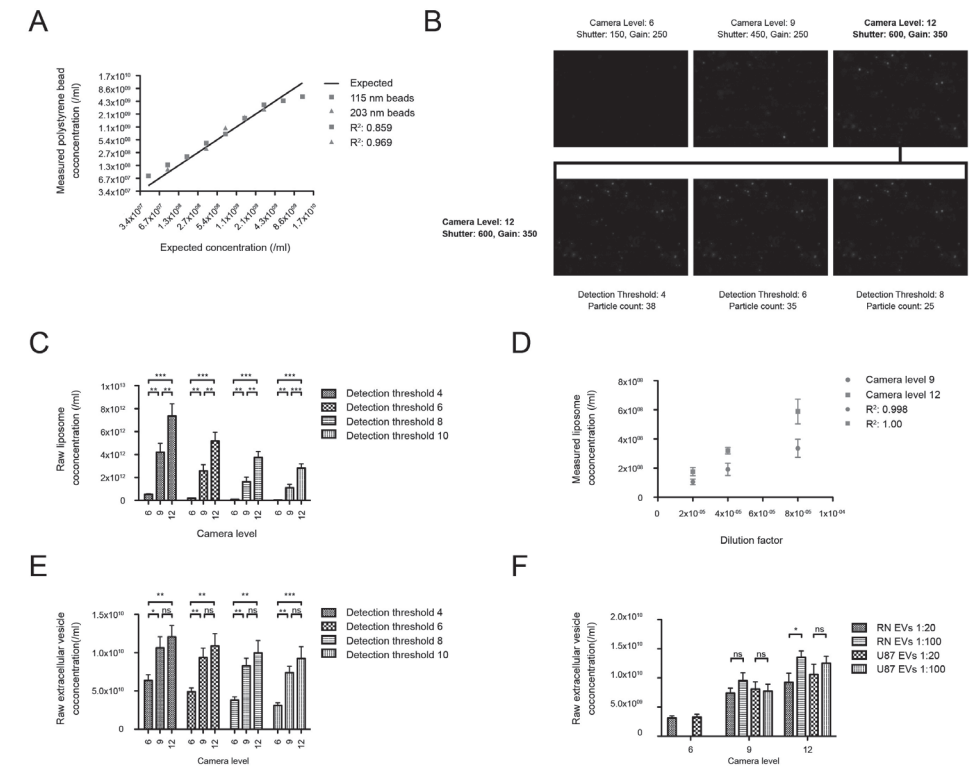


Figure 1. NTA-based quantification of beads, liposomes and EVs. (A) Quantification of 115 and 203 nm polystyrene beads. The measured concentration of the beads is plotted against the expected concentration based on the manufacturer's supplied stock concentration. Detection was performed at camera level 5 (shutter: 100, gain: 200) for the 115 nm beads and camera level 3 (shutter: 20, gain: 0) for the 203 nm beads. (B–D) Quantification of 115 nm-sized liposomes. The effect of camera level and detection threshold was assessed, demonstrating visual differences in particle imaging (screenshots in (B)) as well as differences in the calculation of raw concentrations (C). Dilution of liposomes showed linearity with the measured liposome concentration, at camera levels 9 and 12 (D). (E–F) Quantification of purified EVs. The effect of camera level and detection threshold on quantification of EVs (from RN cells) is shown in (E). The effect of sample dilution (1:20 and 1:100) on quantification is shown in (F), with EVs included from RN cells and U87-MG cells, and analysis at three different camera levels. Data are mean \pm s.d. (n = 3).

tRPS-based particle quantification

As an alternative to NTA, we tested tRPS for liposome and EV quantification, with a specific focus on establishing the most suitable measurement conditions. As tRPS-based quantification requires a linear correlation between the particle count rate (particles per minute) and the concentration of particles, we first measured a dilution

range of polystyrene calibration beads. We observed linearity over a 64-fold dilution range for the 115 nm beads (R^2 : 0.979) and over a 32-fold range for the 203 nm beads (R^2 : 0.994) (**Fig. 2A**).

Particle detection above threshold levels is dependent on the blockade height (resistive pulse) generated by a particle moving through a nanopore. This blockade height is determined by the particle's volume relative to the volume of the nanopore opening, the applied voltage, and buffer used. These parameters together determine a 'tRPS setup' and thus determine if particles surpass threshold levels (0.05 nA at default software settings). High-sensitivity tRPS setups can be used to detect the smallest particles. To obtain a high-sensitivity setup one should apply a high voltage, low stretch (to establish a minimal opening size of the nanopore) and a small nanopore (NP100/NP150) [32,35]. Nanopore characteristics are known to differ between individual nanopores, as well as over time [37]. To assess the effect of this on liposome quantification, we compared three cases. First we compared two new NP100 nanopores (setups #1 and #2). Subsequently, the nanopore used for setup #1 was tested again after approximately 7 h of usage (termed setup #3). The most optimal (i.e. high-sensitivity) settings were applied in all three cases. Measurement of 115 nm polystyrene beads for tRPS calibration showed different mode blockade heights detected for setups #1, #2, and #3, with #2 > #1 > #3 (**Fig. 2B, left panel**). This indicated that the lower detection limit, as determined by the height of the calibration bead blockade relative to the threshold level of 0.05 nA, was different at the different setups. This is illustrated by reconstructing the mean blockade heights of 115 nm calibration particles and liposomes for the three setups (**Fig. 2B, right panel**). Using setup #3, the peaks of the 115 nm calibration particles are closer to the detection threshold level. The lower detection limit in setup #3 is therefore higher than in setups #1 and #2, implicating that the blockade height induced by smaller liposomes may not surpass the detection threshold. This could result in the detection of only larger-sized liposomes. Secondly, these observed differences indicate that characteristics of nanopores, such as resolution, may change over time.

The variation in detectable size range for setups 1–3 resulted in substantial differences in absolute quantification of the liposomes (difference setup #2 versus #3: 2.43 fold; **Fig. 2C**). Setup #3 allowed detection of > 80 nm liposomes only (**Fig. 2C, left-panel**), and consequently yielded the lowest liposome quantification. Differences in particle concentration (1.43 fold) were also observed for setups #1 and #2, despite

the comparable efficiency in detection of small liposomes at these setups (**Fig. 2C, left-panel**).

Besides absolute quantification of liposomes, we also determined how accurate a range of liposome dilutions could be quantified by tRPS (**Fig. 2D**). An NP100 nanopore was used for this test, and we concomitantly investigated whether the pressure level influenced liposome quantification. For both applied pressure levels we observed accurate detection and linearity over a 4-fold dilution range. Surprisingly, changing the applied pressure led to significantly different liposome sizing estimations (**Suppl. Fig. 3A and B**).

EV measurements by tRPS indicated that the size distributions of RN (**Fig. 2E**) and U87-MG derived EVs resembled those obtained using the NTA, with the majority of EVs being 100–200 nm in size. Similar to what we observed for NTA, tRPS showed the presence of a small number of larger (200–600 nm) EVs. Due to the presence of large EVs, we tested two larger nanopores (NP200 and NP150) for EV quantification, to reduce clogging events. Even though frequent nanopore clogging was observed, overall particle detection was stable and reproducible for each triplicate of sample measurements (**Suppl. Fig. S4A**). Applying the NP150 nanopore, which theoretically allows for detection of 100–120 nm particles, yielded significantly higher EV particle concentrations as compared to the measurement with the NP200 pore (**Fig. 2F**) (difference RN-derived EVs 1.45 fold, U87-derived EVs 1.50 fold). The ability to measure smaller sized EVs with the NP150 nanopore (**Suppl. Fig. S4B**), led to significant differences in the calculated mean and mode sizes of the EVs (e.g. mode sizes of 136.3 nm (NP200) and 117.8 nm (NP150) for RN-derived EVs) (**Suppl. Fig. S4C**).

In conclusion, quantifications of liposomes and EVs can differ between (high sensitivity) nanopore setups and this is most likely related to the lower detection limit. Since the required lower detection limit may be unknown for liposomes and EVs, tRPS measurement may result in underestimation of the concentration.

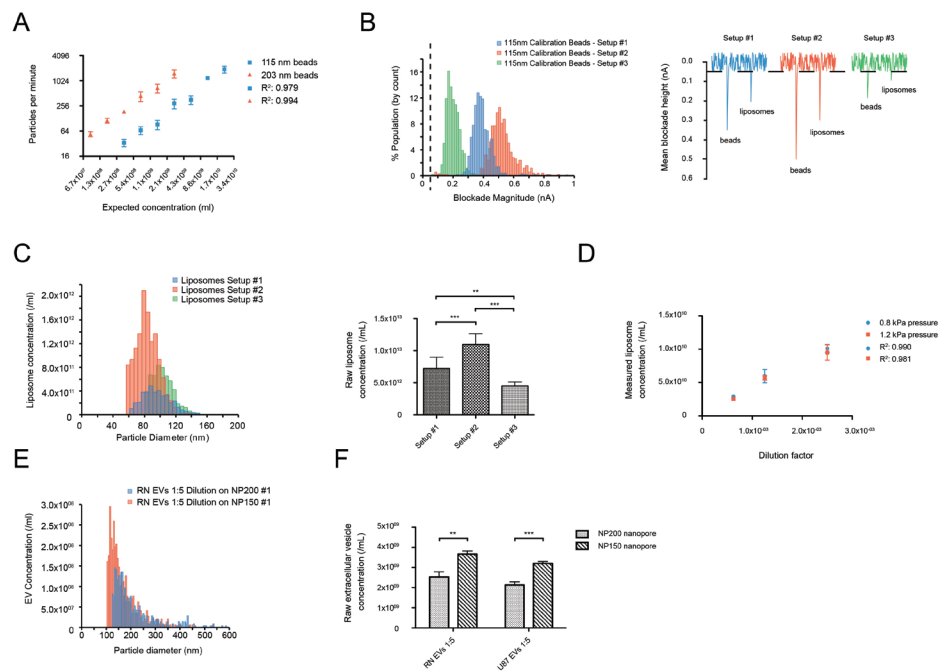


Figure 2. tRPS-based particle quantification. (A) Quantification of 115 and 203 nm polystyrene calibration beads. As tRPS quantification is based on the conversion of observed particle per minute counts to that of polystyrene calibration beads of known concentration, the read-out is displayed as “particles per minute”. (B) Three tRPS setups displaying the observed blockade heights for the same 115 nm calibration beads (left-panel). The dashed line illustrates the detection threshold (both panels). Reconstruction of the recorded data for beads and liposomes at the three different setups (right-panel), illustrating that the lower detection limit is the highest for setup #3, followed by setups #1 and #2. Bin size 15 pA. (C) Representative liposome size-distributions obtained at the three different tRPS setups (left-panel). For each of the three setups the measured concentration was corrected for the dilution factor to obtain raw concentration estimations ($n = 6$) (right-panel). Bin size 5 nm. (D) Quantification of serially diluted liposomes at two different pressure levels ($n = 3$). (E) Representative size-distribution obtained for RN-derived EVs on an NP200 nanopore setup and an NP150A nanopore. Bin size 5 nm. (F) Raw particle concentrations were determined for RN and U87-MG derived EVs at both the NP200 and NP150 nanopore setups ($n = 3$). Data are mean \pm s.d.

hFC-based particle quantification

Reliable quantification of nano-sized particles using fluorescence-based hFC requires that sufficient numbers of fluorophores are associated to the particle to be detected above the fluorescence threshold, and that maximal sensitivity in fluorescence detection is obtained. The optimal configuration and settings for quantitative and qualitative analyses of nano-sized particles using the BD Influx have been determined previously [19,29]. Instrument settings that were found to affect EV measurements

included the nozzle size and the applied sample/sheath fluid pressure. Using the optimal settings, 100 nm fluorescent polystyrene beads were efficiently detected above background noise. Furthermore, for a 16-fold dilution range, hFC accurately detected sample dilutions for both 100 ($R^2: 1.00$) and 200 nm ($R^2: 0.999$) fluorescent polystyrene beads (Fig. 3A).

Calcein labeled, 105 nm sized liposomes could also be detected above the fluorescence threshold (Fig. 3B). As expected, light scattering (FSC and SSC) levels generated by low r.i. liposomes were low and could not be discriminated from those generated by noise, indicating the need for fluorescence-based analysis (data not shown). Within the 16-fold dilution range tested here, liposomes could be quantified with accurate linearity ($R^2: 1.00$) (Fig. 3C).

hFC-mediated detection of RN and U87-MG derived EVs relied on fluorescent labeling of EV and efficient removal of unbound dye by sucrose-gradient ultra-centrifugation [29] (Fig. 3D and Suppl. Fig. 5). Although hFC does not allow for absolute size measurement of EV, variation in size and composition of EV are reflected in the light scattering (FSC and SSC) and fluorescence signals observed. Similar to what was observed in the NTA and tRPS measurements of the RN and U87-MG derived EVs, hFC-based analysis also indicated substantial heterogeneity within these EV populations based on light scattering and PKH67 fluorescence levels (Fig. 3D and Suppl. Fig. 5). Quantification by hFC indicated no significant differences in the estimation of EV concentrations over an 8-fold dilution range for both the RN and U87-derived EVs (Fig. 3E).

In conclusion, once sufficient numbers of fluorophores are associated to liposomes or EVs to allow their detection above the fluorescent threshold, hFC can be used for accurate quantitative analysis of fluorescently labeled liposomes and EVs in a range of sample dilutions.

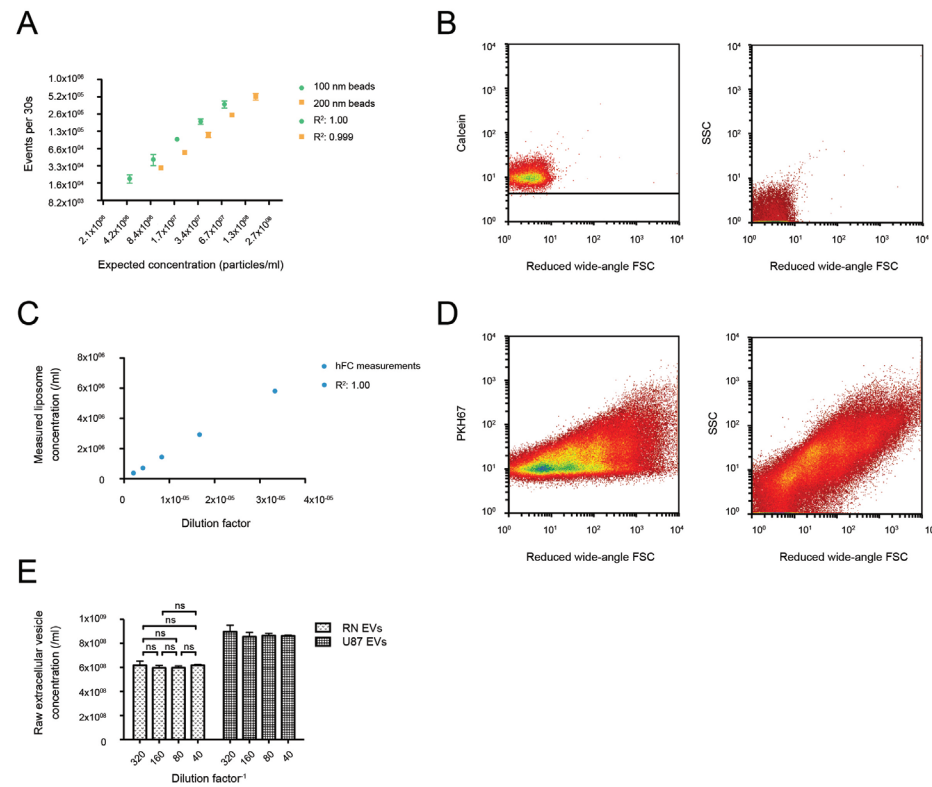


Figure 3. hFC-based particle quantification. (A) Quantification of serially diluted 100 and 200 nm fluorescent polystyrene beads. Indicated are the mean number of beads detected in a fixed time window of 30 s. (B) Dotplots indicating that calcein-loaded liposomes can be detected above the fluorescence threshold (solid horizontal line) that excludes detection of non-fluorescent noise events (left-panel) and that light scattering levels induced by these liposomes are low (right-panel). (C) Quantification of serially diluted calcein-loaded liposomes. Indicated are the mean number of liposomes detected in a fixed time window of 30 s. (D) Dotplots indicating that PKH-67 labeled RN-derived EVs can be detected above the fluorescence detection threshold (left panel) and that the FSC and SSC signals induced by these heterogeneous are highly variable. (E) EVs were measured over an 8-fold range, and corrected for the dilution used to determine the raw concentration estimation. No statistical different raw concentration estimations between the dilutions were observed. Data are mean \pm s.d. ($n = 3$).

Comparison of liposome and EV quantification using NTA, tRPS, and hFC

For clinical application and research purposes, it is of utmost importance to reliably determine the concentrations of (engineered) EVs or synthetic mimics. Ideally, measurements of identical samples with different technologies should yield comparable quantitative data. We therefore compared quantification data obtained by NTA, tRPS, and fluorescence-based hFC. Based on the previous experiments, a single setup was

selected for each instrument. We performed measurements on relatively homogeneous populations of calcein-loaded liposomes with (DLS-based) sizes of 146 and 212 nm (referred to as L146 and L212 respectively), and a more heterogeneous population of purified and PKH67 labeled EVs. NTA camera-levels were selected based on the visually brightest detection of particles, without the occurrence of abundant over-scattering events. The tRPS settings were selected to allow for the highest-sensitivity measurement. More specifically, L146 measurements were performed with NTA camera-level 12/detection-threshold 4 and nanopore NP100. For L212, camera-level 9/detection-threshold 4 and nanopore NP150 were selected. The RN-EVs were analyzed using NTA camera-level 12/detection-threshold 10 and an NP150 nanopore. Optimized settings [19] were used for hFC, and hFC settings were identical for measurements of both liposome populations and EVs. On the three instruments L146 liposomes were quantified within a 12.5 fold difference (**Fig. 4A, left-panel**). The highest concentrations were measured with NTA ($1.86 \times 10^{14}/\text{ml}$), followed by tRPS ($5.33 \times 10^{13}/\text{ml}$), and hFC ($1.5 \times 10^{13}/\text{ml}$). Also for the L212 liposomes, NTA measurements yielded the highest concentrations ($7.73 \times 10^{13}/\text{ml}$), followed by tRPS ($3.27 \times 10^{13}/\text{ml}$) and hFC ($1.12 \times 10^{13}/\text{ml}$) (**Fig. 4A, right-panel**). Overall, the measured L212 concentrations on the three instruments were within a narrower absolute fold-range (6.92). We compared these quantifications with liposome concentration measurements based on dynamic light scattering (DLS)-sizing, lipid composition, and phosphate quantification, as a standard in the liposome field [38]. Using this method, the calculated liposome concentrations were $2.27 \times 10^{13}/\text{ml}$ for L146 and $7.46 \times 10^{12}/\text{ml}$ for L212 liposomes (dotted horizontal lines in Fig. 4A). However, DLS is known to be heavily influenced by outliers [30], which may result in overestimated size measurements. When replacing DLS size measurement with averaged liposome sizing data obtained by NTA and tRPS (124 and 156 nm for the L146 and L212 liposomes, respectively; **Fig. 4B and C**), the calculated liposome concentrations were substantially higher (solid horizontal lines in Fig. 4A) and were most similar to the concentrations obtained by tRPS.

The absolute concentration measurements of EV on the three instruments were within a smaller fold-range difference compared to the measurements of liposomes (4.44 versus 6.92 (L146) or 12.5 (L212); **Fig. 4D**). Interestingly, quantification of EVs by tRPS and hFC yielded absolute particle concentrations in the same range ($1.01 \times 10^9/\text{ml}$ and $1.40 \times 10^9/\text{ml}$). However, similar to the liposome measurements, NTA yielded substantially higher values for the EV concentrations ($4.50 \times 10^9/\text{ml}$) (**Fig. 4D**).

In conclusion, the absolute quantifications as observed for both homogeneous calcein-loaded liposomes and a purified population of more heterogeneous, PKH67 labeled RN derived EVs differed significantly between the instruments. For liposomes, the difference in quantifications between the instruments decreased when measuring liposomes that were larger in size. The smallest difference in absolute concentration measurements between the instruments was found when measuring the more heterogeneous population of EVs, for which tRPS and hFC yielded highly similar results.

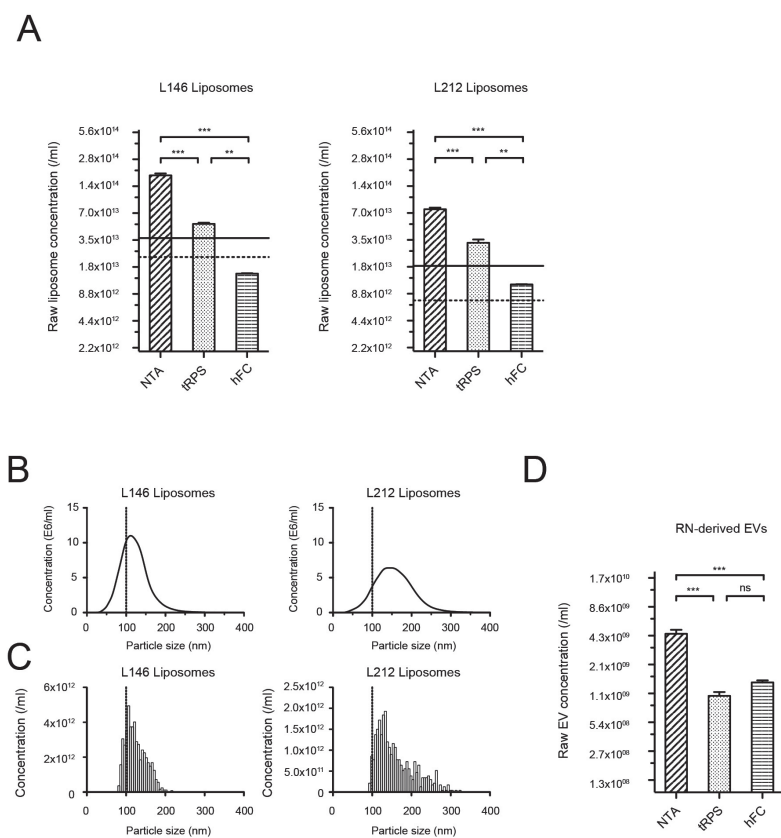


Figure 4. Comparison of liposome and EV quantification using NTA, tRPS and hFC. (A) Comparative quantitative analysis of L146 and L212 liposomes using the three instruments ($n = 3$). Liposomes were diluted to match the required sample concentrations for the different instruments after which measured concentrations were calculated to raw concentrations. Horizontal lines indicate liposome concentration calculations based on lipid composition, phosphate quantification, and dynamic light scattering (DLS) sizing (dotted line) or NTA/tRPS sizing (solid line). Size-distributions for L146 and L212 liposomes as obtained by NTA (**B**) and tRPS (**C**). Bin size 5 nm. (**D**) Comparative quantitative analysis of RN-derived EVs by NTA ($n = 4$), tRPS and hFC ($n = 3$) at instrument specific concentrations, converted to raw concentration estimations. Data are mean \pm s.e.m.

Discussion

Over the last decade, the interest in EVs has greatly intensified due to their proposed role in various biological processes and their potential as biomarkers for disease and as drug delivery systems. Approaches for accurate and standardized quantification of such nano-particles have not yet been established, but are crucial for safe application of EV(-mimics) in clinical settings. Here, we compared quantification of different nano-sized particles, i.e. polystyrene beads, calcein-labeled fluorescent liposomes and purified, PKH67-labeled EVs using three prominent single-EV analysis platforms; NTA, tRPS, and hFC. Moreover, we identified variables that significantly influenced particle quantification using NTA and tRPS.

The particle concentration range at which accurate quantification data could be obtained differed between the instruments. For NTA, the optimal concentration range was 9.0×10^7 /ml– 2.9×10^9 /ml, which is a slightly larger dilution series than previously reported [16]. For tRPS, the required concentration for particle analysis increased as the particle volume decreased. Consequently, 203 nm beads were analyzed at 9.1×10^7 /ml– 2.9×10^9 /ml, whereas 115 nm particles were analyzed at 3.6×10^8 /ml– 2.3×10^{10} /ml. hFC allows accurate quantification at lower particle concentrations (a range of 4.6×10^6 /ml– 7.3×10^7 /ml was analyzed in the current study). Our recent data indicate that concentrations up to 1.0×10^9 /ml can be reliably measured with hFC.

We identified the NTA camera level and detection threshold to be significant factors in the quantification of liposomes (**Fig. 1C**). In contrast, the absolute differences induced by changing these variable settings were less prominent for quantification of EVs (**Fig. 1D**). This may be a result of the relatively higher light-scattering properties of EVs (due to the presence of surface/luminal proteins and/or m(i) RNAs), combined with increased heterogeneity in this population, which may make NTA-based detection of EVs less sensitive to differences in settings as compared to the detection of homogeneous liposomes. Besides the empty liposomes used in this study, liposomes engineered to contain proteins and/or nucleic acids show more structural resemblance with EV and quantification of such particles may accordingly be less sensitive to NTA detection thresholding.

Our tRPS analyses showed inter-experimental variation in the sensitivity of liposome and EV detection (**Fig. 2C and E**), which translated into differences in concentration

measurement. This sensitivity of tRPS-based measurements is determined by the size of the smallest detectable particle. For quantification of homogeneous particle populations of a known size, such as calibration beads, the most suitable nanopore setup for detection of all particles can easily be selected. However, for samples with an unknown size-distribution (e.g. EVs) this is more difficult and the obtained size detection range may be insufficient for detection of all particles. Besides this, we also noted slight differences in tRPS-based concentration measurements (up to ~1.4 fold) between set-ups in which the liposome size-distribution profiles and detection limits were similar (**Fig. 2C**). We hypothesize that subtle differences in nanopore size due to batch variations and nanopore longevity could have caused these variations in particle quantification. The observed differences stress the importance of comparing samples using exactly the same tRPS setup.

Electro-kinetic forces were recently suggested [39] to influence the movement of particles through smaller tRPS nanopore. In case particles possess a different surface-charge compared to the polystyrene calibration particles, one of the two particle types may be more likely to pass through the nanopore. Since this may cause inaccuracy in the calculated particle/minute to concentration calculation, the manufacturer suggested to perform quantifications at two or more pressure levels, after which the tRPS software can determine a surface-charge corrected concentration. Since we observed no difference in the measured liposome concentration at two different pressure levels (**Fig. 2D**), we conclude that electro-kinetic forces at these settings do not significantly influence the quantification of particles. The surface charge of the studied liposomes was -43.0 ± 0.87 mV, which is similar to the reported surface charge characteristics of EVs [40–42]. Single-pressure tRPS quantifications can therefore suffice for accurate EV quantifications. The difference in blockade height when measuring the 115 nm calibration particles at the two pressure settings (**Suppl. Fig. S3A, left-panel**) was unexpected, because the applied pressure does not change the particle volume and nanopore diameter. Implications of this phenomenon for particle characterization need to be further studied. When comparing the liposome size-distributions obtained by tRPS and NTA (**Fig. 2C** and **Suppl. Fig. S2C**), we conclude that both NTA and tRPS allowed detection of liposomes as small as 55–60 nm in size, which for NTA is the theoretical lower limit of liposome detection, limited by the r.i. of the particle [16,20].

In contrast to NTA and tRPS, for hFC the threshold for particle detection is based on fluorescence intensity. Although the sensitivity for detection is largely improved by the use of high power lasers and by increasing the dwell time of the vesicles in the laser beam, particles with low fluorescence intensity (e.g. due to low PKH67 labeling efficiency or because of small size) may not be detected using this technique. Furthermore, the removal of unbound fluorescent dye by density gradient ultracentrifugation can be seen as a time-consuming procedure. However, the same procedure also allows separation of EVs from protein aggregates that are abundantly present in culture media and body fluids. This is essential, since such aggregates can mistakenly be recorded as vesicles by the technologies discussed here.

Comparability analysis of the three techniques indicated that substantially larger differences in quantification were obtained for liposomes, compared to EVs (**Fig. 4A and D**). In fact, no significant difference in raw concentration estimation was observed for quantification of EVs by tRPS versus hFC. One potential explanation is that the EVs exhibit higher fluorescence levels compared to the liposomes, either because EVs are larger in size and incorporate more dye or because of differences in labeling efficiency. Differences between the other instruments are difficult to account for. For both liposome batches and EVs, higher raw concentration estimations were obtained by NTA compared to tRPS. We tested whether background particle detection (from the buffer in which particles were diluted) could explain the observed differences. However, measurement of PBS background particles at camera-level 9 and 12 revealed maximum concentrations of only 2.60×10^7 /ml and 3.3×10^7 /ml, respectively (data not shown), accounting for 3.29% (L146) and 2.33% (L212) of the measured concentrations of the liposomes.

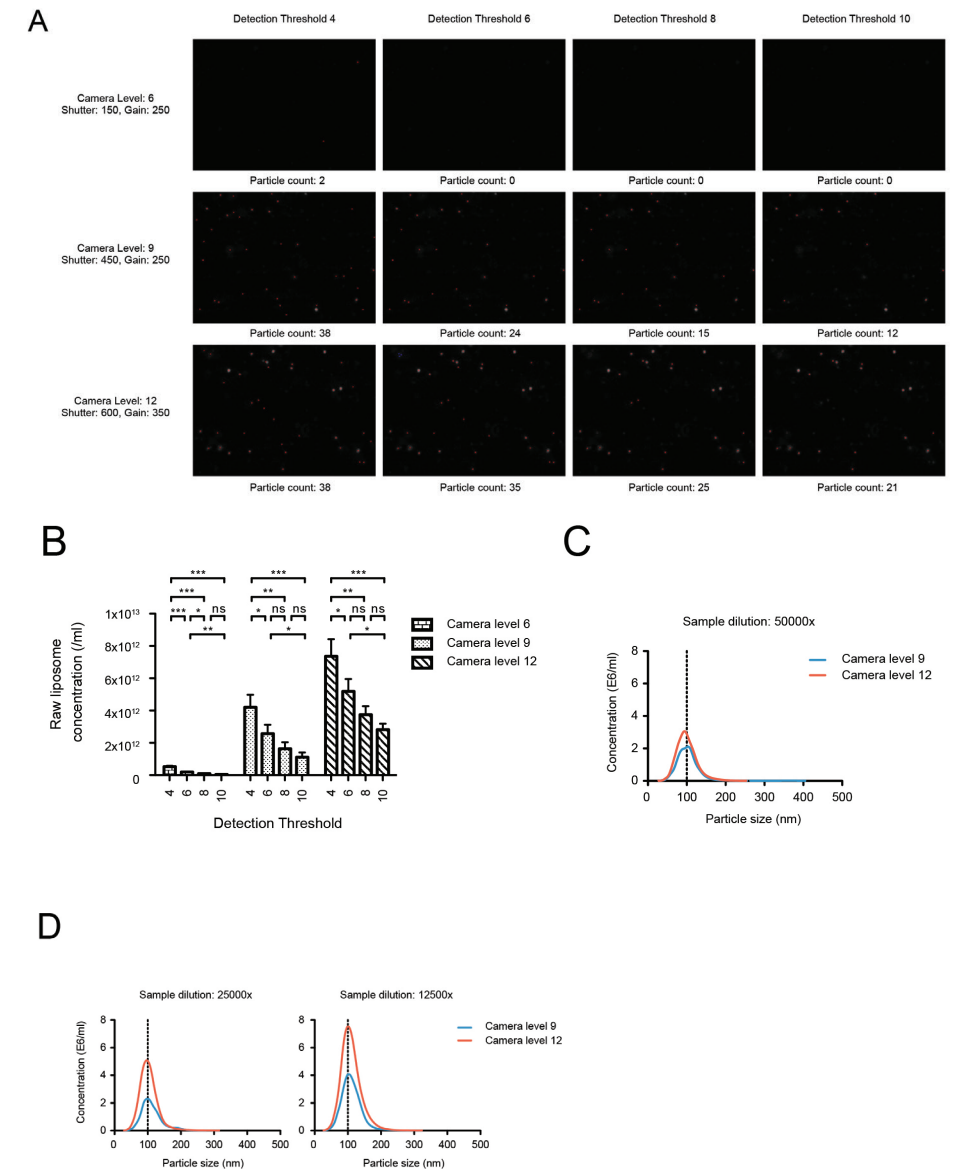
So far, only one other study has directly compared NTA, tRPS and flow cytometry (using a different high-end flow cytometer) by analyzing the size distributions of polystyrene beads and urine-derived EV [32]. Interestingly, comparable EV quantifications by NTA and tRPS were reported, whereas the flow cytometry-based EV quantification was 15 times lower. However, a direct comparison of these data to our current study is difficult, because a crude preparation (1550 ×g centrifugation followed by 0.2 μm filtration) of EVs from a different biological source (urine) was analyzed and because the flow cytometric measurements in that study were light scatter-based. However, it is interesting to note that, in contrast to our findings, EV quantifications by NTA and

tRPS were found to be comparable. This could imply that the type of EV and the degree of EV purification may also influence quantification by the different instruments.

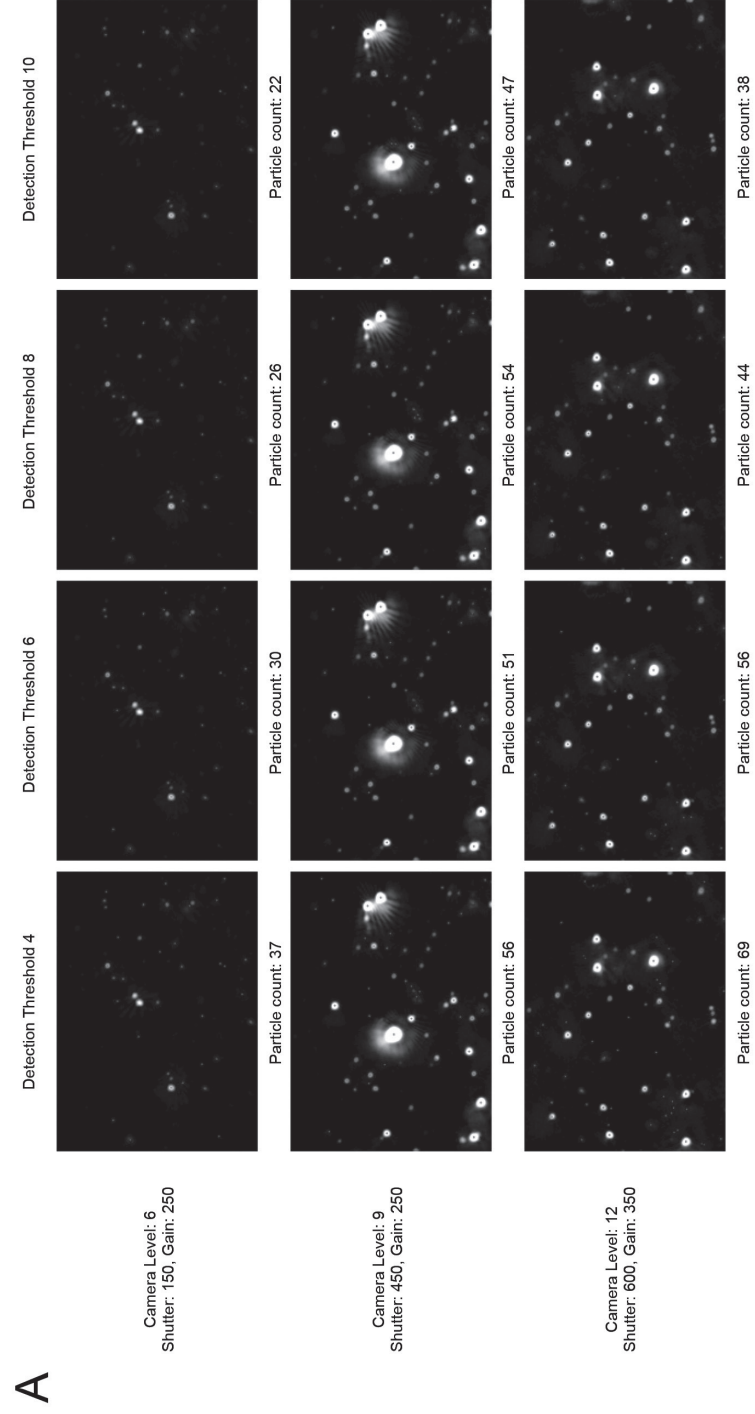
Several strategies have previously been suggested to calibrate particle quantification in EV samples. For tRPS we spiked biological fluids with polystyrene beads of known size and concentration to improve EV quantification accuracy [18]. For NTA, on the contrary, this approach seems less suitable since the methodology does not allow for accurate discrimination of particles of interest from beads with a similar size [17,20,30]. Secondly, spiking a sample with large (N500 nm) silica beads could lead to over-scattering of the EVs and skew characterization [20]. An alternative that has been proposed for NTA calibration is application of a correction factor, based on the measured concentration of silica beads compared to the expected concentration of these beads [17]. Although promising and potentially valuable for measuring relatively homogenous populations of EVs, such a calibration method is unsuitable for analysis of the heterogeneous EV preparations studied here. As NTA is less accurate in the detection of size-based subpopulations [17,20,30], one would have to apply a multitude of silica calibration beads, each covering a subpopulation of EVs and subsequently aggregate analysis of these subpopulations. More research into the accuracy of such a calibration system will be essential before it can be broadly applied.

In conclusion, we identified NTA and tRPS instrument settings that affect particle quantification and showed that the impact of these parameters on quantification varies with the types of nano-sized particles analyzed (i.e. polystyrene beads, liposomes and EVs). Our data clearly indicate that absolute quantification of EVs and liposomes substantially differs using the three different technologies and that a golden standard for quantification of such particles is not available yet. Moreover, our data strongly underline the importance of technical knowledge of the instruments for correct data interpretation, and plead for awareness of the effects of instrument settings in case vesicle populations with unknown concentration and size heterogeneity are measured. Increased understanding of the possibilities and pitfalls of these technologies will benefit standardized and large-scale clinical application of (engineered) EVs and EV mimics in the future.

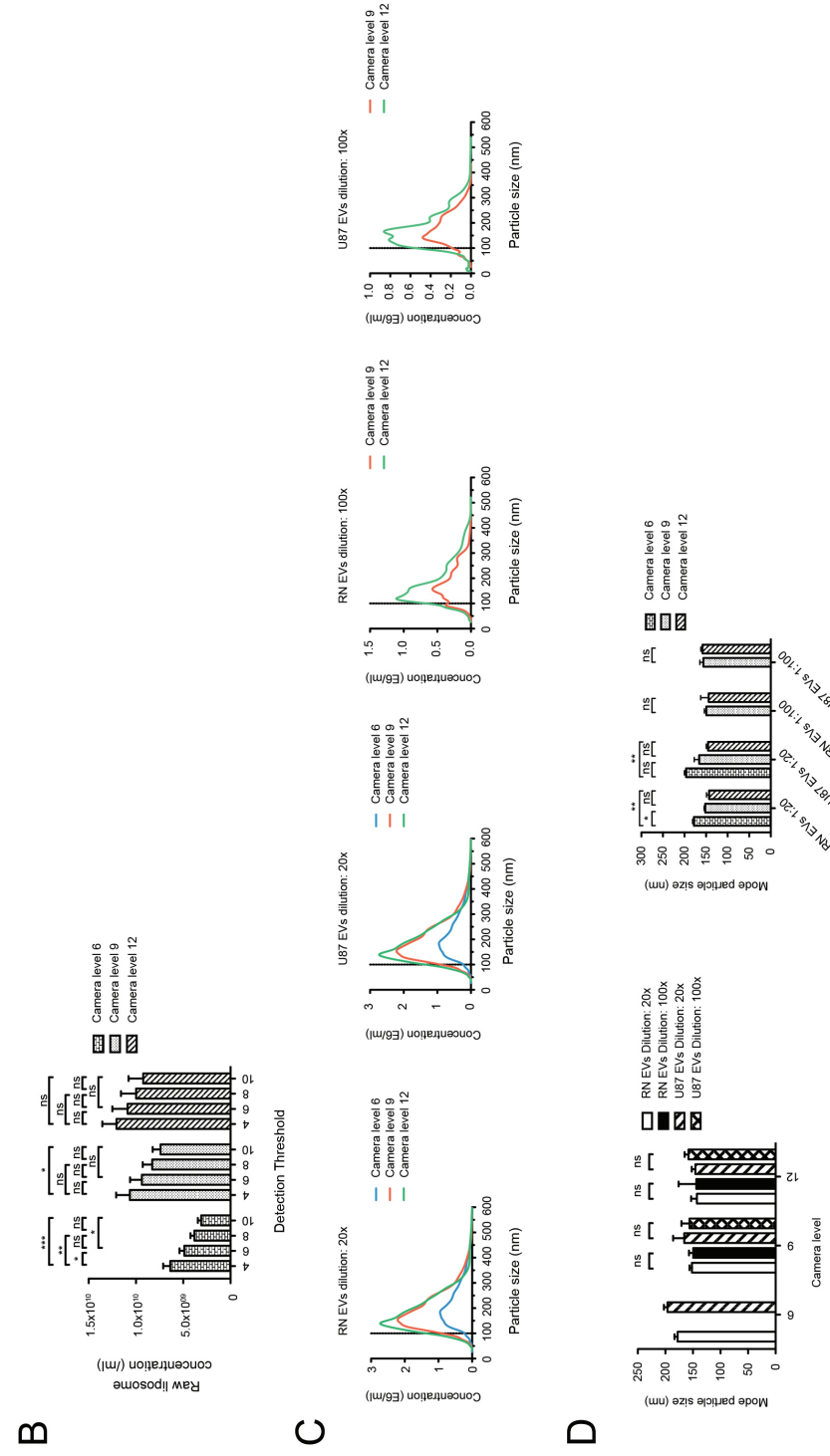
Supplementary Figures



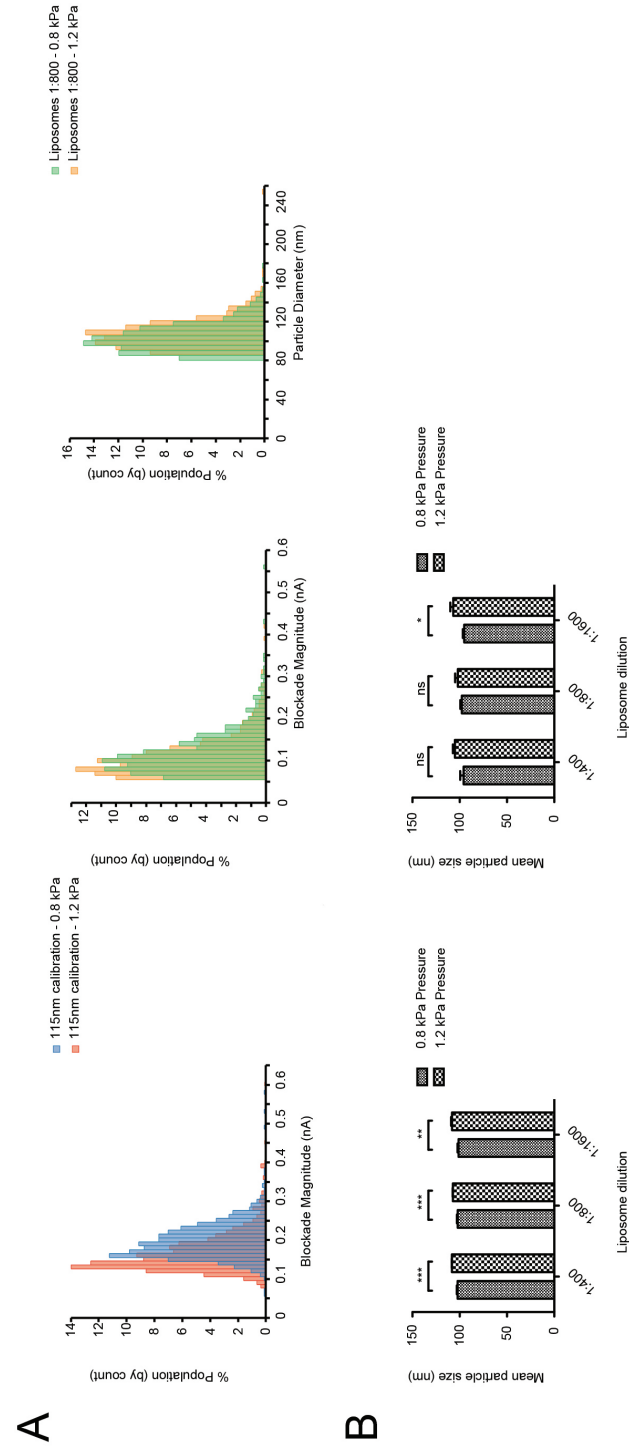
Suppl. Figure S1. NTA-based liposome detection and size-distributions. (A) Matrix indicating the influence of camera-level (vertical) and detection threshold (horizontal) on the detection of 105 nm liposomes. (B) Bar graph indicating the effect of detection threshold on liposome particle quantification after correction for the dilution factor. (C and D) Liposome size-distributions at three different dilutions obtained by recording at camera-levels 9 and 12. Data are mean \pm s.d. (n=3).



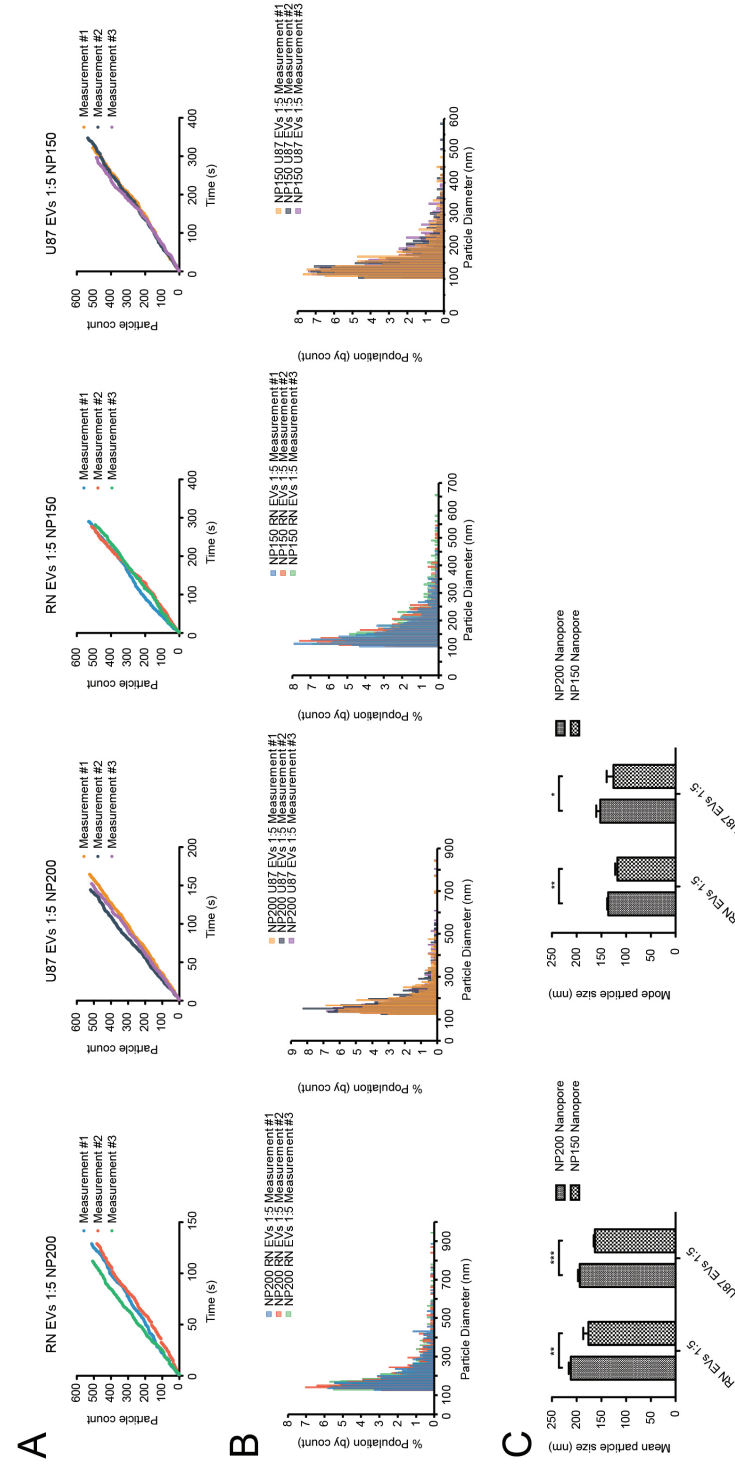
Suppl. Figure S2. NTA-based EV detection and size-distributions. (A) Matrix indicating the influence of camera-level (vertical) and detection threshold (horizontal) on the detection of RN-derived EVs. **(B)** Bar graph indicating the effect of detection threshold on EV particle quantification after correction for the dilution factor. **(C)** Size-distributions of RN and U87-MG derived EVs as obtained at camera-levels 6, 9 and 12 (1:20 sample dilution) and 9 and 12 (1:100 sample dilution). **(D) (left-panel)** Bar-graphs indicating the effects of camera-level on mode particle sizes of RN and U87-MG derived EVs at two different dilutions. The **right-panel** illustrates the effect of EV sample dilution on mode particle sizes respectively. Data are mean \pm s.d. (n=3).



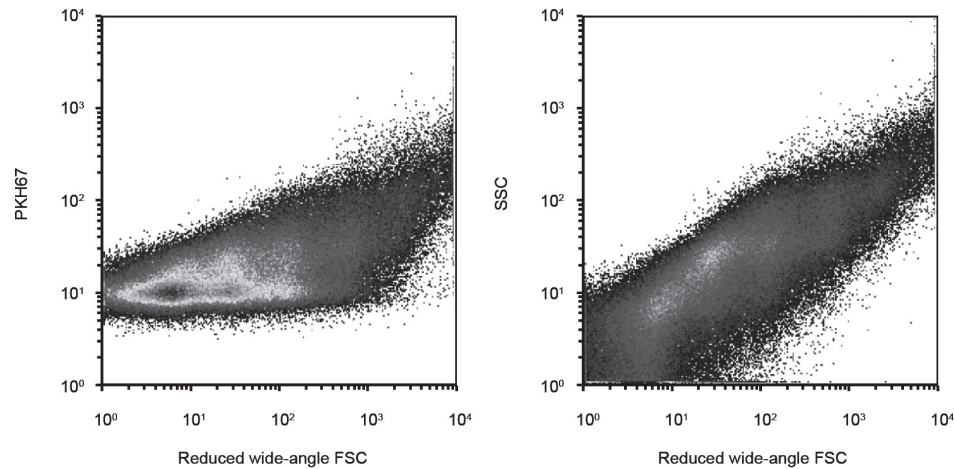
Suppl. Figure S2. Continued.



Suppl. Figure S3. The effect of applied pressure on particle size estimation using tRPS. (A) Representative examples of tRPS-based measurement of blockade height in samples of 115 nm calibration particles (left-panel) and 105 nm liposomes (middle-panel) at two different pressure settings (1.2 and 0.8 kPa). The right-panel illustrates the size-distributions for the 105 nm liposomes calculated based on the 115 nm calibration bead measurement. (B) Bar-graphs of the observed mean (left-panel) and mode (right-panel) calculated liposome particle sizes at two differently applied pressures. Data are mean \pm s.d. (n=3).



Suppl. Figure S4. tRPS-based quantification and size-estimation of EVs. (A) Particle detection over time as obtained for RN and U87-MG derived EVs at NP200 and NP150 nanopores. (B) Representative size-distributions of RN and U87-MG derived EVs analyzed with NP200 and NP150 nanopores. Bin-size 5 nm. (C) Bar-graphs representing mean (left-panel) and mode (right-panel) EV particle sizes for NP200 and NP150 nanopore setups. Data are mean \pm s.d. (n=3).



Suppl. Figure S5. hFC-based analysis of EV. hFC-based detection of U87-MG derived EVs labeled with PKH67 (detected in the FITC channel). The right dot plot illustrates the heterogeneity in FSC and SSC observed in the EV population.

References

- 1 S.ElAndaloussi, I.Mager, X.O.Breakefield, M.J.Wood, Extracellular vesicles: biology and emerging therapeutic opportunities, *Nat. Rev. Drug Discov.* 12 (5) (2013) 347–357.
- 2 A. Bobrie, M. Colombo, G. Raposo, C. Thery, Exosome secretion: molecular mechanisms and roles in immune responses, *Traffic* 12 (12) (2011) 1659–1668.
- 3 J. Kowal, M. Tkach, C. Thery, Biogenesis and secretion of exosomes, *Curr. Opin. Cell Biol.* 29C (2014) 116–125.
- 4 P.D.Robbins, A.E. Morelli, Regulation of immuneresponses by extracellular vesicles, *Nat. Rev. Immunol.* 14 (3) (2014) 195–208.
- 5 I. Del Conde, C.N. Shrimpton, P. Thiagarajan, J.A. Lopez, Tissue-factor-bearing microvesicles arise from lipid rafts and fuse with activated platelets to initiate coagulation, *Blood* 106 (5) (2005) 1604–1611.
- 6 S. Gatti, S. Bruno, M.C. Deregibus, et al., Microvesicles derived from human adult mesenchymal stem cells protect against ischaemia–reperfusion-induced acute and chronic kidney injury, *Nephrol. Dial. Transplant.* 26 (5) (2011) 1474–1483.
- 7 J. Skog, T. Wurdinger, S. Van Rijn, et al., Glioblastoma microvesicles transport RNA and proteins that promote tumour growth and provide diagnostic biomarkers, *Nat. Cell Biol.* 10 (12) (2008) 1470–1476.
- 8 K. Al-Nedawi, B. Meehan, J. Micallef, et al., Intercellular transfer of the oncogenic receptor EGFRvIII by microvesicles derived from tumour cells, *Nat. Cell Biol.* 10 (5) (2008) 619–624.
- 9 S. Saman, W. Kim, M. Raya, et al., Exosome-associated tau is secreted in tauopathy models and is selectively phosphorylated in cerebrospinal fluid in early Alzheimer disease, *J. Biol. Chem.* 287 (6) (2012) 3842–3849.
- 10 H. Zhou, T. Pisitkun, A. Aponte, et al., Exosomal fetuin-A identified by proteomics: a novel urinary biomarker for detecting acute kidney injury, *Kidney Int.* 70 (10) (2006) 1847–1857.
- 11 H. Shao, J. Chung, L. Balaj, et al., Protein typing of circulating microvesicles allows real-time monitoring of glioblastoma therapy, *Nat. Med.* 18 (12) (2012) 1835–1840. [12] D. Sun, X. Zhuang, X. Xiang, et al., A novel nanoparticle drug delivery system: the anti-inflammatory activity of curcumin is enhanced when encapsulated in exosomes, *Mol. Ther.* 18 (9) (2010) 1606–1614.
- 13 R. Van Der Meel, M.H. Fens, P. Vader, W.W. Van Solinge, O. Eniola-Adefeso, R.M. Schiffelers, Extracellular vesicles as drug delivery systems: lessons from the liposome field, *J. Control. Release* 195 (2014) 72–85.
- 14 S.M. Van Dommelen, P. Vader, S. Lakhali, et al., Microvesicles and exosomes: opportunities for cell-derived membrane vesicles in drug delivery, *J. Control. Release* 161 (2) (2012) 635–644.
- 15 K.W. Witwer, E.I. Buzas, L.T. Bemis, et al., Standardization of sample collection, isolation and analysis methods in extracellular vesicle research, *J. Extracell. Vesicles* 2 (2013).
- 16 R.A. Dragovic, C. Gardiner, A.S. Brooks, et al., Sizing and phenotyping of cellular vesicles using nanoparticle tracking analysis, *Nanomedicine* 7 (6) (2011) 780–788.
- 17 C. Gardiner, Y.J. Ferreira, R.A. Dragovic, C.W. Redman, I.L. Sargent, Extracellular vesicle sizing and enumeration by nanoparticle tracking analysis, *J. Extracell. Vesicles* 2 (2013).
- 18 J. De Vrij, S.L. Maas, M. Van Nispen, et al., Quantification of nanosized extracellular membrane vesicles with scanning ion occlusion sensing, *Nanomedicine* 8 (9) (2013) 1443–1458.

- 19 E.N. Nolte-'T Hoen, E.J. Van Der Vlist, M. Aalberts, et al., Quantitative and qualitative flow cytometric analysis of nanosized cell-derived membrane vesicles, *Nanomedicine* 8 (5) (2012) 712–720.
- 20 V. Filipe, A. Hawe, W. Jiskoot, Critical evaluation of nanoparticle tracking analysis (NTA) by nanosight for the measurement of nanoparticles and protein aggregates, *Pharm. Res.* 27 (5) (2010) 796–810.
- 21 G.S. Roberts, D. Kozak, W. Anderson, M.F. Broom, R. Vogel, M. Trau, Tunable nano/ micropores for particle detection and discrimination: scanning ion occlusion spectroscopy, *Small* 6 (23) (2010) 2653–2658.
- 22 D.Kozak, W.Anderson, R.Vogel, S.Chen, F.Antaw, M.Trau, Simultaneous size and zeta-potential measurements of individual nanoparticles in dispersion using size-tunable pore sensors, *ACS Nano* 6 (8) (2012) 6990–6997.
- 23 R. Vogel, G. Willmott, D. Kozak, et al., Quantitative sizing of nano/microparticles with a tunable elastomeric pore sensor, *Anal. Chem.* 83 (9) (2011) 3499–3506. [24] G.R. Willmott, R. Vogel, S.S. Yu, et al., Use of tunable nanopore blockade rates to investigate colloidal dispersions, *J. Phys. Condens. Matter* 22 (45) (2010) 454116. [25] G.S. Roberts, S. Yu, Q. Zeng, et al., Tunable pores for measuring concentrations of synthetic and biological nanoparticle dispersions, *Biosens. Bioelectron.* 31 (1) (2012) 17–25.
- 26 E.Van Der Pol, M.J.VanGemert, A.Sturk, R.Nieuwland, T.G.VanLeeuwen, Single vs. swarm detection of microparticles and exosomes by flow cytometry, *J. Thromb. Haemost.* 10 (5) (2012) 919–930.
- 27 J.A.Gallego-Urrea, J.Tuoriniemi, M.Hassellöv, Applications of particle-tracking analysis to the determination of size distributions and concentrations of nanoparticles in environmental, biological and food samples, *TrAC Trends Anal. Chem.* 30 (3) (2011) 473–483.
- 28 P. Van Der Meeren, M. Kasinos, H. Saveyn, Relevance of two-dimensional Brownian motion dynamics in applying nanoparticle tracking analysis, *Methods Mol. Biol.* 906 (2012) 525–534.
- 29 E.J. Van Der Vlist, E.N. Nolte-'T Hoen, W. Stoorvogel, G.J. Arkesteijn, M.H. Wauben, Fluorescent labeling of nano-sized vesicles released by cells and subsequent quantitative and qualitative analysis by high-resolution flow cytometry, *Nat. Protoc.* 7 (7) (2012) 1311–1326.
- 30 W. Anderson, D. Kozak, V.A. Coleman, A.K. Jamting, M. Trau, A comparative study of submicron particle sizing platforms: accuracy, precision and resolution analysis of polydisperse particle size distributions, *J. Colloid Interface Sci.* 405 (2013) 322–330.
- 31 N.C. Bell, C. Minelli, J. Tompkins, M.M. Stevens, A.G. Shard, Emerging techniques for submicrometer particle sizing applied to Stober silica, *Langmuir* 28 (29) (2012) 10860–10872.
- 32 E. Van Der Pol, F.A. Coumans, A.E. Grootemaat, et al., Particle size distribution of exosomes and microvesicles determined by transmission electron microscopy, flow cytometry, nanoparticle tracking analysis, and resistive pulse sensing, *J. Thromb. Haemost.* 12 (7) (2014) 1182–1192.
- 33 Z. Varga, Y. Yuana, A.E. Grootemaat, et al., Towards traceable size determination of extracellular vesicles, *J. Extracell. Vesicles* 3 (2014).
- 34 G. Rouser, S. Fkeischer, A. Yamamoto, Two dimensional thin layer chromatographic separation of polar lipids and determination of phospholipids by phosphorus analysis of spots, *Lipids* 5 (5) (1970) 494–496.
- 35 S.L.N. Maas, J. De Vrij, M.L.D. Broekman, Quantification and size-profiling of extracellular vesicles using tunable resistive pulse sensing, *J. Vis. Exp.* 92 (Oct 19 2014) e51623.
- 36 E. Van Der Pol, F. Coumans, Z. Varga, M. Krumrey, R. Nieuwland, Innovation in detection of microparticles and exosomes, *J. Thromb. Haemost.* 11 (Suppl. 1) (2013) 36–45.
- 37 G.R. Willmott, R. Chaturvedi, S.J.W. Cummins, L.G. Groenewegen, Actuation of tunable elastomeric pores: resistance measurements and finite element modelling, *Exp. Mech.* 54 (2) (2013) 153–163.
- 38 C. Pidgeon, C.A. Hunt, Calculating number and surface area of liposomes in any suspension, *J. Pharm. Sci.* 70 (2) (1981) 173–176.
- 39 D. Kozak, W. Anderson, M. Trau, Tuning particle velocity and measurement sensitivity by changing pore sensor dimensions, *Chem. Lett.* 41 (10) (2012) 1134–1136.
- 40 D. Marimpietri, A. Petretto, L. Raffaghello, et al., Proteome profiling of neuroblastoma-derived exosomes reveal the expression of proteins potentially involved in tumor progression, *PLoS One* 8 (9) (2013) e75054.
- 41 J.L. Hood, R.S. San, S.A. Wickline, Exosomes released by melanoma cells prepare sentinel lymph nodes for tumor metastasis, *Cancer Res.* 71 (11) (2011) 3792–3801. [42] V. Sokolova, A.K. Ludwig, S. Hornung, et al., Characterisation of exosomes derived from human cells by nanoparticle tracking analysis and scanning electron microscopy, *Colloids Surf. B: Biointerfaces* 87 (1) (2011) 146–150.

4

Based on:

Glioblastoma-derived extracellular vesicles modify the phenotype of monocytic cell

Jeroen de Vrij¹, Sybren L. N. Maas¹, Kitty M.C. Kwappenberg², Rosalie Schnoor¹, Anne Kleijn³, Lennard Dekker⁴, Theo M. Luider⁴, Lot D. de Witte^{5,6}, Manja Litjens⁵, Miriam E. van Strien⁵, Elly M. Hol^{5,7,8}, Jerome Kroonen¹, Pierre A. Robe¹, Martine L. Lamfers³, Marco W. Schilham² and Marike L.D. Broekman¹

¹ Department of Neurosurgery, Brain Center Rudolf Magnus Institute of Neurosciences, University Medical Center, Utrecht, The Netherlands ² Department of Pediatrics, Leiden University Medical Center, The Netherlands. ³ Department of Neurosurgery, Brain Tumor Center, Erasmus Medical Center, Rotterdam, The Netherlands. ⁴ Department of Neurology, Brain Tumor Center, Erasmus Medical Center, Rotterdam, The Netherlands. ⁵ Department of Translational Neuroscience, Brain Center Rudolf Magnus Institute of Neurosciences, University Medical Center, Utrecht, The Netherlands. ⁶ Department of Psychiatry, University Medical Center, Utrecht, The Netherlands. ⁷ Netherlands Institute for Neuroscience, an Institute of the Royal Netherlands Academy of Arts and Sciences, Amsterdam, The Netherlands. ⁸ Swammerdam Institute for Life Sciences, Center for Neuroscience, University of Amsterdam, The Netherlands

Int. J. Cancer 137, 1630–1642 (2015)

Abstract

Glioblastoma multiforme (GBM) is the most common primary brain tumor and is without exception lethal. GBMs modify the immune system, which contributes to the aggressive nature of the disease. Particularly, cells of the monocytic lineage, including monocytes, macrophages and microglia, are affected. We investigated the influence of GBM-derived extracellular vesicles (EVs) on the phenotype of monocytic cells. Proteomic profiling showed GBM EVs to be enriched with proteins functioning in extracellular matrix interaction- and leukocyte migration. GBM EVs appeared to skew the differentiation of peripheral blood-derived monocytes to alternatively activated/M2-type macrophages. This was observed for EVs from an established cell line, as well as for EVs from primary cultures of GBM stem-like cells (GSCs). Unlike EVs of non-GBM origin, GBM EVs induced modified expression of cell surface proteins, modified cytokine secretion (e.g. an increase in vascular endothelial growth factor and IL-6), and increased phagocytic capacity of the macrophages. Most pronounced effects were observed upon incubation with EVs from mesenchymal GSCs. GSC EVs also affected primary human microglia, resulting in increased expression of Membrane Type 1 Metalloprotease, a marker for GBM microglia and functioning as tumor-supportive factor. In conclusion, GBM-derived EVs can modify cells of the monocytic lineage, which acquire characteristics that resemble the tumor-supportive phenotypes observed in patients.

Introduction

Despite extensive treatment, the prognosis of patients with glioblastoma multiforme (GBM), the most common primary brain tumor in adults, remains dismal with a median survival of only 15 months.¹ Many factors contribute to the malignant potential of GBMs, including the capacity of GBMs to modulate the immune system.² Immune-modulation occurs at a systemic level, as well as in the tumor microenvironment, and involves different types of immune cells. Most patients with GBM exhibit changes in the lymphocyte compartment, with an overall decrease in the number of CD4+ helper T-cells and a relative increase in regulatory T-cells with immune-suppressive characteristics.³ In addition, GBMs strongly influence cells of the monocytic lineage (monocytes, macrophages and microglia).⁴ The blood of GBM patients contains monocytes with altered characteristics, such as a reduced expression of receptors involved in antigen presentation.^{3,5,6} Locally, GBMs are characterized by the presence of large numbers of tumor associated macrophages (TAMs), which constitute brain resident microglia as well as macrophages derived from peripheral monocytes.^{4,7,8} Although TAMs consist of different macrophages/microglia subtypes, major part of the TAM population acquires an “alternatively-activated” (M2-type) phenotype.^{4,7,8} As compared to the “classically-activated” (M1-type) macrophages, these cells have a weakened capacity to activate the immune system, and an increased capacity to induce tissue remodeling (by stimulating vascularization and/or degradation of extracellular matrix components), and are therefore considered as tumor-supportive. The accumulation and activity of the M2-type TAMs clearly distinguishes GBMs from lower grade gliomas.⁹ GBM’s ability to modify different components of the immune system may not only contribute to the tumor’s aggressive proliferation and migration, but may also result in reduced efficacy of (experimental) treatments (“immunotherapies”).¹⁰ Still, the mechanisms responsible for the immune modulatory effects remain unknown.

Recently, it has been shown that extracellular vesicles (EVs), including exosomes (50-150nm vesicles formed by fusion of multivesicular bodies with the cell membrane), mediate local and systemic cell communication.^{11,12} Tumor cells were found to transfer their contents, including RNAs and proteins to different types of recipient cells, using EVs as vehicles.¹³ This transfer provides a variety of tumor-supportive features to the tumor environment, for instance leading to the establishment of pre-metastatic niches.^{14,15} EVs from GBM cells were reported to modify recipient cells (of tumor- or

endothelial origin) via the transfer of cell-transforming proteins and messenger RNAs (e.g. epidermal growth factor receptor variant 3 (EGFRvIII)) and specific types of small noncoding RNAs.¹⁶⁻²⁰

In this report, we describe the effects of GBM-derived EVs on the phenotype of monocytic cells, including peripheral-derived monocytes/macrophages and brain-resident microglia. These data identify EVs as a mechanism for GBM to modify the phenotype of monocytic cells, providing them M2-type / alternatively activated phenotypes.

Material and methods

Cell culture

The established cell lines U87-MG/EGFRvIII (GBM) and HOG (oligodendroglioma)²¹ were cultured in Dulbecco's modified Eagle's medium (Invitrogen, Carlsbad, CA, USA) containing 10% fetal bovine serum (FBS) (Invitrogen). The authenticity of the cell lines was confirmed by short tandem repeat (STR) analysis, using the AmpFLSTR[®] Identifier[®] PCR Amplification Kit (Applied Biosystems, Foster City, CA, USA). Mesenchymal stem cells (MSCs) were isolated from human bone marrow as described previously,²² according to the official guidelines of the Leiden University Medical Center (LUMC, Leiden, The Netherlands). MSCs were cultured in alpha-MEM medium (Invitrogen) containing 10% FBS (Invitrogen), 2 mM ascorbic acid, and 1 ng ml⁻¹ bFGF. The FBS was centrifuged at 100,000 x g for 16h to remove contaminating EVs. Primary brain tumor cultures were established by enzymatic and mechanical dissociation from fresh tumor material collected during brain tumor surgery (Dept. of Neurosurgery, Erasmus Medical Center, Rotterdam; Dept. of Neurosurgery, St. Elisabeth Hospital, Tilburg, The Netherlands), according to a previously described protocol and approved by an institutional review board.^{23,24} Tumors were classified as GBM by histological diagnosis. RNA was isolated from tumor material, followed by molecular sub-classification, using previously described protocols.^{23,25} Partek Software (St. Louis, MO, USA) was used to perform Gene Set Enrichment Analysis. The tumor-derived cultures were grown as glioma stem cell-like (GSC) cultures in serum-free medium.²³ All cell cultures were maintained at 37°C in a humidified atmosphere of 5% CO₂. Cell growth medium was supplemented with penicillin (100 units.ml⁻¹) and streptomycin (100 µg.ml⁻¹) (Invitrogen).

Peripheral blood mononuclear cells (PBMCs) were isolated from blood after informed consent. PBMCs were obtained by Ficoll-Paque PLUS (GE Healthcare Life Sciences, Freiburg, Germany)-density gradient centrifugation. CD14⁺ monocytes were isolated magnetically on an LS MACS[®] column (Miltenyi Biotec, Bergisch Gladbach, Germany). PBMCs and monocytes were cultured in RPMI medium (PAA Laboratories GmbH, Pasching, Austria) containing 10% FBS (Invitrogen).

Isolation of EVs

EVs were isolated from cell culture supernatants and blood (Ficoll supernatants after PBMC-isolation), using previously described protocols.^{26,27} Iodixanol-based density-gradient isolation (ultracentrifugation at 192,000 x g for 4 hours), followed by purification on a 30% sucrose cushion (ultracentrifugation at 100,000 x g for 40 min) was used for the side-by-side isolation of U87-MG/EGFRvIII- and GS184 EVs.²⁷ Sequential ultracentrifugation (two times at 100,000 x g for 70 min) was used for the large-panel isolation of GBM- and non-GBM EVs.²⁶ Prior to these ultracentrifugation procedures, cell culture supernatants and Ficoll supernatants were cleared from cellular debris by centrifugation (300 x g for 10 min, followed by 4000 x g for 1 hour) and filtering (0.22-µm vacuum filter (Corning, NY, USA)).

Quantification and size profiling of EVs

Concentration and size of EVs were measured by tunable resistive pulse sensing (tRPS), using the qNano platform (Izon Science, Christchurch, New Zealand). This method relies on the detection of nanosized particles upon their movement through a nano-sized pore, and allows for reliable and rapid measurement of EVs in small sample volumes.²⁷ In brief, purified EVs or cell culture supernatants were spiked with polystyrene beads of known concentration and size. The samples were applied to the qNano and particle flow rates and the particle blockage magnitudes were measured. These parameters allowed for calculation of EV concentration and volume, respectively, using our previously described methods.^{27,28}

Monocyte and macrophage analyses

To assess effects of EVs on non-differentiated monocytes, PBMCs (150,000 cells) or isolated monocytes (50,000 cells) were added to a well of a 96-well round-bottom plate in 100 µl medium. EVs were isolated from cell culture supernatant (U87-MG/EGFRvIII and GS184) and from blood (healthy donors and GBM patients) and added to

the cells (2×10^8 cell culture EVs per well and 10^6 blood EVs per well). After incubation for three days, cells were prepared for flow cytometry analysis.

Monocyte-to-macrophage differentiation was induced by culturing of monocytes (10^6 cells) with Granulocyte Macrophage Colony Stimulating Factor (GM-CSF) ($800 \text{ units.ml}^{-1}$) (Peprotech, NJ, USA) in 24-well plates. EVs were added with equal amounts (0.35×10^8 EVs, as determined by tRPS) at day 0 and day 3 after plating. As an alternative differentiation condition, monocytes were exposed to Macrophage Colony Stimulating Factor (M-CSF) (20 ng.ml^{-1}) (Peprotech 300-25). After incubation for six days, cells were prepared for flow cytometry analysis. Cells were washed twice with PBS/0.02% sodium azide, fixed for 10 min in 4% paraformaldehyde, washed twice with PBS/0.5% BSA/0.02 sodium azide, and stained with antibodies. Antibodies used were anti-CD1a (APC, clone HI149), anti-CD3 (PerCP Cy5.5, SK7), anti-CD14 (APC, clone MfP9), anti-CD14 (FITC, clone MfP9), anti-CD14 (PerCP Cy5.5, clone M5E2), anti-CD25 (FITC, 2A3), anti-CD32 (APC, clone FLI8.26 (2003)), anti-CD40 (FITC, clone 5C3), anti-CD45 (PerCP Cy5.5, clone 2D1), anti-CD86 (FITC, clone 2331 (FUN-1)), anti-CD86 (PE, clone 2331 (FUN-1)), anti-CD163 (PE, clone GHI/61), anti-HLA DR (FITC, clone G46-6), anti-HLA DR (PE, L243) (BD Biosciences, NJ, USA), anti-CD33 (APC, clone D3HL60.251), anti-CD64 (FITC, clone 22), anti-CD127 (PE, R34.34) (Beckman Coulter Company, Marseille, France), anti-CD3 (APC, clone UCHT1), anti-CD19 (APC, J4.119), anti-CD56 (APC, NKH1) (Immunotech). To analyze phagocytic capacity, macrophages were exposed to FITC-dextran beads (1 mg.ml^{-1} for 30 min) (Sigma Aldrich, FD40S, molecular weight 40,000) followed by flow cytometric quantification of FITC uptake. Flow cytometry was carried out on a FACS Calibur (Becton Dickinson) and data were analyzed using CellQuest software (Becton Dickinson). Expression levels are displayed as geometric means.

Cytokines and chemokines in macrophage supernatants were quantified with a magnetic bead-based multiplex assay (Bio-Plex Pro[®] Assay, Bio-Rad Laboratories, CAL, USA).

Quantitative polymerase chain reaction (qPCR) was used to quantify expression levels of Toll-like receptor 2 (TLR-2) and Membrane Type 1 Metalloprotease (MT1-MMP) RNA in macrophages. RNA was isolated from macrophages using the RNeasy Plus Micro kit (Qiagen, Hilden, Germany). Complementary DNA was synthesized using the SuperScript III First-Strand Synthesis System (Invitrogen) using oligo(dT) primers according to the manufacturer's protocol. SYBR Green-based

qPCR (Applied Biosystems) was performed using oligonucleotides TLR-2_forward (5'-CTTCAACTGGTAGTTGTGG-3'), TLR-2_reverse (5'-GGAATGGAGTTAAAGATCCTG-3'), MT1-MMP_forward (5'-ATGGCAAATTCGTCTTCTTC-3') and MT1-MMP_reverse (5'-CGTTGAAACGGTAGTACTTG-3'). The expression levels were normalized to the expression level of Actin- β (Act_forward: 5'-GACGACATGGAGAAAATCTG-3'; Act_reverse: 5'-ATGATCTGGGTCATCTTCTC-3'). PCR amplification (10 min at 95°C , 45 cycles of 95°C for 15s followed by 60s at 60°C , 15s at 95°C) was followed by melt-curve analysis. PCR amplification was performed in triplicate and for each triplicate delta CT values ($\text{CT}_{\text{TLR-2}} - \text{CT}_{\text{Actin-}\beta}$ and $\text{CT}_{\text{MMP14}} - \text{CT}_{\text{Actin-}\beta}$) were calculated.

Mass spectrometry

Highly sensitive mass spectrometry (MS) analysis was performed to quantify and compare the proteomic contents of GBM cells and their secreted EVs. EVs were isolated from the supernatants of U87-MG/EGFRvIII and GS184 monolayer cultures, and were, in parallel with cell pellets, dissolved in lysis buffer (i.e.; 2.5×10^8 EVs or 500 cells were dissolved in 50 ml RapiGest[®] surfactant (1 mg.ml^{-1}) (Waters Corporation, MA, USA) in 50 mM ammoniumbicarbonate). Samples were stored at -80°C until further use. After thawing, reduction and alkylation was performed by adding $2 \mu\text{l}$ of 0.5 M dithiothreitol to each sample, followed by incubation for 30 min at 60°C . After cooling down to room temperature, $10 \mu\text{l}$ of 0.3 M iodoacetamide was added, followed by incubation in the dark for 30 min. Subsequently, $1.5 \mu\text{l}$ of $100 \text{ ng.}\mu\text{l}^{-1}$ gold trade trypsin (Promega, Madison, WI) in 3 mM Tris-HCL (diluted 1:10 in 50 mM NH_4HCO_3) was added to each sample, followed by overnight incubation at 37°C . To inactivate trypsin, $3 \mu\text{l}$ of 25% trifluoroacetic acid was added and samples were incubated for 30 min at 37°C . Next, the samples were centrifuged at $10,000 \times g$ for 15 min at 4°C and the supernatant was transferred to LC/MS-certified vials (Waters Corporation). For each sample, a fraction (10%) of the total volume was measured on a nano-liquid chromatography (nano-LC) system (Ultimate 3000 Nano-LC system, Dionex, Thermo Scientific, Amsterdam, The Netherlands) to determine relative concentrations. Based on these measurements, the injection volume for each individual sample could be adjusted to allow for MS analysis of equal amounts of digested samples. MS analysis was performed as described, using a coupled nano-LC system with an Orbitrap MS platform (LTQ-Orbitrap XL, Thermo Scientific).²⁹

MS spectra were extracted from raw data files and converted into Mascot generic format (MGF) files using Extract-MSN (part of XCalibur (version 2.0.7), Thermo Scientific).

The data files were searched by Mascot (version 2.3; Matrix Science Inc., London, UK) against the UniProt Swiss-Prot database selected for *Homo sapiens* (20070 entries), using the following settings: a maximum of two miss-cleavages, oxidation as a variable modification of methionine, carbamidomethylation as a fixed modification of cysteine, and trypsin selected as digestion enzyme. A peptide mass tolerance of 10 ppm and a fragment mass tolerance of 0.5 Da were allowed. Scaffold proteome analysis software (version 3.6.3; Proteome Software, Portland, OR) was used to visualize protein detections and to add Gene Ontology (GO) Terms. The data files were exported to Microsoft Office Excel 2010 (Microsoft, Redmond, WA) and quantitative analyses were performed (protein filter settings: 'number of spectra ≥ 1 ', 'protein ID probability $\geq 95\%$ '). Quantitative information was obtained on the relative concentration of each protein (number of spectrum counts as percentage of total spectra), as well as on protein enrichment in EVs (i.e.; the difference between the protein concentration in EVs and the protein concentration in the cells). Functional connectivity between proteins was assessed using the STRING 9.1 algorithm (<http://string-db.org/>),³⁰ in which the Kyoto Encyclopedia of Genes and Genomes (KEGG) (www.kegg.jp) was selected as pathway source. Connections between proteins were visualized as 'confidence view', with stronger associations represented by thicker lines.

Statistical analyses

Data analysis was performed using SPSS 20.0 (SPSS Inc, Chicago, IL, USA) or Microsoft Excel 2010 (Microsoft corp., Redmond, WA, USA). Normality of data was tested using the Shapiro-Wilk test, and visualized by Q-Q plots. Equality of variance was tested using Levene's test. Two-tailed independent t-tests, corrected for inequality of variance if present, were used to test differences in means. In case of non-normal distributed data the Mann-Whitney U test was used. MS results were tested for differences in protein levels and differences in GO annotations using Fisher's exact test. Significance was determined as $p < 0.05$ unless stated otherwise. Error bars display means \pm standard error of the mean (SEM).

Results

GBM EVs are enriched with specific types of proteins

We performed a detailed characterization of the EV proteome to obtain better insight into the role of EVs as carriers of cell-transforming proteins. Besides the routinely

used cell line U87-MG/EGFRvIII, the primary GBM stem cell-like culture GS184 was used as a source of EVs. GS184 represents GBM more faithfully as a result of reduced accumulation of (epi)genetic alterations upon cell culturing.²⁴ Both cultures were found to secrete EVs. The size-distribution profiles (ranging from approximately 90 to 180 nm, mode 120 nm) were highly similar (size-profile of U87-MG/EGFRvIII as reported previously,²⁷ the size-profile of GS184 as **Suppl. Fig. S1**). Using mass-spectrometry (MS), 215 and 125 proteins were detected for U87-MG/EGFRvIII EVs and cells, respectively. Slightly more proteins were detected for GS184 EVs and cells; 287 and 300, respectively. (Refer to **Suppl. Table S1** for a complete overview of all detected proteins.) The different architecture of cells and EVs was reflected in Venn diagrams (**Figure 1A**), which demonstrated the majority of proteins to be uniquely detected in either EVs ("EV-specific") or cells ("cell-specific"). The stem cell-like phenotype of GS184 was confirmed by the abundance of the neural stem cell marker *nestin* (**Suppl. Table S1**). For GS184, the most abundant EV-specific proteins were chondroitin sulfate proteoglycan 4, prostaglandin F2 receptor negative regulator, and disco-interacting protein 2 homolog B. For U87-MG/EGFRvIII, the most abundant EV-specific proteins were alpha-2-macroglobulin, EGF-like repeat-discoidin I-like domain-containing protein 3, and hemoglobin subunit beta. Remarkably, GS184 EVs and U87-MG/EGFRvIII EVs shared several abundant proteins, including chondroitin sulfate proteoglycan 4, alpha-2-macroglobulin, lactadherin, EGFR and different types of integrins (**Suppl. Table S1**). Gene Ontology classification revealed that both cells and EVs are abundant in proteins of *cytoplasmic*-, *intracellular organelle*-, *organelle part*- or *plasma membrane* origin (**Figure 1B**). However, EVs are relatively enriched with proteins of *extracellular region*-, *membrane*- or *plasma membrane*- origin, whilst proteins of *cytoskeleton*-, *nuclear*- or *organelle part*- origin are relatively scarce (**Figure 1C**). This clearly reflects the differences in architecture between cells (e.g. containing a nucleus, organelles, and cytoskeleton) and EVs.

We speculated that GBM cells may benefit from the selective incorporation (and thereby transfer) of certain types of proteins in EVs. A list of the EV-enriched *plasma membrane*- and *cytoplasmic* proteins is provided in **Suppl. Table S2**. Of interest, protein pathway analysis, which included a database of hundreds of pathways, identified a few protein pathways that were significantly enriched in the membrane of the EVs; *regulation of actin cytoskeleton*-, *ECM-receptor interaction*-, *focal adhesion*-, and *leukocyte transendothelial migration* (**Suppl. Fig. S2**). The same pathways appeared to be enriched in the U87-MG/EGFRvIII EVs as in the GS184 EVs, despite the intrinsic

differences between the two cell types. The selective enrichment of proteins involved in leukocyte recruitment and focal adhesion mechanisms (which are especially functioning in monocytic leukocytes to stimulate proliferation, movement and phagocytosis⁸) triggered us to further investigate the influence of GBM derived EVs on monocytes and macrophages.

Fig 1A

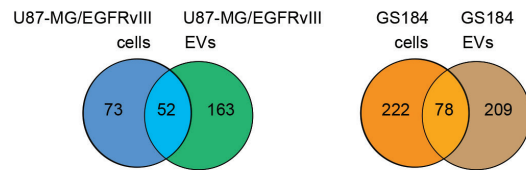


Fig 1B

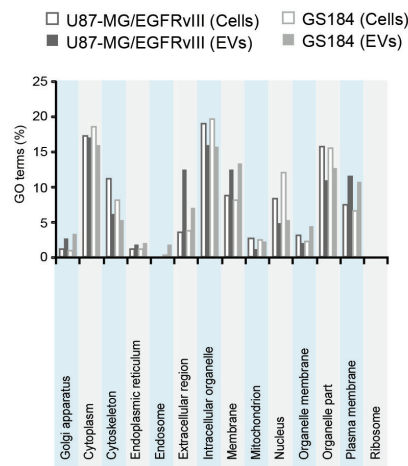


Fig 1C

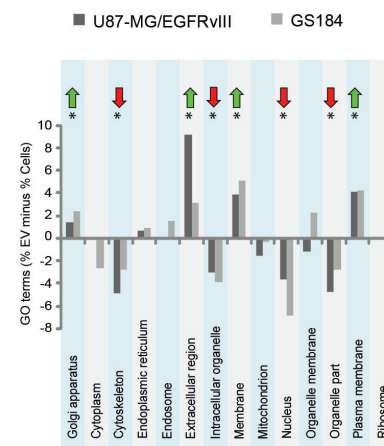


Figure 1. Proteomic analyses of U87-MG/EGFRvIII- and GS184-derived EVs. (A) Venn diagrams summarizing the number of proteins detected by MS analysis. Detection is grouped as 'cells-only', 'EV-only' or 'cells and EV shared'. (B, C) Assignment of *subcellular origin* GO terms to proteins. Graph (B) shows the relative distribution of GO terms within the proteome of either U87-MG/EGFRvIII cells, U87-MG/EGFRvIII EVs, GS184 cells or GS184 EVs. Graph (C) shows differences in GO term annotation between EVs and their donor cells, obtained by subtracting the cell-associated percentages from the EV-associated percentages. Significant EV-versus-cell differences ($P < 0.001$ for GS184 and U87-MG/EGFRvIII) are indicated with arrows.

GBM EVs modify monocytes

We pursued an *ex vivo* screening approach to gain insight in the effects of GBM EVs on leukocytes (Figure 2A). Remarkably, incubation of PBMCs with GS184 EVs severely affected the monocytic population, demonstrating a decrease in cell surface expression level of HLA-DR (Control: MFI = 730.4; EV: MFI = 223.4) and an increase in the expression of CD14 (Control: MFI = 21.2; EV: MFI = 260.6) (Figure 2B). We obtained similar results with EVs from U87-MG/EGFRvIII cells (Suppl. Fig. S3D), again showing a decrease in HLA-DR expression (Control: MFI = 263.7; EV: MFI = 119.9). CD14 expression was not modified by the U87-MG/EGFRvIII EVs. In addition to these effects on cell surface markers, the GS184 EVs also affected the survival of monocytes (Figure 2B). The viability of the control monocytes dramatically decreased over time, presumably caused by the absence of monocyte-survival factors, such as GM-CSF. However, in the presence of EVs this reduction was less severe (Control incubation: 3.5% monocytes; EV incubation: 7.0% monocytes). The effects of the EVs on monocytes occurred in a direct manner (that is; without the involvement of other leukocyte cell types), since similar effects were observed on purified monocytes (Figure 2C). In this context, the effect on monocyte survival was even more pronounced (Control incubation: 5.6% monocytes; EV incubation: 44.1% monocytes). Exposure of GS184 EVs to PBMCs from another donor showed similar results (Suppl. Fig. S3A and S3B). No effects were observed on the viability and surface marker expression (CD25) of T lymphocytes (Suppl. Fig. S3C).

It has previously been shown that the blood of GBM patients contains monocytes with an aberrant phenotype, in particular characterized by a reduced cell surface presentation of HLA-DR.^{6, 31, 32} We speculated that the EVs secreted by GBM cells may enter the systemic circulation, and may subsequently modify the phenotype of monocytes. However, we did not observe an effect on the expression of cell surface markers (i.e. HLA-DR and CD14) after exposing healthy monocytes with EVs from patient's blood (that is, the total pool of EVs, consisting of non-tumor EVs plus a minor fraction of GBM EVs) (Figure 2D).

Fig 2A

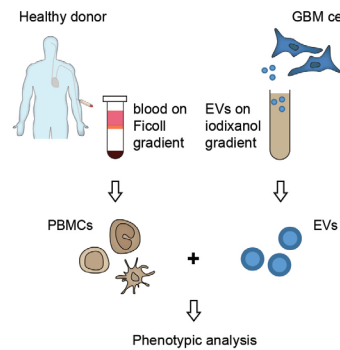


Fig 2B

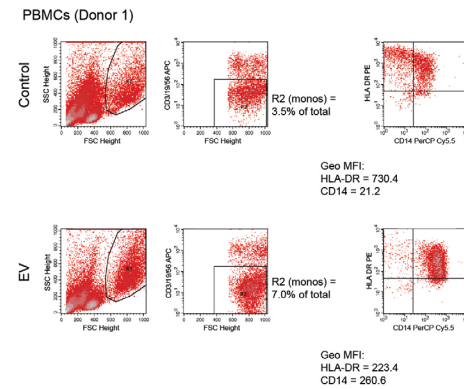


Fig 2C

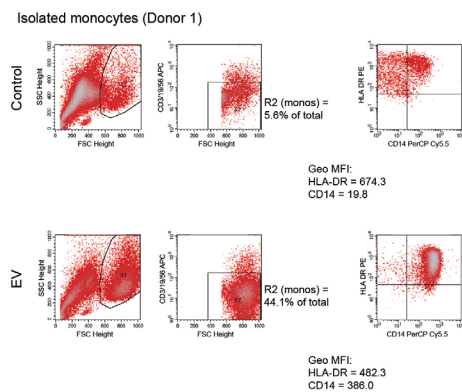


Fig 2D

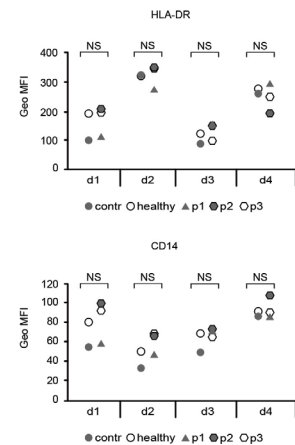


Figure 2. GBM-derived EVs modify the phenotype of monocytes. (A) Schematic illustration of the experimental set-up to screen for effects of GBM EVs on PBMCs. Isolation of EVs from cell culture (using iodixanol-based density gradient centrifugation) and isolation of PBMCs (using Ficoll-based density gradient centrifugation) are shown. (B, C, D) Flow cytometric analysis of CD14 and HLA-DR on the surface of monocytes. (B): Incubation of total PBMCs (from healthy Donor 1) with GS184-derived EVs or PBS only (control). (C): Incubation of purified monocytes (from healthy Donor 1) with GS184-derived EVs or PBS only (control). (D): Incubation of PBMCs (from four healthy donors (d1-d4)) with “EV pools” (that is; all blood-residing EVs are included) from the blood of GBM patients (p1-p3), a healthy donor, or PBS only (control). The monocyte populations were defined by gating on R1 (FSC, SSC) and R2 (CD3^{neg}, CD19^{neg}, CD56^{neg}). Monocyte percentages (expressed as fraction of the total number of PBMCs) are indicated in the dotplots of (B) and (C).

GBM EVs affect the differentiation of monocytes to macrophages

The observed effects on monocytes prompted the question whether GBM EVs can affect the differentiation of monocytes into macrophages. As the effects of EVs may vary between different GBM cultures, we included EVs from a panel of primary GSC cultures, obtained from different patients. (Patient information is shown in **Suppl. Table S3**). The cultures showed differences in growth pattern, varying from monolayers to spheres (**Figure 3A**). Using tRPS, we were able to accurately quantify EV secretion per cell (**Figure 3B**). This revealed large differences between the cultures, with EV secretion levels ranging from 85 EVs per cell (culture GS184) to 1050 EVs per cell (culture GS224). These findings could not be attributed to the EV isolation procedure, since similar quantification results were obtained on non-purified culture supernatants (data not shown).

The isolated EVs were added to monocytes, which were differentiated to M1-type macrophages using the cytokine GM-CSF. Besides the GSC-derived EVs, EVs were included from U87-MG/EGFRvIII cells, HOG cells (low-grade glioma), mesenchymal stem cells, and blood of healthy donors. Remarkably, all GBM-derived EV preparations similarly affected the monocyte-to-macrophage differentiation, while effects were absent or less stringent for the EVs of other origin. The difference between incubation with tumor- and non-tumor EVs was readily seen by standard microscopy, revealing a large proportion of macrophages with irregular shapes and increased granulation after exposure to GBM EVs (**Figure 3C**). Moreover, exposure to GBM EVs induced a significantly higher expression of the macrophage M2-type marker CD163, as measured by flow cytometry (**Figure 3D**). In addition, significant differences in expression levels were observed for the surface molecules HLA-DR-, CD14-, CD16-, CD32-, and CD45 (**Suppl. Fig. S4**). Also, incubation with GBM EVs significantly increased the phagocytic capacity of macrophages, as compared to incubation with non-GBM EVs (**Figure 3E**). The results were similar for the macrophages obtained from two independent donors. Overall, the GBM EV-induced changes resembled the changes induced after incubation with the cytokine M-CSF, which was included as a control for macrophage M2-type differentiation.

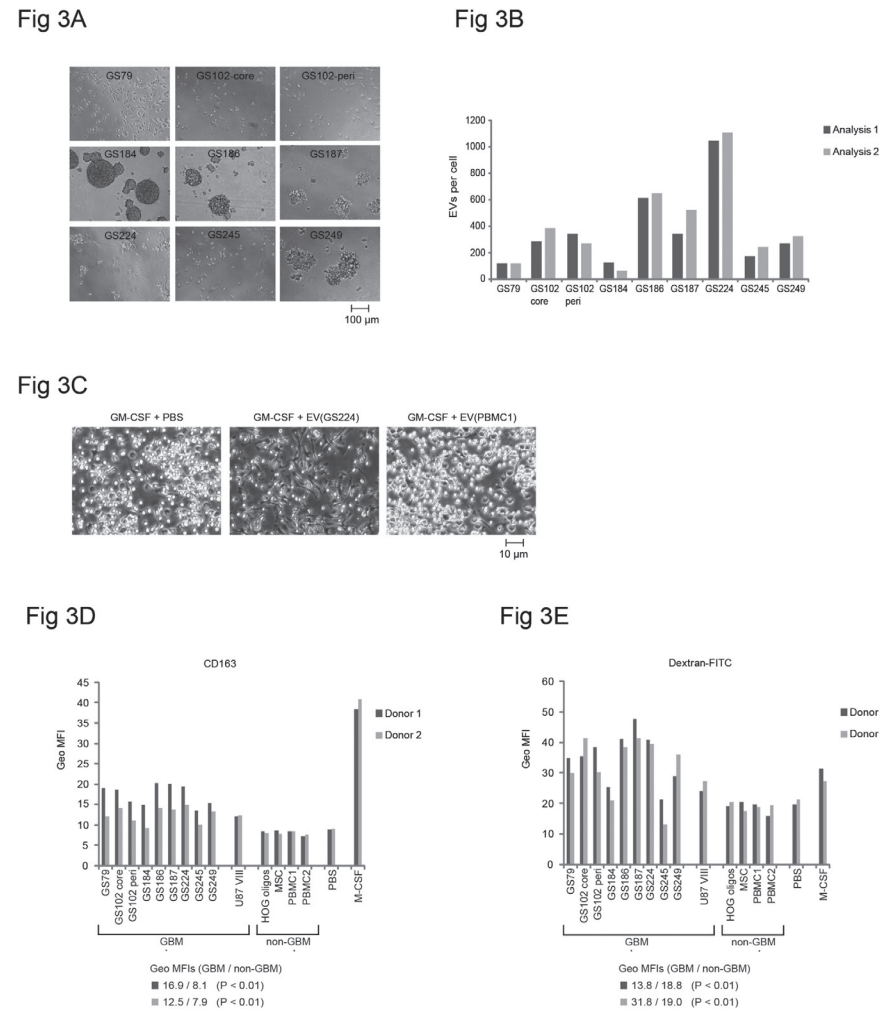


Figure 3. GBM-derived EVs modify monocyte to macrophage differentiation. (A) GSC cultures (grown as 'neurospheres') were established from tumor material and subsequently used for EV isolation. Phase contrast microscopy showed differences in cell growth appearance. Cultures GS102-core and GS102-peri were obtained from different locations of the tumor, from respectively core and peripheral region. (B) tRPS-based quantification of GSC-derived EVs. EV secretion per cell (based on the number of cells at the moment of harvesting EVs) was calculated. Two independent analyses were performed. (C, D, E) Addition of EVs to the culture medium upon GM-CSF-induced differentiation of monocytes to macrophages. GBM-derived EVs (from nine GSCs and U87-MG/EGFRvIII cells), as well as non-GBM-derived EVs (from HOG cells, MSCs and blood of two healthy donors (PBMC1, PBMC2)) were included. To facilitate comparison, the different types of EVs were added at equal numbers. (C) Representative microscopy pictures showing a differential effect of GBM EVs on the morphology of macrophages. As compared with control incubations (PBS only or EVs from blood of a healthy donor ("EV-PBMC1")), incubation with GBM EVs yielded macrophages that were relatively stretched. After incubation with non-GBM EVs, a large fraction of the cells detached and increased light scattering. (D, E) Flow cytometry-based phenotyping of macrophages. As compared to the non-GBM EV incubations, the presence of GBM EVs results in increased cell surface expression of the macrophage M2-type marker CD163 (D) and increased uptake of dextran-FITC beads (E). M-CSF was included as a positive control for differentiation to M2-type macrophages. Incubations were performed with monocytes of two independent donors. For each donor, the mean values are depicted for the GBM group and the non-GBM group. Statistical significance of this difference (determined by a two-tailed t-test) is indicated as well.

Upon incubation with GBM-derived EVs, cytokine secretion of cells showed an increase in secretion of interleukin 6 (IL-6), monocyte chemoattractant protein-1 (MCP-1), and vascular endothelial growth factor receptor (VEGF) (Suppl. Fig. S5A). To gain insight in the mechanism by which GBM EVs affect the monocytes, we analyzed the expression of Membrane Type 1 Metalloprotease (MT1-MMP) (Suppl. Fig. S5B). This protein is over-expressed in glioma-associated microglia and acts as an important tumor-supportive factor.^{31,33,34} Expression of MT1-MMP is induced by the binding of soluble factors to TLRs (TLR-2), but the identity of these factors remains to be identified. We speculated that the differentiation of monocytes to macrophages is accompanied by an increase in MT1-MMP, in the presence of GBM EVs. However, our RNA expression analysis did not point towards such an effect (Suppl. Fig. S5B).

GBM EVs affect microglia

Driven by our results on macrophages we performed similar analyses on microglia, since these cells are also highly abundant in the microenvironment of GBM and play important roles in the tumor's biology. We isolated primary human microglia from post-mortem brain tissues of two donors. For each donor, microglia were isolated from different brain regions (GTS, Gyrus Frontalis Medius; GFM; Gyrus Temporalis Superior; CC, Corpus Callosum; SVZ; Subventricular Zone). In contrast to our findings on macrophages, the GSC EVs only marginally affected expression of the cell surface marker HLA-DR (Suppl. Fig. S6A, Suppl. Fig. S6B). For Donor 1, the GFM-derived microglia showed a relative increase in HLA-DR for the GS184 EV incubation (as compared with mock), whilst this effect was absent for the CC-derived microglia. For Donor 2, microglia from GTS and SVZ showed a relative increase in HLA-DR for the GS184 EV incubation (as compared with mock), after 72 hours incubation. This increase in HLA-DR expression was not significant (T-test, GS184 incubations (n=3) versus mock incubations (n=3) at 72 hours; P = 0.3) Similarly, the GBM EVs did not significantly alter the expression of CD163 (Suppl. Fig. S6C, Suppl. Fig. S6D).

As outlined above, MT1-MMP is well-known for its over-expression in GBM-associated microglia. Strikingly, and in contrast to our analysis on macrophages, incubation with GBM EVs demonstrated an increase in MT1-MMP expression in the microglia of both donors (Figure 4A). Suggestive evidence for this increase was obtained after 6 hours, whilst the effect was significant after 72 hours (Figure 4B).

Fig 4A

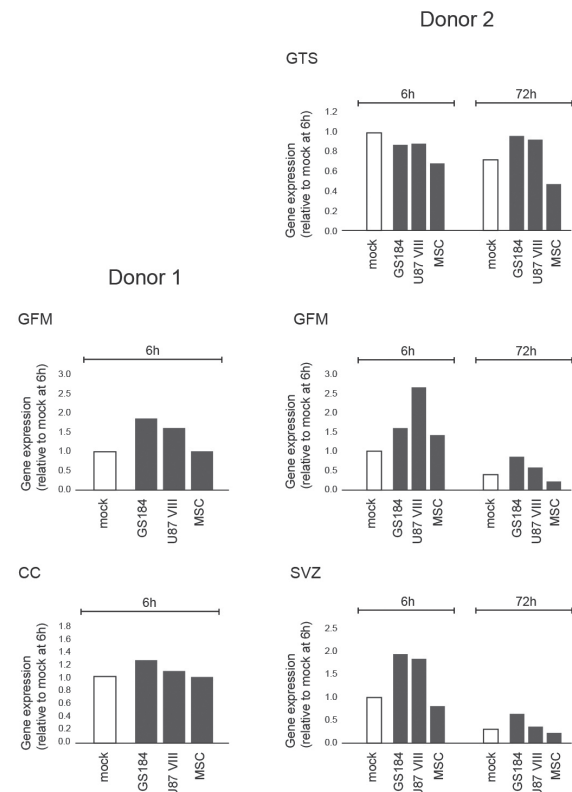


Fig 4B

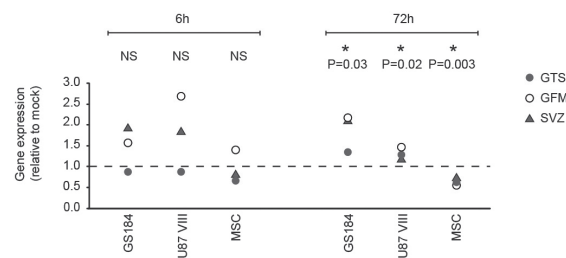


Figure 4. GBM-derived EVs increase MT1-MMP expression in microglia. (A) Primary human microglia (isolated from different brain regions of two donors) were incubated for 6 or 72 hours with EVs (from GS184, U87-MG/EGFRvIII and MSCs) or mock treated. Q-PCR was used to determine the expression levels of MT1-MMP. At both time points, the expression levels are normalized to the levels obtained after 6 hours mock incubation. (Donor 1 = Parkinson's disease donor, Donor 2 = healthy subject.) (B) Graph displaying the results of each EV type, with grouping of the GTS, GFM and SVZ data (Donor 2). The 6h and 72h mock incubations were used to normalize the levels obtained for the 6h and 72h EV incubations. The mock values are indicated by the dotted line. Significant differences between EV incubations and mock incubations (determined by two-tailed t-test) are indicated by asterisks and P values. (GTS = Gyrus Frontalis Medius, GFM = Gyrus Temporalis Superior, CC = Corpus Callosum, SVZ = Subventricular Zone.)

EVs from mesenchymal-classified tumors display the strongest effects on monocytic cells

We noticed that the GSC cultures with the highest EV secretion levels (GS186, GS187, GS224) also showed the most pronounced modulation of the monocyte to macrophage differentiation. This was not caused by adding different numbers of EVs, since these were exactly identical for all incubations. Based on this observation, we speculated that these cultures were derived from tumor material with common characteristics that belong to a specific molecular subclass. Indeed, comparison of the tumor's RNA expression profiles revealed a set of differentially expressed genes in the EV-high-associated- tumors (**Figure 5A**). Also, enriched gene sets were identified; *Regulation of Defense Response* and *Interferon Gamma Production* (**Figure 5B**). The majority of genes within these sets has previously been implicated in immune modulatory functions. Strikingly, the EV-high-associated- tumors were specifically classified as transcriptional subclass 23 (according to the "Gravendeel" method^{23, 25}) (**Figure 5C**). This corresponds to The Cancer Genome Atlas (TCGA) *mesenchymal* subtype.³⁵ The EV-low-associated- tumors were classified as 16/17 or 18 (corresponding to the *neural* or *classical* subtype³⁵).

Fig 5A

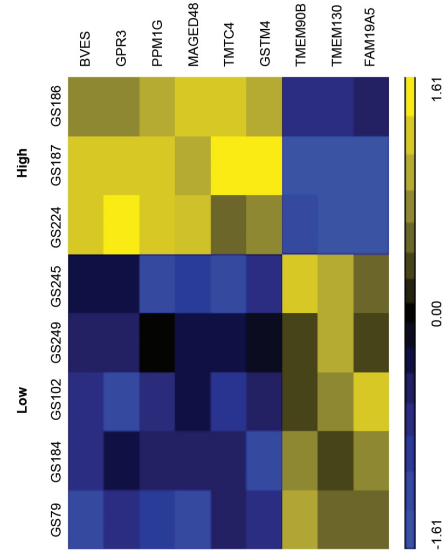


Fig 5C

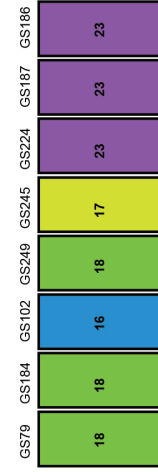


Fig 5B

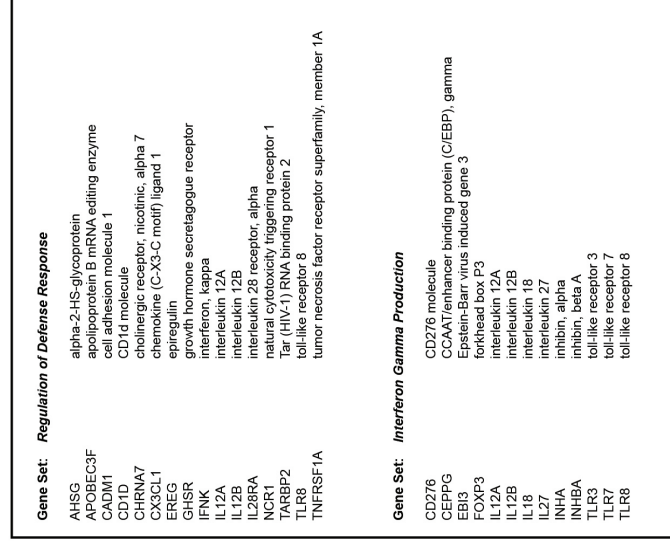


Figure 5. Gene expression analysis of tumors. EV secretion of the GSC cultures was used as a discriminating factor to categorize tumors as *EV-low-associated* or *EV-high-associated* (EV-low: GS79, GS102, GS184, GS245, GS249; EV-high: GS186, GS187, GS224). Expression of genes was determined by micro-array analysis.²³ **(A)** Heat map showing differentially expressed genes ($P < 0.01$) in the *EV-high-associated* or *EV-low-associated* group. **(B)** GSEA to identify the most significantly enriched gene sets in the *EV-high-associated* group (False Discovery Rate < 10%, Normalized Enrichment Scores: Regulation of Defense Response = 2.01, Interferon Gamma Production = 1.97). **(C)** Gene-expression based classification of the tumors.^{23, 25} Note that classification as either 16/17, 18 or 23 corresponds to a TCGA-based classification as respectively *neural*, *classical* or *mesenchymal*.³⁵

Discussion

GBM patients exhibit severe changes in their immune cell repertoire.^{2, 3} This is particularly characterized by major alteration of cells of the monocytic lineage, which systemically adapt to a phenotype that is typical for monocytic myeloid-derived suppressor cells.^{5, 6} In addition, specific types of monocytic cells appear to accumulate in the tumor, where they support tumor growth.^{4, 7-9} GBM's mechanisms responsible for these alterations remain to be elucidated. In this report, we demonstrate that the phenotype of monocytic cells is affected by EVs released by GBM cells.

To better understand the modes of action of GBM-derived EVs, we first performed detailed proteomic profiling. This revealed the selective enrichment in EVs of proteins functioning in *focal adhesion* and *leukocyte transendothelial migration*. Possibly, GBM cells have acquired mechanisms to selectively incorporate these proteins in EVs, thereby facilitating tumor-supporting changes in recipient cells. The findings of our proteomic analyses further strengthened the hypothesis that GBM EVs can modify monocytic cells, including macrophages. Focal adhesion complexes are highly important in the biology of macrophages, to support proliferation, phagocytosis and motility.⁸

Interestingly, multiple proteins were identified in the membrane of GBM EVs that appear to be undetectable in EVs of non-tumor origin, as concluded from a large survey in the EVpedia database (<http://evpedia.info/>) (**Table 1**). These proteins include lactadherin, syntenin-1, myristoylated alanine-rich C-kinase substrate (MARCKS), integrin alpha-V, integrin alpha-3, and EGFR, which were all detected in both GS184 EVs and U87-MG/EGFRVIII EVs. These findings may be of diagnostic value as well. Technologies to detect and quantify EVs in bodily fluids, which would allow for non-invasive diagnostics for GBM, are currently under development.^{27, 36-39}

GBM patients are in general characterized by aberrations in their T cell compartment, for instance characterized by a general CD4 T cell lymphopenia.³ Our analyses revealed no signs of EV-induced death of T cells (**Suppl. Fig. S3C**). This is in contrast to the effects observed for EVs from other types of cancer (i.e. from ovarian-, oral-, and prostate cancer).⁴⁰⁻⁴²

We observed strong effects of GBM-derived EVs on the phenotype of monocytes. Incubation of PBMCs with U87-MG/EGFRVIII- and GS184 EVs resulted in reduced

expression of HLA-DR- and increased expression of CD14 on the cell surface. Of interest, a similar CD14^{high}/HLA-DR^{low} phenotype, resembling myeloid-derived suppressor cells, is regularly observed in the systemic monocyte population of GBM patients.^{6,31,32} Still, our findings did not point towards EVs in the blood of patients as inducers of this phenotype; isolated EVs (consisting of the total pool of plasma EVs, including GBM- and non-GBM EVs) did not change HLA-DR and CD14 on naïve monocytes (**Figure 2D**). It is likely, however, that the particular experimental procedure was insufficient to faithfully simulate the systemic bio-distribution of GBM EVs in patients. Possibly, GBM-derived EVs accumulate at specific locations in the body where they are in contact with monocytes or their precursors. Such a mechanism has been described for melanoma-derived EVs, which home to sites in the bone marrow.¹⁵ Alternatively, monocytes may migrate to the tumor site where they receive high numbers of tumor-derived EVs, followed by redistribution of the cells to the peripheral blood stream.

GBM-derived EVs considerably affected the differentiation of monocytes into macrophages, which was in contrast to EVs derived from cells of non-GBM origin. The phenotypic changes included modified expression of cell surface molecules (i.e., increased CD14-, CD16-, CD32-, CD45-, CD163- and HLA-DR expression) and increased secretion of IL-6, MCP-1 and VEGF, thereby resembling the phenotype of M2-type / “alternatively activated” macrophages. Presumably, the modified cytokine secretion will severely impact the tumor surroundings. As such, secretion of IL-6 may stimulate GBM proliferation and resistance to therapy.⁴³ The GBM EVs also induced an increased phagocytic capacity of macrophages (**Figure 3E**), which may facilitate the migration of tumor cells as a result of enhanced degradation of extracellular matrix components.^{44, 45}

By implementing a novel technology for EV quantification (tRPS, which allows for particle measurement instead of bulk-protein measurement²⁷) we were technically successful in comparing the EV secretion between a panel of different GSC cultures. Surprisingly, this revealed remarkable variation, with some cultures, in particular these from mesenchymal GBM, displaying higher EV secretion levels as compared to others. The mesenchymal EVs were not only characterized by higher secretion levels, but also by more pronounced effects on monocyte to macrophage differentiation. This suggests that EV secretion occurs at higher levels, and may be of higher relevance, in mesenchymal GBMs. Interestingly, mesenchymal GBMs display an increased

infiltration of tumor-supportive monocytic cells, as a result of currently unknown mechanisms.^{46, 47}

Our findings on macrophages provided a strong rationale to analyze the effects of GBM EVs on brain-resident microglia, which (besides the peripheral-derived macrophages) constitute large part of the monocytic cell population in GBMs' micro-environment. Interestingly, the microglia's response to GBM EVs appeared to differ from the responses observed upon monocyte-to-macrophage differentiation. Expression of cell surface markers HLA-DR and CD163 was not significantly altered (**Suppl. Fig. 6**). Despite their overlapping functions,⁴⁸ macrophages and microglia are highly different cell types, and it is therefore conceivable that they respond differently to EVs.

We hypothesized that TLR-2, a monocytic receptor, is involved in our observed phenomena. GBM EVs are highly abundant in small RNA molecules,⁴⁹ which were previously reported as potent binders to TLRs.¹⁹ TLR-2 binding, followed by downstream expression of MT1-MMP, has been implicated in the establishment of M2-type characteristics in GBM-associated microglia.^{33,34} We did not find evidence for an effect of GBM EVs on MT1-MMP expression in the context of monocyte-to-macrophage differentiation (**Suppl. Fig. S5B**). However, MT1-MMP was significantly up-regulated by GBM EVs in microglia (**Figure 4**). This strongly suggests that EVs are a mechanism for GBMs to induce MT1-MMP expression in GBM-associated microglia, thereby supporting tumor growth. Effects of GBM EVs on monocytic cells of non-microglia type (monocytes/macrophages) appear to occur via a different mechanism, not involving MT1-MMP.

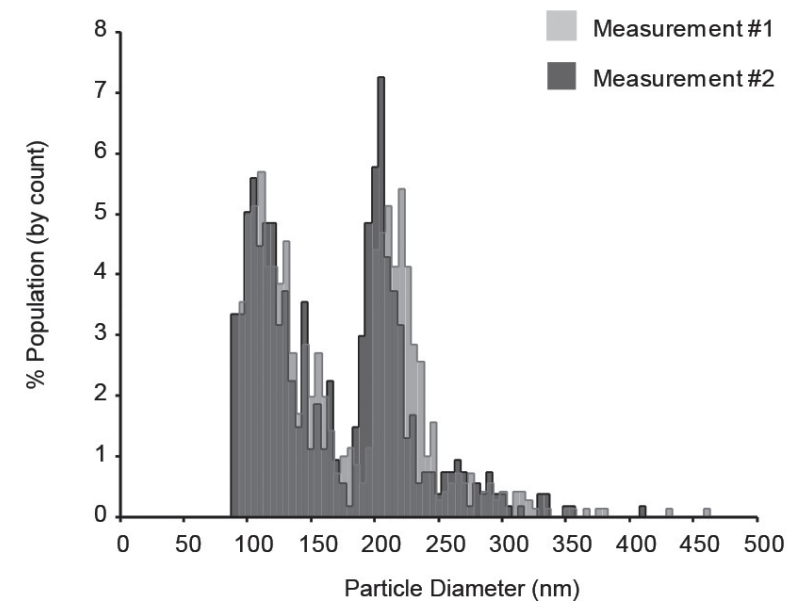
The therapeutic potential of targeting GBM-associated monocytic cells has already been shown in pre-clinical models. For example, GBM growth can be inhibited (in proneural GBM models) by blocking colony stimulating factor-1 receptor (CSF-1R), thereby skewing the differentiation of microglia from M2-type to M1-type.⁵⁰ Taken together, our findings suggest that similar effects may be obtained by blocking the transfer of GBM EVs to monocytic cells. Indeed, our study identifies for the first time EVs of GBM cells as potent modulators of cells of the monocytic lineage altering them to resemble the tumor-supportive phenotypes described in patients. These findings corroborate on the previously described tumor-supportive effects of GBM-derived EVs on endothelial cells and tumor cells.¹⁶⁻²⁰ Further research will be imperative to

gain more insight into the biology of GBM-derived EVs, which, eventually, may lead to novel (EV-targeted) therapies and/or improvement of current therapies.

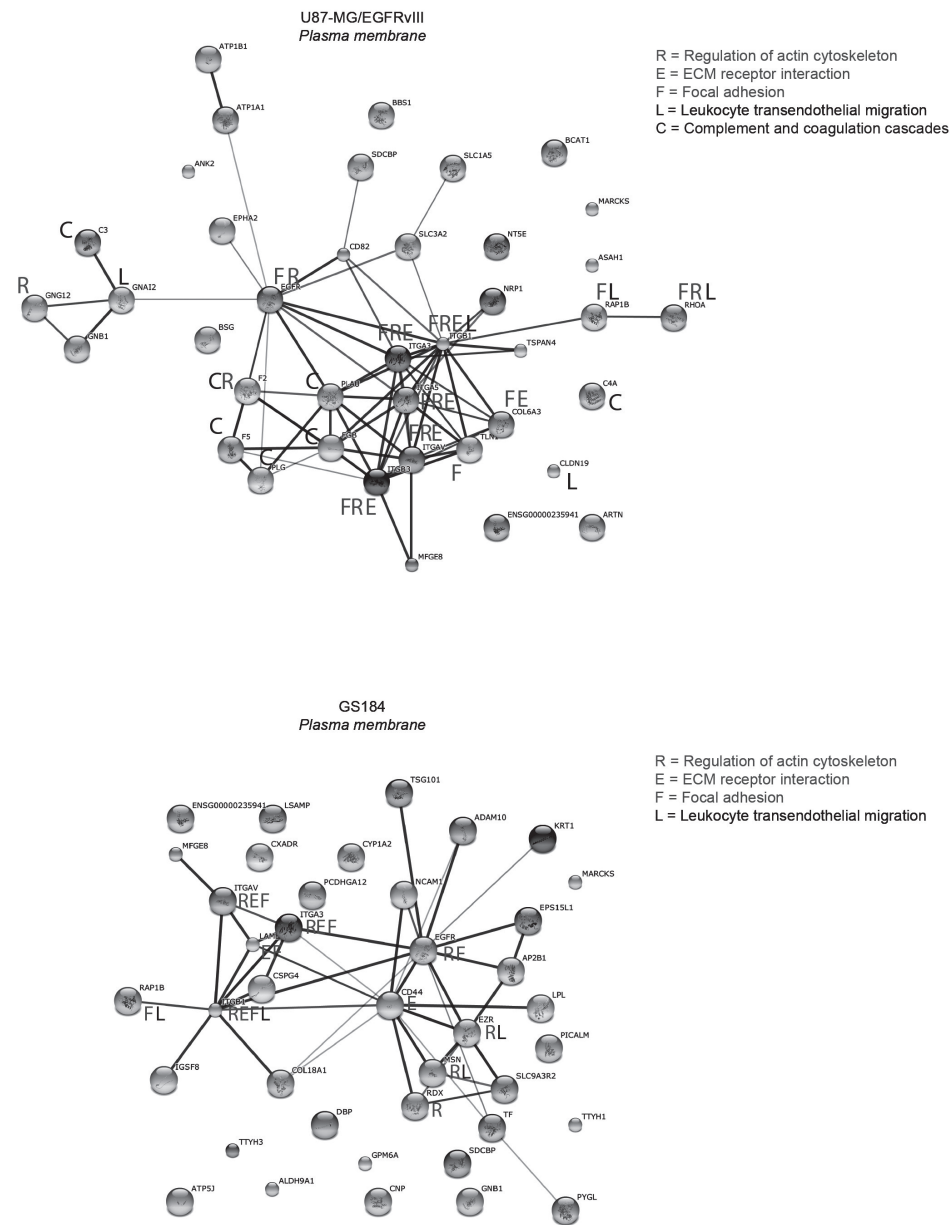
Tables

Table 1 and supplementary tables are available online at doi.org/10.1002/ijc.29521

Supplementary Figures



Suppl. Figure S1. tRPS-based quantification and size profiling of GS184-derived EVs. The left peak represents the EV population, the right peak represents the polystyrene beads that were included as an internal reference for accurate EV quantification.



Suppl. Figure S2. Overview of the proteins with significant EV-versus-cell enrichment within the sub-selected group of cytoplasmic membrane-associated proteins. Using STRING pathway analysis, functional connectivity between proteins, as well as significant association with specific cellular pathways was found. Results are shown for U87-MG/EGFRVIII and GS184. Additional information on the displayed proteins (including protein names and enrichment scores) is provided in **Suppl. Table S2**.

Fig S3B

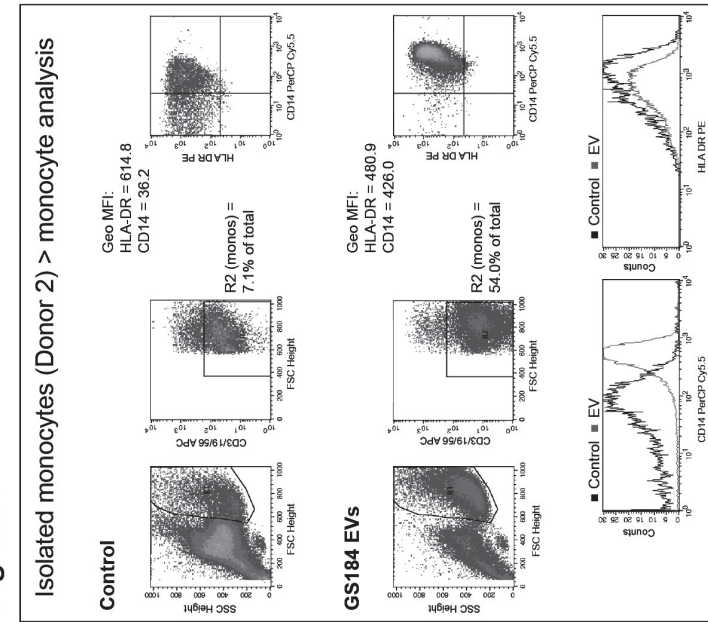
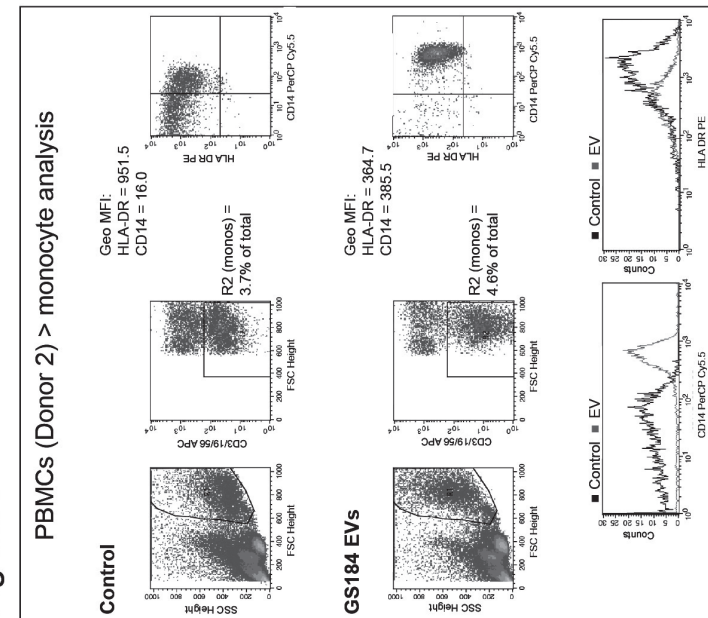
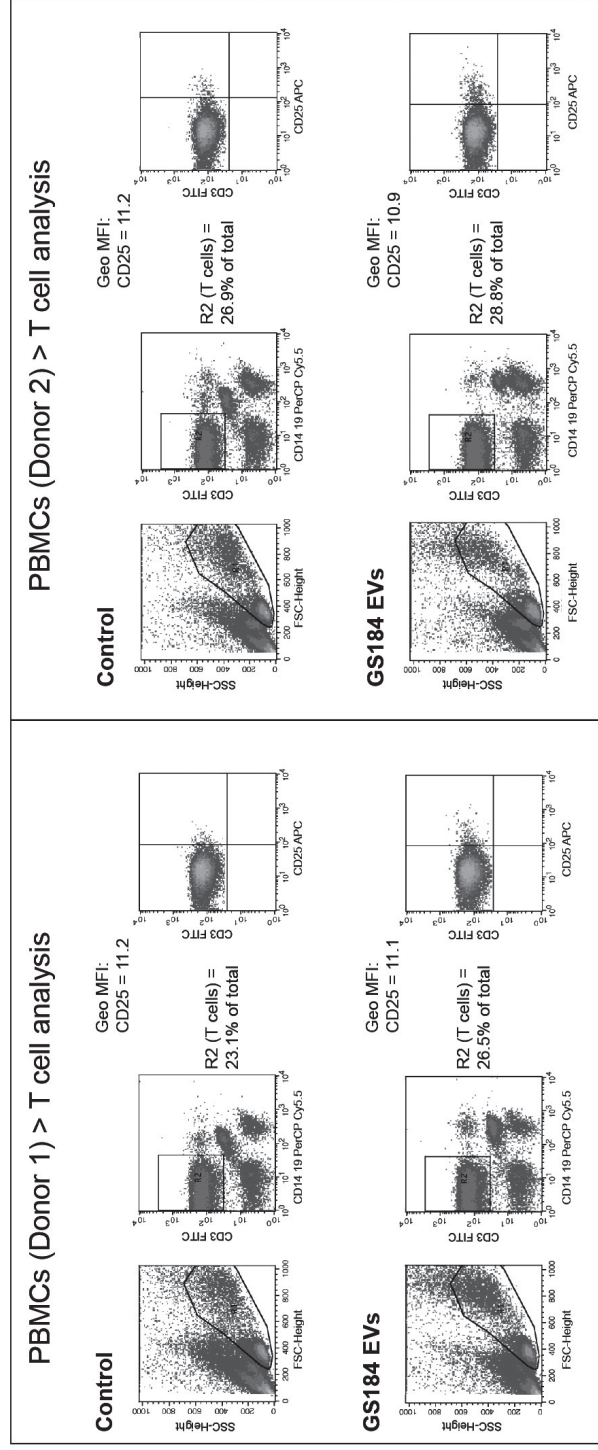


Fig S3A



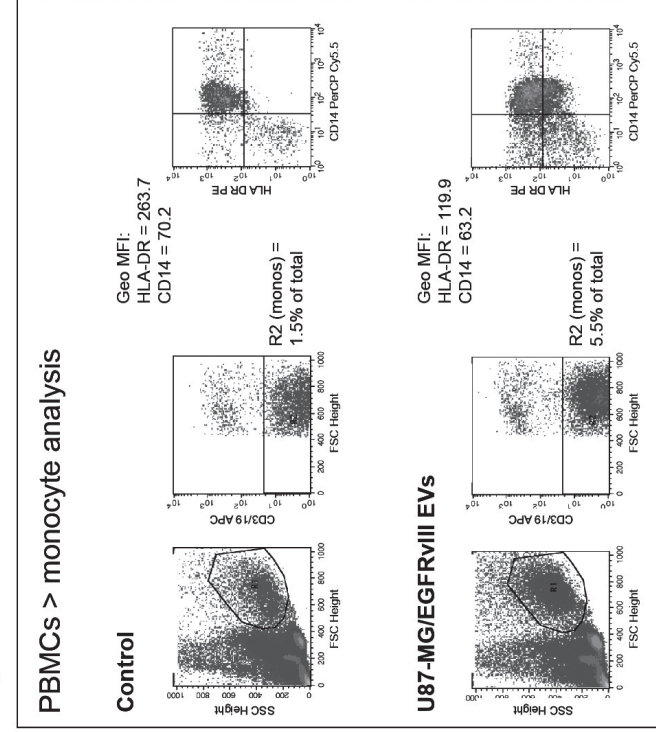
Suppl. Figure S3. Phenotypic analysis of PBMCs after incubation with GBM-derived EVs. PBMCs were incubated with EVs or PBS only (control) for three days, followed by flow cytometric analysis of cell surface proteins. (A) Incubation of PBMCs (from Donor 2) with GS184 EVs, followed by analysis of CD14 and HLA-DR on monocytes. (B) Incubation of purified monocytes (from Donor 2) with GS184 EVs, followed by analysis of CD14 and HLA-DR. (C) Incubation of PBMCs (from Donor 1 and Donor 2) with GS184 EVs, followed by analysis of CD25 on T cells. (D) Incubation of PBMCs with U87-MG/EGFRVIII EVs, followed by analysis of CD14 and HLA-DR on monocytes. The applied gating strategies to select monocyte- or T cell populations are indicated (R1 followed by R2), as well as the values for monocyte- and T cell percentages (expressed as fraction of the total number of PBMCs).

Fig S3C

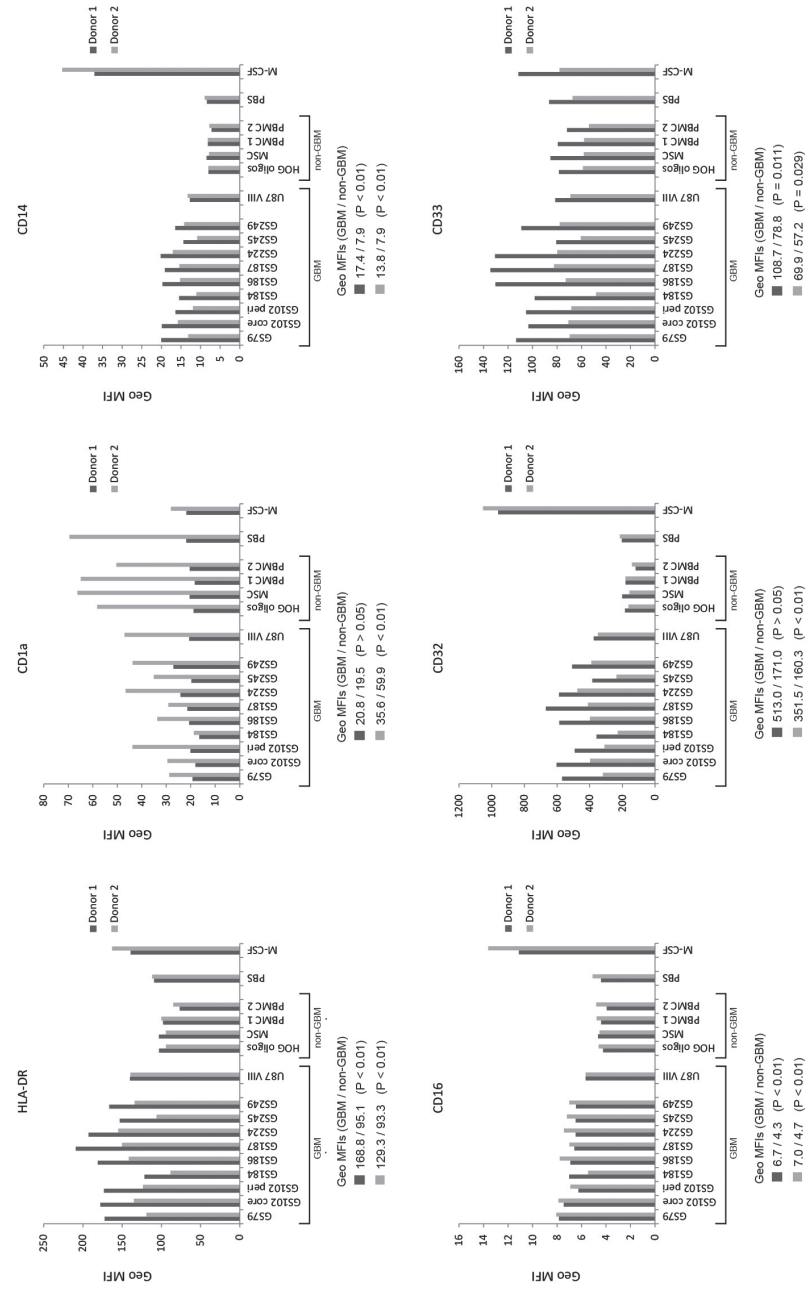


Suppl. Figure S3. Continued.

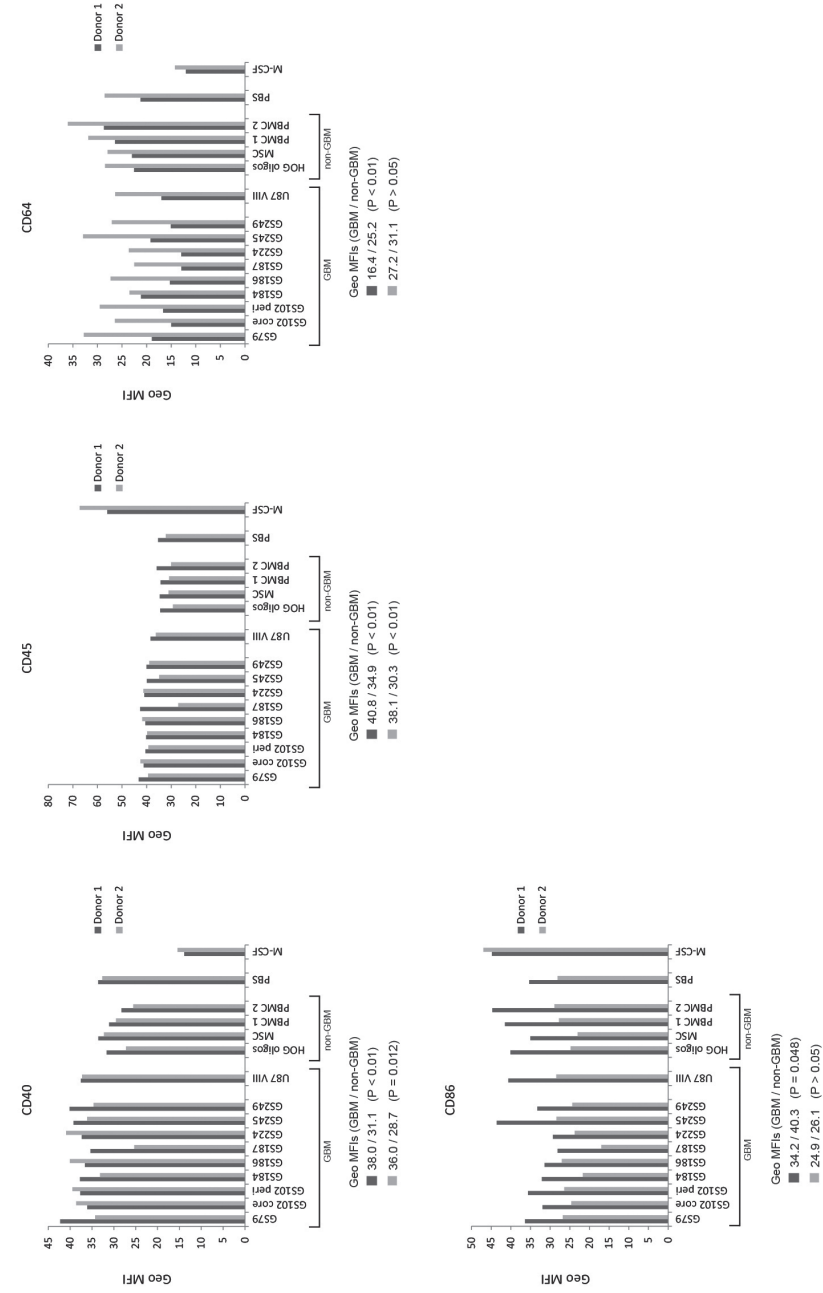
Fig S3D



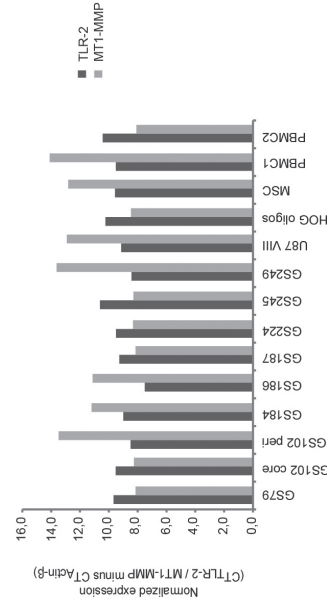
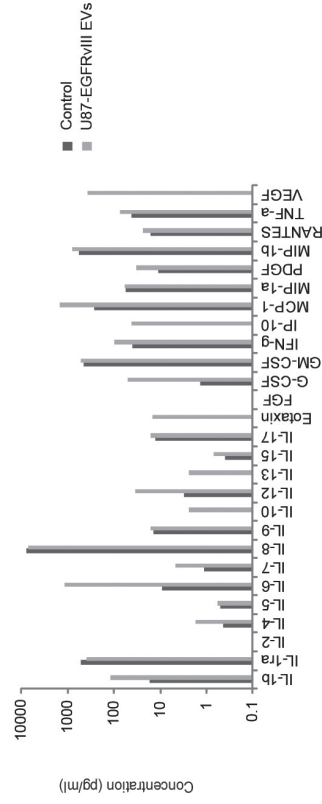
Suppl. Figure S3. Continued.



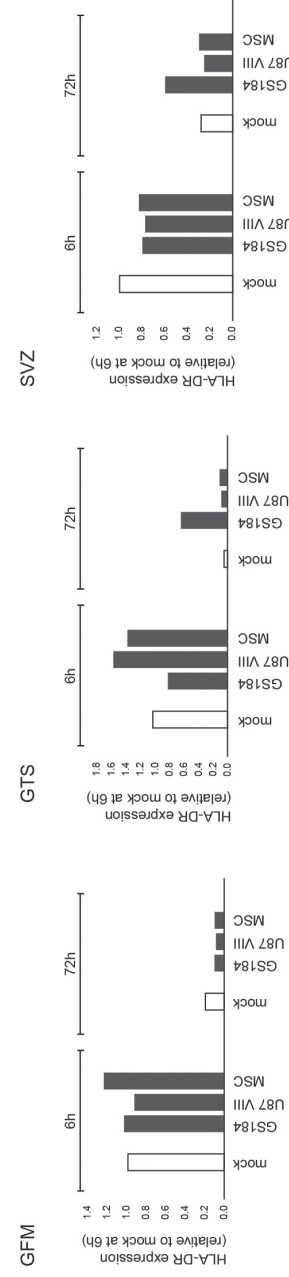
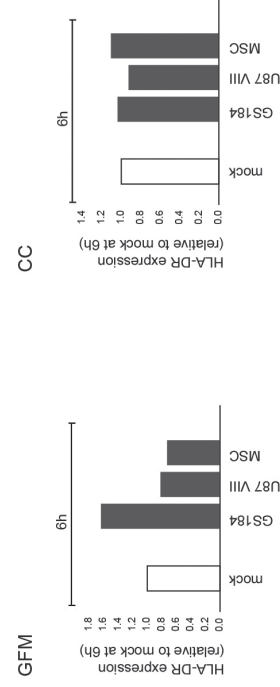
Suppl. Figure S4. Phenotypic analyses of macrophages after co-incubation with or without GBM-derived EVs. Flow cytometry was used to quantify expression levels of macrophage surface molecules after GM-CSF induced monocyte-to-macrophage differentiation. Monocytes had been isolated from two healthy donors. Incubations were performed in the presence of GBM EVs (from GSC cultures and U87-MG/EGFR^{III}), non-GBM EVs (from HOG cells, MSCs and blood of healthy donors) and PBS only. M-CSF incubation was included as a positive control for M2-type macrophage induction. For each donor, the mean values are depicted for the GBM group and the non-GBM group. Statistical significance of this difference (determined by a two-tailed t-test) is indicated as well.



Suppl. Figure S4. Continued.



Suppl. Figure S5. Quantification of macrophages' cytokine secretion and gene expression after co-incubation with or without GBM-derived EVs. (A) Quantification of cytokines in the conditioned media of macrophages, which had been differentiated in the presence of U87-MG/EGFRVIII EVs or PBS only (control). (B) Quantitative PCR to quantify expression levels of TLR-2 and MTT1-MMP RNA in macrophages, which had been differentiated in the presence of GBM EVs (from GSC cultures and U87-MG/EGFRVIII) or non-GBM EVs (from HOG cells, MSCs and blood of healthy donors). The expression levels were normalized to the expression level of actin β (CT_{TLR-2} - CT_{Actin- β} or CT_{MTT1-MMP} - CT_{Actin- β}).



Suppl. Figure S6. Quantification of HLA-DR and CD163 expression in microglia after co-incubation with or without GBM-derived EVs. Primary human microglia (isolated from different brain regions of two donors) were incubated for 6 or 72 hours with EVs (derived from GS184, U87-MG/EGFRVIII and MSC), or mock treated. Q-PCR was used to determine gene expression levels, which were normalized to the levels obtained after 6 hours mock incubation. (A) Microglia from Donor 1, HLA-DR quantification, (B) Microglia from Donor 2, HLA-DR quantification, (C) Microglia from Donor 1, CD163 quantification, (D) Microglia from Donor 2, CD163 quantification. (Donor 1 = Parkinson's disease donor, Donor 2 = healthy subject.) (GTS = Gyrus Frontalis Medius, GFM = Gyrus Temporalis Superior, CC = Corpus Callosum, SVZ = Subventricular Zone.)

Fig S6C

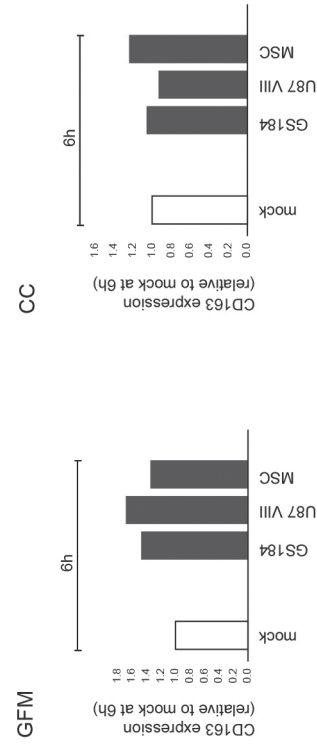
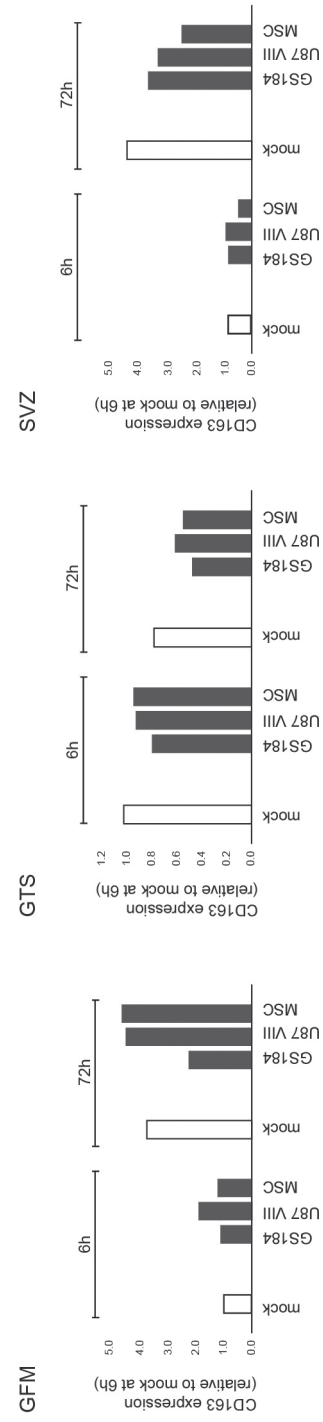


Fig S6D



Suppl. Figure S6. Continued.

References

- Stupp R, Hegi ME, Mason WP, van den Bent MJ, Taphoorn MJ, Janzer RC, Ludwin SK, Allgeier A, Fisher B, Belanger K, Hau P, Brandes AA, et al. Effects of radiotherapy with concomitant and adjuvant temozolomide versus radiotherapy alone on survival in glioblastoma in a randomised phase III study: 5-year analysis of the EORTC-NCIC trial. *Lancet Oncol* 2009;10:459-66.
- Avril T, Vauleon E, Tanguy-Royer S, Mosser J, Quillien V. Mechanisms of immunomodulation in human glioblastoma. *Immunotherapy* 2011;3:42-4.
- Waziri A. Glioblastoma-derived mechanisms of systemic immunosuppression. *Neurosurg Clin N Am* 2010;21:31-42.
- da Fonseca AC, Badie B. Microglia and macrophages in malignant gliomas: recent discoveries and implications for promising therapies. *Clin Dev Immunol* 2013;2013:264124.
- Kohanbash G, Okada H. Myeloid-derived suppressor cells (MDSCs) in gliomas and glioma-development. *Immunol Invest* 2012;41:658-79.
- Gustafson MP, Lin Y, New KC, Bulur PA, O'Neill BP, Gastineau DA, Dietz AB. Systemic immune suppression in glioblastoma: the interplay between CD14+HLA-DRlo/neg monocytes, tumor factors, and dexamethasone. *Neuro Oncol* 2010;12:631-44.
- Gabrusiewicz K, Ellert-Miklaszewska A, Lipko M, Sielska M, Frankowska M, Kaminska B. Characteristics of the alternative phenotype of microglia/macrophages and its modulation in experimental gliomas. *PLoS One* 2011;6:e23902.
- Ellert-Miklaszewska A, Dabrowski M, Lipko M, Sliwa M, Maleszewska M, Kaminska B. Molecular definition of the pro-tumorigenic phenotype of glioma-activated microglia. *Glia* 2013;61:1178-90.
- Prosniak M, Harshyne LA, Andrews DW, Kenyon LC, Bedelbaeva K, Apanasovich TV, Heber-Katz E, Curtis MT, Cotzia P, Hooper DC. Glioma grade is associated with the accumulation and activity of cells bearing M2 monocyte markers. *Clin Cancer Res* 2013;19:3776-86.
- Han SJ, Zygourakis C, Lim M, Parsa AT. Immunotherapy for glioma: promises and challenges. *Neurosurg Clin N Am* 2013;23:357-70.
- Gyorgy B, Szabo TG, Pasztoi M, Pal Z, Misjak P, Aradi B, Laszlo V, Pallinger E, Pap E, Kittel A, Nagy G, Falus A, et al. Membrane vesicles, current state-of-the-art: emerging role of extracellular vesicles. *Cell Mol Life Sci* 2011;68:2667-88.
- EL Andaloussi S, Mager I, Breakefield XO, Wood MJ. Extracellular vesicles: biology and emerging therapeutic opportunities. *Nat Rev Drug Discov* 2013;12:347-57.
- Al-Nedawi K, Meehan B, Rak J. Microvesicles: messengers and mediators of tumor progression. *Cell Cycle* 2009;8:2014-8.
- Bobrie A, Krumeich S, Reyat F, Recchi C, Moita LF, Seabra MC, Ostrowski M, Thery C. Rab27a supports exosome-dependent and -independent mechanisms that modify the tumor microenvironment and can promote tumor progression. *Cancer Res* 2012;72:4920-30.
- Peinado H, Aleckovic M, Lavotshkin S, Matei I, Costa-Silva B, Moreno-Bueno G, Hergueta-Redondo M, Williams C, Garcia-Santos G, Ghajar C, Nitadori-Hoshino A, Hoffman C, et al. Melanoma exosomes educate bone marrow progenitor cells toward a pro-metastatic phenotype through MET. *Nat Med* 2012;18:883-91.
- Al-Nedawi K, Meehan B, Micallef J, Lhotak V, May L, Guha A, Rak J. Intercellular transfer of the oncogenic receptor EGFRvIII by microvesicles derived from tumour cells. *Nat Cell Biol* 2008;10:619-24.

17. Al-Nedawi K, Meehan B, Kerbel RS, Allison AC, Rak J. Endothelial expression of autocrine VEGF upon the uptake of tumor-derived microvesicles containing oncogenic EGFR. *Proc Natl Acad Sci U S A* 2009;106:3794-9.
18. Skog J, Wurdinger T, van Rijn S, Meijer DH, Gainche L, Sena-Esteves M, Curry WT, Jr., Carter BS, Krichevsky AM, Breakefield XO. Glioblastoma microvesicles transport RNA and proteins that promote tumour growth and provide diagnostic biomarkers. *Nat Cell Biol* 2008;10:1470-6.
19. Li CC, Eaton SA, Young PE, Lee M, Shuttleworth R, Humphreys DT, Grau GE, Combes V, Bebawy M, Gong J, Brammah S, Buckland ME, et al. Glioma microvesicles carry selectively packaged coding and noncoding RNAs which alter gene expression in recipient cells. *RNA Biol* 2013;10.
20. Bronisz A, Wang Y, Nowicki MO, Peruzzi P, Ansari KI, Ogawa D, Balaj L, De Rienzo G, Mineo M, Nakano I, Ostrowski MC, Hochberg F, et al. Extracellular Vesicles Modulate the Glioblastoma Microenvironment via a Tumor Suppression Signaling Network Directed by miR-1. *Cancer Res* 2014;74:738-50.
21. Post GR, Dawson G. Characterization of a cell line derived from a human oligodendroglioma. *Mol Chem Neuropathol* 1992;16:303-17.
22. Knaan-Shanzer S, van de Watering MJ, van der Velde I, Goncalves MA, Valerio D, de Vries AA. Endowing human adenovirus serotype 5 vectors with fiber domains of species B greatly enhances gene transfer into human mesenchymal stem cells. *Stem Cells* 2005;23:1598-607.
23. Balvers RK, Kleijn A, Kloezeman JJ, French PJ, Kremer A, van den Bent MJ, Dirven CM, Leenstra S, Lamfers ML. Serum-free culture success of glial tumors is related to specific molecular profiles and expression of extracellular matrix-associated gene modules. *Neuro Oncol* 2013;15:1684-95.
24. Fael Al-Mayhani TM, Ball SL, Zhao JW, Fawcett J, Ichimura K, Collins PV, Watts C. An efficient method for derivation and propagation of glioblastoma cell lines that conserves the molecular profile of their original tumours. *J Neurosci Methods* 2009;176:192-9.
25. Gravendeel LA, Kouwenhoven MC, Gevaert O, de Rooij JJ, Stubbs AP, Duijij JE, Daemen A, Bleeker FE, Bralten LB, Kloosterhof NK, De Moor B, Eilers PH, et al. Intrinsic gene expression profiles of gliomas are a better predictor of survival than histology. *Cancer Res* 2009;69:9065-72.
26. Thery C, Amigorena S, Raposo G, Clayton A. Isolation and characterization of exosomes from cell culture supernatants and biological fluids. *Curr Protoc Cell Biol* 2006;Chapter 3:Unit 3 22.
27. de Vrij J, Maas SL, van Nispen M, Sena-Esteves M, Limpens RW, Koster AJ, Leenstra S, Lamfers ML, Broekman ML. Quantification of nanosized extracellular membrane vesicles with scanning ion occlusion sensing. *Nanomedicine (Lond)* 2013.
28. Maas SL, De Vrij J, Broekman ML. Quantification and size-profiling of extracellular vesicles using tunable resistive pulse sensing. *J Vis Exp* 2014:e51623.
29. Dekker LJ, Zenayedpour L, Brouwer E, van Duijn MM, Sillevs Smitt PA, Luiders TM. An antibody-based biomarker discovery method by mass spectrometry sequencing of complementarity determining regions. *Anal Bioanal Chem* 2011;399:1081-91.
30. Franceschini A, Szklarczyk D, Frankild S, Kuhn M, Simonovic M, Roth A, Lin J, Minguez P, Bork P, von Mering C, Jensen LJ. STRING v9.1: protein-protein interaction networks, with increased coverage and integration. *Nucleic Acids Res* 2013;41:D808-15.
31. Woiciechowsky C, Asadullah K, Nestler D, Schoning B, Glockner F, Docke WD, Volk HD. Diminished monocytic HLA-DR expression and ex vivo cytokine secretion capacity in patients with glioblastoma: effect of tumor extirpation. *J Neuroimmunol* 1998;84:164-71.

32. Ogden AT, Horgan D, Waziri A, Anderson D, Louca J, McKhann GM, Sisti MB, Parsa AT, Bruce JN. Defective receptor expression and dendritic cell differentiation of monocytes in glioblastomas. *Neurosurgery* 2006;59:902-9; discussion 9-10.
33. Markovic DS, Vinnakota K, Chirasani S, Synowitz M, Raguette H, Stock K, Sliwa M, Lehmann S, Kalin R, van Rooijen N, Holmbeck K, Heppner FL, et al. Gliomas induce and exploit microglial MT1-MMP expression for tumor expansion. *Proc Natl Acad Sci U S A* 2009;106:12530-5.
34. Vinnakota K, Hu F, Ku MC, Georgieva PB, Szulzewsky F, Pohlmann A, Waiczies S, Waiczies H, Niendorf T, Lehnardt S, Hanisch UK, Synowitz M, et al. Toll-like receptor 2 mediates microglia/brain macrophage MT1-MMP expression and glioma expansion. *Neuro Oncol* 2013;15:1457-68.
35. Verhaak RG, Hoadley KA, Purdom E, Wang V, Qi Y, Wilkerson MD, Miller CR, Ding L, Golub T, Mesirov JP, Alexe G, Lawrence M, et al. Integrated genomic analysis identifies clinically relevant subtypes of glioblastoma characterized by abnormalities in PDGFRA, IDH1, EGFR, and NF1. *Cancer Cell* 2010;17:98-110.
36. Nolte-t Hoen EN, van der Vlist EJ, Aalberts M, Mertens HC, Bosch BJ, Bartelink W, Mastrobattista E, van Gaal EV, Stoorvogel W, Arkesteijn GJ, Wauben MH. Quantitative and qualitative flow cytometric analysis of nanosized cell-derived membrane vesicles. *Nanomedicine* 2011;8:712-20.
37. Shao H, Chung J, Balaj L, Charest A, Bigner DD, Carter BS, Hochberg FH, Breakefield XO, Weissleder R, Lee H. Protein typing of circulating microvesicles allows real-time monitoring of glioblastoma therapy. *Nat Med* 2012;18:1835-40.
38. Dragovic RA, Gardiner C, Brooks AS, Tannetta DS, Ferguson DJ, Hole P, Carr B, Redman CW, Harris AL, Dobson PJ, Harrison P, Sargent IL. Sizing and phenotyping of cellular vesicles using Nanoparticle Tracking Analysis. *Nanomedicine* 2011;7:780-8.
39. Maas SL, de Vrij J, van der Vlist EJ, Geragousian B, van Bloois L, Mastrobattista E, Schiffelers RM, Wauben MH, Broekman ML, Nolte-t Hoen EN. Possibilities and limitations of current technologies for quantification of biological extracellular vesicles and synthetic mimics. *J Control Release* 2015;200:87-96.
40. Taylor DD, Gercel-Taylor C, Lyons KS, Stanson J, Whiteside TL. T-cell apoptosis and suppression of T-cell receptor/CD3-zeta by Fas ligand-containing membrane vesicles shed from ovarian tumors. *Clin Cancer Res* 2003;9:5113-9.
41. Kim JW, Wieckowski E, Taylor DD, Reichert TE, Watkins S, Whiteside TL. Fas ligand-positive membranous vesicles isolated from sera of patients with oral cancer induce apoptosis of activated T lymphocytes. *Clin Cancer Res* 2005;11:1010-20.
42. Abusamra AJ, Zhong Z, Zheng X, Li M, Ichim TE, Chin JL, Min WP. Tumor exosomes expressing Fas ligand mediate CD8+ T-cell apoptosis. *Blood Cells Mol Dis* 2005;35:169-73.
43. Sasaki A, Ishiuchi S, Kanda T, Hasegawa M, Nakazato Y. Analysis of interleukin-6 gene expression in primary human gliomas, glioblastoma xenografts, and glioblastoma cell lines. *Brain Tumor Pathol* 2001;18:13-21.
44. Rey-Giraud F, Hafner M, Ries CH. In vitro generation of monocyte-derived macrophages under serum-free conditions improves their tumor promoting functions. *PLoS One* 2012;7:e42656.
45. Wels J, Kaplan RN, Rafii S, Lyden D. Migratory neighbors and distant invaders: tumor-associated niche cells. *Genes Dev* 2008;22:559-74.
46. Rutledge WC, Kong J, Gao J, Gutman DA, Cooper LA, Appin C, Park Y, Scarpace L, Mikkelsen T, Cohen ML, Aldape KD, McLendon RE, et al. Tumor-infiltrating lymphocytes in glioblastoma are associated with specific genomic alterations and related to transcriptional class. *Clin Cancer Res* 2013;19:4951-60.

47. Engler JR, Robinson AE, Smirnov I, Hodgson JG, Berger MS, Gupta N, James CD, Molinaro A, Phillips JJ. Increased microglia/macrophage gene expression in a subset of adult and pediatric astrocytomas. *PLoS One* 2012;7:e43339.
48. Butovsky O, Jedrychowski MP, Moore CS, Cialic R, Lanser AJ, Gabriely G, Koeglsperger T, Dake B, Wu PM, Doykan CE, Fanek Z, Liu L, et al. Identification of a unique TGF-beta-dependent molecular and functional signature in microglia. *Nat Neurosci* 2014;17:131-43.
49. Fabbri M, Paone A, Calore F, Galli R, Gaudio E, Santhanam R, Lovat F, Fadda P, Mao C, Nuovo GJ, Zanesi N, Crawford M, et al. MicroRNAs bind to Toll-like receptors to induce prometastatic inflammatory response. *Proc Natl Acad Sci U S A* 2012;109:E2110-6.
50. Pyonteck SM, Akkari L, Schuhmacher AJ, Bowman RL, Sevenich L, Quail DF, Olson OC, Quick ML, Huse JT, Teijeiro V, Setty M, Leslie CS, et al. CSF-1R inhibition alters macrophage polarization and blocks glioma progression. *Nat Med* 2013;19:1264-72.

5

Based on:

Glioblastoma Hijacks Microglial Transcriptional Networks independently of TREM2

Sybren L.N. Maas^{1,2*}, Erik R. Abels^{1*}, Lieke L. Van De Haar¹, Xuan Zhang¹, Srinjoy Sil³, Joana Guedes^{4,5}, Pritha Sen⁴, Shilpa Prabhakar¹, Suzanne E. Hickman^{4,6}, Charles P. Lai^{1,7}, David T. Ting³, Xandra O. Breakefield¹†, Marike L.D. Broekman^{1,2}† and Joseph El Khoury^{4,6}†

¹Departments of Neurology and Radiology, Massachusetts General Hospital, and Harvard Medical School. Boston, 02129, Massachusetts, USA. ² Department of Neurosurgery, Brain Center Rudolf Magnus, University Medical Center, Utrecht University, 3584 CX, Utrecht, The Netherlands ³ Cancer Center, Massachusetts General Hospital, and Harvard Medical School. Boston, 02129, Massachusetts, USA. ⁴ Center for Immunology & Inflammatory Diseases, Massachusetts General Hospital, and Harvard Medical School. Boston, 02129, Massachusetts, USA. ⁵ Center for Neuroscience and Cell Biology, University of Coimbra, 3004-517, Coimbra, Portugal ⁶Department of Medicine, Massachusetts General Hospital, and Harvard Medical School. Boston, 02129, Massachusetts, USA. ⁷ Current affiliation: Institute of Atomic and Molecular Sciences / Academia Sinica, 10617, Taipei, Taiwan

* These authors contributed equally.

† Co-senior authors

Under review

Abstract

Glioblastomas are the most common and lethal primary brain tumors. Microglia, the resident immune cells of the brain survey their environment and respond to pathogens, toxins, and tumors. Glioblastoma cells communicate with microglia, in part by releasing extracellular vesicles (EVs) that include microvesicles and exosomes. We analyzed the transcriptional networks of microglia in mice with glioblastoma, focusing on microglia that had taken up tumor-derived EVs and therefore are within and immediately adjacent to the tumor. We show that these microglia have downregulated networks involved in sensing tumor cells and tumor-derived danger signals, as well as networks used for tumor killing. In contrast, expression of genes involved in clearing debris and facilitating tumor spread were upregulated. The homeostatic TGF- β pathway is downregulated, whereas the immunosuppressive Interleukin 4 and 10 pathways and numerous genes in the Interleukin 6/STAT3 and Interferon- γ pathways that promote tumor proliferation and migration are upregulated in glioblastoma microglia. These changes appear to be at least in part EV-mediated, since intracranial injection of EVs in normal mice leads to similar changes. This transcriptomic signature was also observed when datasets from human patients with glioblastoma were analyzed. These transcriptional changes are independent of Triggering receptor expressed on myeloid cells 2 (*Trem2*), a key microglial immune checkpoint, but likely dependent on apolipoprotein E (*ApoE*), another regulator of microglial gene expression and phenotype. Furthermore, *Trem2* deficiency did not affect tumor growth. Our data define an *ApoE*-regulated Microglia_{Glioblastoma} specific phenotype, whereby glioblastomas have hijacked gene expression in the neuroimmune system to avoid tumor sensing, suppress the immune response, clear a path for invasion and enhance tumor propagation. For further exploration we developed an interactive online tool at www.glioma-microglia.com with all expression data and additional functional and pathway information for each available gene.

Introduction

Harnessing the power of the immune system to treat a variety of cancers has gained significant momentum in recent years. Glioblastomas are diffusely infiltrating tumors of the brain. Because of their invasive nature, total surgical resection of glioblastomas is not possible resulting in tumor recurrence even following adjunctive chemo- and radiotherapy¹. Therefore, new effective treatment strategies for glioblastomas are desperately needed, including therapies utilizing the patients' own immune system². Understanding how glioblastoma cells interact with the immune system is key to developing immune-based treatments for this cancer². Microglia are the principal innate neuroimmune cells of the brain and are involved in brain development, aging, response to injury, and various pathological conditions³⁻⁵. In physiological conditions, microglia have three major functions in the central nervous system (CNS). First, they continuously survey their milieu to sense changes in their environment. Second, they help protect the brain from invading pathogens and noxious stimuli, including tumor cells in early stages of tumorigenesis. Third, they promote homeostasis and synaptic remodeling in development and learning^{3,6}. Microglia express clusters of genes that allow them to perform their different functions and have a number of distinct transcriptomic signatures, which vary with the physiological and/or pathological state of the brain⁷.

Glioblastomas recruit neighboring resident microglia and peripheral monocytes through the secretion of various chemokines and cytokines^{8,9}. Once in the tumor environment the monocytes differentiate into macrophages¹⁰. Local microglia and infiltrating monocytes and macrophages can make up to 44% of the glioblastoma tumor mass^{11,12}. However, in spite of the presence of large numbers of microglia and macrophages in glioblastoma, the tumors continue to grow and immune cells appear incapable of controlling such growth. It is accepted that glioblastoma-associated microglia and macrophages play a role in promoting tumor growth^{10,13}. Indeed, depletion of microglia results in reduced glioma invasion and growth in organotypic brain slices and *in vivo*^{14,15}. While the evidence that supports this assertion is growing, the exact microglial transcriptional networks involved in this tumor-supportive process are only beginning to be elucidated and have not been comprehensively characterized. Furthermore, the effect(s) of microglia that are within the tumor environs versus microglia in other areas of the tumor-bearing brain have not been investigated.

Tumor cells can alter their milieu in part by releasing extracellular vesicles (EVs), including exosomes and microvesicles^{16,17}. EVs are a heterogeneous collection of membrane-bound carriers with complex cargoes, including proteins, lipids and nucleic acids¹⁷⁻¹⁹. Tumor-derived EV uptake by microglia and macrophages leads to changes in expression of some genes in these cells as established *in vitro*^{20,21}. We have previously visualized such interactions both *in vitro* and *in vivo* using a syngeneic mouse glioblastoma model expressing palmitoylated green or red fluorescent proteins (palmGFP and palmtmTomato, respectively)^{21,22}. These palmitoylated fluorescent proteins label membranes of tumor cells as well as EVs produced by them (e.g. EV-GFP)²². This model allowed us to visualize and isolate microglia and macrophages that had taken up tumor-derived EVs *in vivo* and are therefore closely interacting with glioblastoma cells. We then analyzed the microglial transcriptome using RNASeq to investigate the transcriptional networks of tumor associated microglia and macrophages.

We found that microglia that are closely associated with glioblastoma cells have significantly reduced expression of sense genes⁷ suggesting a reduced ability to sense tumor cells and reduced expression of genes potentially involved in tumor killing. In contrast, these microglia have enhanced expression of genes involved in phagocytosis and debris clearance. The immunosuppressive Interleukin 4 (IL4) and Interleukin 10 (IL10) and several genes of the Interleukin 6 (IL6)/STAT3 and Interferon- γ (IFN γ) pathways, all of which could favor tumor growth, were upregulated.

To understand the mechanism(s) by which glioblastoma cells influence microglial transcriptional networks, and since microglial gene expression and phenotype in neurodegenerative diseases have been shown to be regulated by several immune checkpoints, including a TREM2 and a possible TREM2/APOE pathway^{23,24}, we compared the transcriptomes of glioblastoma-associated microglia with those of microglia from *Trem2*^{-/-} and *ApoE*^{-/-} mice. We found that *Trem2* indeed regulates expression of several microglial genes, however the changes noted in glioblastoma-associated microglia were divergent from those observed in *Trem2*^{-/-} microglia. Furthermore, we did not observe significant differences in tumor growth between tumors implanted in wild type compared to those implanted in *Trem2*^{-/-} mice. In contrast, these glioblastoma-associated changes in microglia paralleled *ApoE*-dependent changes. Contrary to a possible single TREM2/APOE pathway recently identified in neurodegenerative diseases²⁴, our findings define a *Trem2*-independent, likely *ApoE*-dependent microglial transcriptional network hijacked by glioblastoma that could promote tumor growth.

Results

Diffuse microglia and macrophage infiltration in glioblastoma.

To identify immune cells that had taken up EV-GFP (**Figure 1A**), we implanted syngeneic mouse glioma cells, GL261.BpalmGFP (**Suppl. Figure 1A**) or carrier fluid in adult C57BL6.CCR2^{RFP/WT} mice that express red fluorescent protein (RFP) in peripheral blood monocytes and monocyte-derived macrophages, but not in microglia²⁵. Four weeks following implantation, the mice were euthanized and the brains used for immunofluorescent staining of brain sections or for FACS of brain cells. Using this model, tumor cells express GFP, microglia are labeled with antibodies to IBA-1, and recruited monocytes and macrophages express RFP (**Figure 1B and C** and **Suppl. Figure 1B**). Microglia and monocytes/macrophages that are closely interacting with glioblastoma cells are positive for IBA-1 and RFP, respectively (**Figure 1B**). Confocal microscopy and 3-dimensional reconstruction confirmed that EV-GFP particles are found inside microglial cells labeled with IBA-1 (**Figure 1C** and **Suppl. Video S1**).

For FACS, we generated highly enriched microglia, monocyte and macrophage populations from the brains of tumor-bearing and control mice using an established protocol for cell dissociation, isolation and analysis^{7,26}. Microglia were sorted based on levels of CD11b and CD45 (**Figure 1D**). Monocytes and macrophages were separated by additional staining for F4/80 and LY6C, as well as by expression of CCR2-RFP (not shown). Microglial cells were isolated from brains injected with only carrier fluid (control), GL261 or GL261.BpalmGFP tumor cells. Microglia were then sorted based on their level of GFP fluorescence to separate cells that had taken up tumor-derived EV-GFP from those that had not (**Figure 1D**). The GFP cut-off was determined by comparing the relative GFP intensity detected in our target cell subsets isolated from brains injected with GL261 wild type (no GFP) to brains injected with GL261.BpalmGFP (**Figure 1D**). By separately analyzing the tumor area, as well as the remaining ipsilateral and the contralateral side of the brain (**Figure 1E**), EV-GFP positive (EV-GFP^{pos}) microglia were only found within and immediately adjacent to the tumor, confirming that the EV-GFP^{pos} microglia are closely associated with tumor cells (**Figure 1F**). Total RNA was isolated and sequencing libraries were made using SMARTer Ultra Low Input RNA Kit. Sequencing was done using an Illumina NextSeq and bioinformatic analysis was performed using DESeq2 in R²⁷. Using this approach, we generated a comprehensive dataset with comparative transcriptomes of control microglia (carrier-injected mice), glioblastoma-associated EV-GFP^{pos} microglia and monocytes/macrophages, and

glioblastoma EV-GFP^{neg} microglia and monocytes/macrophages. Initial analysis showed marked differences between EV-GFP^{pos} tumor-associated microglia and EV-GFP^{neg} microglia (**Figure 1G**), and lesser differences between EV-GFP^{pos} and EV-GFP^{neg} monocytes/macrophages (**Figure 1G** and **H**). Based on this finding we focused subsequent analysis on microglia. Normalized expression counts and differential expression data available for all genes passing quality metrics are available in **Suppl. Table S1**. When analyzing the highest expressed genes in the control, EV-GFP^{neg} and EV-GFP^{pos} microglia, multiple established microglia genes such as *Cx3cr1*, *HexB* and *P2ry12* were among the most highly expressed genes⁷ (**Suppl. Table S1**).

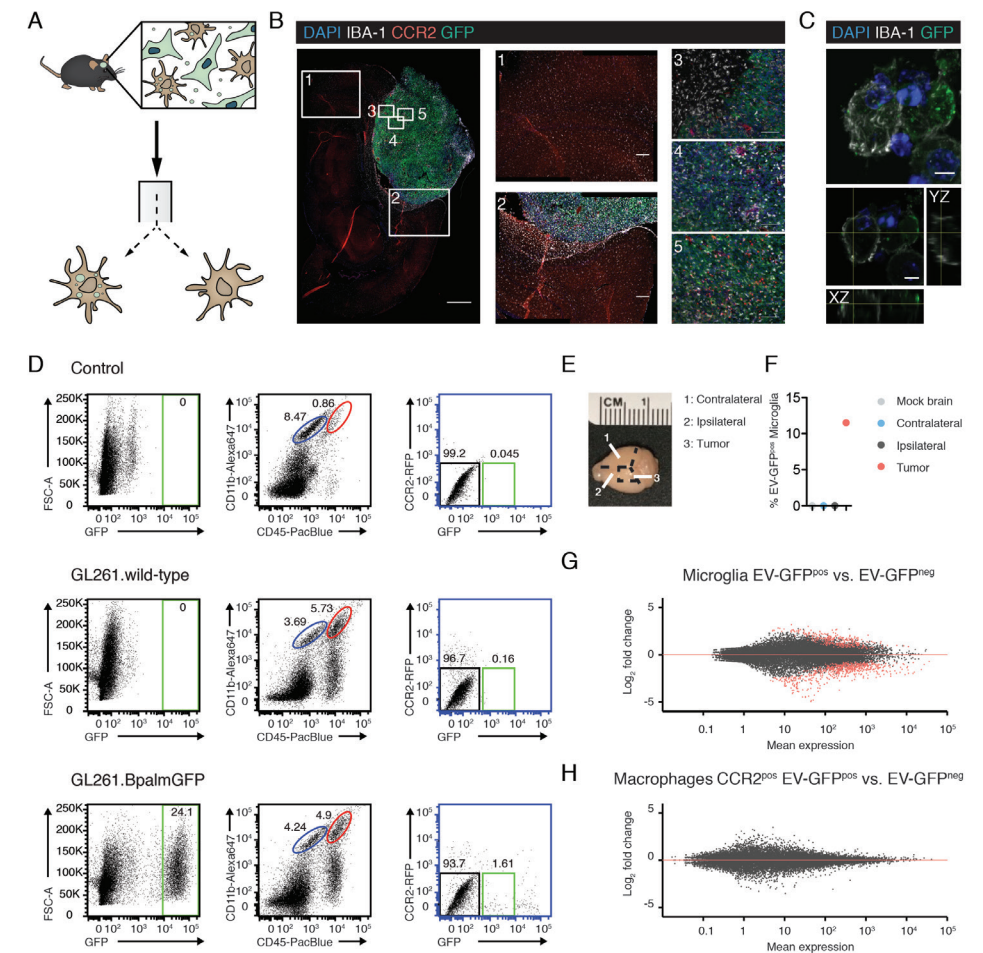


Figure 1. Glioblastoma-associated microglia and monocytes/macrophages internalized EV-GFP (A) A schematic illustrating our model of C57BL6.CCR2^{RFP/WT} mice implanted with GL261.BpalmGFP glioma cells that release palmGFP fluorescent extracellular vesicles (EVs). Four weeks after tumor implantation, brains were harvested and microglia, monocytes and macrophages were sorted based on cell specific antigens and EV-GFP uptake. (B) IBA-1 positive microglia were present throughout the brain (1) and infiltrated the GFP-positive tumor (2-5). CCR2-positive (RFP-labeled) myeloid-derived cells infiltrated the tumor, but were mostly absent in other parts of the brain (1). See Suppl. **Figure 1 B** for single color channel images (C) Confocal microscopy images show that EV-GFP particles were taken up by IBA-1 positive microglia (refer to Suppl. Video S1 for a 3D projection). (D) Microglia were identified as CD11b^{high}/CD45^{med} cells (dark blue gate). Microglia were then sorted based on the GFP signal detected as the upper limit in the control (no tumor) and GL261 wild-type (no GFP) implanted mice. Only in mice implanted with GL261.BpalmGFP, a population of GFP-positive microglia was identified (green gate in the GFP/CCR2 plot). (E) Delineation of brain areas separated for microglial isolation in F. (F) Only microglia isolated from the tumor contained EV-GFP. Results from a representative experiment shown. (G) MAplot shows 384 significantly up- or downregulated genes plotted in red when comparing EV-GFP^{pos} to EV-GFP^{neg} microglia. (H) MAplot shows that uptake of EV-GFP did not alter gene expression in CCR2^{pos} macrophages. Scale bars: (B) 1000µm, 1-2;200µm, 3-5;100µm (C) 5µm.

Correlation between gene and protein expression levels.

To determine if differential RNAseq expression correlated with differential protein levels, we performed immunofluorescent staining for IBA-1, CD68, CD74 and ARG1 comparing the level in microglia from control brains versus tumor-bearing brains. No significant differences between control microglia, EV-GFP^{neg} and EV-GFP^{pos} tumor microglia were detected at the RNA-level for signature genes, *Iba1* and *Cd68* (**Figure 2A**). In contrast, *Cd74* transcripts were significantly elevated in EV-GFP^{pos} tumor microglia (\log_2 fold-change: 5.92), and to a lesser extent in EV-GFP^{neg} tumor microglia (\log_2 fold-change: 5.35) as compared to control microglia. Similarly, *Arg1* transcripts are significantly and highly enriched compared to control microglia in EV-GFP^{neg} tumor microglia (\log_2 fold-change: 6.80) and even more so in EV-GFP^{pos} tumor microglia (\log_2 fold-change: 8.16). To test if changes in the levels of RNA correlated with changes at the protein levels, we performed semi-quantitative immunofluorescent staining for IBA-1, CD68, CD74 and ARG1 on brain sections containing GL261.BpalmGFP tumor or control brain. We found that, as seen with RNA levels, IBA-1 protein levels were not different, whereas both CD74 and ARG1 protein levels were significantly upregulated in tumor-associated microglia compared to control microglia (**Figure 2B** and **C**). Unlike for *Cd68* RNA, which showed no change, CD68 protein showed a small, but significant increase in tumor-associated microglia. Overall these results showed a strong correlation between RNA and protein levels and are in line with our previous results⁷. Of note, CD74 is a receptor for macrophage migration inhibitory factor (MIF)²⁸. Inhibition of MIF-CD74 signaling promotes macrophage activation leading to tumor cell death in several tumor models, including gliomas²⁹. Similarly, ARG1 also promotes tumor growth and suppresses antitumor immune responses³⁰. These data confirm that glioblastoma-associated microglia upregulate specific genes and their corresponding proteins that have the potential to promote tumor growth.

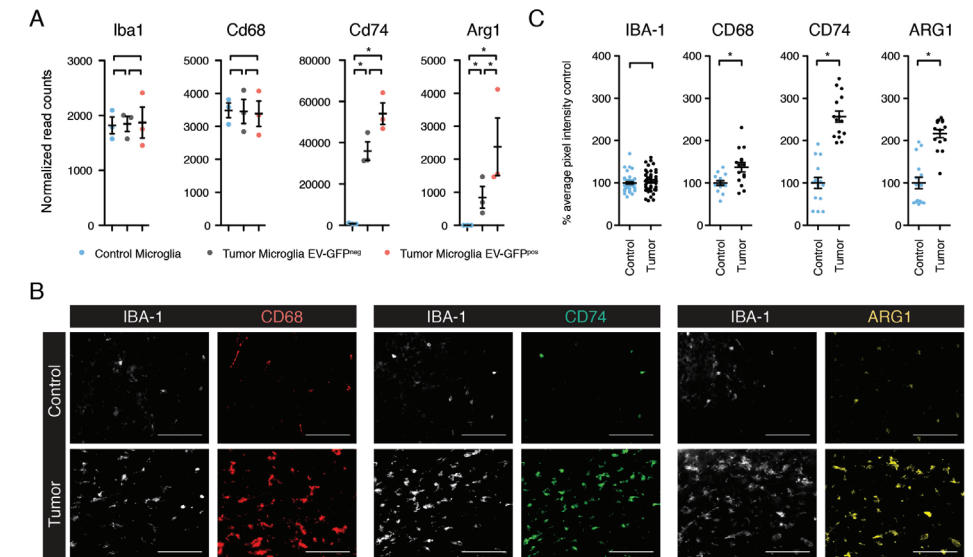


Figure 2. RNA levels correlated with protein levels in control and tumor-bearing brains. (A) The microglial marker *Iba1* and the microglia/monocyte/macrophage marker *Cd68* were equally expressed in control and tumor-associated microglia, whereas *Cd74* and *Arg1* expression was increased in tumor-associated microglia as measured by RNAseq. **(B)** Immunofluorescence staining of IBA1, CD68, CD74 and ARG1 in control and tumor-bearing mouse brains. **(C)** Quantification of immunofluorescent staining seen in **(B)** Fluorescent intensity was quantified per pixel within identified cells. Tumor and control tissues were individually compared for each marker. IBA1, CD74 and ARG1 fluorescence quantification correlated with RNA data whereas CD68 was only slightly upregulated at the protein level, but unchanged at the RNA level. Scale bars 100 μ m, asterisk indicates multiple testing adjusted p-value <0.05, error bar represents SEM.

EV-GFP^{pos} microglia represent the most influenced tumor-associated microglia.

Unsupervised clustering of the top 750 most differentially changed genes showed a clear separation of microglia from control versus tumor-bearing mice, as well as a separation based on GFP status of microglia in tumor-bearing mice (**Figure 3A**). When plotting the differential expression for all genes, comparing expression of EV-GFP^{neg} as well as EV-GFP^{pos} versus control microglia, we found that for most genes differential expression was stronger for EV-GFP^{pos} than EV-GFP^{neg} versus control microglia (**Figure 3B**). Expression of 380 genes was significantly changed in both EV-GFP^{neg} and EV-GFP^{pos} microglia compared to control microglia. In contrast, 2242 genes were significantly changed only in EV-GFP^{pos} microglia (but not in EV-GFP^{neg} microglia) compared to control. (**Figure 3B**). Comparison of differential expression between EV-GFP^{pos} versus EV-GFP^{neg} or control microglia, showed that most genes that are significantly altered

in EV-GFP^{pos} versus EV-GFP^{neg} microglia are also significantly changed in EV-GFP^{pos} versus control microglia (**Figure 3C**). Genes upregulated in both comparisons often showed a higher differential expression for EV-GFP^{pos} compared to control than to EV-GFP^{neg} microglia indicating an EV-effect as well as a generic tumor effect other than EV-GFP uptake (**Figure 3C**). Comparing EV-GFP^{neg} to either EV-GFP^{pos} or control microglia confirmed these results (**Figure 3D**). Evaluation of overlap between the top 750 genes expressed by the three sets of microglia showed mostly unique genes expressed by either control or EV-GFP^{pos} microglia with EV-GFP^{neg} microglia being in-between (**Figure 3E**). This analysis indicates that EV-GFP^{pos} microglia represent a subset of microglial cells that are most influenced by the tumor.

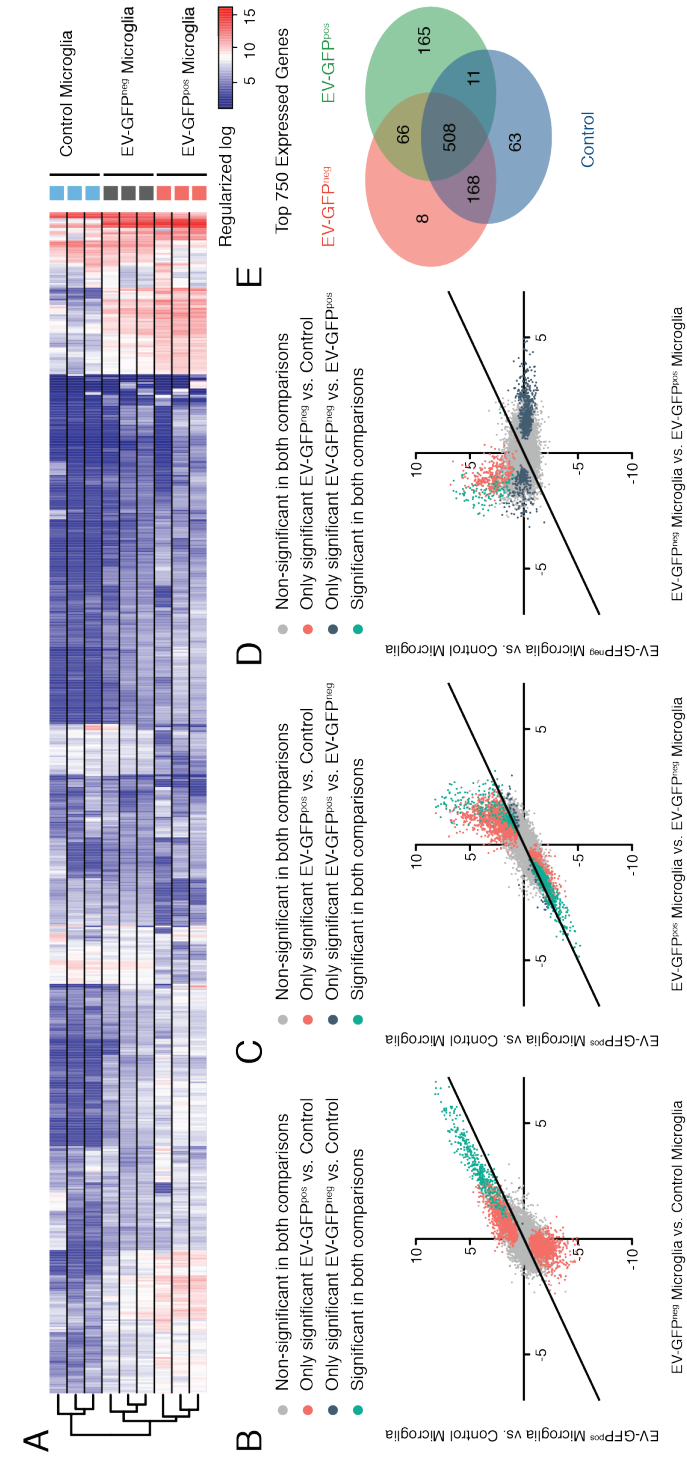


Figure 3. More changes in gene expression were seen in EV-GFP^{pos} compared to EV-GFP^{neg} tumor-associated microglia. (A) In unsupervised clustering microglia cluster together based on tumor status and EV-GFP uptake status. (B) Comparative analysis of differential expression levels of EV-GFP^{pos} and EV-GFP^{neg} microglia compared to control microglia showed 380 shared significantly upregulated genes (green). Overall, the differential expression was higher for EV-GFP^{pos} microglia. These microglia expressed 1426 significantly upregulated and 1196 downregulated genes (red). (C) Most genes significantly changed between EV-GFP^{pos} and EV-GFP^{neg} microglia were also significantly altered in EV-GFP^{pos} microglia compared to control. (D) These patterns were confirmed in the comparisons of EV-GFP^{neg} to either EV-GFP^{pos} or control. (E) Venn diagram showed overlap between top 750 expressed genes. EV-GFP^{neg} tumor microglia shared most genes with control microglia and EV-GFP^{pos} tumor microglia. This confirmed that EV-GFP^{pos} microglia represent the most altered tumor-associated phenotype.

Effect of glioblastoma cells on genes involved in key microglial functions.

To determine the effects of glioblastoma cells on the three essential microglial functions - sensing, host defense and homeostasis- we mined our dataset for genes and pathways involved in each of these functions. To encourage others to explore our data, we setup an online tool that interactively displays all (differential) expression data as well as functional and pathway related information for each gene at www.glioma-microglia.com (temporary password "Microglia1").

Sensing. The ability to sense changes in the cellular environment in the brain is a major microglial function that allows these cells to adapt to and influence the changing milieu^{31,32}. The armamentarium of 100 genes that allow microglia to perform such functions is termed the sensome⁷ (**Suppl. Table S2**). These include pattern recognition receptors (25%), receptors involved in cell-cell interaction (10%), chemoattractant and chemokine receptors (10%), cytokine receptors (10%), Fc receptors (7%), purinergic receptors (8%), receptors for extracellular matrix (ECM) proteins (6%), other receptors or transporters (13%) and potential sensome proteins with no known ligands (11%)⁷. Interestingly, we found significant differential gene expression in only 4% of sensome genes when comparing EV-GFP^{neg} to control microglia (**Figure 4A** and **Suppl. Table S2**). These genes (e.g. *Cd74*, *Clec7a*, *Cxcl16* and *Fcgr4*) were all upregulated compared to control microglia. In contrast, we found significant changes in gene expression between EV-GFP^{pos} versus EV-GFP^{neg} and control microglia in 57% of sensome transcripts. Remarkably 48% of sensome genes were downregulated in EV-GFP^{pos} microglia and only 9% upregulated (**Figure 4A**).

Similar to EV-GFP^{neg} microglia, *Cd74*, *Clec7a*, *Cxcl16*, *Fcgr4*, *Ccr12*, *Cd22*, *Cd52*, *Fcgr2b* and *Pilra* RNAs were significantly upregulated in EV-GFP^{pos} microglia compared to control microglia. As discussed, CD74 signaling has been shown to suppress macrophage activation and subsequent tumor killing and promote tumor growth in gliomas and several other tumor models²⁹. In pancreatic ductal carcinoma, cancer derived EVs deliver MIF (a binding factor for the CD74 receptor) protein to Kupfer cells in the liver to induce a pre-metastatic niche, promoting metastasis to the liver³³. Similar to macrophage suppression, CLEC7A binds the s-type lectin galectin 9 (LGALS9) expressed by pancreatic ductal carcinoma cells leading to accelerated progression of this tumor³⁴, and LGALS9 has also been shown to be expressed by glioblastoma cells³⁵. *Cxcl16* is significantly upregulated in both EV-GFP^{neg} and EV-GFP^{pos} microglia (log₂ fold-change 1.23 and 2.06, respectively). CXCL16 is a chemokine that binds to its receptor (CXCR6)

expressed on highly active glioma stem cells³⁶. Because CXCL16-CXCR6 interactions induce glial cell migration³⁷, this pathway could enhance microglia-induced glioma stem cell migration and subsequent tumor cell invasion. These data suggest that sensome genes that are upregulated in microglia which have taken up tumor-EVs could promote enhanced tumor growth and progression.

Sensome transcripts that were downregulated in EV-GFP^{pos} compared to EV-GFP^{neg} and control microglia can be divided into three groups. Group one includes transcripts encoding proteins that directly mediate microglia-glioblastoma cellular interactions. Indeed, Sialic-acid-binding immunoglobulin-like lectin-H (*Siglech*) is a CD33-related Siglec that is a microglial sensor of glioma cells³⁸. *Siglech* is significantly downregulated in EV-GFP^{pos} compared to EV-GFP^{neg} and control microglia (log₂ fold-change -1.84 and -1.97, respectively) (**Figure 4B**). Interestingly, *Cd33* is also significantly downregulated in EV-GFP^{pos} compared to EV-GFP^{neg} and control microglia (log₂ fold-change -1.62 and -1.72, respectively) (**Figure 4B**). It is not known if CD33, like SIGLECH is also a sensor of glioblastoma cells. Another microglial receptor that is capable of sensing lysophosphatidylserine exposed on glioblastoma cells is GPR34^{39,40}. Similar to *Siglech*, *Gpr34* is downregulated in EV-GFP^{pos} compared to EV-GFP^{neg} and control microglia (log₂ fold-change -1.96 and -2.37, respectively). These data indicate that EV-GFP^{pos} microglia, but not other microglia in the same tumor-bearing brain, have reduced expression of at least two transcripts, encoding the proteins SIGLECH and GPR34, known to directly sense ligands expressed on glioblastoma cells.

A second group of transcripts that is downregulated in EV-GFP^{pos}, but not in EV-GFP^{neg} microglia includes those encoding proteins that sense metabolic products potentially released by glioblastoma cells. These transcripts include *Gpr183*, *Adora3*, *Il6ra*, *Cx3cr1*, *P2ry12*, *P2ry13*, *Csf1r* and *Csf3r* (**Figure 4C-E**). GPR183 is a sensor for oxysterols, which are released by glioblastoma cells and play a role in recruitment of immune cells⁴¹. ADORA3 is a sensor for adenosine that is released by glioblastoma cell ectonucleotidases. Adenosine promotes tumor growth, can activate toll-like receptors (TLRs) and induce microglial responses via an ADORA3-dependent mechanism⁴². IL6Ra is a receptor for IL6, and elevated levels for IL6 are found in glioblastomas and have been associated with poor survival in glioblastoma patients⁴³. The expression of CX3CR1, the receptor for fractalkine was also decreased and loss of CX3CR1 has been shown to promote gliomagenesis⁴⁴. P2RY12 and P2RY13, purinergic receptors for ATP, which is an important signaling molecule in the CNS, are both down. This

could promote tumor growth by two different pathways. First, necrosis, one of the hallmarks of glioblastoma, liberates nucleotides into the extracellular milieu. These nucleotides are hydrolyzed very slowly by glioblastomas and induce neuronal cell death and glioblastoma proliferation⁴⁵. Second, extracellular ATP activates microglia P2RY12 receptors that are utilized to trigger an acute inflammatory response in microglia via rapid CCL3 induction after ADP stimulation⁴⁶. Therefore, downregulating microglial receptors for ATP could preserve the ability of the nucleotides to promote tumor growth, while reducing the ability of microglia to respond to the tumor, thereby further enhancing the tumor's advantage.

It is not clear if all downregulation of metabolic sensing genes is tumor supportive. *Csf1r*, encoding a receptor for CSF1 is downregulated, but CSF1R blockade has been shown to suppress glioma progression⁴⁷. However, this observed effect of CSF1R blockade is likely mediated by tumor infiltrating macrophages, not microglia⁴⁷. Interestingly, resistance to CSFR1 blockade is observed in 50% of mice treated with a CSFR1 inhibitor and is mediated by microglia/macrophage-derived insulin-like growth factor-1 (IGF1)⁴⁸. *Igf1* RNA is significantly upregulated in both EV-GFP^{neg} and EV-GFP^{pos} microglia (log2fold 3.06 and 4.54, respectively). These data suggest that while CSF1R downregulation may be associated with suppression of glioma growth by macrophages, such effect could be counterbalanced by upregulation of microglial IGF1.

A third group of transcripts that were downregulated or unchanged include some that have been identified as playing a role in tumor suppression, such as that encoding the antimicrobial peptide lactotransferrin (*Ltf*)⁴⁹, and those whose effect on glioblastoma remains to be elucidated. The latter include *Tmem8c*, *C5ar1*, *Tmem37*, *Gpr84*, *Ly86*, *Cd180*, *Slc2a5*, *Tmem119*, *Slco2b1*, *Cmtm7* and *Tlr13* (Figure 4F).

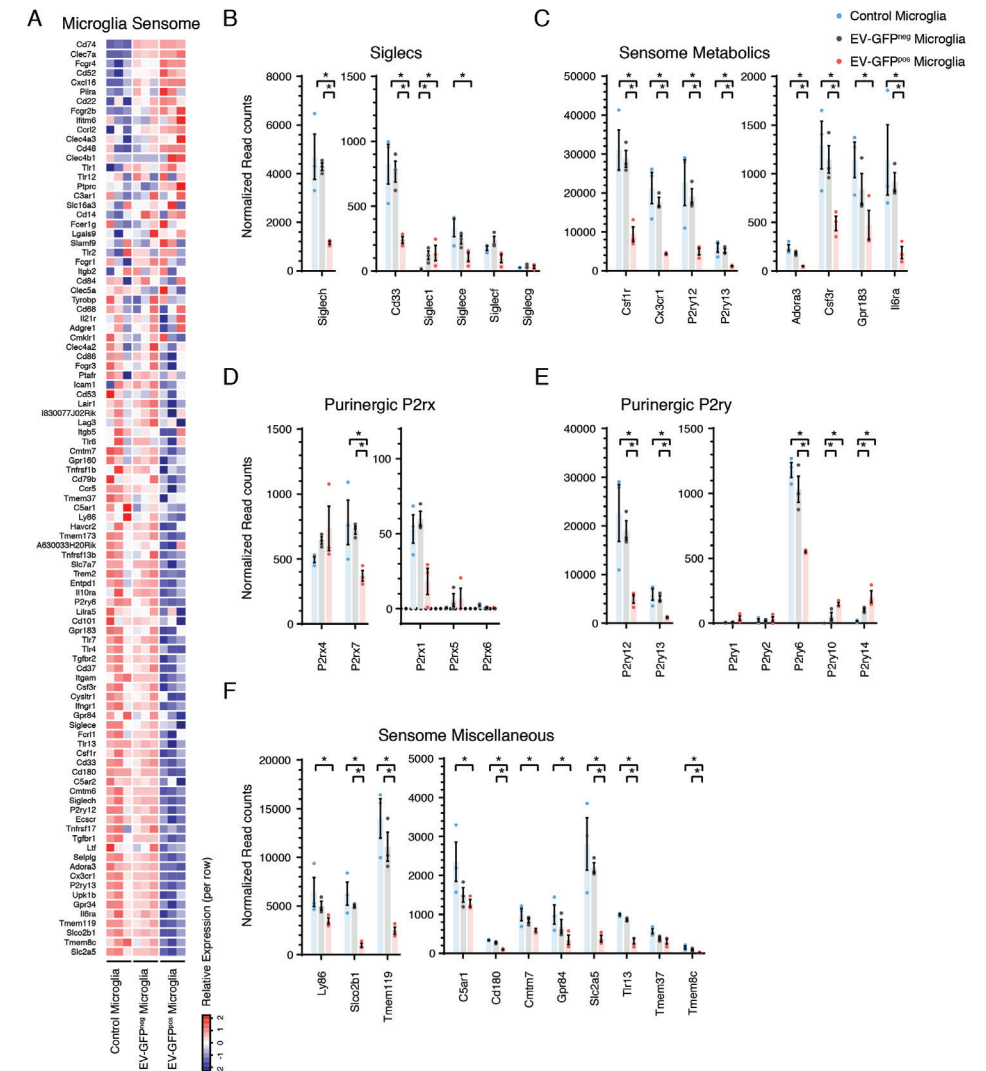


Figure 4. Microglia sensome genes involved in danger sensing were downregulated in EV-GFP^{pos} microglia. (A) EV-GFP^{pos} tumor microglia showed significantly reduced levels of 57% of microglial sensome genes compared to EV-GFP^{neg} indicating reduced capability of sensing of tumor cells and tumor-derived danger signals in EV-GFP^{pos} microglia. (B) Normalized read counts of Siglecs, involved in direct glioblastoma-microglial cellular interactions, showed significant downregulation of Cd33, Siglece and Siglech in (EV-GFP^{pos}) tumor associated-microglia whereas only Siglec1 was upregulated. (C) Seven out of eight sensome genes involved in the sensing of metabolic signals, were significantly downregulated in EV-GFP^{pos} tumor microglia. (D and E) Purinergic P2rx (D) and P2ry (E) genes showed significant changes for P2rx7, P2ry6, P2ry10, P2ry12, P2ry13 and P2ry14. (F) Multiple microglial genes with known tumor suppressive function were downregulated or unchanged in EV-GFP^{pos} microglia. Asterisk (*) indicates significant (multiple testing adjusted p-value < 0.05) differential expression. Error bar represents the SEM, bar represents the mean and dots display individual measurements (n=3).

Host defense. An important macrophage and microglial function is host defense against viral, bacterial, fungal and parasitic infections, but also against tumor cells⁵⁰. We mined our dataset for microglial genes involved in this function. Interestingly, in contrast to what we found with sensome genes, changes in several genes involved in host defense were associated with the presence of glioblastoma, but not specifically with uptake of glioblastoma derived-EVs. IFITMs are interferon-induced transmembrane proteins involved in the host response against viral infections, such as influenza, Dengue virus, Ebola virus, flaviviruses, SARS coronavirus and other⁵¹. *Ifitm1-3* RNAs are upregulated in glioblastoma microglia regardless of whether they took up glioblastoma EVs or not (**Figure 5A**). It is not known whether IFITMs play a role in the host response to tumor cells.

Major histocompatibility complex II (*Mhc-II*) genes encode cell surface proteins that are involved in binding to antigens derived from pathogens and presenting these antigens to T-cells. We found that several MHC-II transcripts are upregulated in glioblastoma microglia independent of glioblastoma EV uptake (**Figure 5B**). The roles of these genes in glioblastoma-microglial interaction remains unclear in the generally immune suppressive environment of brain tumors.

Interactions of the programmed cell death 1 receptor (PD1) on activated T-cells with its ligands programmed death ligand 1 and 2 (PD-L1 and 2) maintain immunologic tolerance through the suppression of auto-reactive T-cells⁵². PD-L1 and PD-L2 are expressed on antigen-presenting cells, as well as on tumor cells including glioblastoma^{53,54}. As expected very little *Pd1* RNA was expressed in microglia as it is usually expressed on T cells⁵⁵. However increased expression of *Pd-11* and *Pd-12* transcripts was higher in EV-GFP^{pos} as compared to EV-GFP^{neg} microglia with both being significantly higher than for control microglia (**Figure 5C**). These data identify another pathway by which glioblastoma can possibly evade the immune system, by altering microglia to suppress T cell activation through modulation of T cell immune checkpoints. This finding gains added importance as PD1/PD-L1 directed immune checkpoint therapy is being used against a number of peripheral tumors.

Homeostasis. The role of microglia in maintaining homeostasis in the brain includes debris breakdown and removal by matrix metalloproteases (Mmp)⁷. These enzymes could also play an important role in promoting tumor growth by making space for tumor cells to migrate, invade and proliferate^{9,14,15}. In glioblastoma MMP2 serves as

an important MMP to degrade the extracellular matrix (ECM) subsequently enabling the invasive properties of glioma⁵⁶. MMP2 is secreted by glioblastoma cells in a pro-form (pro-MMP2) which needs to be cleaved by Mmp14 (MT1-MMP) to be active^{14,15}. Tumor microglial cells are an important source of MMP14^{14,15}. Previously we showed that microglia *Mmp14* levels are increased after uptake of glioblastoma-derived EVs *in vitro*²⁰. Here, *in vivo*, *Mmp14* was among the three *Mmps* (*Mmp12*, *Mmp13* and *Mmp14*) that were significantly upregulated in EV-GFP^{pos} and to a lesser extent in EV-GFP^{neg} microglia (**Figure 5E**). Since only tumor cells secrete MMP2, no changes in *Mmp2* were detected in microglia. These data indicate that glioblastoma alters microglial gene expression patterns in a manner that could favor tumor spread and migration by clearing debris and digesting the ECM in the tumor microenvironment.

In addition to changes in *Mmps*, we also found that glioblastoma was associated with an increased expression of the RNAs encoding microglial phagocytic receptors - *Cd93*, *Msr1*, *Cd36*, *Olr1*, *Megf10*, *Clec7a*, and *Scarf1* (**Figure 5D**). The roles of these phagocytic receptors in promoting debris clearance and subsequent tumor growth have not been investigated. However, since these receptors promote clearance of apoptotic cells⁵⁷, it is plausible that these receptors, in conjunction with *Mmps*, promote the phagocytic clearance of debris in the tumor environment further facilitating tumor spread.

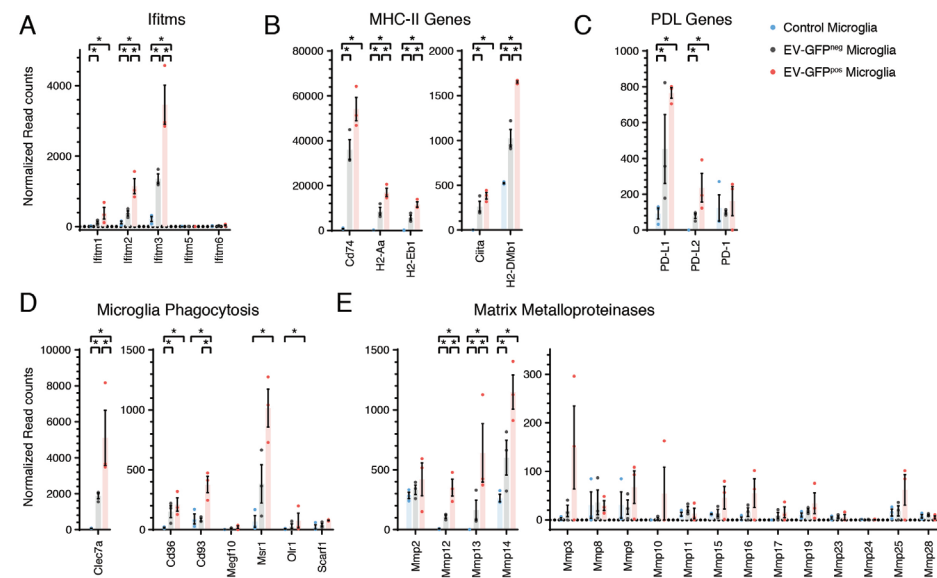


Figure 5. Tumor-associated microglia express increased levels of IFITMs, major histocompatibility complex II, immune checkpoint, phagocytic and specific matrix metalloproteinase transcripts. (A) Interferon-induced transmembrane (IFITM) genes were upregulated in tumor-associated microglia. (B) MHC class II genes were significantly upregulated in tumor-associated microglia. (C) Programmed death ligand 1 and 2 (Pd-L1 and Pd-L2) were significantly upregulated in tumor-associated microglia. (D) Genes involved in phagocytic activity in microglial cells were upregulated. *Cd93* and *Clec7a* were significantly higher in EV-GFP^{pos} than EV-GFP^{neg} microglia. (E) Matrix metalloproteinase (MMPs) were upregulated in tumor microglia. *Mmp12*, *Mmp13* and *Mmp14* were significantly upregulated tumor supportive genes. Asterisk (*) indicates significant (multiple testing adjusted p-value < 0.05) differential expression. Error bar represents the SEM, bar represents the mean and dots display individual measurements (n=3).

Cytokine pathways

The concept that microglia are activated to either an “M1” (INF γ stimulated) or “M2” (IL4 stimulated) state is actively debated in current literature^{5,58}. However, it is obvious that mononuclear phagocytes respond to different stimuli differently and cannot be “boxed” into an M1 or M2 phenotype^{3,5,58,59}. We analyzed our dataset to determine if glioblastoma affects microglial cytokine pathways *in vivo*. We focused on five pathways regulated by IL4, IL10, INF γ , IL6/STAT3 and TGF- β . These sets of immune related genes, feature mostly unique genes, however some level of overlap between the sets as well as with the microglial sensome is observed (Suppl. Figure S2 and Suppl. Table S2).

The IL4 pathway is involved in resolution of inflammation, tissue repair and healing and in promoting pro-tumor activities in macrophages and microglia⁶⁰. We found that genes in the IL-4 pathway are mostly upregulated in EV-GFP^{pos} microglia and to a lesser

degree in EV-GFP^{neg} microglia (Figure 6A and Suppl. Table S2). These upregulated transcripts include several genes that are known to have tumor-enhancing properties in glioblastoma, including ECM degradation proteins, such as *Adam19* and *Mmp12*, which were upregulated in EV-GFP^{neg} and EV-GFP^{pos} microglia compared to control (log₂ fold-change 3.21 and 5.05, respectively). ADAM19 is a transmembrane metallopeptidase that is upregulated in glioblastoma, with increased levels correlating with more invasiveness⁶¹. RNA for the chemokine *Ccl22* is also highly upregulated in EV-GFP^{pos} microglia (log₂ fold-change 5.31). CCL22 preferentially attracts immunosuppressive regulatory T-cells to glioblastoma⁶² and as such could facilitate a more pronounced immune suppressive state within glioblastoma tumors. *Wnt5a*, one of the IL4-related genes in our set, was recently found to be a major driver of glioblastoma stem cell differentiation and angiogenesis⁶³. Our results show that EV-GFP^{pos} microglia may be an alternative source for WNT5A, as its expression is significantly upregulated only in these microglia (log₂ fold-change 3.24 to control microglia) (Figure 6A).

Similarly, IL10 has been shown to be associated with inhibition of T cell effector functions⁶⁴⁻⁶⁶ thereby facilitating tumor progression. Similar to IL4, IL10-associated genes were significantly upregulated in EV-GFP^{neg} microglia and more so in EV-GFP^{pos} microglia (Figure 6B and Suppl. Table S2). Upregulated transcripts within this gene set include several genes involved in migration and microglial activation (e.g. *Cxcl16*). Superoxide dismutase 2 (SOD2) is a mitochondrial antioxidant enzyme and is one of the IL10-related genes only significantly upregulated in EV-GFP^{pos} microglia. SOD2 increases tolerance to oxidative stress and reduces the level of pro-inflammatory cytokines, which could benefit the tumor⁶⁷ (Figure 6B).

The IL6/STAT3 signaling pathway, comprising 83 genes involved in activation of the inflammatory responses, was overall upregulated in EV-GFP^{pos} microglia (Figure 6C and Suppl. Table S2). IL6, a pro-inflammatory cytokine, is correlated with enhanced glioblastoma cell invasion⁶⁸. It has been shown that this cytokine is also required for glioma development and targeting this cytokine using an IL6 knockout model, reduced stem cell survival and tumor growth^{69,70}. Other members of this signaling pathway that are significantly upregulated in EV-GFP^{pos} microglia compared to both control and EV-GFP^{neg} microglia are *Ccl7* and *Cd38*. CCL7 (MCP-3) is a secreted chemokine and has been reported to attract CD68-positive microglia and macrophages to glioblastoma⁷¹. Thus, microglial cells most closely associated with the tumor have a transcriptional profile that favors the infiltration of more microglia and macrophages to the tumor, potentially creating a tumor supportive loop (log₂ fold-change to control and EV-GFP^{neg}

microglia 2.66 and 1.24, respectively). *Cd38* encodes another IL6-related cell surface glycoprotein upregulated in EV-GFP^{pos} to control and EV-GFP^{neg} microglia (log₂fold 3.01 and 1.73 respectively). In a mouse glioblastoma model CD38 deficiency has been associated with increased survival and decreased levels of MMP12, thus suggesting a tumor supportive role for this gene⁷² (**Figure 6C**).

Another key cytokine involved in tumor immunity is IFN γ , which activates cytotoxic lymphocytes to induce tumor killing and prevent tumor progression. However, IFN γ has a dual role in cancer, stimulating certain tumor supportive mechanisms as well as inhibiting others⁷³. We found very low expression of IFN γ in control microglia whereas both EV-GFP^{neg} and EV-GFP^{pos} microglia show significantly upregulated levels of IFN γ compared to control (log₂ fold-change 3.52 and 5.58 respectively). Overall expression of the IFN γ -associated genes was highly elevated in tumor-associated microglia (**Figure 6D** and **Suppl. Table S2**). Interestingly, among IFN γ -associated transcripts that were significantly altered, we found several tumor-supportive as well as tumor-suppressive genes. For example, IL-1 β signaling has been described to induce several tumor supportive responses in glioblastoma⁷⁴. In contrast, both EV-GFP^{neg} and EV-GFP^{pos} microglia significantly upregulated *Il1rn* which encodes for the IL-1 receptor antagonist protein, suggesting a tumor-suppressive function. Multiple tumor supportive genes are also significantly upregulated in the IFN γ geneset including genes previously discussed (i.e. *Pd-1* (*Cd274* gene), *Ccl22* and *Cd38*). Interferon regulatory factor 7 (*Irf7*) is a key regulator of the interferon response and the pro-inflammatory to anti-inflammatory switch in microglia⁷⁵. Overexpression of *Irf7* in microglia induced glioblastoma growth and stemness⁷⁶ and IL6 secretion by glioblastoma cells. We found that *Irf7* expression is significantly upregulated in both EV-GFP^{neg} and EV-GFP^{pos} microglia (log₂fold 4.51 and 5.53 respectively), suggesting an important IRF7 tumor-supportive axis in EV-GFP^{pos} microglia.

Overall, analysis of the cytokine signatures in our dataset shows that several tumor-supportive genes belonging to multiple cytokine-related pathways are upregulated in glioblastoma-associated microglia *in vivo* indicating a more complicated profile than the binary M1/M2 classification. It is important to note here that while individual genes in each pathway are important, we need to take into consideration the overall direction into which the pathway changed. For example, for each of the IL4, IL10, IL6/STAT3 and IFN γ cytokine sets between 65.9 and 76.6% of genes were upregulated in EV-GFP^{pos} microglia compared to control (**Suppl. Table S2**)

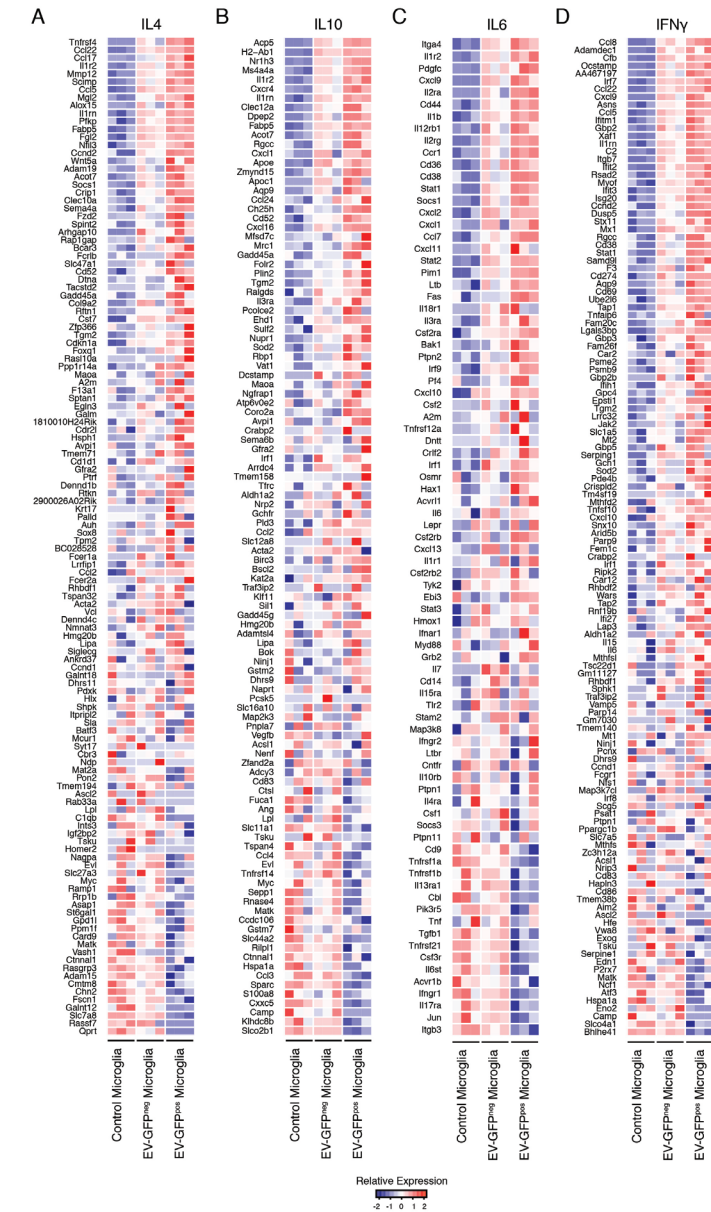


Figure 6. IL4, IL10, IL6 and IFN γ pathway genes were upregulated in tumor-associated microglia. (A) The IL4 associated genes were mostly upregulated in tumor-associated microglia with increased expression in EV-GFP^{pos} microglia. The significantly upregulated genes in EV-GFP^{pos} versus EV-GFP^{neg} microglia included known tumor supportive genes such as *Mmp12*, *Adam19* and *Wnt5a*. (B) IL10 related genes were upregulated in tumor microglia. *Sod2*, a tumor supportive gene, was among the genes significantly upregulated in EV-GFP^{pos} microglia. (C) IL6 related genes were upregulated in tumor-associated microglia. Among the significantly upregulated IL6 genes is *Ccl7* (MCP-3), a secreted chemokine involved in the attraction of microglia and macrophages to the tumor suggesting a tumor supportive infiltration loop. (D) Overall, increased expression of IFN γ related genes was observed with the strongest expression in EV-GFP^{pos} microglia. Among the significantly upregulated genes in EV-GFP^{pos} microglia was *Irf7*, a key regulator of pro-inflammatory to anti-inflammatory switching in microglia.

Pathways controlling microglial transcriptional networks

TGF- β regulates the microglial homeostatic phenotype²⁴⁻⁷⁷. In cancer, TGF- β plays a dual role with both tumor suppressive functions by reduction of cellular proliferation, as well as tumor supportive functions including the stimulation of invasive migration, angiogenesis and immune suppression⁷⁸. We found that only in EV-GFP^{pos} microglia both *Tgf- β 1* and the *Tgf- β* receptor 1 (*Tgf- β r1*) are significantly downregulated compared to control microglia (\log_2 fold-change -1.00 and -2.11 respectively) (**Figure 7A** and **Suppl. Table S2**). In contrast to the IL4, IL10, IL6/STAT3 and IFN γ sets, only 35.8% of TGF- β genes are upregulated when comparing EV-GFP^{pos} to control microglia. Similarly *Smad3*, one of the key downstream effectors in the TGF- β pathway, is also significantly downregulated in EV-GFP^{pos} microglia (\log_2 fold-change -2.10). This correlates with the observed upregulation of *Irf7* in our dataset as discussed above. Overall, these data imply that TGF- β signaling is downregulated in EV-GFP^{pos} microglia suggesting a disruption in the homeostatic microglial transcriptional network.

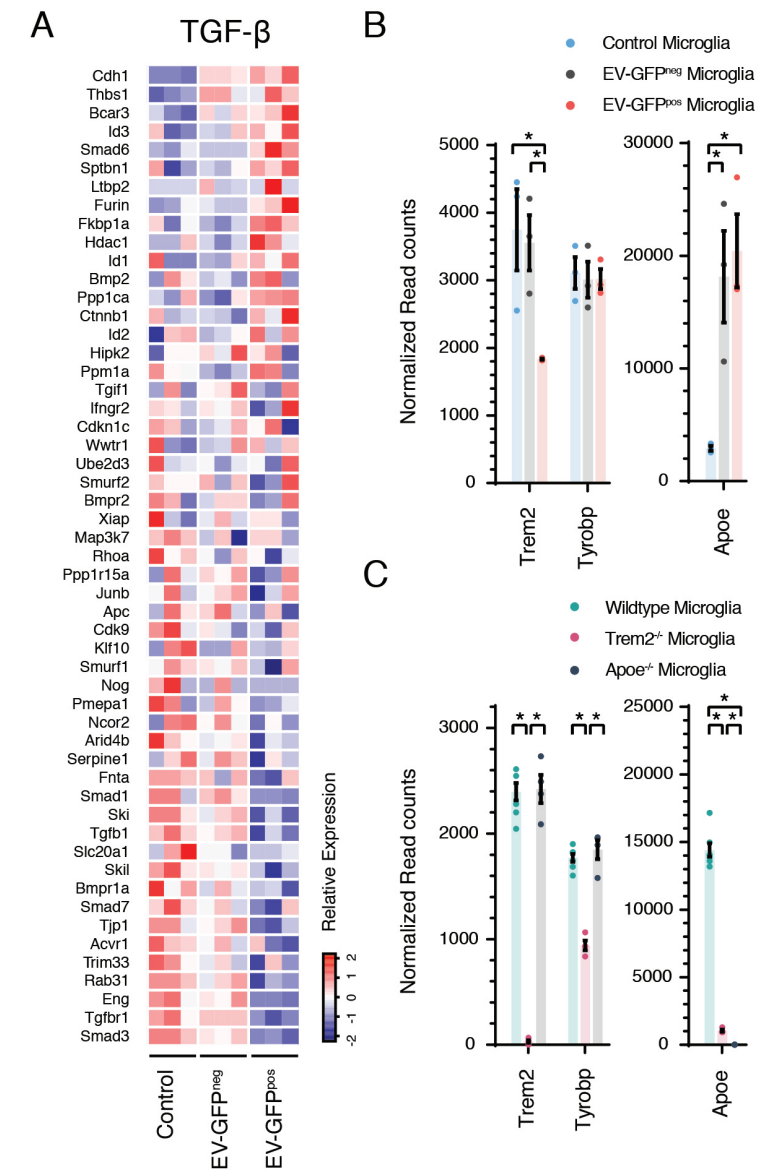


Figure 7. TGF- β regulated microglial homeostasis is disrupted in glioblastoma microglia that express significantly altered levels of Trem2 and Apoe. (A) TGF- β is the key regulator for microglial homeostasis. In glioblastoma microglia, *Tgfb1* and downstream signaling genes including *Smad3* are significantly downregulated, indicating a disruption of homeostatic functions. (B) In EV-GFP^{pos} microglia, Triggering receptor expressed on myeloid cells 2 (*Trem2*), a key microglial regulator, is significantly downregulated. Apolipoprotein E (*Apoe*), another key microglial regulator that is downstream of TREM2 is significantly upregulated in glioblastoma microglia. Expression of *Tyrobp*, a TREM2 binding partner, is unchanged in the context of glioblastoma. (C) In the *Trem2*^{-/-} microglia, *Trem2*, *Tyrobp* and *Apoe* are all significantly downregulated. In *Apoe*^{-/-} microglia only *Apoe* is significantly downregulated. Asterisk (*) indicates significant (multiple testing adjusted p-value <0.05) differential expression. Error bar represents the SEM, bar represents the mean and dots display individual measurements (B: n=3, C: wildtype n=7, *Trem2*^{-/-} and *Apoe*^{-/-} n=4).

Trem2 and Apoe

Since glioblastoma appears to disrupt microglial homeostatic transcriptional networks, we investigated possible alternate pathways that may have taken over control of microglial gene expression and therefore may be regulating the microglial phenotype. Recent reports describe TREM2 as an important microglial immune checkpoint³ and a major regulator of microglia in neurodegeneration when homeostatic regulation by TGF- β is disrupted^{23,24}. Such regulation was described to be either completely or partially TREM2 dependent²³. Our own previous data also suggested that some genes may be regulated via *Trem2*^{7,79,80}. *Trem2* expression is downregulated in EV-GFP^{pos} microglia (**Figure 7B**). To test if changes in the sensome of EV-GFP^{pos} microglia could be mediated specifically by downregulation of TREM2, we isolated microglia from adult control (TREM2 wildtype) and *Trem2*^{-/-} mice and compared their gene expression profile via RNASeq (differential expression data available for all genes passing quality metrics in **Suppl. Table S3**). We found that deficiency in *Trem2* indeed regulated expression of the majority of sensome genes (**Figure 8A**). However, analysis of individual genes showed that in contrast to the changes observed in EV-GFP^{pos} microglia, numerous changes seen in *Trem2*^{-/-} microglia occur in the opposite direction (**Figures 4A, Figure 8A-E, Suppl. Figure S4 and Suppl. Table S4**). Since changes observed in *Trem2*^{-/-} microglia are divergent from those observed in EV-GFP^{pos} microglia, our data suggest that downregulation of Trem2 in EV-GFP^{pos} microglia is not likely to be the driving force behind the observed transcriptional changes, and suggest that glioblastoma alters gene expression in microglia in a mechanism that is independent of *Trem2*. This observation was further corroborated when no significant difference in tumor growth was observed by IVIS imaging of GL261 tumors implanted in wild type and *Trem2*^{-/-} mice (**Suppl. Figure S5**). Together these data support our transcriptomic data that *Trem2* deficiency, while causing significant changes in the microglial transcriptome, does not affect tumor growth and imply that *Trem2* does not regulate the effects of the tumor on microglia.

A recent published report suggested that APOE is an important component of the TREM2 pathway that regulates microglial gene expression in neurodegenerative diseases including Alzheimer's disease²⁴. Our own analysis of the transcriptome of *Trem2*^{-/-} microglia, showed that *Apoe* is also significantly downregulated in these cells (**Figure 7C**) suggesting that *Apoe* expression may be dependent on *Trem2*. Surprisingly, while *Trem2* is significantly downregulated in EV-GFP^{pos} tumor microglia, *Apoe* is significantly upregulated (**Figure 7B**). These data indicate that in glioblastoma

microglia *Apoe* expression is independent of *Trem2*, and suggest that APOE may be part of a TREM2-independent pathway that regulates microglial gene expression and phenotype. To test this, we performed RNASeq on microglia isolated from *Apoe*^{-/-} mice and analyzed expression of key genes upregulated by APOE as well as genes downregulated in APOE stimulated microglia (**Figure 8, and Suppl. Figure 4 and Suppl. Table 3**) and compared the transcriptomes of these cells to those of EV-GFP^{pos} and EV-GFP^{neg} microglia (**Figure 8 D-H**)^{23,24 81}. We found that the majority of key *Apoe* upregulated genes are upregulated in glioblastoma microglia whereas those downregulated genes in *Apoe* deficient microglia are also downregulated in glioblastoma microglia (**Figure 8 D-H**). As noted above, microglia from *Trem2*^{-/-} mice that express *Apoe* at significantly downregulated levels, show gene expression at opposite directions of the glioblastoma microglia (**Figure 8 D-H**).

Overall the data from *Trem2*^{-/-} and *Apoe*^{-/-} microglia, that both display significantly downregulated levels of *Apoe*, show direct opposite expression of the microglia sensome (**Figure 8A**), key *Apoe* regulated genes (**Figure 8 D-H**) and other microglial sensing, host defense and homeostasis genes (**Suppl. Table S4**) when compared to tumor microglia that express significant upregulated *Apoe* levels (**Figure 7B**). This data suggests that APOE is a key mediator of altered gene expression in tumor microglia and indicate that contrary to microglia in neurodegenerative diseases, changes in the gene expression profile of microglia in glioblastoma are *Trem2* independent. These data also suggest that TREM2 and APOE are not part of the same pathway that regulates microglial function and gene expression in glioblastoma.

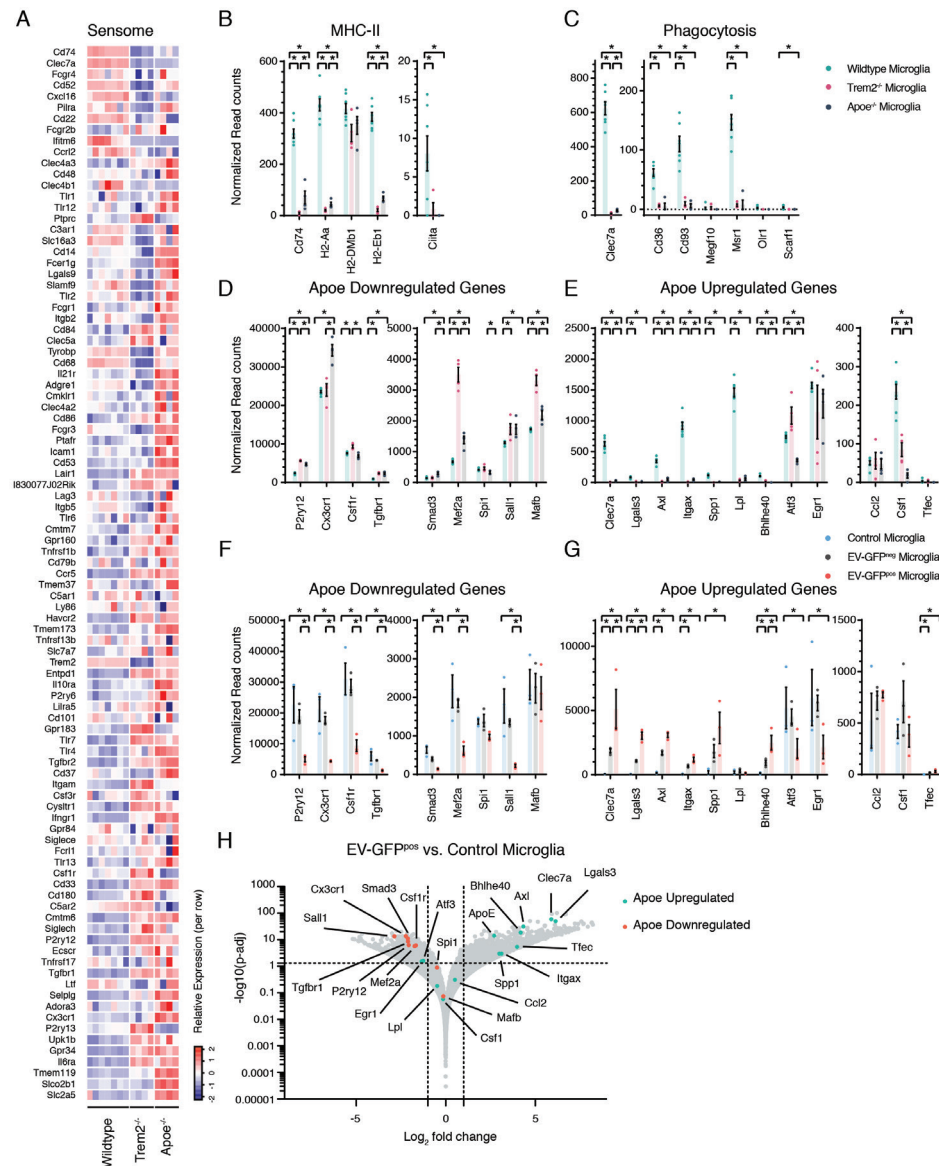


Figure 8. Glioblastoma microglia transcriptomic changes are Trem2 independent, Apoe dependent. (A) Heatmap of sensome genes ordered top to bottom by highest up- to downregulated for EV-GFP^{pos} tumor microglia compared to wildtype (same order as Figure 4A). (A-G) In Trem2^{-/-} and Apoe^{-/-} microglia compared to wildtype, gene expression is in majority opposite compared to glioblastoma microglia gene expression. (D-G) The majority of key Apoe upregulated genes are upregulated in glioblastoma microglia whereas those downregulated genes in Apoe deficient microglia are downregulated in glioblastoma microglia. Trem2^{-/-} and Apoe^{-/-} microglia, that express Apoe at significantly downregulated levels, show gene expression at opposite directions of the glioblastoma microglia confirming Apoe as a key regulator for glioblastoma microglia. (H) Apoe up- and downregulated genes plotted on the background of all genes support that glioblastoma microglia transcriptomic changes are Apoe dependent. Asterisk (*) indicates significant (multiple testing adjusted p-value <0.05) differential expression. Error bar represents the SEM, bar represents the mean and dots display individual measurements (B-E: wildtype n=7, Trem2^{-/-} and Apoe^{-/-} n=4, F-G: n=3).

Microglial uptake of EVs is associated with decreased sensome expression

To explore the relationship between microglial uptake of glioblastoma derived EVs and the expression of sensome genes and *Apoe* regulated genes, we evaluated RNA expression by microglia isolated from control (non-tumor bearing) C57BL6.CCR2^{RFP/WT} mice injected with carrier fluid or EVs isolated from GL261.BpalmGFP cells. EVs were isolated using standard step-wise (ultra)centrifugation (Figure 9A) and as expected the isolated EVs were within the 80-400 nm size range (Figure 9B) expressing the EV associated proteins ALIX, TSG101 and Flotillin-1 as well as GFP (Figure 9C). Sixteen hours after EV injection, microglia were isolated based on EV-uptake and their transcriptomes analysed by RNASeq (Figure 9D). Similar to the results from EV-GFP^{pos} microglia isolated from tumor bearing brains, overall downregulation of the microglia sensome genes was observed in microglia that took GFP-EVs injected into the brain (Suppl. Table S5, S6 and Figure 9E). In addition, similar to the profiles observed in the tumor bearing mice, *Apoe* expression is upregulated and *Trem2* is downregulated in EV-GFP^{pos} microglia compared to EV-GFP^{neg} and mock injection microglia although the differential expression failed to reach significance (Figure 9F). Similar patterns were observed for *Apoe* down- and upregulated gene sets that mimic expression of EV-GFP^{pos} microglia from tumor bearing brains (Figure 9G and 9H). It is possible that some of the changes observed in EV-GFP^{pos} microglia did not reach significance because the number of EVs added and timepoint of analyses may bias the result. These data show parallels between tumor microglia and microglia isolated after EV-injection and open the door for further investigation of specific EV contents that may induce the changes observed.

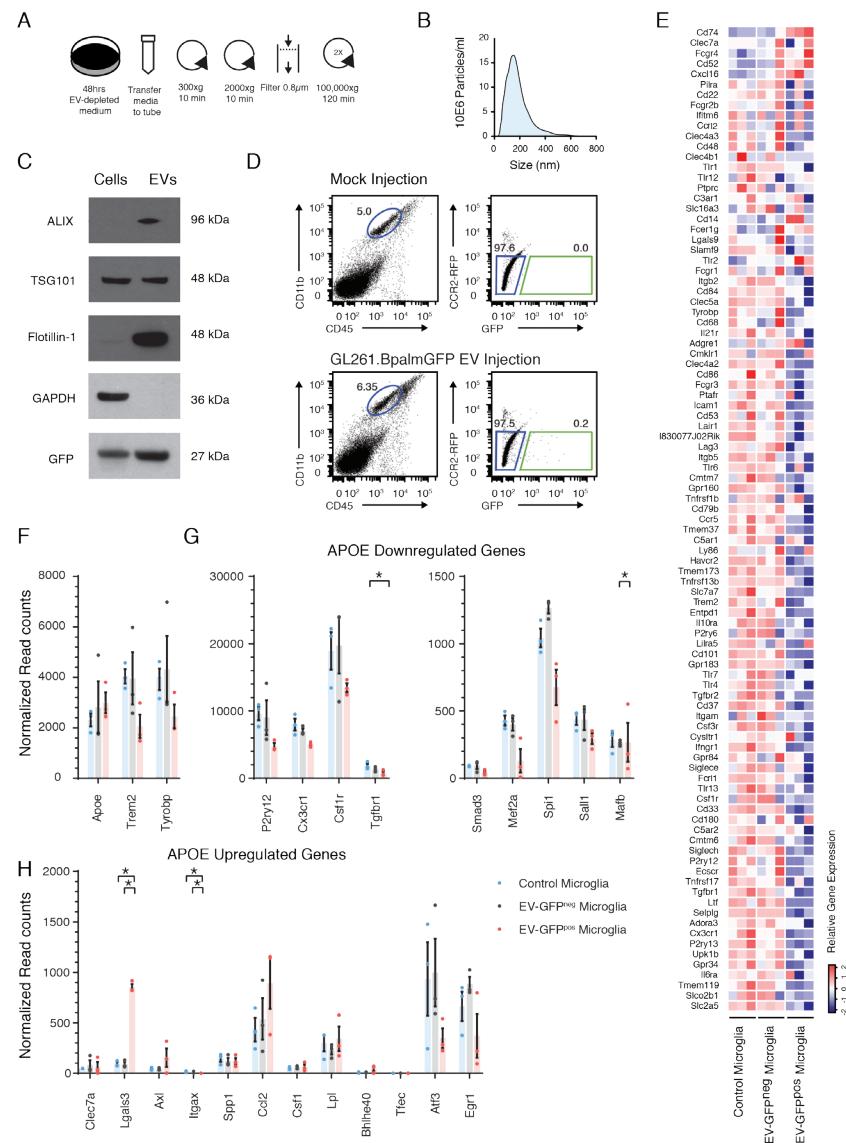


Figure 9. Uptake of intracranial injected glioma-derived fluorescent EVs is associated with a decrease in sensing capability. (A) Schematic overview of EV isolation from glioma cells in culture using differential centrifugation. (B) Size distribution analysis using NTA of isolated EVs shows small and larger vesicles present in the EV preparation. (C) Western blot analysis shows GFP present in cells and EV, extracellular vesicles markers (ALIX, TSG101 and Flotillin-1) enriched in vesicles lysate and GAPDH is detected in cellular lysate only. (D) Microglia were identified as CD11b^{high}/CD45^{med} cells (blue gate). Microglia were then sorted based on the GFP signal detected as the upper limit in control. In mice injected with GL261.BpalmGFP EVs, a population of GFP-positive microglia was identified (green gate in the GFP/RFP plot). (E) Heatmap of sensome genes ordered top to bottom by highest up- to downregulated for mouse EV-GFP^{pos} tumor microglia compared to wildtype (same order as **Figure 4A**). Similar patterns are observed for genes up- and downregulated compared to the mouse tumor derived profile. (F-H) Normalized read count of individual genes for Trem2/Apoe/Tyrobp (F) and Apoe up- and downregulated genes (G-H). Asterisk (*) indicates significant (multiple testing adjusted p-value <0.05) differential expression. Error bar represents the SEM, bar represents the mean and dots display individual measurements (n=3).

Human glioblastoma associated microglia are APOE upregulated and express an APOE dependent gene pattern.

To determine if changes in gene expression in human glioblastoma associated microglia are similar to those observed in mouse microglia, we analyzed existing published datasets of human microglia isolated from post-mortem brains (controls) and CD11b^{pos} macrophage/microglia isolated from glioblastoma samples (GEO Accession GSE80338⁸²). As expected, the control and glioblastoma-associated cells cluster separately with some heterogeneity within the glioblastoma samples (**Figure 10A**). Interestingly, TREM2 and its binding partner TYROBP did not change significantly. In contrast, APOE expression is significantly increased in human glioblastoma microglia, similar to what we found in mice (**Figure 10B**). In line with the APOE expression, APOE downregulated genes are in general downregulated in human glioblastoma microglia whereas APOE upregulated genes are upregulated (**Figure 10C** and **10D**). We then evaluated if the human microglial sensome changes similarly to the mouse sensome (**Figure 4A**). As expected for heterogeneous samples, more variance within the experimental groups was observed, however similar patterns in up- and downregulated sensome genes in human CD11b^{pos} cells and mouse microglia was detected. Overall, 77% of significantly changed genes are up- or downregulated in the same directionality compared to the murine profile, (**Suppl. Table S7**). These data imply that both mouse and human glioblastoma associated microglia display a gene expression pattern that is *Trem2* independent, *Apoe* dependent.

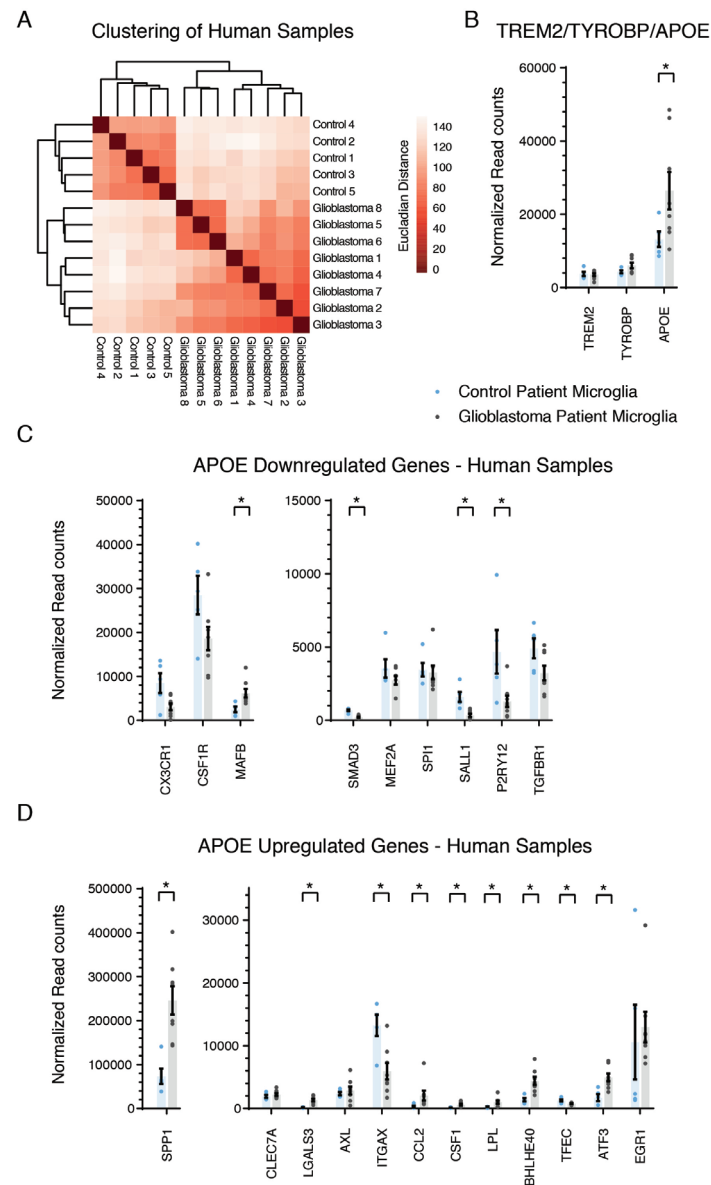


Figure 10. In human glioblastoma associated microglia APOE is upregulated and an APOE dependent gene pattern is expressed. (A) Analysis of published RNAseq data from CD11Bpos microglia harvested from postmortem control brains or glioblastoma patients, shows differences based on patient group as well as heterogeneity between glioblastoma derived cells. (B) Similar to microglia derived from glioma bearing mice, human glioblastoma microglia are APOE upregulated whereas TREM2 and its binding partner TYROBP remain unchanged. (C and D) Key APOE downregulated genes are downregulated in human glioblastoma microglia (C) whereas upregulated genes are upregulated (D). Asterisk (*) indicates significant (multiple testing adjusted p-value <0.05) differential expression. Error bar represents the SEM, bar represents the mean and dots display individual measurements (control n=5, glioblastoma n=8).

Discussion

Glioblastomas are the most aggressive malignant brain tumors leading invariably to death. To date, no effective therapy has been found for this devastating disease. These tumors are heavily infiltrated with innate immune cells including resident brain microglia. Yet, despite such a large immune cell presence, glioblastomas continue to grow and are thought to co-opt the innate immune system of the host to promote tumor spread⁹. To determine how glioblastomas interact with the innate immune system, we analyzed the gene expression profile of microglia in a mouse model of this tumor using RNA sequencing. By using glioblastoma cells with fluorescently labeled membranes releasing fluorescently labeled EVs, we could identify and separate microglial cells closely associated with the tumor that had taken up these fluorescent vesicles (EV-GFP^{pos}) versus ones further away that had not (EV-GFP^{neg}), and compare them with each other and with microglia isolated from control brains. Our data show that EV-GFP^{pos} microglia have a unique gene expression profile that distinguishes them from other microglia, and that this glioblastoma-associated expression profile is more complex than the prior classification of M1 versus M2 states^{5,58}. Instead we identified a disease-specific Microglia_{Glioblastoma} state that is characterized by markers found in both M1 and M2 polarization states. This Microglia_{Glioblastoma} state can be further subclassified based on proximity of the microglia to the tumor and/or their level of interaction with tumor cells. Since our model labels all membranes, we cannot exclude that the observed transcriptome changes in the EV-GFP pos microglia were caused by phagocytosis of membranous fragments. However, the results of the EV-injection experiment suggest that at least part of the transcriptome changes in EV-GFP^{pos} microglia were EV mediated. In general, our data also indicate that genes that suppress tumor functions are downregulated, whereas genes that promote tumor growth, invasion and immune suppression are upregulated. We further explored the mechanisms of these glioblastoma-induced changes and found that they are *Trem2*-independent but appears to be *ApoE* dependent.

We identified three pathways by which tumor-interacting microglia may become less effective in combating the tumor and appear to be hijacked by tumor cells to promote tumor growth. First, we found that EV-GFP^{pos} microglia, in contrast to other microglia in the same brain, have reduced expression of genes involved in sensing. Sensing is an important function of microglia that allows these cells to perform their other functions, including host defense against invading pathogens and injurious stimuli.

A majority of the genes involved in sensing (somsome genes⁷) were downregulated in EV-GFP^{pos} microglia. The somsome transcripts that were downregulated in EV-GFP^{pos} microglia, compared to other microglia in the same brain and control microglia, can be divided into three groups. Group one includes transcripts encoding proteins that directly mediate microglia-glioblastoma cellular interactions, including *Siglech*. Indeed, *Siglech* is a CD33-related gene that is exclusively expressed in microglia in the brain⁷. SIGLECH has been shown to bind glioblastoma cells, including GL261 in culture³⁸, but it is not clear what ligand on these glioma cells is recognized by SIGLECH. Another microglial receptor capable of sensing glioblastoma cells that is downregulated in glioblastoma-interacting microglia is GPR34. GPR34 is a receptor for phosphatidylserine, a membrane phospholipid that resides in the inner (cytosolic) leaflet of the plasma membrane of normal, healthy cells, but becomes exposed on the outer surface in many tumors, including glioblastoma^{39,40}. Our data indicate that EV-GFP^{pos} microglia, but not other microglia in the same brain, have reduced levels of RNA encoding *Siglech* and *Gpr34* that are directly involved in sensing ligands/receptors expressed on glioblastoma cells. This indicates that EV-GFP^{pos} microglia might have a reduced capability to sense tumor cells, which likely interferes with their ability to initiate an effective anti-tumor response.

A second group of microglial transcripts altered by glioblastoma cells reflects a disarming of their usual host defense anti-tumor functions. These include suppression of activation of cytotoxic T cells, which can kill tumor cells, as well as of direct tumor killing by microglia. We found that genes involved in antigen presentation, such as MHC-II genes, are upregulated in EV-GFP^{pos} microglia, suggesting an enhanced capacity for antigen presentation, which should lead to T cell activation and subsequent tumor suppression. However, this is accompanied by upregulation of PD-L1 and PD-L2 which help maintain immunologic tolerance by causing T cell exhaustion and would ultimately reduce tumor killing capacity of T cells⁸³. Even though additional functional studies are needed, these findings suggest that targeted therapy against microglial PD-L1 and/or PD-L2 may be a useful strategy in combating glioblastoma as is being done for peripheral tumors. Our data also highlight a novel potential pathway that microglia could use for tumor killing which is downregulated in glioblastoma-associated microglia. The antimicrobial peptides Ngp, Cathelicidin and Ltf are highly expressed in microglia in control brains, but have reduced levels in EV-GFP^{pos} microglia. Such peptides, while initially described as involved in bacterial and fungal killing, have also been found to kill colon cancer cells⁸⁴ and may act as tumor suppressors in oral squamous cell

carcinoma⁸⁵. Additional work to evaluate whether these antimicrobial peptides have antitumor activity in glioblastoma is needed. Nonetheless our findings support the ideas that glioblastoma interacting microglia suppress the adaptive immune response to the tumor and may have a reduced capability to directly kill tumor cells.

A third group of transcripts in glioblastoma-associated microglia acts to promote tumor spread, including genes that could alter the extracellular milieu surrounding tumor cells. Because one of the hallmarks of glioblastoma is the presence of excessive debris and necrotic tissue, clearing such necrotic material is important for tumor cell spread and growth. We found that glioblastoma-interacting microglia have increased expression of several phagocytic receptors, while either maintaining or increasing expression of extracellular matrix degrading enzymes. Clearing debris and necrotic tissue from the tumor milieu would boost the migratory capacity of tumor cells, one of the key characteristics of this invasive tumor. These data indicate that glioblastoma-interacting microglia may help promote tumor growth and migration by clearing debris in the tumor microenvironment.

In addition to specific cellular mechanisms, we show that tumor microglia upregulate responses to multiple cytokine-regulated pathways. In microglia in close proximity to tumor cells, IL4, IL10, IL6/STAT3 and IFN γ responses are all upregulated. Of these, the changes in the IFN γ gene set are very interesting. IFN γ is usually produced by lymphocytes and activates cytotoxic lymphocytes to induce tumor killing and thereby prevent tumor progression. Microglia and macrophages have also been shown to produce IFN γ when stimulated by lipopolysaccharide and *Toxoplasma*⁸⁶⁻⁸⁹. IFN γ production by microglia in response to tumor stimuli has been reported, but so far it has not been known if glioblastoma-associated microglia produce IFN γ *in vivo*. Interestingly, we found that both IFN γ itself and IFN γ -related genes are significantly upregulated in glioblastoma microglia isolated from mouse brain, and to a greater extent in EV-GFP^{pos} microglia. When exploring the upregulated IFN γ associated genes we found several genes including *Ccl22*, *Cd38*, *Pd-11* (*Cd274*) and *Irf7* that possess tumor supportive functions. *Irf7* is of specific interest as it has been described as a key regulator of the pro-inflammatory to anti-inflammatory switch in microglia⁷⁵. The fact that IL4, IL10, IL6/STAT3 and IFN γ responses are all upregulated underscores that *in vitro* studies of activation of microglial cells by a single cytokine do not reflect the true *in vivo* tumor-associated activation state of microglia where multiple cytokines are involved.

TGF- β has been shown to be a key regulator of microglial homeostasis. In the glioblastoma microglia, TGF- β and downstream signaling genes are significantly downregulated indicating a disruption of homeostatic functions. In neurodegeneration, such downregulation of TGF- β has been associated with upregulation of a TREM2-regulated transcriptional network where APOE is a major component^{23,24}. In contrast to neurodegenerative diseases, our data show that the microglia response in glioblastoma is *Trem2*-independent but is likely *ApoE* dependent. This suggests that there are key differences in the pathways regulating microglial function between neurodegenerative diseases and glioblastoma especially in the disease-specific upstream activating factor. The divergence between Microglia_{Glioblastoma} and Microglia_{Neurodegeneration} further supports the concept that microglial gene expression changes are disease specific. Additional studies are needed to determine whether similar differences exist even among the various neurodegenerative diseases. This is reminiscent of the findings by Xue et al. showing that different stimuli elicit different gene expression profiles in human monocyte derived macrophages⁵⁹.

The molecular mechanisms by which glioblastoma cells activate the APOE pathway in microglia are not clearly defined and undoubtedly reflect a combination of factors that together with spatiotemporal circumstances determine the overall effect on microglial genes. Our novel method of identifying microglia that have taken up tumor-derived EVs *in vivo* allows us to select microglia with which the tumor appears to have interacted directly with a physical exchange of membrane and cytoplasmic factors. Simultaneously, this could suggest that some of the gene expression changes observed are related to the uptake of EVs. Interestingly, when performing proteomics on EVs isolated from the human glioblastoma cell-line U87/EGFRvIII, we previously detected APOE in glioblastoma EVs²⁰. However, in the *in vivo* model described here, all tumor lipid bilayers are GFP-positive and thus it is not clear whether all GFP^{pos} microglia have taken up EVs *per se* or may possibly have taken up tumor cell membrane debris. Other intercellular communication modes such as secreted molecules⁹⁰, exchange of molecules through gap junctions between cells⁹¹ and cell connecting nano/microtubes may contribute to the observed effects as well.

Glioblastomas are heterogeneous tumors at the inter- and intratumor level and they express gene patterns associated with mesenchymal, proneural and classical subtypes. We recognize that a single, highly clonal, murine cell line may not recapitulate this heterogeneity. To address this issue, we analyzed existing datasets obtained

from human patients with glioblastoma and found that these data support the conclusions obtained with our mouse model and reflect the true heterogeneity of human glioblastoma tumors, further asserting the validity of our analysis and its applicability to human disease.

For the sake of exploratory analysis and to increase the impact of our dataset, we established an online tool (www.glioma-microglia.com, temporary password "Microglia1") for everyone to use to make the discovery of unconventional gene sets easier. This tool displays gene (differential) expression for all genes as well as functional and pathway related information. Overall, our data opens the door for future investigations to specifically identify how glioblastoma hijack the microglial immune response to promote tumor growth, and will possibly help identify novel microglia-specific targets for therapy of this highly aggressive and inevitably lethal disease.

Methods

Mice

Animal experimentation was conducted under the oversight of the Massachusetts General Hospital Institution Animal Care and Use Committee. C57BL/6 mice (Charles River Laboratories) were crossed with homozygous C57/BL6.CCR2RFP/RFP knock-in mice²⁵ to generate heterozygous C57BL6.CCR2^{RFP/WT} knock-in mice. For *Trem2*^{-/-} studies age-matched C57BL/6 (Jackson Laboratory), *Trem2*^{-/-} (knock-out mouse project KOMP, UC Davis) mice were backcrossed on a C57BL/6 background and used. B6.129P2-Apoetm1Unc/J (Jackson Laboratory) mice were used for *ApoE*^{-/-} studies. Mice were maintained under a 12 hrs light/dark cycle with access to water and food. Adult mice ranging from 12 - 18 weeks were used in this study. Male and female mice were randomly assigned to experimental groups, with three animals per group. Mice had similar tumor sizes. RNAseq on male and female animals shows no differences in the mRNA expression between males and females (data not shown). The four week time point was chosen as this is the time point at which mice implanted with GL261 cells first start to develop physical signs and, have to be sacrificed per animal welfare guidelines.

Cell culture

Mouse glioma cell-line GL261 wild type (NCI Tumor Repository) was cultured in Dulbecco's modified Eagle's medium (DMEM) (Corning) supplemented with 10% fetal

bovine serum (FBS) (Gemini Bioproducts), penicillin (100 units.ml⁻¹) and streptomycin (100 µg.ml⁻¹) (Corning). Cells were cultured at 37°C in a 5% CO₂ humidified incubator. Cells were periodically tested for mycoplasma contamination and found negative.

Stable transduction reporter

To introduce reporter molecules, the mouse glioma cell-line GL261 wild type (NCI Tumor Repository) was stably transduced using a CSCW2 lentiviral vector⁹² encoding a *Gaussia* luciferase trans-membrane biotin acceptor domain fusion protein (GlucB) and GFP separated by an internal ribosome entry site (IRES) domain⁹³. A second transduction was performed using a CSCW2 lentiviral vector encoding palmitoylated GFP for pan membrane associated GFP expression, including in EVs released by these tumor cells^{22,94}. To validate viral transduction and reporter expression, the resulting GL261.GlucB-IRES-GFP.palmGFP (GL261.BpalmGFP) cells were seeded on poly-D-lysine (Sigma-Aldrich) coated glass coverslips and incubated for 48 h. Cells were then washed in PBS and fixed using 4% paraformaldehyde (PFA; Electron Microscopy Sciences) in PBS. Cells were washed in PBS twice after which the coverslips were mounted on microscopy slides using ProLong® Diamond Antifade Mountant (Thermo Fisher). For bioluminescence imaging experiments, prior to implantation the GL261 cell line was stably transduced with a CSCW2 lentivirus vector carrying an expression cassette for firefly luciferase (Fluc) and GFP fluorescent protein separated by an internal ribosome entry site (IRES) domain. Selection of transduced GL261.Fluc.GFP cells was done based on GFP expression using FACS (BD FACSAria II SORP Cell Sorter).

Intracranial tumor implantation

After anesthetizing the animals using 70µl of a mixture of ketamine (Bioniche Pharma) (17.5mg.ml⁻¹) and xylazine (Santa Cruz Biotechnology) (2.5mg.ml⁻¹), C57BL6.CCR2^{RFP/wt} adult mice (12 - 18 weeks old) were implanted in the striatum with 1 × 10⁵ GL261.BpalmGFP or GL261 wild type cells in 2 µl plain DMEM using a stereotactic frame. Cells were implanted using the coordinates from lambda: 2 mm anterior, 0.5 mm left and a depth of 2.5 mm from the skull. Four weeks after implantation, the mice were deeply anesthetized with 120µl of a mixture of ketamine (17.5 mg.ml⁻¹) and xylazine (2.5 mg.ml⁻¹) followed by transcardial perfusion with 50ml PBS for FACS or 4% PFA (VWR) for immunohistochemistry using a perfusion pump (Minipump Variable Flow, Fisher Scientific).

Bioluminescence imaging

Bioluminescence imaging was performed using the Xenogen IVIS 200 Imaging System (PerkinElmer) 10 minutes after intraperitoneal injection of 150µl d-Luciferin (25mg/L, Gold Biotechnology). Prior to imaging mice are sedated with isoflurane and hair removed using scalpel.

EV isolation and intracranial injection

EVs were isolated from supernatant of GL261.BpalmGFP cultured for 48 hours in DMEM with penicillin (100 units.ml⁻¹) and streptomycin (100 µg.ml⁻¹) (Corning) and EV-depleted FBS. FBS was depleted of EVs by overnight (16 hours) ultra-centrifugation at 200.000 × g (*k*-factor 110.5). EV isolation was done using differential ultracentrifugation protocol consistent of centrifugation of supernatant at 300 × g for 10 minutes, 2000 × g 10 minutes, filtering through 0.8µm filter (Sigma) and 100.000 × g (*k*-factor of 220.1) 120 minutes in Quick-Seal® Polypropylene Tubes (Beckman) using Type 70 Ti in Optima™ XE ultracentrifuge (Beckman) to pellet EVs. EV pellets were concentrated by centrifugation at 100.000 × g (*k*-factor of 190.7) for 120 minutes in Thinwall Polypropylene Tubes (Beckman) using MLS-50 Swinging-Bucket Rotor (Beckman) in a Optima™ MAX-XP Ultracentrifuge (Beckman). Pelleted EVs were resuspended in PBS and subsequent characterization of EV pellet was performed by size distribution analysis using nanoparticle tracking analysis (Malvern) and western blot analysis. For western blot analysis EV pellets and cells were resuspended in RIPA buffer. Equal amount of protein as measured by Pierce BCA protein assay (Thermo Fisher) were loaded and ran on 10% SDS-PAGE gel (Thermo Fisher). Proteins were transferred onto nitrocellulose membrane and probed for ALIX (Santa Cruz, sc-53538, 1:200), TSG101 (Abcam, ab125011, 1:500), Flotillin-1 (Abcam, ab133497, 1:500), GAPDH (Millipore, CB1001, 1:1000) and GFP (Thermo Fisher, A-11120, 1:1000).

EV or carrier fluid (PBS) was injected intracranial following identical procedures as described in intracranial tumor implantation method section. Using NTA 2.2 with shutter set at 1000 and gain at 400, a 1 to 500 dilution of EV concentrate was measured with >1000 completed tracks⁹⁵. A total of 3 µl with a concentration of 1.4e12 particles.ml⁻¹ was injected. Microglia were isolated 16 hours after injection of EV or DPBS following procedures as described in methods sections harvesting of brains and preparation of single-cell suspensions and cell staining and FACS.

Immunohistochemistry

Brains were collected and placed in 4% PFA for 24h and subsequently placed in 25% sucrose for 48h. The brains were then frozen in optimal cutting temperature compound (OCT) media (Sakura) in a dry ice bath containing 2-methyl butanol. Twelve μm cryosections were prepared, placed on glass slides and stored at -80°C . For processing, sections were washed for 10 min in PBS and permeabilized with 0.5% Triton-X PBS for 1h at room temperature. Sections were blocked for 1h at room temperature using 5% Normal Goat Serum (NGS) (Abcam) in PBS. Subsequently, the sections were labeled with a primary goat antibody and blocked using 5% Bovine Serum Albumin (BSA; Sigma-Aldrich) in PBS. Primary antibodies were diluted in 1.5% NGS or 1.5% BSA. Slides were then incubated with primary antibody solution overnight at 4°C . After incubation, slides were washed 3 x 10 min in PBS. The secondary antibodies were diluted in 1.5% NGS or 1.5% BSA. Sections were then incubated with secondary antibody solution for 1h at room temperature and subsequently washed 3 x 10 min using PBS. DAPI (0.1 $\mu\text{g}/\text{ml}$, Thermo Fisher) staining was performed for 30 min at room temperature. Next, the slides were washed for 10 min using PBS. Sections were mounted using ProLong Diamond Antifade Mountant (Thermo Fisher). Primary antibodies used were goat-anti-mouse Arg1 (Santa Cruz Biotechnology, sc18354, 1:200), goat-anti-mouse CD74 (Santa Cruz Biotechnology, sc5438, 1:200), rat-anti-mouse CD68 (AbD Serotec, MCA1957, 1:200), rabbit-anti-mouse Iba1 (Wako, 019-19741, 1:1000) and mouse-anti-GFP tag antibody (Thermo Fisher, A-11120, 1:200). Secondary antibodies were donkey-anti-goat IgG Alexa Fluor 647 (Thermo Fisher, A21447, 1:500), donkey-anti-rabbit IgG Alexa Fluor 405 (Thermo Fisher, A31556, 1:500), goat-anti-rat Alexa Fluor 647 (Abcam, ab150155, 1:500) and goat-anti-mouse IgG Alexa Fluor 488 (Thermo Fisher, A31560, 1:500).

Microscopy

Fluorescence microscopy images were acquired on the Zeiss Axio Imager M2 (Carl Zeiss). Confocal images were obtained using the Zeiss LSM 710 inverted confocal microscope.

Harvesting of brains and preparation of single-cell suspensions

After anesthetizing and perfusing with PBS, brains were removed and processed into single cell suspension as described⁷. Briefly, brains were cut into small pieces and placed into a GentleMacs™ C-tube (Miltenyi Biotech, San Diego, CA, USA) with Roswell Park Memorial Institute (RPMI) 1640 with L-glutamine (no phenol red) medium

(Fisher Scientific) containing Dispase ($2\text{U}\cdot\text{ml}^{-1}$) (Corning) and Collagenase Type 3 at a final concentration of $200\text{U}\cdot\text{ml}^{-1}$ (Worthington Biochemicals) or the Neural Tissue Dissociation Kit (P) (Miltenyi Biotech) for *Trem2*^{-/-} and *ApoE*^{-/-} brains. The resulting mixtures were processed using the gentleMACS Dissociator (Miltenyi Biotech) on the brain program settings according to manufacturer's directions. Thus, the brains were subjected to three rounds of dissociation each followed by a period of incubation at 37°C for 10 min. DNase I grade II (Roche Applied Science) was added to a final concentration of $40\text{U}\cdot\text{ml}^{-1}$ and incubated for an additional 10 min before the final round of dissociation. After dissociation steps, PBS/EDTA containing 5% FBS was added to inactivate the enzyme mixture and brain pieces were gently triturated gently, passed through a $100\text{ }\mu\text{m}$ filter (Fisher Scientific) and centrifuged at $400 \times g$ for 10 min. Cell pellets were resuspended in 10.5 ml RPMI/L-glutamine, mixed gently with 4.5 ml physiologic Percoll® (Sigma Aldrich) and centrifuged at $850 \times g$ without brake for 40 min or with magnetic anti-myelin beads (Miltenyi Biotech) for *Trem2*^{-/-} and *ApoE*^{-/-} mixtures to remove myelin. The subsequent pellets were then rinsed in PBS and centrifuged again at $400 \times g$ for 10 minutes. Red blood cells in the pellets were lysed using RBC lysis buffer (Boston BioProducts) for 2 min at room temperature followed by a washing step using RPMI/L-glutamine medium. The final cell suspensions were then re-suspended in PBS with 0.2% FBS or in DPBS, 1X without calcium (Ca^{2+}) and magnesium (Mg^{2+}) (Corning) supplemented with 2mM EDTA (Thermo Fisher) and 0.5% BSA (Sigma Aldrich), followed by staining and FACS. The interval between perfusion to FACS was approximately 5 hours.

Cell staining and FACS

To block non-specific binding of immunoglobulin to the Fc receptors, cells in suspension were incubated for 10 min on ice with TruStain fcX™ (anti-mouse CD16/32, BioLegend, #101319, clone 93, 1:100). Cells identification was based on levels of expression of CD45 and CD11b (microglia), CD45, CD11b, F4/80, Ly6C and CCR2 (monocytes/macrophages). For microglia, anti-CD45-pacificBlue (BioLegend, #103125, clone 30-F11, 1:100), and anti-CD11b-Alexa647 (BioLegend, #101220, clone M1/70, 1:100) for tumor cells and EVs injected mice or anti-CD11b-Alexa488 (Biolegend #101219, clone M1/70, 1:100) for *Trem2*^{-/-} and *ApoE*^{-/-} microglia were used. In samples from *Trem2*^{-/-} and *ApoE*^{-/-} mice, CCR2 expression was detected using anti-CCR2-APC (RnD systems, FAB5538A-025, 1:25). For the monocytes/macrophages, anti-CD45-pacificBlue (BioLegend, #103125, clone 30-F11, 1:100), anti-CD11b-PE-Cy7 (Biolegend, #101215, clone M1/70, 1:100), anti-Ly6C-BV605 (Biolegend, #128035, clone HK1.4, 1:500) and anti-F4/80-APC (Biolegend,

#123115, clone BM8, 1:75) were used. Cells were stained for 30 min on ice with gentle mixing every 10 min by pipetting the mixture up and down. To remove unbound antibodies, cells were centrifuged at $400 \times g$ for 8 min, resuspended in 0.2% FBS in PBS and passed through a 35 μm nylon mesh strainer (BD Falcon). Cells were then sorted using a BD FACSAria II SORP Cell Sorter.

RNA isolation and preparation for RNA-sequencing

Cells isolated from brains injected with tumor, EVs and carrier fluid were directly sorted into 1.5 ml Eppendorf (Hauppauge) tubes containing 350 μl RLT Plus lysis buffer (Qiagen) at 4°C. After FACS was completed, the tubes were weighed and additional RLT Plus was added to the 1.5 ml Eppendorf if the sorted volume was larger than 50 μl at a ratio of a maximum of 50 μl 0.2% FBS PBS to 350 μl RLT Plus buffer. 2-mercaptoethanol (Sigma) was added to the tubes at a ratio of 10 μl per 1 ml of RLT buffer and RNA was then isolated using the RNeasy Plus Micro kit (Qiagen) using the total RNA isolation protocol. Eluted RNA was aliquoted and stored at -80°C. Before preparation of cDNA fragments for RNA-sequencing, RNA concentrations and quality were determined using the Agilent 2100 Bioanalyzer (Agilent Technologies) Pico-chips. cDNA for RNA-sequencing was synthesized from RNA aliquots using the SMARTer Ultra Low Input RNA Kit for Sequencing – v3 (Clontech Takara) according to the manufacturer's protocol. A total of 500 pg RNA was used for subsequent library generation. One μl of a 1:50,000 dilution of ERCC RNA Spike-In Mix (Life Technologies) was added to each sample. Then, first-strand synthesis and tailing of RNA molecules was performed using 3'-SMART CDS primer II A (selecting for poly-A-tails) followed by extension and template switching by reverse transcriptase. Amplified cDNA was purified with 1x Agencourt AMPure XP beads (Beckman Coulter), in accordance with the SMARTer protocol. The eluted cDNA was stored at -20 °C. The Nextera® XT DNA Library Preparation kit (Illumina) was used for sample barcoding and fragmentation according to the manufacturer's protocol. cDNA samples were thawed and a total of 1 ng of amplified cDNA was used for the enzymatic tagmentation followed by 12 cycles of amplification and unique dual-index barcoding of individual libraries. PCR product was purified with 1.8x Agencourt AMPure XP beads as detailed in the Nextera XT protocol, omitting the bead-based library normalization step. Library validation and quantification was performed by quantitative PCR using the SYBR® FAST Universal qPCR Kit (KAPA Biosystems). The individual libraries were pooled with equal concentrations, and the pool concentration was re-determined using the KAPA SYBR® FAST Universal qPCR Kit. The pool of libraries was subsequently

diluted, denatured, and loaded onto the NextSeq 500 sequencer (Illumina) according to the manufacturer's guidelines with the addition of 1% PhiX Sequencing Control V3 (Illumina). A NextSeq 500/550 High Output v2 kit (150 cycles) was used to run 75-bp paired-end sequencing.

For *Trem2*^{-/-} and *ApoE*^{-/-} studies cDNA libraries were prepared using QuantSeq 3' mRNA-Seq Library Prep Kit FWD for Illumina (Lexogen) following manufacturer's protocol. Quality of libraries was analyzed using high sensitivity DNA chip (Agilent). Library quantification was performed by quantitative PCR using the KAPA Library Quantification Kits (KAPA Biosystems). Equal molar amounts of libraries were multiplexed (8 libraries per run for final concentration of 1.8 pM) and loaded onto the MiniSeq High Output Cartridge (75-cycles) (Illumina).

Immunofluorescent quantification

Zen Pro 2012 (Carl Zeiss) and ImageJ 1.49v (NIH) software packages were used to process the images. For immunofluorescence quantification, the fluorescence intensity of the microscopic pictures was analyzed using ImageJ for immunofluorescence quantification. Four microscopic pictures were taken per section. The average background intensity of 3 measurements was subtracted from each image. A total of 15 cells per section were selected using the freehand drawing tool and the area and integrated density were measured. The following formula was used to obtain the fluorescence intensity: fluorescence per pixel = total integrated density / total area.

Data processing and statistical analysis

The raw sequencing data was aligned to the mm10 genome using the STAR v2.4.0h aligner with the default settings. Duplicate reads were marked using the MarkDuplicates tool in picard-tools-1.8.4 and removed. The uniquely aligned reads were then counted against Gencode's GRCm38.p3 GTF annotations using htseq-count in the intersection-strict mode. For *Trem2*^{-/-} and *ApoE*^{-/-} studies, FASTQ files generated were aligned to the mm10 genome using STAR version 2.4.2a with resulting BAM files further processed using Samtools version 2.0.10. Final readcount files were generated with HTSeq-count version 0.6.1p1. Data analysis of mapped counts was performed in R 3.2.3 using the DESeq2 package (version 1.10)²⁷. Samples with less than 6000 genes with at least 5 mapped reads were excluded from analysis (n=0). For unsupervised clustering, sample read counts were normalized using the regularized logarithm transformation method, which is similar to log2 transformation for genes with high counts and shrinks

together the values for low count genes²⁷. The regularized logarithm (rlog) values were used to plot heatmaps using the `gplots` (version 2.17) `heatmap.2` function in R. Unsupervised clustering was performed based on the top-750 most variable genes between samples. Differential expression analysis was performed in DESeq2 and only two-sided Benjamini and Hochberg multiple testing adjusted p-values are reported in this manuscript. The level of significance used is <0.05 Benjamini and Hochberg multiple testing adjusted p-value. Error bars display mean \pm standard error of the mean (SEM). The “n” represents three individual mice for EV-GFP^{pos} and EV-GFP^{neg} tumor and control injection experiments, for wildtype microglia seven individual mice were used and four individual mice for both the *Trem2*^{-/-} and *ApoE*^{-/-} studies.

For analysis of specific gene sets, the microglial sensome was extracted from Hickman et al. 2013⁷. The IL6/STAT3 and TGF- β sets were extracted from the Gene set enrichment analysis (GSEA) hallmarks collection⁹⁶. The IL4, IL10 and IFN γ sets were calculated from the Xue et al.⁵⁹ study by extracting the 150 highest upregulated genes compared to baseline. For the IL6/STAT3, TGF- β , IL4, IL10 and IFN γ sets, human to mouse homolog conversions were performed using The Jackson Laboratory Human and Mouse Homology Report (accessed February 18th 2016) supplemented by manual curation. The UpSet graph was generated using the UpSetR R package⁹⁷(version 1.3.3). Venn diagrams were generated using the VennDiagram R package (version 1.6.16)⁹⁸. Principal component analysis (PCA) was performed by utilization of the DESeq2's built-in PCA function using the default settings. Final bar graph, dotplots, PCA and MA plots were generated in GraphPad Prism (version 5.0c and 7.02).

Analysis of human glioblastoma macrophage/microglia data

Data on human glioblastoma macrophages/microglia was downloaded from the NCBI Gene Expression Omnibus (GSE80338) as deposited by Szulzewsky et. al.⁸². For comparative expression analysis, only samples from glioblastoma patients (n=8) and postmortem controls (n=5) were used. Samples with less than 6000 genes with at least 5 mapped reads were excluded from analysis (n=0). The sample-to-sample heatmap was generated using the Pheatmap R package version 1.08 using the Euclidian distance between samples.

Data availability

Raw and processed transcriptomic data described in this manuscript are deposited in NCBI's Gene Expression Omnibus (GEO) and are accessible using GEO Series

accession number GSE106775 at <https://www.ncbi.nlm.nih.gov/geo/query/acc.cgi?acc=GSE106775>. Token for early data access available upon request.

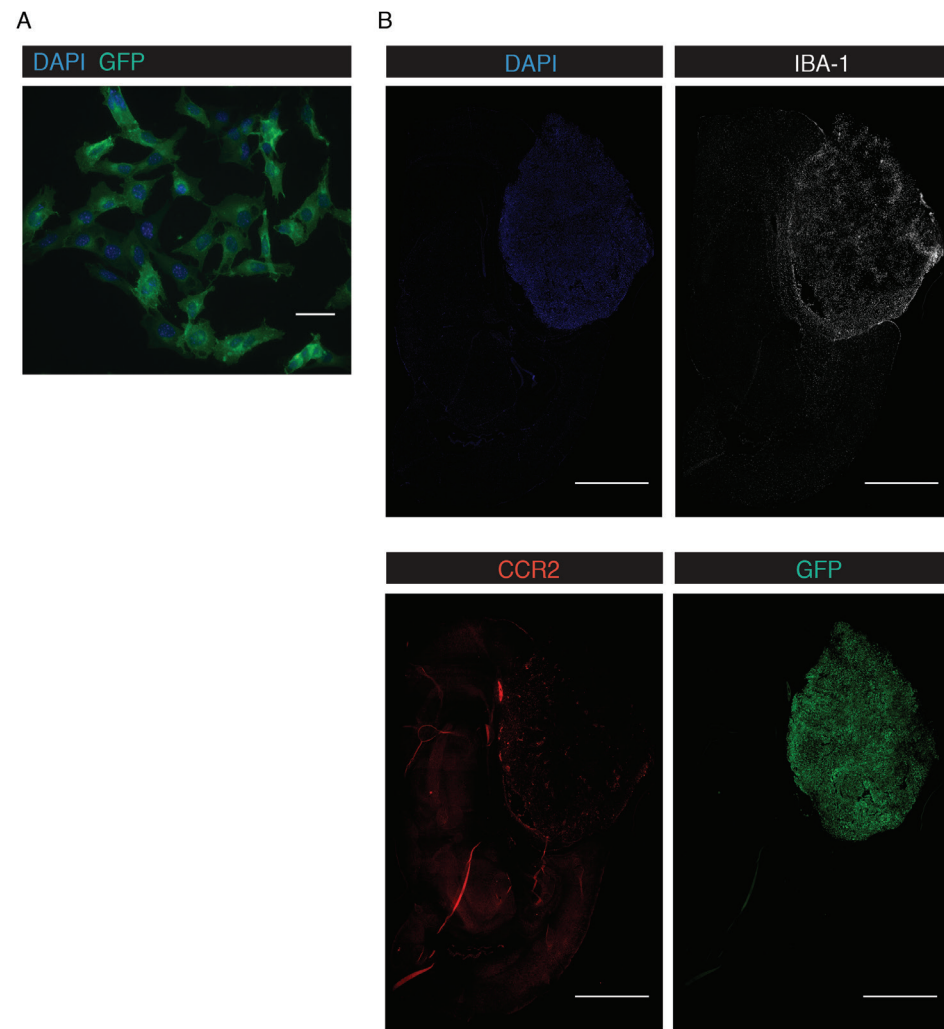
Code availability

All R scripts written for data processing and the generation of figures included in this manuscript are available online in a git repository. This includes the R `sessionInfo()` data for compatibility information. The files and information can be accessed at: <https://github.com/slnmaas/Glioblastoma-Microglia-Project>

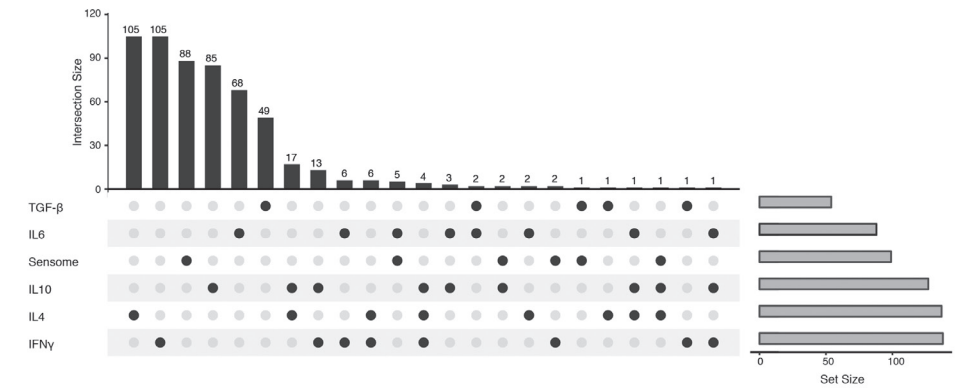
Supplementary tables and supplementary video

All supplementary tables as well as the supplementary video accompanying this chapter can be obtained from the author (s.l.n.maas-4@umcutrecht.nl).

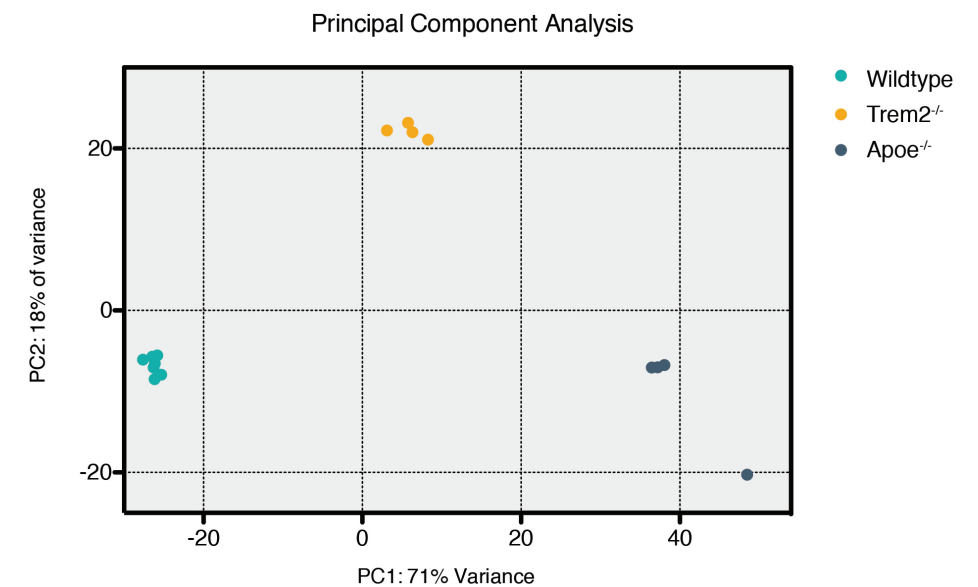
Supplementary Figures



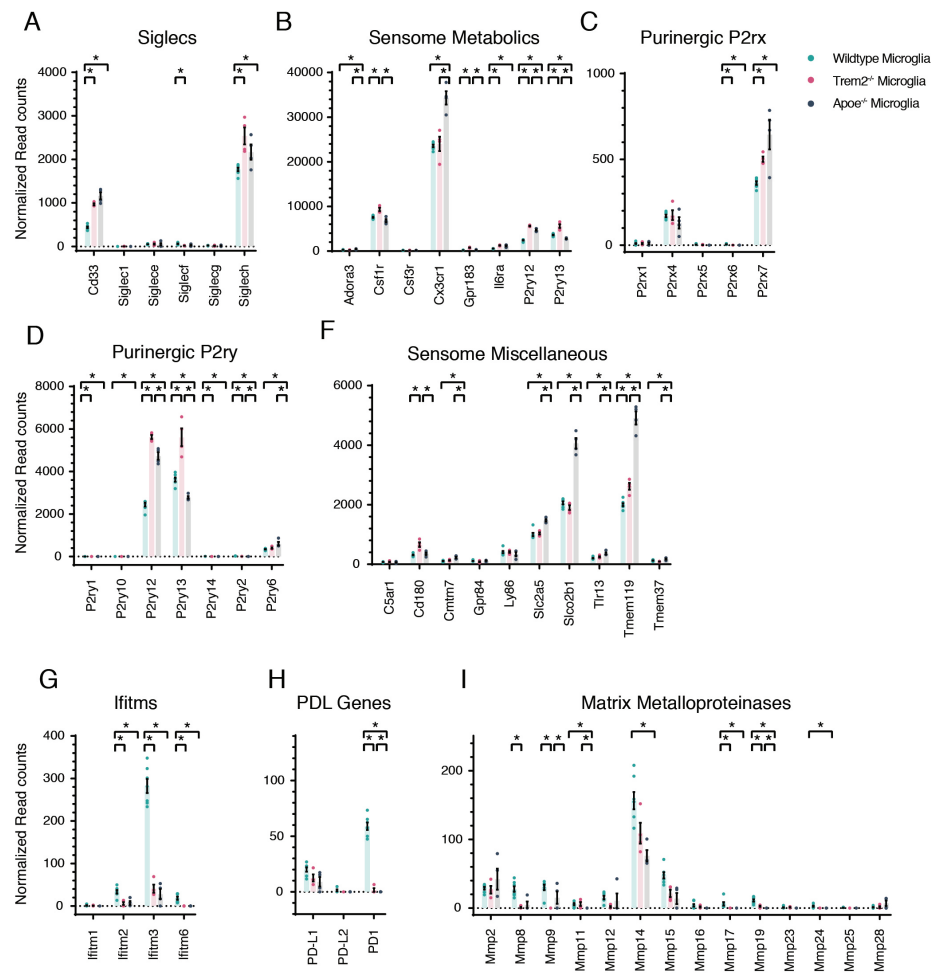
Suppl. Figure S1. A palmitoylated green fluorescent protein (palmGFP) modified GL261 murine glioma cell-line was used to identify *in vivo* extracellular vesicle transfer. (A) GL261.BpalmGFP cells were modified to express palmitoylated GFP which labels all cellular membranes including that of (released) EVs. (B) Unmerged panels corresponding to figure 1B. Scale bars: (A) 50 μ m (B) 1000 μ m.



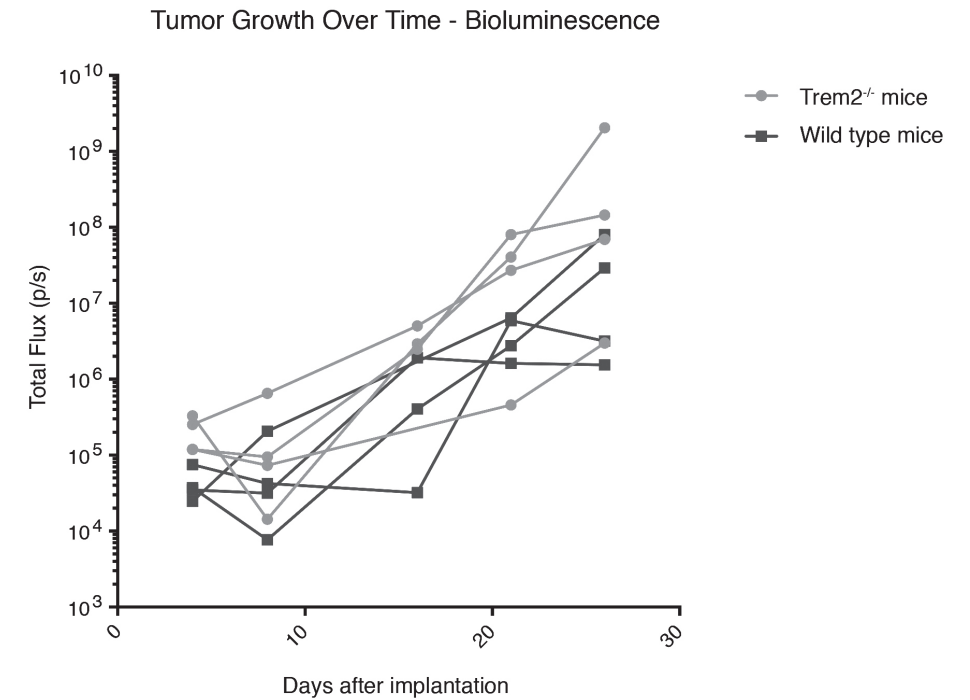
Suppl. Figure S2. UpSet analysis of IL4, IL10, IL6/STAT3, IFN γ and Sensome gene sets. Investigation of gene sets associated with IL4, IL10, IL6/STAT3 and IFN γ pathways as well as the microglial sensome showed mostly unique genes per set.



Suppl. Figure S3. Principal component analysis identifies separate clusters of wildtype microglia, Trem2^{-/-} and Apoe^{-/-} microglia. Principal component analysis was performed on the regularized logarithm (rlog) RNAseq values from wildtype, Trem2^{-/-} and Apoe^{-/-} microglia. Clear separation between the sample groups is observed.



Suppl. Figure S4. Differential expression of Trem2^{-/-} and Apoe^{-/-} versus wildtype microglia. Normalized read counts of genes part of the siglec, sensome metabolics, purinergic p2rx, purinergic p2ry, sensome miscellaneous, ifitm, PD-L1 and matrix metalloproteinases sets, show overall opposite expression compared to glioblastoma microglia. Asterisk (*) indicates significant (multiple testing adjusted p-value < 0.05) differential expression. Error bar represents the SEM, bar represents the mean and dots display individual measurements (wildtype n=7, Trem2^{-/-} and Apoe^{-/-} n=4).



Suppl. Figure S5. Knockout of Trem2 does not affect tumor growth. In vivo bioluminescence imaging of GL261.Fluc.GFP cells implanted intracranially into wild type C57BL6 and Trem2^{-/-} mice over 30 days. No significant difference in growth was detected between wild type and Trem2^{-/-} mice.

References

1. Stupp, R. et al. Effects of radiotherapy with concomitant and adjuvant temozolomide versus radiotherapy alone on survival in glioblastoma in a randomised phase III study: 5-year analysis of the EORTC-NCIC trial. *Lancet Oncol.* **10**, 459–466 (2009).
2. Reardon, D. A. et al. Immunotherapy advances for glioblastoma. *Neuro-oncology* **16**, 1441–1458 (2014).
3. Hickman, S., Izzy, S., Sen, P., Morsett, L. & Khoury, El, J. Microglia in neurodegeneration. *Nature Neuroscience* **21**, 1359–1369 (2018).
4. Ransohoff, R. M. & Khoury, El, J. Microglia in Health and Disease. *Cold Spring Harb Perspect Biol* **8**, a020560 (2015).
5. Jassam, Y. N., Izzy, S., Whalen, M., McGavern, D. B. & Khoury, El, J. Neuroimmunology of Traumatic Brain Injury: Time for a Paradigm Shift. *Neuron* **95**, 1246–1265 (2017).
6. Salter, M. W. & Stevens, B. Microglia emerge as central players in brain disease. *Nat. Med.* **23**, 1018–1027 (2017).
7. Hickman, S. E. et al. The microglial sensome revealed by direct RNA sequencing. *Nature Neuroscience* **16**, 1896–1905 (2013).
8. Li, W. & Graeber, M. B. The molecular profile of microglia under the influence of glioma. *Neuro-oncology* **14**, 958–978 (2012).
9. Hambardzumyan, D., Gutmann, D. H. & Kettenmann, H. The role of microglia and macrophages in glioma maintenance and progression. *Nature Neuroscience* **19**, 20–27 (2016).
10. Poon, C. C., Sarkar, S., Yong, V. W. & Kelly, J. J. P. Glioblastoma-associated microglia and macrophages: targets for therapies to improve prognosis. *Brain* **140**, 1548–1560 (2017).
11. Morantz, R. A., Wood, G. W., Foster, M., Clark, M. & Gollahon, K. Macrophages in experimental and human brain tumors. Part 2: studies of the macrophage content of human brain tumors. *J. Neurosurg.* **50**, 305–311 (1979).
12. Morantz, R. A., Wood, G. W., Foster, M., Clark, M. & Gollahon, K. Macrophages in experimental and human brain tumors. Part 1: Studies of the macrophage content of experimental rat brain tumors of varying immunogenicity. *J. Neurosurg.* **50**, 298–304 (1979).
13. Broekman, M. L. et al. Multidimensional communication in the microenvirons of glioblastoma. *Nat Rev Neurol* **14**, 482–495 (2018).
14. Markovic, D. S. et al. Gliomas induce and exploit microglial MT1-MMP expression for tumor expansion. *Proc. Natl. Acad. Sci. U.S.A.* **106**, 12530–12535 (2009).
15. Markovic, D. S., Glass, R., Synowitz, M., Rooijen, N. V. & Kettenmann, H. Microglia stimulate the invasiveness of glioma cells by increasing the activity of metalloprotease-2. *J. Neuropathol. Exp. Neurol.* **64**, 754–762 (2005).
16. D'Asti, E., Chennakrishnaiah, S., Lee, T. H. & Rak, J. Extracellular Vesicles in Brain Tumor Progression. *Cell Mol Neurobiol* **36**, 383–407 (2016).
17. Maas, S. L. N., Breakefield, X. O. & Weaver, A. M. Extracellular Vesicles: Unique Intercellular Delivery Vehicles. *Trends in Cell Biology* **27**, 172–188 (2017).
18. Cocucci, E. & Meldolesi, J. Ectosomes and exosomes: shedding the confusion between extracellular vesicles. *Trends in Cell Biology* **25**, 364–372 (2015).
19. Tkach, M. & Théry, C. Communication by Extracellular Vesicles: Where We Are and Where We Need to Go. *Cell* **164**, 1226–1232 (2016).
20. de Vrij, J. et al. Glioblastoma-derived extracellular vesicles modify the phenotype of monocytic cells. *Int. J. Cancer* **137**, 1630–1642 (2015).
21. van der Vos, K. E. et al. Directly visualized glioblastoma-derived extracellular vesicles transfer RNA to microglia/macrophages in the brain. *Neuro-oncology* **18**, 58–69 (2016).
22. Lai, C. P. et al. Visualization and tracking of tumour extracellular vesicle delivery and RNA translation using multiplexed reporters. *Nature Communications* **6**, 7029 (2015).
23. Keren-Shaul, H. et al. A Unique Microglia Type Associated with Restricting Development of Alzheimer's Disease. *Cell* **169**, 1276–1290.e17 (2017).
24. Krasemann, S. et al. The TREM2-APOE Pathway Drives the Transcriptional Phenotype of Dysfunctional Microglia in Neurodegenerative Diseases. *Immunity* **47**, 566–581.e9 (2017).
25. Saederup, N. et al. Selective Chemokine Receptor Usage by Central Nervous System Myeloid Cells in CCR2-Red Fluorescent Protein Knock-In Mice. *PLOS ONE* **5**, e13693 (2010).
26. Hickman, S. E., Allison, E. K. & Khoury, El, J. Microglial dysfunction and defective beta-amyloid clearance pathways in aging Alzheimer's disease mice. *J. Neurosci.* **28**, 8354–8360 (2008).
27. Love, M. I., Huber, W. & Anders, S. Moderated estimation of fold change and dispersion for RNA-seq data with DESeq2. *Genome Biol.* **15**, 550 (2014).
28. Leng, L. et al. MIF signal transduction initiated by binding to CD74. *J. Exp. Med.* **197**, 1467–1476 (2003).
29. Ghoochani, A. et al. MIF-CD74 signaling impedes microglial M1 polarization and facilitates brain tumorigenesis. *Oncogene* **35**, 6246–6261 (2016).
30. Weber, C. et al. Macrophage Infiltration and Alternative Activation during Wound Healing Promote MEK1-Induced Skin Carcinogenesis. *Cancer Res.* **76**, 805–817 (2016).
31. Nimmerjahn, A., Kirchhoff, F. & Helmchen, F. Resting microglial cells are highly dynamic surveillants of brain parenchyma in vivo. *Science* **308**, 1314–1318 (2005).
32. Davalos, D. et al. ATP mediates rapid microglial response to local brain injury in vivo. *Nature Neuroscience* **8**, 752–758 (2005).
33. Costa-Silva, B. et al. Pancreatic cancer exosomes initiate pre-metastatic niche formation in the liver. *Nat. Cell Biol.* **17**, 816–826 (2015).
34. Daley, D. et al. Dectin 1 activation on macrophages by galectin 9 promotes pancreatic carcinoma and peritumoral immune tolerance. *Nat. Med.* **23**, 556–567 (2017).
35. Liu, Z. et al. Expression of the galectin-9-Tim-3 pathway in glioma tissues is associated with the clinical manifestations of glioma. *Oncol Lett* **11**, 1829–1834 (2016).
36. Hattermann, K., Held-Feindt, J., Ludwig, A. & Mentlein, R. The CXCL16-CXCR6 chemokine axis in glial tumors. *J. Neuroimmunol.* **260**, 47–54 (2013).
37. Hattermann, K., Ludwig, A., Gieselmann, V., Held-Feindt, J. & Mentlein, R. The chemokine CXCL16 induces migration and invasion of glial precursor cells via its receptor CXCR6. *Mol. Cell. Neurosci.* **39**, 133–141 (2008).
38. Kopatz, J. et al. Siglec-h on activated microglia for recognition and engulfment of glioma cells. *Glia* **61**, 1122–1133 (2013).
39. Kitamura, H. et al. GPR34 is a receptor for lysophosphatidylserine with a fatty acid at the sn-2 position. *J. Biochem.* **151**, 511–518 (2012).
40. Riedl, S. et al. In search of a novel target - phosphatidylserine exposed by non-apoptotic tumor cells and metastases of malignancies with poor treatment efficacy. *Biochim. Biophys. Acta* **1808**, 2638–2645 (2011).
41. Eibinger, G. et al. On the role of 25-hydroxycholesterol synthesis by glioblastoma cell lines. Implications for chemotactic monocyte recruitment. *Exp. Cell Res.* **319**, 1828–1838 (2013).

42. van der Putten, C. et al. Differential expression of adenosine A3 receptors controls adenosine A2A receptor-mediated inhibition of TLR responses in microglia. *J. Immunol.* **182**, 7603–7612 (2009).
43. Cheng, W. et al. Bioinformatic profiling identifies an immune-related risk signature for glioblastoma. *Neurology* **86**, 2226–2234 (2016).
44. Feng, X. et al. Loss of CX3CR1 increases accumulation of inflammatory monocytes and promotes gliomagenesis. *Oncotarget* **6**, 15077–15094 (2015).
45. Morrone, F. B. et al. In vivo glioblastoma growth is reduced by apyrase activity in a rat glioma model. *BMC Cancer* **6**, 226 (2006).
46. Tozaki-Saitoh, H. et al. P2Y12 receptors in primary microglia activate nuclear factor of activated T-cell signaling to induce C-C chemokine 3 expression. *J. Neurochem.* **141**, 100–110 (2017).
47. Pyonteck, S. M. et al. CSF-1R inhibition alters macrophage polarization and blocks glioma progression. *Nat. Med.* **19**, 1264–1272 (2013).
48. Quail, D. F. et al. The tumor microenvironment underlies acquired resistance to CSF-1R inhibition in gliomas. *Science* **352**, aad3018–aad3018 (2016).
49. Arcella, A. et al. In vitro and in vivo effect of human lactoferrin on glioblastoma growth. *J. Neurosurg.* **123**, 1026–1035 (2015).
50. Chao, M. P. et al. Calreticulin is the dominant pro-phagocytic signal on multiple human cancers and is counterbalanced by CD47. *Sci Transl Med* **2**, 63ra94–63ra94 (2010).
51. Bailey, C. C., Zhong, G., Huang, I.-C. & Farzan, M. IFITM-Family Proteins: The Cell's First Line of Antiviral Defense. *Annu Rev Virol* **1**, 261–283 (2014).
52. Fife, B. T. et al. Interactions between PD-1 and PD-L1 promote tolerance by blocking the TCR-induced stop signal. *Nat. Immunol.* **10**, 1185–1192 (2009).
53. Heiland, D. H. et al. Comprehensive analysis of PD-L1 expression in glioblastoma multiforme. *Oncotarget* **8**, 42214–42225 (2017).
54. Schachtele, S. J., Hu, S., Sheng, W. S., Mutnal, M. B. & Lokensgard, J. R. Glial cells suppress postencephalitic CD8+ T lymphocytes through PD-L1. *Glia* **62**, 1582–1594 (2014).
55. Bardhan, K., Anagnostou, T. & Boussiotis, V. A. The PD1:PD-L1/2 Pathway from Discovery to Clinical Implementation. *Front Immunol* **7**, 550 (2016).
56. Lin, H.-C., Song, T.-Y. & Hu, M.-L. S-Adenosylhomocysteine promotes the invasion of C6 glioma cells via increased secretion of matrix metalloproteinase-2 in murine microglial BV2 cells. *Toxicol. Sci.* **112**, 322–330 (2009).
57. PrabhuDas, M. R. et al. A Consensus Definitive Classification of Scavenger Receptors and Their Roles in Health and Disease. in **198**, 3775–3789 (2017).
58. Ransohoff, R. M. A polarizing question: do M1 and M2 microglia exist? *Nature Neuroscience* **19**, 987–991 (2016).
59. Xue, J. et al. Transcriptome-based network analysis reveals a spectrum model of human macrophage activation. *Immunity* **40**, 274–288 (2014).
60. Suzuki, A., Leland, P., Joshi, B. H. & Puri, R. K. Targeting of IL-4 and IL-13 receptors for cancer therapy. *Cytokine* **75**, 79–88 (2015).
61. Wildeboer, D., Naus, S., Amy Sang, Q.-X., Bartsch, J. W. & Pagenstecher, A. Metalloproteinase disintegrins ADAM8 and ADAM19 are highly regulated in human primary brain tumors and their expression levels and activities are associated with invasiveness. *J. Neuropathol. Exp. Neurol.* **65**, 516–527 (2006).

62. Crane, C. A., Ahn, B. J., Han, S. J. & Parsa, A. T. Soluble factors secreted by glioblastoma cell lines facilitate recruitment, survival, and expansion of regulatory T cells: implications for immunotherapy. *Neuro-oncology* **14**, 584–595 (2012).
63. Hu, B. et al. Epigenetic Activation of WNT5A Drives Glioblastoma Stem Cell Differentiation and Invasive Growth. *Cell* **167**, 1281–1295.e18 (2016).
64. Fujieda, S., Sunaga, H., Tsuzuki, H., Fan, G. K. & Saito, H. IL-10 expression is associated with the expression of platelet-derived endothelial cell growth factor and prognosis in oral and oropharyngeal carcinoma. *Cancer Lett.* **136**, 1–9 (1999).
65. Yue, F. Y. et al. Interleukin-10 is a growth factor for human melanoma cells and down-regulates HLA class-I, HLA class-II and ICAM-1 molecules. *Int. J. Cancer* **71**, 630–637 (1997).
66. Taylor, A., Verhagen, J., Blaser, K., Akdis, M. & Akdis, C. A. Mechanisms of immune suppression by interleukin-10 and transforming growth factor-beta: the role of T regulatory cells. *Immunology* **117**, 433–442 (2006).
67. Ishihara, Y., Takemoto, T., Itoh, K., Ishida, A. & Yamazaki, T. Dual role of superoxide dismutase 2 induced in activated microglia: oxidative stress tolerance and convergence of inflammatory responses. *J. Biol. Chem.* **290**, 22805–22817 (2015).
68. Liu, Q. et al. IL-6 promotion of glioblastoma cell invasion and angiogenesis in U251 and T98G cell lines. *J Neurooncol* **100**, 165–176 (2010).
69. Weissenberger, J. et al. IL-6 is required for glioma development in a mouse model. *Oncogene* **23**, 3308–3316 (2004).
70. Wang, H. et al. Targeting interleukin 6 signaling suppresses glioma stem cell survival and tumor growth. *STEM CELLS* **27**, 2393–2404 (2009).
71. Okada, M. et al. Tumor-associated macrophage/microglia infiltration in human gliomas is correlated with MCP-3, but not MCP-1. *Int. J. Oncol.* **34**, 1621–1627 (2009).
72. Levy, A. et al. CD38 deficiency in the tumor microenvironment attenuates glioma progression and modulates features of tumor-associated microglia/macrophages. *Neuro-oncology* **14**, 1037–1049 (2012).
73. Zaidi, M. R. & Merlino, G. The two faces of interferon- γ in cancer. *Clin. Cancer Res.* **17**, 6118–6124 (2011).
74. Tarassishin, L., Casper, D. & Lee, S. C. Aberrant expression of interleukin-1 β and inflammasome activation in human malignant gliomas. *PLOS ONE* **9**, e103432 (2014).
75. Cohen, M. et al. Chronic exposure to TGF β 1 regulates myeloid cell inflammatory response in an IRF7-dependent manner. *EMBO J.* **33**, 2906–2921 (2014).
76. Li, Z. et al. Interferon Regulatory Factor 7 Promoted Glioblastoma Progression and Stemness by Modulating IL-6 Expression in Microglia. *J Cancer* **8**, 207–219 (2017).
77. Butovsky, O. et al. Identification of a unique TGF- β -dependent molecular and functional signature in microglia. *Nature Neuroscience* **17**, 131–143 (2014).
78. Joseph, J. V., Balasubramanian, V., Walenkamp, A. & Kruyt, F. A. E. TGF- β as a therapeutic target in high grade gliomas - promises and challenges. *Biochem. Pharmacol.* **85**, 478–485 (2013).
79. Hickman, S. E. & Houry, E. J. TREM2 and the neuroimmunology of Alzheimer's disease. *Biochem. Pharmacol.* **88**, 495–498 (2014).
80. Gong, Y. et al. Microglial dysfunction as a key pathologic change in adrenomyeloneuropathy. *Ann. Neurol.* (2017). doi:10.1002/ana.25085
81. Pimenova, A. A., Marcora, E. & Goate, A. M. A Tale of Two Genes: Microglial Apoe and Trem2. *Immunity* **47**, 398–400 (2017).

82. Szulzewsky, F. et al. Human glioblastoma-associated microglia/monocytes express a distinct RNA profile compared to human control and murine samples. *Glia* **64**, 1416–1436 (2016).
83. Mirzaei, R., Sarkar, S. & Yong, V. W. T Cell Exhaustion in Glioblastoma: Intricacies of Immune Checkpoints. *Trends Immunol.* **38**, 104–115 (2017).
84. Ren, S. X. et al. Host immune defense peptide LL-37 activates caspase-independent apoptosis and suppresses colon cancer. *Cancer Res.* **72**, 6512–6523 (2012).
85. Chen, X. et al. DNA methylation directly downregulates human cathelicidin antimicrobial peptide gene (CAMP) promoter activity. *Oncotarget* **8**, 27943–27952 (2017).
86. Darwich, L. et al. Secretion of interferon-gamma by human macrophages demonstrated at the single-cell level after costimulation with interleukin (IL)-12 plus IL-18. *Immunology* **126**, 386–393 (2009).
87. Wang, X. & Suzuki, Y. Microglia produce IFN-gamma independently from T cells during acute toxoplasmosis in the brain. *J. Interferon Cytokine Res.* **27**, 599–605 (2007).
88. Kraaij, M. D. et al. Human monocytes produce interferon-gamma upon stimulation with LPS. *Cytokine* **67**, 7–12 (2014).
89. Kawanokuchi, J. et al. Production of interferon-gamma by microglia. *Mult. Scler.* **12**, 558–564 (2006).
90. Okawa, S. et al. Proteome and Secretome Characterization of Glioblastoma-Derived Neural Stem Cells. *STEM CELLS* **35**, 967–980 (2017).
91. Sin, W. C. et al. Astrocytes promote glioma invasion via the gap junction protein connexin43. *Oncogene* **35**, 1504–1516 (2016).
92. Sena-Esteves, M., Tebbets, J. C., Steffens, S., Crombleholme, T. & Flake, A. W. Optimized large-scale production of high titer lentivirus vector pseudotypes. *Journal of Virological Methods* **122**, 131–139 (2004).
93. Lai, C. P. et al. Dynamic Biodistribution of Extracellular Vesicles in Vivo Using a Multimodal Imaging Reporter. *ACS Nano* **8**, 483–494 (2014).
94. McCabe, J. B. & Berthiaume, L. G. Functional Roles for Fatty Acylated Amino-terminal Domains in Subcellular Localization. *Mol. Biol. Cell* **10**, 3771–3786 (1999).
95. Maas, S. L. N. et al. Possibilities and limitations of current technologies for quantification of biological extracellular vesicles and synthetic mimics. *J Control Release* **200**, 87–96 (2015).
96. Liberzon, A. et al. The Molecular Signatures Database (MSigDB) hallmark gene set collection. *Cell Syst* **1**, 417–425 (2015).
97. Conway, J. R., Lex, A. & Gehlenborg, N. UpSetR: An R Package for the Visualization of Intersecting Sets and their Properties. *Bioinformatics* (2017). doi:10.1093/bioinformatics/btx364
98. Chen, H. & Boutros, P. C. VennDiagram: a package for the generation of highly-customizable Venn and Euler diagrams in R. *BMC Bioinformatics* **12**, 35 (2011).

6

Summary and Discussion

Summary

Chapter one provides an overview of glioblastoma and the glioblastoma microenvironment. In adult patients, glioblastoma is the most common and lethal primary malignancy of the central nervous system. The bleak statistics associated with glioblastoma patients underline the need to better understand glioblastoma biology in order to identify new therapeutic targets. In the past years, large-scale genomic analyses have identified important cellular pathways involved in glioblastoma biology and currently three molecular subtypes of glioblastoma are defined¹. In isocitrate dehydrogenase (IDH) wildtype glioblastoma, proneural, classical, and mesenchymal subtypes are recognized¹. Extensive research is ongoing to determine (novel) drugs can be identified that specifically target glioblastoma tumors that predominantly express genes associated with one of the three subclasses. So far these searches have not led to the routine application of new drugs for glioblastoma patients. Although the term “mesenchymal glioblastoma” may infer that this subtype is particularly composed of non-glioblastoma cells, all glioblastoma tumors contain many non-tumor cells that form the tumor microenvironment². These non-tumor cells are for instance the endothelial cells of (newly formed) blood vessels, astrocytes, neurons, monocytes, macrophages and microglial cells². Within this microenvironment there are many methods of intercellular communication. This communication may be due to direct cellular contact, secreted molecules or extracellular vesicles (EVs). EVs, including exosomes and microvesicles, are vesicles sized approximately 50 to 10,000 nm, released from all cells through different cellular pathways and contain a heterogeneous combination of donor cell derived molecular contents³. In this thesis the transfer of glioblastoma cell derived EVs cells to monocytes, macrophages and microglia is investigated *in vitro* and *in vivo*. Due to their small size, EVs cannot be detected by conventional techniques such as light microscopy and traditional cell-based flowcytometry. To characterize EVs, research groups started to use techniques more suitable for the nano-sized range. These techniques include; tunable resistive pulse sensing (tRPS), nanoparticle tracking analysis (NTA) and high-resolution flow-cytometry (hFC)⁴. However, as these techniques were not designed with heterogeneous EVs in mind, their application in the EV-field has to be tested and validated.

In **chapter two** tRPS for the characterization of EVs is introduced and discussed. In tRPS, particles are detected as they alter the ionic current through a nano-sized pore. The rate, magnitude and speed of these disruptions is compared to the rate,

magnitude and speed of disruption induced by polystyrene beads of known diameter and concentration. Based on the calibration metrics, the diameter and concentration of the unknown sample can be calculated⁵. However, when working with a heterogeneous sample such as EVs, the larger particles often clog the nanopore resulting in disrupted measurements or measurements with different parameters (for example an altered baseline current), so that direct comparison to the calibration sample is impossible. In this chapter we introduce a modified tRPS approach in which the calibration particles are added to the sample of analysis. This “spiked” sample can then be run on the platform and after the run the ratio between large (calibration particles) and small (EVs) particles can be calculated. Since the concentration of the calibration particles is known, the concentration of the EVs can be easily extracted. This method enabled us to measure the concentration of EV-sized particles in small (30µl) biological fluids such as pleural fluid, urine and plasma. This modified tRPS methodology was then applied to test if interference in cellular pathways involved with EV release can lead to reduced EV secretion in glioblastoma cells. To accomplish this we introduced a short hairpin RNA (shRNA) in a glioblastoma cell line targeting Rab27b, involved in the docking of multivesicular bodies containing exosomes to the cellular membrane⁶. We were then able to detect a reduced amount of EVs in the cell culture supernatant directly, as well as after specific isolation of EVs using iodixanol based gradient ultra-centrifugation. Exploring this technique further we demonstrated its ability to detect non-significant differences between the calculated stock concentration between different EV dilutions and non-significant changes between multiple EV freeze-thaw cycles.

In **chapter three**, two additional specialized techniques for the characterization of EVs are evaluated and compared. Using (fluorescent) polystyrene beads, liposomes and EVs isolated from a glioblastoma and a lymphoblastoma cell line, the possibilities and limitations of tRPS, NTA and hFC were evaluated. For each of the three techniques we showed that they have a technical “detection threshold” that determines whether or not EVs can be detected. For tRPS, we showed that the particle volume required to disrupt the ionic flow above background noise levels defines the detection threshold. This threshold is a major contributor to inter-experimental differences to the obtained EV concentration. For EV measurements the volume of the smallest EV in the sample is unknown, and thus this could lead to underestimations of the true EV concentration as the smallest EVs are simply not detected. Similarly, NTA has detection threshold defined as the amount of light scattering required for a particle to be detected. This detection threshold, together with the shutter speed and gain settings of the CCD

camera, all significantly influence the quantification obtained from a NTA measurement. In hFC, the detection threshold was already defined previously and is based on the fluorescent threshold that EVs need to surpass in order to be detected⁷. For tRPS, NTA and hFC we were able to accurately measure dilutions of polystyrene beads, liposomes and EVs indicating that for each of the platforms individually, different concentrations between samples can accurately be detected. However, when directly comparing the concentrations obtained of liposomes and EVs by tRPS, NTA and hFC, significant differences between the machines were detected. The only exception to this was the EV concentration obtained by tRPS and hFC as it showed a non-significant difference.

In **chapter four** we applied the obtained knowledge on the characterization of EVs to different sets of glioblastoma derived EVs. By comparing the cell counts to the concentration of EVs in supernatant or isolated EV preparations, we identified differences between the EV-to-cell ratios for nine different primary cultures of glioblastoma stem-like cells. We detected the highest amounts of EVs per cell in three cultures from predominantly mesenchymal glioblastoma subtypes. Using proteomic analysis we then further investigated the contents of EVs and detected a selected upregulation of proteins involved in the proliferation, movement and phagocytosis of monocytes/macrophages. To test if these proteins were functional, we incubated peripheral blood mononuclear cells (PBMCs) with glioblastoma derived EVs. By comparing the incubation with glioblastoma EVs to control settings, we detected increased proliferation of monocytes in the glioblastoma EV setting. Simultaneously, co-incubation with glioblastoma derived EVs was associated with decreased monocytic HLA-DR expression, similar to the phenotype of circulating monocytes in glioblastoma patients⁸. To further investigate the effects of glioblastoma derived EVs on macrophage functions, we then co-incubated monocytes with EVs from non-tumor origins and from primary glioblastoma cultures. In macrophages that were co-cultures with glioblastoma derived EVs, we detected increased levels of markers associated with tumor supportive functions (e.g. CD163) as well as increased phagocytic function and cytokine production (e.g. VEGF, IL4, IL6, IL10 and IFN γ). In a similar experiment co-incubating primary human microglia with glioblastoma derived EVs, we detected an increase in MT1-MMP (MMP14), a key matrix metalloproteinase involved in the remodeling of the glioblastoma extracellular matrix. Overall, *in vitro* co-incubation of glioblastoma derived EVs with primary monocytes, macrophages or microglia led to the upregulation of markers associated with tumor supportive functions.

In **chapter five** *in vivo* analyses of the mRNA expression of microglial cells, including microglial cells that took up glioma derived EVs, was presented. Using murine glioma cells modified to express a palmitoylated-GFP reporter, all cellular lipid bilayers are GFP positive including the cell's derived EVs⁹. This system enabled us to isolate monocytes, macrophages and microglia from control mice (no tumor) and microglia from tumor bearing brains with (EV-GFP^{pos}) or without EV-GFP (EV-GFP^{neg}) uptake. The uptake of EV-GFP only occurs in or near the tumor suggesting that the EV-GFP status can be used to detect microglia that closely interact with the tumor cells. Using mRNA sequencing we detected that the EV-GFP status was associated with marked differences in microglia mRNA expression whereas the monocytes and macrophages were only minimally changed when comparing EV-GFP^{pos} versus EV-GFP^{neg} cells. For microglia though, the EV-GFP^{pos} cells showed the most distinctly altered mRNA expression compared to control microglia. When analyzing the overall expression of cytokine associated gene sets, we showed that the glioma *in vivo* microglial activation is much more subtle than the previously assumed binary IFN γ "M1 tumor-suppressive" or IL-4 "M2 tumor-supportive" differentiation. In fact, we detected activation of IL-4, IL-10, IL6/STAT3 as well as IFN γ associated genes, covering a large part of different reported *in vitro* differentiation states¹⁰. When diving deeper into specific microglial functions we investigated the three essential microglial functions: sensing of changes in the environment, host defense and homeostasis. We found significant changes in all three microglial functions when comparing tumor microglia to control microglia. EV-GFP^{pos} microglia have significantly reduced expression of microglia senseome genes with 48% of senseome genes significantly downregulated versus only significant upregulation of 9% of senseome genes. For host defense we detected, among others, significant upregulation of *Pd-11* and *Pd-12* suggesting a reduced T-cell response in the tumor microenvironment. Homeostasis in microglia isolated from tumor brains was altered with significant upregulation in genes involved with phagocytosis and the degradation of the extracellular matrix (ECM). Together these results suggested major changes to the microglial gene expression with reduced capabilities in the sensing of pathological (malignant) signals, with simultaneously reduced host defense functions and increased capacity to clear debris and the ECM.

To further investigate if we could identify regulators for the observed patterns, we explored reported microglial regulatory pathways. In normal, non-diseased settings, TGF- β regulates microglia homeostasis¹¹. In glioma microglia, we detected downregulation of TGF- β and key TGF- β regulated genes. Simultaneously, in

neurodegeneration, a pathway containing Triggering receptor expressed on myeloid cells 2 (TREM2) and apolipoprotein E (APOE) has been suggested to be a key regulator of microglial gene expression when the homeostatic TGF- β regulation is disrupted^{12,13}. This regulation is in part TREM2 dependent and in part TREM2 independent. In glioma associated microglia we found significant downregulation of *Trem2*, yet significant upregulation of *ApoE*. Using RNA sequencing from *Trem2* and *ApoE* knockout mice, we identified that the observed changes in the microglial sensome, host-defense and homeostasis genes are *Trem2* independent, more likely *ApoE* dependent. To further substantiate these observations we analyzed published RNA sequencing data from human control and glioblastoma macrophage/microglia¹⁴, in which we also detected significant upregulation of *APOE* and *APOE* dependent genes whereas *TREM2* levels were not significantly changed.

Overall, we established a model in which EVs can be used to identify the microglia that are most actively interacting with glioma cells. These microglia cells express a gene pattern that is *Trem2* independent, most likely *ApoE* dependent that includes the activation of multiple cytokine associated gene patterns, decreased sensing and host defense as well as disturbed TGF- β regulated homeostasis. By injecting glioma derived EVs in the brains of control mice, we were able to replicate some of the observed patterns suggestion that at least some of the tumor associated gene activation patterns is associated with glioma EV-uptake.

Discussion

Characterization of EVs

As discussed extensively throughout this thesis, EVs are a heterogeneous group of lipid bilayer vesicles differing in diameter and molecular building blocks³. When setting up experiments, this fact underlines the major challenge researchers are faced with when trying to figure out the quantity of EVs. Over time, different approaches have been applied to solve this problem ranging from bulk analysis to more sophisticated (optimized) single particle analyses^{4,15,16}. When Clothilde Thery et. al. published their extensive manuscript filled with protocols for the isolation and characterization of exosomes in 2006, only indirect quantification methods were described¹⁷. In this publication, that helped spark the broad interesting in EVs, immunoblotting of specific exosome proteins, total protein analysis using the Bradford assay, as well as exosome

quantification using exosome surface marker-receptor binding to latex beads are described¹⁷. Although these measurements can indeed give a rough estimation of the vesicle concentration, differences in the quantity of (surface) proteins or protein levels per EVs can result in over- and underestimation of true EV concentrations. We attempted to evaluate the validity of novel methods that measure individual particles rather than EV-related proteins. Although the detection of individual particles is most likely an improved method to obtain EV concentrations, multiple variables and technical limitations still hamper us to obtain the true vesicle concentration of an experimental sample. The first limitation is the absence of a gold standard. In our experiment comparing an EV sample using NTA, tRPS and hFC we obtained significant higher concentrations using NTA compared to the other techniques. This is in line with a later study that compared the quantification of EVs obtained from the cerebrospinal fluid (CSF) of glioblastoma patients using NTA, tRPS and an EV-optimized flowcytometry instrument (different instrument, settings and fluorescent marker compared to our setup)^{18,19}. In this CSF experiment NTA also obtained higher concentrations compared to tRPS and flowcytometry. In a different study using EVs isolated from the urine of healthy donors, comparable levels of EVs were obtained for NTA and tRPS with 15-fold lower levels for (again) a different EV-optimized flowcytometry instrument²⁰. Although NTA is likely to detect protein contaminants as particles, especially at more sensitive instrument settings^{21,22}, without a gold standard we cannot distinctly determine if the higher concentration is due to these protein particles or that the NTA detected EVs the other systems simple missed.

Our extensive evaluation of the NTA, tRPS and hFC instruments did determine that by using the same settings, we are able to accurately detect sample dilutions regardless of instrument settings. This implies that in general, isolations of EV samples can be compared using the same instrument at the same settings. However, as each instrument uses specific physical properties of the EVs, interfering with these properties may result in inaccurate quantifications. For example, we showed reduced levels of EV secretion after the introduction of shRNA against Rab27b using tRPS. Although interference of Rab27b was shown not to alter the expression of specific EV-related proteins⁶, it is unknown if Rab27b interference results in smaller EVs that are simply below the tRPS detection threshold. Alternatively, EVs that are too large will not pass through the opening and will also escape detection. For optical system such as NTA and hFC particle diameter also has a major influence on the detection of particles²³. As the scattering of light for particles smaller than 1/10 of the wavelength of the light used,

differ 10^6 times when the diameter changes just 10 times, the volume of the particle has a tremendous influence on the detectability of EVs²⁴. Secondly, interference in intercellular pathways may also result in different EV protein incorporation, a second mode for altered light scattering of EVs^{3,25,26}. However, so far it is unknown to what extent (surface bound) EV proteins influence the EV light scattering²⁷.

Setting up single particle EV analyses often requires the utilization of non-EV controls for quantitative or system calibration. We have used polystyrene and calcein fluorescent silica beads as controls for dilution and sizing experiments. Although applicable for these experiments, polystyrene and silica beads do differ in their optical properties compared to EVs²⁷. First, these particles have refractive indexes (RI) that are higher than that of EVs. Smaller EVs (<200 nm) have RIs of 1.37-1.39, with slightly higher RIs for EVs >200 nm (1.40-1.41), most likely due to increase protein levels²⁷. Polystyrene and silica beads have higher RIs (1.47 and 1.63, respectively) that will allow for the detection of smaller particles due to increased light scattering at smaller volume. Ideally, EVs of known diameter and contents are developed that could help individual labs to set up standardized settings for the characterization of EVs to make intra- and inter-laboratory results more comparable. In fact, an international effort to measure the inter-laboratory variance in tRPS EV quantification using aliquots of a single EV isolation found inter-laboratory coefficients of variance of 52.5%²⁸.

Overall, we identified methods for the characterization of EVs at the single particle level. For each instrument specific variables determine the quantification thus making direct comparisons by between instruments impossible. Within an instrument, in general, accurate differences between samples can be detected. To facility the reproducibility of EV characterization using NTA, tRPS or hFC it is important that all variables are recorded and reported. Fortunately these recommendations are now part of the minimal informations for studies on EVs (MISEV) that also suggest to perform two different but complementary techniques for accurate characterization of EVs²⁹.

Interaction between glioblastoma and monocytes, macrophages and microglia cells

In the tumor microenvironment glioblastoma cells interact with stromal cells both directly and indirectly². The indirect interaction occurs both through secreted molecules, including different cytokines, as well as EVs^{2,30,31}. A decade ago, glioblastoma derived EVs were reported to transfer (mutated) mRNA to both other glioblastoma cells and

endothelial cells *in vitro*^{32,33}. As infiltrating monocytes, macrophages and microglial cells make up a significant proportion of the tumor mass^{31,34}, we investigated the transfer to those cells of glioblastoma derived EVs both *in vitro* and *in vivo*.

In vitro, our results suggest that in general, monocyte to macrophages differentiation in the presence of glioblastoma derived EVs, induces the production of proteins with ascribed tumor supporting functions. Although our *in vitro* analysis of glioblastoma EV incubation with microglial cells was limited, others have studied this in more detail and obtained data that show similarities to our monocyte to macrophage differentiation data³⁵. By incubating mouse microglial with glioma EVs, increased cytokine production including IL6, was observed for a subset of cytokines analysed³⁵. This study also suggested a possible mechanism for the observed effects, as EV-mediated micro-RNAs (miR) miR-21 and miR-451 transfer lowered microglial cMyc mRNA levels. Although later analyses by a different group showed that EV-associated miR-451 detection is most likely a contaminant from the bovine serum used in *in vitro* studies, highlighting the difficulties with *in vitro* EV experiments³⁶. Further *in vivo* experiments should try to validate the role of glioblastoma EV-mediated miR-21 transfer on microglial gene expression.

Although interesting results were obtained, *in vitro* EV experiments are by definition biased and will not accurately recapitulate the complex *in vivo* glioblastoma (micro) environment. One of the major biases is introduced by the method of EV isolation. In general, smaller and larger EVs exist based on the cellular pathway from which they originate (exosomal, multivesicular body derived versus surface blebbing)³⁷. The (ultra)centrifugation protocols used will subselect for specific subpopulations of EVs, or can even induce aggregation of EVs^{38,39}. The recent discovery that even a clonal glioblastoma cell-line releases at least 11 different EV subpopulations further underlines the complexity of EV subpopulations⁴⁰. Additionally, the EV release by a clonal cell-line cultured *in vitro* may not recapitulate the spatiotemporal characteristics of glioblastoma EV release *in vivo*. For example, our results suggest that glioblastoma tumors with a predominant genetic profile of the mesenchymal subtype, release the most EVs per cell⁴¹. As increased expression of Rab27a, one of the key genes involved in EV release, is part of the cluster of genes defining the mesenchymal subtype, it's not known if the observed association represents a phenomenon part of a biological subgroup of glioblastoma cells, or is merely due to the selection of glioblastoma cells more actively releasing EVs through upregulated levels of Rab27a^{6,42}. Either way, as

single cell analysis of glioblastoma tumors has established that all subgroups are present in a single tumor, different parts of the tumor may release more EVs than others^{1,43}. Other than spatial, the temporal properties of EVs in the glioblastoma microenvironment are unknown. It is reported that hypoxia induces the release of EVs with different properties⁴⁴. As glioblastoma tumors grow in volume, different areas may become hypoxic over time⁴⁵. This may imply that different areas may release different types of EVs over time. Lastly, it is unknown at what concentration EVs are present in a glioblastoma tumor, again introducing an unknown variable that force researchers to pick one or multiple EV concentrations, rather than being able to model true *in vivo* concentration. These arguments imply that *in vitro* analysis of EVs can be attempted to solve some questions regarding the role of EVs in glioblastoma biology, yet *in vivo* validation should be attempted to address the arguments raised.

We investigated EVs *in vivo* by implanting a murine glioma cell-line modified to express a palmytilated green fluorescent (palmGFP) reporter⁹. With the palmGFP reporter, all cellular (derived) lipid bilayers are GFP positive and thus EV release can be detected and monitored *in vivo*⁹. We implanted these cells in a C57BL6.CCR2^{RFP/WT} mouse model in which mice express red fluorescent protein (RFP) in peripheral monocytes and monocyte-derived macrophages, but not in microglia^{46,47}. By including fluorescent antibodies to Cd45, Cd11b, Ly6c and F4/80 we detected *in vivo* EV-GFP uptake in the three cell types of interest^{48,49}. Although some significant changes in mRNA expression could be detected in monocytes and macrophages when compared for EV-GFP status, much stronger changes were detected in microglia. This raises the question to what extend the observed EV-induced changes in monocytes and macrophages observed and discussed in chapter four, are present in the *in vivo* tumor microenvironment. It could indicate that *in vivo*, other factor such as secreted cytokines dominate the mRNA expression patterns in infiltrating monocytes and macrophages^{50,51}. Alternatively, since we performed pooled RNA sequencing, we were unable to detect EV-induced changes at the single cell level. For microglia we showed that EV-GFP uptake only occurs in and near the tumor, whereas EV-GFP^{neg} microglia can be detect both in, near and away from the tumor. Thus, the EV-GFP^{pos} microglia, represent a population of microglia that are closely associated with the tumor and thus allowed us to investigate the mRNA expression patterns in glioma microglia. Interestingly, in microglia, some of the observed *in vitro* EV-uptake associated changes were also present in the EV-GFP^{pos} tumor microglia, as well as in the EV-GFP^{pos} microglia isolated from non-tumor bearing brains 16h after glioblastoma EV injection. These changes include

the significant upregulation of Mt1-mmp (Mmp14), a key metalloproteinase in the glioblastoma microenvironment^{52,53}.

Traditionally, it was assumed that depending on environmental cues, macrophages and microglia would differentiate into one of two possible differentiation states. This binary model assumed either a “classical” M1 (IFN γ induced) or “alternative” M2 (IL-4 induced) differentiation⁵⁴. This was mostly based on *in vitro* studies where differentiating monocytes were stimulated and a limited set of markers was profiled after stimulation. Although these models were later expanded to include subtypes of the M2 class (M2a, M2b and M2c), *in vivo* profiling of glioblastoma associated macrophages, revealed upregulation of genes part of all M2 subclasses as well as M1 genes^{14,55,56}. By examining the expression of genesets induced by different cytokines covering all of the M1, M2a, M2b and M2c subclasses, we showed that for *in vivo* glioma associated microglia, similar upregulation of all subclasses can be observed. This includes many genes part of the IFN γ (“M1”) associated gene sets, including IFN γ itself. This (again) underscores that the M1/M2 model is inaccurate and more relevant disease specific microglia differentiation should be studied⁵⁴.

This disease specific microglial phenotype (microglia_{Glioblastoma}) expresses multiple sets of altered mRNAs that warrant further discussion. The three major microglia functions are: sensing of changes in their environment, host defense to ensure neuroprotection and homeostasis⁵⁷. By evaluating the mRNA expression in EV-GFP^{neg} and EV-GFP^{pos} tumor microglia, we detected significant changes in all three of the essential microglial functions. Perhaps the most pronounced changes were detected in expression of sensing genes. The 100 genes identified to regulate microglial sensing are termed the microglial “sosome”⁵⁸. In the tumor context, microglia_{Glioblastoma} the expression of the majority ofosome genes are downregulated, suggesting that the microglia have reduced capacity to detect pathogenic changes in their surroundings. This could potentially explain why microglia heavily infiltrate glioblastoma tumors, yet are unable to stop malignant progression. Even if “danger signals” would be identified, a proper response to fight off the malignant cells is most likely reduces as we identified significant alteration in the genes involved in the microglia host-defense arsenal. For example, both *Pd-11* and *Pd-12* are significantly upregulated in tumor microglia (both EV-GFP^{neg} and EV-GFP^{pos}). This suggests that, overall host-defense is reduced as increased PD-L1/PD-L2 expression by either tumor or stromal cells, results in reduced T-cell anti-tumor response⁵⁹. Drug based interference of PD-L1/PD1 binding has led

to improved survival in multiple different malignancies and is now part of standard clinical practice in lung cancer (adenocarcinoma and squamous cell carcinoma) and melanoma patients⁵⁹. Although interference with the PD-L1/PD1 axis in glioblastoma patients seems attractive, results so far have been disappointed. In the Phase 3 CheckMate-143 study for recurrent glioblastoma patients, no survival benefit was observed for patients receiving Nivolumab (PD1 antagonist) compared to a VEGF antagonist (Bevacizumab)⁶⁰. As PD1/PD-L1 interference trials for newly diagnosed glioblastoma patients are ongoing^{61,62}, preclinical murine research suggests that combinational therapy of anti-PD1, anti-CTLA and an oncolytic herpesvirus expressing murine IL-12, can boost the macrophage/microglia infiltration and T-cell effector cells resulting in effective clearing of glioma cells⁶³. This suggests that additional activation and infiltration of innate immune cells into the glioblastoma tumor is required for adequate T-cell response. As IFN γ was shown to be a central activator of the macrophage/microglia and T-cell response, boosting the increased expression of IFN γ in microglia_{Glioblastoma} that we detected even further, may be an alternative pharmaceutical approach for more efficient PD1/PD-L induced T-cell response⁶³.

Concerning the homeostatic capacity of microglia, we detected significant changes in the genes associated with TGF- β , including its key downstream effector Smad3, that are part of the homeostatic microglial transcriptional network¹¹. Simultaneously the EV-GFP^{pos} microglia, express significantly downregulated levels of *Trem2* and significantly upregulated levels of *Apoe* and *Apoe* associated genes^{64,65}. In neurodegenerative diseases, including Alzheimer's disease, microglia also display altered mRNA expression patterns compared to homeostatic TGF- β regulated control settings^{12,13}. By single cell sequencing of Alzheimer's disease associated microglia, homeostatic (TGF- β regulated), intermediate and diseased microglia were identified¹². This progression was shown to be independent of *Trem2* in the progression of homeostatic microglia to intermediate microglia and dependent on *Trem2* when intermediate microglia differentiated to diseased microglia. By profiling Alzheimer's, amyotrophic lateral sclerosis (ALS) and multiple sclerosis (MS) murine microglia, other researches also identified the central role for the Trem2-Apoe pathway in the differentiation of normal to diseased microglia¹². In our experiments profiling microglia from Trem2^{-/-} and Apoe^{-/-} mice, as well as tumor growth experiments in Trem2^{-/-} mice, we established that the microglia_{Glioblastoma} profile is *Trem2* independent, more likely *Apoe* dependent. Thus, although the underlying pathological conditions are vastly different, diseased microglia in the both the context of glioma and neurodegenerative diseases may share

some common *Apoe* regulated molecular pathways and differentiation states. Further experiments should be performed though in which microglia_{Glioblastoma} are profiled at the single cell level, as this will be necessary to determine if microglia_{Glioblastoma} also have an intermediate state that may be more dependent on *Trem2*. Secondly, to determine the overall influence of microglia *Apoe* expression on glioblastoma growth, the generation of mouse models in which *Apoe* knockout is microglia promotor specific supplemented by *Apoe* overexpression models, will be needed.

To what extent the observed mRNA expression in mouse microglia_{Glioblastoma} can be translated to human microglia patients and to what extent the observed patterns are induced by glioblastoma derived EVs, remains to be investigated. So far the mouse microglia sensome has not been validated in human microglia. Although overall mRNA expression between human and mouse microglia was reported to be similar (Pearson's $r = 0.806$), 13% of mouse sensome genes were among the genes preferentially upregulated in mouse microglia⁶⁶. Therefore, further identification and confirmation of the "human microglia sensome" is needed to draw definitive conclusions regarding the sensing capacity of human glioblastoma associated microglia. Although the application of the palmGFP model helped us to address many of the issues regarding *in vitro* EV research outlined before, this model can still only allow for the identification of EV-associated changes rather than EV-directed changes. For example, EV-GFP^{pos} microglia can express an mRNA pattern that is completely induced by tumor secreted cytokines in which EV uptake is simply a bystander rather than a regulator. However, since we were able to confirm some of the changes in microglia that took up injected glioma derived EVs in non-tumor bearing brains, this suggests that at least some of the observed changes are due to EV-uptake. Overall though, by profiling microglia that took up tumor derived EVs, we were able to study the mRNA expression of microglia most closely associated with the tumor, that led us to identify major changes to the three key microglial functions.

References

1. Wang, Q. *et al.* Tumor Evolution of Glioma-Intrinsic Gene Expression Subtypes Associates with Immunological Changes in the Microenvironment. *Cancer Cell* **32**, 42–56.e6 (2017).
2. Broekman, M. L. *et al.* Multidimensional communication in the microenvirons of glioblastoma. *Nature Reviews Neurology* **14**, 482–495 (2018).
3. Maas, S. L. N., Breakefield, X. O. & Weaver, A. M. Extracellular Vesicles: Unique Intercellular Delivery Vehicles. *Trends in Cell Biology* **27**, 172–188 (2017).
4. van der Pol, E., Coumans, F., Varga, Z., Krumrey, M. & Nieuwland, R. Innovation in detection of microparticles and exosomes. *J Thromb Haemost* **11**, 36–45 (2013).
5. DeBlois, R. W. & Wesley, R. K. Sizes and concentrations of several type C oncornaviruses and bacteriophage T2 by the resistive-pulse technique. *J. Virol.* **23**, 227–233 (1977).
6. Ostrowski, M. *et al.* Rab27a and Rab27b control different steps of the exosome secretion pathway. *Nat Cell Biol* **12**, 19–30– sup pp 1–13 (2010).
7. Nolte-’t Hoen, E. N. M. *et al.* Quantitative and qualitative flow cytometric analysis of nanosized cell-derived membrane vesicles. *Nanomedicine: Nanotechnology, Biology, and Medicine* **8**, 712–720 (2012).
8. Gustafson, M. P. *et al.* Systemic immune suppression in glioblastoma: the interplay between CD14+HLA-DRlo/neg monocytes, tumor factors, and dexamethasone. *Neuro-Oncology* **12**, 631–644 (2010).
9. Lai, C. P. *et al.* Visualization and tracking of tumour extracellular vesicle delivery and RNA translation using multiplexed reporters. *Nat Commun* **6**, 7029 (2015).
10. Xue, J. *et al.* Transcriptome-Based Network Analysis Reveals a Spectrum Model of Human Macrophage Activation. *Immunity* **40**, 274–288 (2014).
11. Butovsky, O. *et al.* Identification of a unique TGF- β -dependent molecular and functional signature in microglia. *Nat. Neurosci.* **17**, 131–143 (2014).
12. Keren-Shaul, H. *et al.* A Unique Microglia Type Associated with Restricting Development of Alzheimer’s Disease. *Cell* **169**, 1276–1290.e17 (2017).
13. Krasemann, S. *et al.* The TREM2-APOE Pathway Drives the Transcriptional Phenotype of Dysfunctional Microglia in Neurodegenerative Diseases. *IMMUNI* **47**, 566–581.e9 (2017).
14. Szulzewsky, F. *et al.* Human glioblastoma-associated microglia/monocytes express a distinct RNA profile compared to human control and murine samples. *Glia* **64**, 1416–1436 (2016).
15. Coumans, F. A. W. *et al.* Methodological Guidelines to Study Extracellular Vesicles. *Circ. Res.* **120**, 1632–1648 (2017).
16. Rupert, D. L. M., Claudio, V., Lässer, C. & Bally, M. Methods for the physical characterization and quantification of extracellular vesicles in biological samples. *BBA - General Subjects* **1861**, 3164–3179 (2017).
17. Théry, C., Amigorena, S., Raposo, G. & Clayton, A. Isolation and characterization of exosomes from cell culture supernatants and biological fluids. *Curr Protoc Cell Biol* **Chapter 3**, Unit 3.22–3.22.29 (2006).
18. Stoner, S. A. *et al.* High sensitivity flow cytometry of membrane vesicles. *Cytometry* **89**, 196–206 (2015).
19. Akers, J. C. *et al.* Comparative Analysis of Technologies for Quantifying Extracellular Vesicles (EVs) in Clinical Cerebrospinal Fluids (CSF). *PLoS ONE* **11**, e0149866–11 (2016).
20. van der Pol, E. *et al.* Particle size distribution of exosomes and microvesicles determined by transmission electron microscopy, flow cytometry, nanoparticle tracking analysis, and resistive pulse sensing. *J Thromb Haemost* **12**, 1182–1192 (2014).
21. Gardiner, C., Ferreira, Y. J., Dragovic, R. A., Redman, C. W. G. & Sargent, I. L. Extracellular vesicle sizing and enumeration by nanoparticle tracking analysis. *Journal of Extracellular Vesicles* **2**, 525 (2013).
22. Dragovic, R. A. *et al.* Sizing and phenotyping of cellular vesicles using Nanoparticle Tracking Analysis. *Nanomedicine: Nanotechnology, Biology, and Medicine* **7**, 780–788 (2011).
23. Filipe, V., Hawe, A. & Jiskoot, W. Critical Evaluation of Nanoparticle Tracking Analysis (NTA) by NanoSight for the Measurement of Nanoparticles and Protein Aggregates. *Pharm Res* **27**, 796–810 (2010).
24. van der Pol, E. *et al.* Optical and non-optical methods for detection and characterization of microparticles and exosomes. *J Thromb Haemost* **8**, 2596–2607 (2010).
25. Yáñez-Mó, M. *et al.* Biological properties of extracellular vesicles and their physiological functions. *Journal of Extracellular Vesicles* **4**, 27066 (2015).
26. Abels, E. R. & Breakefield, X. O. Introduction to Extracellular Vesicles: Biogenesis, RNA Cargo Selection, Content, Release, and Uptake. *Cellular and Molecular Neurobiology* **36**, 301–312 (2016).
27. Gardiner, C. *et al.* Measurement of refractive index by nanoparticle tracking analysis reveals heterogeneity in extracellular vesicles. *Journal of Extracellular Vesicles* **3**, 25361–7 (2014).
28. Vogel, R. *et al.* A standardized method to determine the concentration of extracellular vesicles using tunable resistive pulse sensing. *Journal of Extracellular Vesicles* **5**, 31242–14 (2016).
29. Lötvall, J. *et al.* Minimal experimental requirements for definition of extracellular vesicles and their functions: a position statement from the International Society for Extracellular Vesicles. *Journal of Extracellular Vesicles* **3**, 26913–7 (2014).
30. Quail, D. F. & Joyce, J. A. The Microenvironmental Landscape of Brain Tumors. *Cancer Cell* **31**, 326–341 (2017).
31. Hambardzumyan, D., Gutmann, D. H. & Kettenmann, H. The role of microglia and macrophages in glioma maintenance and progression. *Nat. Neurosci.* **19**, 20–27 (2015).
32. Al-Nedawi, K. *et al.* Intercellular transfer of the oncogenic receptor EGFRVIII by microvesicles derived from tumour cells. *Nat Cell Biol* **10**, 619–624 (2008).
33. Skog, J. *et al.* Glioblastoma microvesicles transport RNA and proteins that promote tumour growth and provide diagnostic biomarkers. *Nat Cell Biol* **10**, 1470–1476 (2008).
34. Morantz, R. A., Wood, G. W., Foster, M., Clark, M. & Gollahon, K. Macrophages in experimental and human brain tumors. Part 2: studies of the macrophage content of human brain tumors. *J. Neurosurg.* **50**, 305–311 (1979).
35. van der Vos, K. E. *et al.* Directly visualized glioblastoma-derived extracellular vesicles transfer RNA to microglia/macrophages in the brain. *Neuro-Oncology* nov244 (2015). doi:10.1093/neuonc/nov244
36. Wei, Z., Batagov, A. O., Carter, D. R. F. & Krichevsky, A. M. Fetal Bovine Serum RNA Interferes with the Cell Culture derived Extracellular RNA. *Sci Rep* 1–6 (2016). doi:10.1038/srep31175
37. van Niel, G., D’Angelo, G. & Raposo, G. Shedding light on the cell biology of extracellular vesicles. *Nat. Rev. Mol. Cell Biol.* **19**, 213–228 (2018).
38. Kowal, J. *et al.* Proteomic comparison defines novel markers to characterize heterogeneous populations of extracellular vesicle subtypes. *Proc Natl Acad Sci USA* **113**, E968–E977 (2016).

39. Rong, Y., Durden, D. L., Van Meir, E. G. & Brat, D. J. 'Pseudopalisading' necrosis in glioblastoma: a familiar morphologic feature that links vascular pathology, hypoxia, and angiogenesis. *Journal of neuropathology and experimental neurology* **65**, 529–539 (2006).
40. Lee, K. *et al.* Multiplexed Profiling of Single Extracellular Vesicles. *ACS Nano* **12**, 494–503 (2018).
41. de Vrij, J. *et al.* Glioblastoma-derived extracellular vesicles modify the phenotype of monocytic cells. *Int. J. Cancer* **137**, 1630–1642 (2015).
42. Verhaak, R. G. W. *et al.* Integrated genomic analysis identifies clinically relevant subtypes of glioblastoma characterized by abnormalities in PDGFRA, IDH1, EGFR, and NF1. *Cancer Cell* **17**, 98–110 (2010).
43. Patel, A. P. *et al.* Single-cell RNA-seq highlights intratumoral heterogeneity in primary glioblastoma. *Science* **344**, 1396–1401 (2014).
44. Svensson, K. J. *et al.* Hypoxia triggers a proangiogenic pathway involving cancer cell microvesicles and PAR-2-mediated heparin-binding EGF signaling in endothelial cells. *Proc. Natl. Acad. Sci. U.S.A.* **108**, 13147–13152 (2011).
45. Rong, Y., Durden, D. L., Van Meir, E. G. & Brat, D. J. 'Pseudopalisading' necrosis in glioblastoma: a familiar morphologic feature that links vascular pathology, hypoxia, and angiogenesis. *Journal of neuropathology and experimental neurology* **65**, 529–539 (2006).
46. Saederup, N. *et al.* Selective Chemokine Receptor Usage by Central Nervous System Myeloid Cells in CCR2-Red Fluorescent Protein Knock-In Mice. *PLoS ONE* **5**, e13693 (2010).
47. Mizutani, M. *et al.* The fractalkine receptor but not CCR2 is present on microglia from embryonic development throughout adulthood. *J. Immunol.* **188**, 29–36 (2012).
48. Ginhoux, F. & Jung, S. Monocytes and macrophages: developmental pathways and tissue homeostasis. *Nature Publishing Group* **14**, 392–404 (2014).
49. Hoeffel, G. *et al.* Adult Langerhans cells derive predominantly from embryonic fetal liver monocytes with a minor contribution of yolk sac-derived macrophages. *J. Exp. Med.* **209**, 1167–1181 (2012).
50. Li, W. & Graeber, M. B. The molecular profile of microglia under the influence of glioma. *Neuro-Oncology* **14**, 958–978 (2012).
51. Wurdinger, T., Deumelandt, K., van der Vliet, H. J., Wesseling, P. & de Gruij, T. D. Mechanisms of intimate and long-distance cross-talk between glioma and myeloid cells: how to break a vicious cycle. *Biochim. Biophys. Acta* **1846**, 560–575 (2014).
52. Hambardzumyan, D., Gutmann, D. H. & Kettenmann, H. The role of microglia and macrophages in glioma maintenance and progression. *Nat. Neurosci.* **19**, 20–27 (2015).
53. Hu, F. *et al.* Glioma-derived versican promotes tumor expansion via glioma-associated microglial/macrophages Toll-like receptor 2 signaling. *Neuro-Oncology* **17**, 200–210 (2014).
54. Ransohoff, R. M. A polarizing question: do M1 and M2 microglia exist? *Nat. Neurosci.* **19**, 987–991 (2016).
55. Szulzewsky, F. *et al.* Glioma-associated microglia/macrophages display an expression profile different from M1 and M2 polarization and highly express Gpnmb and Spp1. *PLoS ONE* **10**, e0116644 (2015).
56. Gabrusiewicz, K. *et al.* Glioblastoma-infiltrated innate immune cells resemble M0 macrophage phenotype. *JCI Insight* **1**, 1–19 (2016).
57. Hickman, S., Izzy, S., Sen, P., Morsett, L. & Khoury, E. J. Microglia in neurodegeneration. *Nat. Neurosci.* **21**, 1359–1369 (2018).
58. Hickman, S. E. *et al.* The microglial sensome revealed by direct RNA sequencing. *Nat. Neurosci.* **16**, 1896–1905 (2013).
59. Sun, C., Mezzadra, R. & Schumacher, T. N. Regulation and Function of the PD-L1 Checkpoint. *IMMUNI* **48**, 434–452 (2018).
60. Reardon, D. A. *et al.* OS10.3 Randomized Phase 3 Study Evaluating the Efficacy and Safety of Nivolumab vs Bevacizumab in Patients With Recurrent Glioblastoma: CheckMate 143. *Neuro-Oncology* **19**, iii21–iii21 (2017).
61. Sampson, J. H. *et al.* A randomized, phase 3, open-label study of nivolumab versus temozolomide (TMZ) in combination with radiotherapy (RT) in adult patients (pts) with newly diagnosed, O-6-methylguanine DNA methyltransferase (MGMT)-unmethylated glioblastoma (GBM): CheckMate-498. *Journal of Clinical Oncology* **34**, TPS2079–TPS2079 (2016).
62. Weller, M. *et al.* A randomized phase 2, single-blind study of temozolomide (TMZ) and radiotherapy (RT) combined with nivolumab or placebo (PBO) in newly diagnosed adult patients (pts) with tumor O6-methylguanine DNA methyltransferase (MGMT)-methylated glioblastoma (GBM)—CheckMate-548. *Annals of Oncology* **27**, (2016).
63. Saha, D., Martuza, R. L. & Rabkin, S. D. Macrophage Polarization Contributes to Glioblastoma Eradication by Combination Immunovirotherapy and Immune Checkpoint Blockade. *Cancer Cell* **32**, 253–267.e5 (2017).
64. Pimenova, A. A., Marcora, E. & Goate, A. M. A Tale of Two Genes: Microglial Apoe and Trem2. *IMMUNI* **47**, 398–400 (2017).
65. Butovsky, O. & Weiner, H. L. Microglial signatures and their role in health and disease. *Nat. Rev. Neurosci.* 1–14 (2018). doi:10.1038/s41583-018-0057-5
66. Gosselin, D. *et al.* An environment-dependent transcriptional network specifies human microglia identity. *Science* **356**, eaal3222–13 (2017).

Addenda

**Nederlandse samenvatting
List of publications
Curriculum vitae
Dankwoord**

Inleiding en context van dit proefschrift

In volwassenen zijn glioblastomen de meest voorkomende en meest dodelijke primaire hersentumor. Patiënten bij wie een glioblastoom gediagnostiseerd wordt, ondergaan wanneer de klinische conditie dit toestaat, maximale chirurgie gevolgd door chemoradiatie therapie. Ondanks deze combinatie van verschillende behandelingsmodaliteiten zijn de overlevingsstatistieken van glioblastoom patiënten bijzonder slecht. Patiënten die chirurgie en chemoradiatie ondergaan hebben een mediane overleving van net iets meer dan 15 maanden. Deze statistiek is in de afgelopen 15 jaar slechts minimaal toegenomen. Wereldwijd wordt daarom veel onderzoek gedaan naar glioblastoom tumoren in een poging om de biologie van deze tumoren beter te begrijpen en zo tot nieuwe behandelingsmogelijkheden te komen. Eén van de onderwerpen waar de afgelopen jaren veel aandacht voor is geweest, is het identificeren van moleculaire subtypen van glioblastoom tumoren. Zo heeft genetisch onderzoek aangetoond dat er, wanneer naar het totaalprofiel van een tumor gekeken wordt, in IDH wildtype glioblastoom tumoren grofweg drie moleculaire subtypen geïdentificeerd kunnen worden. Deze typen zijn het proneurale, klassieke en mesenchymale subtype. Vooralsnog zijn er geen medicamenten gevonden die beter werken wanneer ze gegeven worden aan een patiënt met een specifiek subtype glioblastoom. Dit komt mede omdat recent onderzoek aangetoond heeft dat wanneer men op individueel celniveau gaat kijken, een glioblastoom tumorcellen bevat van alle drie de subtypen. Om tot nieuwe behandelingsstrategieën te komen is dus nog meer kennis nodig over de biologie van een glioblastoom tumor.

Naast moleculaire subtypen van de tumor wordt ook veel onderzoek gedaan naar niet-tumorcellen die onderdeel uitmaken van de directe omgeving van de tumorcellen. In geval van glioblastomen betreft dit onder andere endotheelcellen van (nieuwgevormde) bloedvaten, astrocyten, neuronen, lymfocyten en cellen van het aangeboren afweersysteem zoals monocytten, macrofagen en microglia. Samen met de maligne cellen vormen deze cellen een micro-milieu dat over het algemeen de groei van de maligne cellen lijkt te stimuleren. Tussen de glioblastoom cellen en de normale cellen in de directe omgeving van de tumor wordt op verschillende manieren gecommuniceerd, namelijk via direct contact, uitgescheiden moleculen en/of extracellulaire membraanblaasjes (extracelullar vesicles, EVs). Deze EVs zijn 50 tot 10.000 nanometer in diameter en kunnen op verschillende manieren door de cel uitgescheiden worden. EVs zijn net als een cel opgebouwd uit een bilipide laag en bevatten een soort cytosol waarin moleculen liggen die van de donorcel afkomstig

zijn. Glioblastoom cellen scheiden dus EVs uit die tumor specifieke moleculen (RNA en eiwitten) bevatten. Wanneer deze glioblastoom EVs door de normale cellen in de directe omgeving worden opgenomen, zou het kunnen dat de normale cellen hierdoor veranderen. Dit kan potentieel leiden tot een directe omgeving van de tumor die de tumor ondersteunt in plaats van aanvalt. Omdat de EVs echter zo klein zijn, is het bestuderen van deze EVs een uitdaging en zijn er nieuwe methoden nodig om de EVs te kunnen karakteriseren en zo hun functie te identificeren. Pas wanneer dit mogelijk is kan het daadwerkelijke effect van glioblastoom EVs op de cellen in de directe omgeving van de tumor onderzocht worden en hun tumor ondersteunende potentie bepaald worden.

Dit proefschrift

In dit proefschrift worden de resultaten beschreven van de experimenten die gedaan zijn om twee doelstellingen te behalen. De eerste doelstelling was om experimenten uit te voeren met detectoren die, gezien hun detectieresolutie, deeltjes met de diameters van EVs kunnen onderscheiden. Er zijn in dit kader experimenten gedaan om de mogelijkheden en beperkingen van deze machines te beoordelen en verifiëren. Als tweede doelstelling zijn er met behulp van deze detectoren experimenten gedaan om het effect van glioblastoom EVs op cellen van het aangeboren afweersysteem (monocytten, macrofagen en microglia) in de directe omgeving van de tumorcellen te testen. Allereerst is dit in celkweek omstandigheden gedaan (*in vitro*) en vervolgens in levende muizen (*in vivo*) om een meer realistische directe omgeving van de tumorcellen te kunnen bestuderen.

In **hoofdstuk twee** wordt een specifieke nieuwe EV-detectie techniek, namelijk tunable resistive pulse sensing (tRPS) geïntroduceerd en beoordeeld. In tRPS worden deeltjes gedetecteerd wanneer deze door een zeer kleine opening (nanopore) gaan die twee vloeistofcompartimenten scheidt. Omdat er een spanningsverschil is tussen de twee vloeistofcompartimenten verplaatsen zich door de opening naast EVs ook ionen. Wanneer een EV door deze nanopore gaat wordt de stroom van ionen aangepast hetgeen in de vorm van een veranderd spanningsverschil gemeten kan worden. Naast een meting met EVs worden ook polystyrene beads met een bekende diameter en concentratie gemeten. De mate van onderbreking van de ionenstroom die de beads met bekende diameter veroorzaken, kunnen gebruikt worden om de diameter van

de EVs te bepalen. Naast de mate van onderbreking wordt bij tRPS ook de frequentie van onderbrekingen gemeten. Omdat de concentratie van de beads bekend is, kan de frequentie van onderbrekingen in een EV-sample omgerekend worden naar een concentratie EVs in de vloeistof. tRPS kan zodoende in potentie in een EV-vloeistof sample de afmeting en hoeveelheid van EVs bepalen.

De realiteit is echter dat er snel problemen ontstaan wanneer er met biologische samples, zoals met EV-samples, gewerkt wordt. De nanopore in het tRPS apparaat raakt bijvoorbeeld verstopt door grote EVs, of de EVs veranderen andere parameters zoals de baseline spanning zodat er geen betrouwbare conversieberekeningen tussen calibratie beads en EVs gedaan kunnen worden. In hoofdstuk twee introduceerden wij een aangepaste tRPS methode waarin we de calibratie beads niet los gemeten, maar juist in het EV-sample opgelost werden. In deze samples kunnen vervolgens kleine (EVs) en grotere deeltjes (calibratie beads) geïdentificeerd worden en door middel van de klein-tot-groot ratio de concentratie EVs, op basis van de concentratie toegevoegde beads, berekend worden. Met deze methode lukte het ons in kleine volumes (30µl) biologische vloeistoffen zoals urine, pleuravocht en plasma EVs te meten. Dit kon al na slechts minimale voorbehandeling van het sample waarbij potentieel selectie introducerende factoren zoals filtratie en ultracentrifugatie overgeslagen konden worden.

Deze methode hebben we daarna gebruikt om de hoeveelheid EVs van aangepaste glioblastoomcellen te meten, om te zien of we die hoeveelheid konden beïnvloeden. Dit kan bijvoorbeeld helpen bij onderzoek naar de rol van EVs in tumorgroei. Om dit te bereiken werden door middel van lentivirale transductie short-hairpin RNA-moleculen in glioblastoom cellijnen geïntroduceerd die Rab27b expressie verlagen. Rab27b is een eiwit dat het naderen van multivesiculaire lichamen (MVB) met het plasmamembraan faciliteert. MVB bevatten meerdere blaasjes die wanneer het MVB succesvol fuseert met het plasmamembraan de cel verlaten als EVs. Nadat we door middel van de short-hairpin RNAs verminderde Rab27b expressie veroorzaakt hadden, konden we inderdaad verlaagde hoeveelheden EVs meten zowel direct in het supernatant van de cellen als ook na speciale iodixanol gebaseerd ultra-centrifugatie isolatie van exosomen, een EV-subtype. De door ons ontwikkelde aangepaste tRPS techniek stelde ons daarna in staat om uit verschillende verdunningen van EVs dezelfde basisconcentratie te berekenen en om aan te tonen dat meerdere vries-ontdooicycli de concentratie van glioblastoom EVs niet doet veranderen. Deze gemodificeerde tRPS

techniek maakte het dus mogelijk om samples EVs te kwantificeren en vergelijken om zo dus experimenten met EVs uit te voeren.

Vervolgens worden in **hoofdstuk drie** nog twee andere EV-karakterisatiemethoden getest en vergeleken. Deze andere technieken zijn nanoparticle tracking analysis (NTA) en high-resolution flow-cytometry (hFC). De tRPS, NTA en hFC technieken werden onderzocht op hun mogelijkheden en beperkingen op het gebied van EV-karakterisatie door elke techniek te gebruiken bij het meten van (fluorescente) polystyrene beads, liposomen, EVs geïsoleerd van glioblastoom en een lymfoblastaire cellijn. Voor elke techniek lieten we zien dat er, op basis van de onderliggende detectiemethode, een "detectie drempel" is die bepaalt of een EV gedetecteerd wordt of niet. Bij de uitvoering van EV-karakterisatie door middel van het gebruik van (één van) deze technieken is het dus van groot belang rekening te houden met deze detectie drempel.

Voor tRPS lieten we zien dat de relatie van de diameter van de EV tot de nanopore waar deze doorheen gaat bepaalt of de EV gedetecteerd wordt. Wanneer de opening te groot is, is de verstoring van ionenstroom te klein om gedetecteerd te worden. Omdat EV-samples een heterogene populatie van deeltjes zijn waarbij de diameter van de kleinste deeltjes niet bekend is, kan dit tot onderschatting van de ware EV-concentratie leiden omdat de kleinste deeltjes niet gemeten worden. De grotere EVs bepalen immers hoe nauw de nanopore afgesteld kan worden voordat deze verstopt raakt.

Bij NTA worden deeltjes op een totaal andere manier gedetecteerd maar ook hier is een potentieel limiterende detectie drempel aanwezig. Bij NTA worden deeltjes gedetecteerd op basis van de hoeveelheid licht die ze verstrooien. Dit verstrooide licht wordt opgewekt door een laser en gedetecteerd door een camera die op een microscoop gemonteerd is. De gevoeligheid en meetintensiteit van deze camera kan aangepast worden zodat deeltjes van verschillende afmeting en compositie gedetecteerd kunnen worden. We lieten zien dat het veranderen van de camera gain en sluitersnelheid leidt tot significant verschillend gemeten EV-concentraties. Het zijn hier met name de grotere EVs die verstorend zijn omdat de hoeveelheid verstrooid licht met de factor 1 miljoen toeneemt wanneer de diameter slechts 10 maal groter wordt. De aanwezigheid van enkele grotere EVs maakt het gebruik van minder gevoelige instellingen van het apparaat dus noodzakelijk waardoor de kleinere EVs, net als bij tRPS, niet gedetecteerd kunnen worden.

hFC is een gemodificeerde flowcytometrie methode waarbij fluorescente subcellulaire deeltjes gemeten kunnen worden door onder andere de vloeistofstroom door de machine en de licht gevoeligheid aan te passen. Alleen EVs die voldoende fluoriserend zijn kunnen gedetecteerd worden en zodoende bepaalt deze parameter de detectie drempel voor EVs bij hFC metingen.

Ondanks de beperkingen per geteste techniek lukte het ons om voor alle drie de technieken accuraat verdunningen van zowel polystyrene beads, liposomen en EVs te meten. Dit betekent dat wanneer, voor het opzetten van een experiment, verschillende EV-samples qua concentratie gelijkgesteld kunnen worden, metingen binnen een individuele techniek gedaan kunnen worden met exact dezelfde instellingen. Wanneer we echter metingen van liposomen en EVs tussen tRPS, NTA en hFC vergeleken, werden significante verschillen tussen de metingen van de machines gedetecteerd. Alleen de gemeten EV-concentraties tussen NTA en hFC toonde een niet-significant verschil. Een gemeten EV-concentratie is dus niet direct te vergelijken tussen technieken of binnen een techniek wanneer verschillende instellingen gebruikt worden.

De kennis die werd opgedaan in de eerdere hoofdstukken wordt vervolgens in **hoofdstuk vier** toegepast op de karakterisatie van glioblastoom EVs en hun effect op monocytten, macrofagen en microglia *in vitro*. Door het aantal cellen en de EV-concentratie om te rekenen naar een "EV-tot-cel" ratio, vonden we grote verschillen in deze ratio tussen negen primaire glioblastoom stamcelkweken. Deze kweken zijn opgezet met tumormateriaal direct afgenomen bij glioblastoom patiënten en bevatten dus verschillende eigenschappen omdat ze van verschillende primaire tumoren komen. We detecteerden de hoogste EV-tot-cel ratio's in de drie kweken afkomstig van tumoren met een mesenchymal dominant moleculair subtype.

Vervolgens hebben we gekeken naar de eiwitten die in de EVs van glioblastoom cellen zitten. Bij deze analyse werd sterk verhoogde expressie van eiwitten gedetecteerd die betrokken zijn bij de proliferatie, beweging en fagocytose van monocytten en macrofagen. Om te kijken of deze eiwitten ook daadwerkelijk functioneel zijn, werd een experiment uitgevoerd waarin glioblastoom EVs aan mononucleaire cellen (oa. monocytten) uit het bloed van gezonde donoren werden toegevoegd. Dit liet zien dat in vergelijking tot incubatie met identieke hoeveelheden EVs van niet-maligne cellen, incubatie met glioblastoom EVs zorgde voor een verhoogde proliferatie van deze cellen. Tegelijkertijd werd er bij incubatie met tumor EVs verminderde expressie

gedetecteerd van HLA-DR op het oppervlak van monocytten. Verminderde HLA-DR expressie op monocytten wordt gezien bij glioblastoom patiënten en is een teken van verminderde afweer. Om dieper in te gaan op het veranderde immuunprofiel van monocytten na co-incubatie met glioblastoom EVs werden monocytten tot macrofaag gedifferentieerd in combinatie met EVs afkomstig van glioblastoom kweken of met EVs van normale cellen als controle conditie. In macrofagen die gedifferentieerd waren samen met glioblastoom EVs konden we verhoogde expressie detecteren van markers die geassocieerd zijn met tumor ondersteunende functies (bijvoorbeeld CD163), alsook verhoogde fagocytair capaciteit en cytokine productie (bijvoorbeeld VEGF, IL4, IL6, IL10 en IFN γ). In een vergelijkbaar experiment waarbij humane microglia gekweekt werden met glioblastoom EVs konden we verhoogde expressie van MT1-MMP (MMP14) meten, een belangrijke metalloprotease die betrokken is bij het aanpassen van de extracellulaire matrix (ECM) in glioblastoom tumoren.

Samengevat, *in vitro* co-incubatie van glioblastoom EVs met primaire monocytten, macrofagen en microglia resulteerde in verhoogde expressie van markers en functies die geassocieerd zijn met een tumor ondersteunend milieu.

Hoofdstuk vijf gaat over de resultaten van de analyse van mRNA expressiepatronen van microgliacellen die geïsoleerd zijn uit het brein van muizen met een glioom. De glioomcellen van deze tumoren waren aangepast om palmitoylated-GFP, een versie van GFP dat zich in alle bilipide lagen van de cel nestelt, tot expressie te brengen. Deze palmitoylated-GFP reporter komt ook in de bilipide laag van de EVs en met dit systeem kunnen dus *in vivo* EVs gemarkeerd worden met het groen fluorescerende eiwit GFP. Uit de muizenbreinen werden vervolgens monocytten, macrofagen en microglia geïsoleerd die EVs hadden opgenomen (EV-GFP^{pos}) of juist niet (EV-GFP^{neg}). Door naar verschillende delen van de muizenbreinen te kijken, zagen we dat er alleen EV-GFP opname in microglia gedetecteerd kon worden in of direct naast de tumor. De EV-GFP status kan dus gebruikt worden om microglia te identificeren die in nauw contact staan met de tumorcellen. Door vervolgens naar de resultaten van mRNA sequencing te kijken, zagen we dat de EV-GFP opname geassocieerd is met grote verschillen in mRNA expressie in microglia cellen. Tegelijk zagen we bij monocytten en macrofagen slechts geringe verschillen tussen EV-GFP^{pos} en EV-GFP^{neg} cellen. Omdat we geïnteresseerd zijn in het verschil tussen cellen die wel of niet EVs opgenomen hebben, hebben we ervoor gekozen het overgrote deel van de analyses op microglia te richten.

In de *in vitro* (tumor)biologie werd traditioneel vaak aangenomen dat macrofagen en microglia ofwel anti-tumor zijn (M1) of juist de tumor helpen in de groei (M2). Deze M1 of M2 profielen kunnen geïnduceerd worden door de cellen te differentiëren middels toevoeging van cytokinen zoals bijvoorbeeld IFN γ voor M1 en IL-4 voor M2. Door naar de mRNA expressie profielen te kijken van genen die geassocieerd zijn met deze specifieke cytokinen (IL4, IL6, IL10 en IFN γ), zagen we dat *in vivo* de EV-GFP^{pos} microglia juist een heel gecompliceerd differentiatieprofiel tonen met zowel kenmerken van M1 als van M2 *in vitro* microglia. Om nog dieper naar de expressieprofielen te kijken van tumor microglia hebben we vervolgens naar de drie essentiële functies van microglia gekeken: het registreren van veranderingen in de omgeving, afweer en homeostase. Voor alle drie deze functies vonden we grote verschillen in de expressieprofielen van tumor microglia in vergelijking met controle microglia. EV-GFP^{pos} microglia hebben bijvoorbeeld een significant gereduceerde expressie van 48% van de registratiegenen versus 9% significante verhoogde expressie. Microglia in nauw contact met glioomcellen kunnen (gevaar)signalen, zoals de aanwezigheid van tumorcellen, dus minder goed registreren.

Op het gebied van de afweer werden ook interessante veranderingen gedetecteerd. Zo vonden we significant verhoogde expressie van *Pd-I1* en *Pd-I2*. Deze twee genen zijn geassocieerd met het onderdrukken van de T-cel respons in het micro-milieu van tumoren waardoor de host-versus-tumor respons verminderd wordt. Het efficiënt opruimen van tumorcellen door het immuunsysteem is door de hoge *Pd-I1* en *Pd-I2* expressie dus niet mogelijk.

Op het gebied van homeostase werden ook significante verschillen gedetecteerd in microglia die uit tumor breinen geïsoleerd werden. Zo zagen we significant verhoogde expressie van genen die betrokken zijn bij fagocytose en het afbreken van de ECM. Fagocytose en het afbreken van ECM kan tumorcellen helpen om het brein te infiltreren.

Samengenomen suggereren deze resultaten dat *in vivo* EV-GFP^{pos} microglia verminderde mogelijkheden hebben om (pathologische) veranderingen te registreren en verminderde functie hebben om een T-cel immuunrespons te induceren met tegelijk een verhoogde mogelijkheid om debris op te ruimen en infiltratie van het brein te faciliteren.

Om verder te zoeken naar pathways die de gevonden expressiepatronen kunnen verklaren, hebben we vervolgens naar pathways gekeken die mRNA expressie in

microglia kunnen reguleren. In normale, niet zieke, microglia reguleert TGF- β de homeostase van microglia. In de tumor microglia zagen wij dat er sprake was van significant verlaagde expressie van TGF- β en door TGF- β gereguleerde genen. In neurodegeneratieve ziekten is beschreven dat wanneer de TGF- β regulatie van homeostase ontwricht is, een pathway met Triggering receptor expressed on myeloid cells 2 (TREM2) and apolipoprotein E (APOE) de regulatie van homeostase reguleert. Deze regulatie is voor een deel afhankelijk en voor een deel onafhankelijk van TREM2. In de microglia van muizen met een glioom vonden wij significant verminderde expressie van *Trem2*, maar tegelijk ook significant verhoogde expressie van *ApoE*. Dit suggereert dat in de context van gliomen APOE belangrijker is dan TREM2 in de regulatie van mRNA expressie. Door vervolgens te kijken naar de RNA sequencing profielen van microglia geïsoleerd uit muizen die helemaal geen *Trem2* of *ApoE* tot expressie brengen (knock-out muizen), zagen we dat de veranderingen in de expressie van registratie, afweer en homeostase genen inderdaad *Trem2* onafhankelijk en waarschijnlijk juist *ApoE* afhankelijk zijn. Om verder aan te tonen dat APOE in glioom microglia de meest waarschijnlijke regulator van RNA expressie is, hebben we vervolgens gekeken naar gepubliceerde datasets van humane microglia en microglia van glioblastoom patiënten. Ook in deze analyse zagen we een significant verhoogde expressie van APOE en door APOE gereguleerde genen, terwijl het expressie niveau van TREM2 geen significante veranderingen liet zien. Om verder te onderzoeken of *in vivo* de veranderingen in tumor microglia net als *in vitro* door EVs geïnduceerd kunnen worden, hebben we geïsoleerde tumor EVs in de breinen van controle muizen geïnjecteerd. Vervolgens hebben we naar de mRNA profielen gekeken van microglia die EVs opgenomen hadden en zagen we dezelfde veranderingen in registratie en *ApoE* gereguleerde genen. Een deel van deze veranderingen was echter (nog) niet significant. Desondanks suggereren deze resultaten dat op z'n minst een deel van het tumor geassocieerde microglia mRNA expressiepatroon geassocieerd is met EV-opname. Samengevat hebben we laten zien dat microglia *in vivo* tumor EVs opnemen, dat dit in of zeer dichtbij de tumor gebeurt, dat de tumor microglia een fenotype hebben met kenmerken van M1 en M2 profielen en dat dit meest waarschijnlijk gereguleerd wordt door APOE. Tot in welke mate EVs *in vivo* een rol spelen in deze complexe differentiatie staat zal verder onderzocht moeten worden. Daarbij moet onderzocht worden of het mogelijk is in te grijpen op de APOE pathway om de microglia in een staat te krijgen waarin ze de tumor aanvallen in plaats van faciliteren.

List of publications

S. L. N. Maas*, E. R. Abels*, L. L. Van De Haar, X. Zhang, S. Sil, J. Guedes, P. Sen, S. Prabhakar, S. E. Hickman, C. P. Lai, D. T. Ting, X. O. Breakefield, M. L. D. Broekman and J. El Khoury. Glioblastoma Hijacks Microglial Transcriptional Networks independently of TREM2. Under Review.

* equal author contribution

C. Théry, K. W. Witwer, E. Aikawa, [...], T. R. Lunavat, **S. L. N. Maas**, H. Malhi, [...], D. Zocco, and E. K. Zuba-Surma. Minimal information for studies of extracellular vesicles 2018 (MISEV2018): a position statement of the International Society for Extracellular Vesicles and update of the MISEV2014 guidelines. *Journal of Extracellular Vesicles*, vol. 7, no. 1, p. 1535750, Nov. 2018.

M. L. D. Broekman, **S. L. N. Maas**, E. R. Abels, T. R. Mempel, A. M. Krichevsky, and X. O. Breakefield. Multidimensional communication in the microenvirons of glioblastoma. *Nature Reviews Neurology*, vol. 14, no. 8, pp. 482–495, Aug. 2018.

B. Mateescu, E. J. K. Kowal, B. W. M. van Balkom, [...], M. J. Lorenowicz, **S. L. N. Maas**, I. Mäger, [...], M. H. M. Wauben, K. W. Witwer, and E. N. M. Nolte-'t Hoen, Obstacles and opportunities in the functional analysis of extracellular vesicle RNA – an ISEV position paper. *Journal of Extracellular Vesicles*, vol. 6, no. 1, pp. 1286095–35, Mar. 2017.

S. L. N. Maas, X. O. Breakefield, and A. M. Weaver. Extracellular Vesicles: Unique Intercellular Delivery Vehicles. *Trends in Cell Biology*, vol. 27, no. 3, pp. 172–188, Mar. 2017.

S. L. N. Maas, M. L. D. Broekman, and J. de Vrij. Tunable Resistive Pulse Sensing for the Characterization of Extracellular Vesicles. in *Microarray Methods for Drug Discovery*, vol. 1545, no. 9, New York, NY: Springer New York, 2016, pp. 21–33.

R. Vogel, F. A. W. Coumans, R. G. Maltesen, A. N. Böing, K. E. Bonnington, M. L. Broekman, M. F. Broom, E. I. Buzás, G. Christiansen, N. Hajji, S. R. Kristensen, M. J. Kuehn, S. M. Lund, **S. L. N. Maas**, R. Nieuwland, X. Osteikoetxea, R. Schnoor, B. J. Scicluna, M. Shambrook, J. de Vrij, S. I. Mann, A. F. Hill, and S. Pedersen. A standardized method to determine the concentration of extracellular vesicles using tunable resistive pulse sensing. *Journal of Extracellular Vesicles*, vol. 5, no. 1, pp. 31242–14, Dec. 2016.

J. de Vrij, **S. L. N. Maas**, K. M. C. Kwappenberg, R. Schnoor, A. Kleijn, L. Dekker, T. M. Luider, L. D. de Witte, M. Litjens, M. E. van Strien, E. M. Hol, J. Kroonen, P. A. Robe, M. L. Lamfers, M. W. Schilham, and M. L. D. Broekman. Glioblastoma-derived extracellular vesicles modify the phenotype of monocytic cells. *Int. J. Cancer*, vol. 137, no. 7, pp. 1630–1642, Oct. 2015.

R. Schnoor, **S. L. N. Maas**, and M. L. D. Broekman. Heparin in malignant glioma: review of preclinical studies and clinical results. *J Neurooncol*, pp. 1–6, Jun. 2015.

S. L. N. Maas, J. de Vrij, E. J. van der Vlist, B. Geragousian, L. van Bloois, E. Mastrobattista, R. Schifflers, M. H. M. Wauben, M. L. Broekman, and E. N. M. Nolte-'t Hoen. Possibilities and limitations of current technologies for quantification of biological extracellular vesicles and synthetic mimics. *J Control Release*, no. 200: pp. 87–96. Dec. 2014.

S. L. N. Maas, J. de Vrij, and M. L. D. Broekman. Quantification and Size-profiling of Extracellular Vesicles Using Tunable Resistive Pulse Sensing. *J Vis Exp*, no. 92, 2014.

J. de Vrij*, **S. L. N. Maas***, M. van Nispen, M. Sena-Esteves, R. W. A. Limpens, A. J. Koster, S. Leenstra, M. L. Lamfers, and M. L. D. Broekman, “Quantification of nanosized extracellular membrane vesicles with scanning ion occlusion sensing,” *Nanomedicine (Lond)*, vol. 8, no. 9, pp. 1443–1458, Sep. 2013.

* equal author contribution

J. de Vrij, **S. L. N. Maas**, J. P. Hegmans, M. L. Lamfers, C. M. F. Dirven, and M. L. D. Broekman. [Exosomes and cancer]. *Ned. Tijdschr Geneeskunde*, vol. 155, no. 51, p. A3677, 2011.

Curriculum Vitae

Sybren Lein Nikola Maas was born on September 10th, 1985 in Utrecht, The Netherlands. He graduated secondary school from College Blaucapel in Utrecht and at the Utrecht University he started medical school in 2004. In 2007 – 2008 he paused medical school to spend one year as a front-end software developer at the social media website UGAME.net based in Southampton, United Kingdom. After continuing medical school in 2008 he performed his first scientific internship on the role of extracellular vesicles in glioblastoma tumors in the laboratory of Ass. Prof. Miguel Sena-Esteves at the University of Massachusetts Medical School in Worcester, MA, United States of America. This work was continued during a second scientific internship in the laboratory of Marike Broekman, PhD JD at the University Medical Center in Utrecht, The Netherlands. After completion of medical school in 2012, he enrolled in the PhD program of the Utrecht University neuroscience graduate school of life sciences in the laboratory of Marike Broekman again studying extracellular vesicles in glioblastoma tumors. For a period of 16 months this work was performed in the laboratory of Prof. Xandra Breakefield at Massachusetts General Hospital (MGH)/Harvard Medical School, Boston, MA, United States of America. During this visit a close collaboration with the lab of Ass. Prof. Joseph El Koury, also at MGH was established focusing on the biology of microglia in glioblastoma tumors. In 2016 he enrolled in the pathology residency program of the University Medical Center of the Utrecht University. This residency is combined with a part-time appointment in the Broekman laboratory, shifting his focus to the bioinformatics part of the Broekman/Breakefield/El Khoury collaborative efforts.

